Petrogenesis of the Sunday Lake Intrusion, Jacques Township, Ontario, Canada

Kevin Mexia Durán

A thesis presented to Lakehead University in partial fulfillment of the requirements for the degree of Master of Science in Geology



Department of Geology

Thunder Bay, Ontario, Canada, 2025

Abstract

The Sunday Lake Intrusion (SLI) is an early-phase (1109.0±1.3 Ma) mafic-ultramafic intrusion associated with the Midcontinent Rift System. It was emplaced along the Crock Lake Fault, a splay of the regional Quetico fault. The intrusion is a layered funnel/tabular-shaped intrusion divided into Gabbro, Upper Ultramafic, Lower Ultramafic and Marginal zones. The intrusion hosts significant Ni-Cu-Platinum group-elements (PGE) mineralization within the Marginal Zone, which contains up to 2.11 g/t platinum, 0.95 g/t palladium, 0.16 g/t gold, 0.26% copper and 0.11% nickel. In total, this contact-type deposit hosts an estimated 20.4 Mt at an average grade of 2.5 g/t combined Pt+Pd+Au. Mineralization reflects late-stage exsolution of PGM from sulfide melt, including maslovite, michenerite, sperrylite and native silver, platinum and palladium.

The SLI comprises wehrlite, olivine clinopyroxenite, feldspathic olivine clinopyroxenite, melagabbro, gabbro, leucogabbro, quartz monzonite and quartz gabbro. Trace element and radiogenic isotope data support a mantle plume origin, with patterns resembling ocean island basalts (OIB) and likely tied to the Keweenaw Plume. Mass-balance calculations yield a calculated parental magma composition of ~11.15 wt. % FeO and ~19.5 wt. % MgO, consistent with a high-Mg tholeiitic basaltic magma. Compositional variations in olivine and whole-rock MgO (wt. %) suggest the SLI was formed from two discrete magma injections: the first formed the Lower Ultramafic Zone and Marginal Zone, and the second formed the Upper Ultramafic Zone.

Radiogenic isotopes values (ɛNd and ⁸⁷Sr/⁸⁶Sr) are mostly mantle-like, though early-pulse samples show negative Nb anomalies from limited interaction with the subcontinental lithospheric mantle beneath the lithosphere. A later injection of purely primitive, plume-derived magma appears to have flushed the staging chamber, depleting the subcontinental lithosphere mantle (SCLM) signature and resetting the sulfur isotope system to near-mantle values. This two-stage model explains the combination of mantle-like isotopes with localized Nb depletion.

Some radiogenic samples from the Gabbro and Marginal zones record isotopic and trace element evidence for assimilation of Quetico metasedimentary rocks. Negative ε Nd values and Nb-Th anomalies, together with decreased Fo in olivine at the Lower Ultramafic Zone-Marginal Zone contact, suggest localized interaction of magma with country rocks. Although this process may have introduced a crustal sulfur signature into the system, it was largely diluted or reset by the later primitive recharge, leaving the overall sulfur isotope system dominated by mantle values.

Acknowledgments

I express my deepest gratitude to Dr. Pete Hollings for his unconditional support, patience and incredible feedback through the entire process of this project. Without your guidance, this thesis wouldn't have been possible. I am greatly grateful.

I thank Impala Canada, for allowing me to conduct this research. Special thanks to Jami Brown who provided support with sampling, database access and providing me with guidance.

I am also sincerely grateful to the NSERC Alliance Grant for making this thesis possible. Many thanks to the Dr. Melville Bartley Memorial CESME Award, the 2024 International Ni-Cu Symposium Award, the Robert Middleton Graduate Award in Geology and the SEGF Student Research Grants. Your generosity made this thesis possible.

Special thanks to Dr. James Tolley for your guidance and invaluable feedback.

I also appreciate the support provided by Dr. Jim Miller and Steve Flank, whose advice contributed enormously to this project.

Thank you, Kristi Tavener and Dr. Jonas Valliunas, who were helpful with sample processing.

A sincere thank you to my family for your constant motivation and support, you were the reason why I gave my best even on the hard times. Thanks for your patience, feedback and laughs.

Special thanks to Dan, Andrea, Jordan, Luis, Chase and Vlad.

Lastly, I would also like to express my deepest gratitude to Génesis. Thank you for cheering me on, even during the challenging days, and for unconditionally believing in me. You were the starting point of this journey, and you are the reason it became one of the best experiences of my life.

Table of Contents

Abstract	i
Acknowledgments	111
Chapter 1: Introduction	1
1.1 Background	1
1.2 Objectives	3
Chapter 2: Regional and Local Geology	5
2.1 Superior Province	5
2.1.1 Quetico Basin	7
2.1.2 Paleo-Mesoproterozoic Rocks	8
2.2 Midcontinent Rift System	9
2.2.1 Intrusive complexes of the Thunder Bay area	11
2.3 Sunday Lake Intrusion	12
Chapter 3: Methods	16
3.1 Sampling	16
3.2 Analytical methods	17
3.2.1 Portable X-Ray Fluorescence	17
3.2.2 Petrography	18
3.2.3 Whole Rock Geochemistry	18
3.2.4 Scanning Electron Microscopy	19
3.2.5 Sulfur isotopes	19
3.2.6 Olivine compositional analyses	21
3.2.7 Strontium and Neodymium isotopes	21
Chapter 4: Results	23
4.1 Magnetic susceptibility and pXRF	23
4.2 Petrology and petrography	26
4.2.1 Gabbro Zone	26
4.2.2 Upper Ultramafic Zone	35
4.2.3 Lower Ultramafic Zone	40
4.2.4 Marginal Zone	43
4.2.5 Host rock – Quetico metasdimentary rocks	47
4.2.6 Platinum group minerals	49
4.3 Whole-rock geochemistry	52

4.4 Stable isotopes	55
4.4.1 Sulfur isotopes	55
4.5 Radiogenic isotopes	57
4.5.1 Strontium-Neodymium isotopes	57
4.6 Mineral chemistry	58
4.6.1 Olivine chemistry	58
Chapter 5: Discussion	60
5.1 Lithostratigraphy	60
5.2 Sulfides and Fe-Ti oxides paragenesis	67
5.2.1 Sulfide phase	68
5.2.2 Fe-Ti Oxides	71
5.3 Tectonic setting and source	72
5.4 Contamination	74
5.4.1 Radiogenic isotopes	78
5.5 Sulfur isotopes and trace elements	82
5.5.1 Microdrilling vs in-situ Laser Ablation	82
5.5.2 Sulfur enrichment	84
5.6 Olivine chemistry and parental magma composition	90
5.7 Petrogenetic model of the Sunday Lake Intrusion	94
5.7.1 Stage A	95
5.7.2 Stage B	96
5.7.3 Stage C	97
5.7.4 Stage D	99
Chapter 6: Conclusions	101
Chapter 7: References	105
Appendix one – Sample information	119
Appendix two – Petrographic descriptions	119
Appendix three – Whole-rock geochemistry	148
Appendix four – Portable XRF data	163
Appendix five – Olivine compositions	184
Appendix six – Sulfur isotopes	218
Appendix seven – Radiogenic isotopes	221

List of figures

Figure 2.1 Terranes and domains of the Superior Province	6
Figure 2.2 Distribution of rocks related to the Midcontinent Rift System	10
Figure 2.3 Sumarry figure of the Sunday Lake Intrusion	14
Figure 3.1 Schematic cross-section of the Sunday Lake Intrusion	17
Figure 4.1 Drill hole SL-17-18B and SL-19-26 chemostratigraphic downhole plots	24
Figure 4.2 Classification diagram for the GZ samples	27
Figure 4.3 Representative drill core samples from the Gabbro Zone	28
Figure 4.4 Photomicrographs of needle-style plagioclase	29
Figure 4.5 Photomicrographs of zoned hematization on plagioclase	30
Figure 4.6 Photomicrographs of various Fe-Ti oxides textures	30
Figure 4.7 Photomicrographs of altered gabbros and apatite phenocrysts	31
Figure 4.8 Photomicrographs of a graphic texture	32
Figure 4.9 Drill core samples of the breccia zone	33
Figure 4.10 Representative pictures of the fragments reaction halo	34
Figure 4.11 Ternary classification diagram for the UUZ samples	35
Figure 4.12 Representative core samples from the UUZ	36
Figure 4.13 Photomicrographs of hornblende chadacrysts	36
Figure 4.14 Photomicrographs of poikilitic and granular textures of the UUZ	37
Figure 4.15 Photomicrographs of chloritized amphiboles	38
Figure 4.16 Photomicrographs of biotite and hornblende associated to Fe-Ti oxides	38
Figure 4.17 Photomicrographs of interstitial and blebby magnetite associated with Ccp	39
Figure 4.18 Ternary classification diagram for the LUZ samples	40
Figure 4.19 Representative drill core samples of the LUZ	40
Figure 4.20 Photomicrographs of representative textures of the LUZ	41
Figure 4.21 Photomicrograph of interstitial oxides and sulfides	42
Figure 4.22 Ternary classification diagram fro the MZ samples	43
Figure 4.23 Representative drill core samples from the MZ.	43
Figure 4.24 Photomicrographs of chromite inclusions	44
Figure 4.25 Photomicrographs of the MZ and various sulfides	46

Figure 4.26 Photomicrographs of various sulfide textures and exsolution minerals	47
Figure 4.27 Representative drill core samples of the Quetico metasedimentary rocks	48
Figure 4.28 Photomicrographs of the Quetico metasedimentary rocks.	49
Figure 4.29 Pie chart of the PGM abundance percentages.	50
Figure 4.30 Back scattered electron images of platinum-group minerals in chalcopyrite	50
Figure 4.31 Back scattered electron images of platinum-group minerals in pyrrhotite	51
Figure 4.32 Chondrite-normalized, whole-rock trace-element variation diagram for the SLI	53
Figure 4.33 Primitive mantle normalized spider diagrams for the SLI zones	54
Figure 4.34 Primitive mantle normalized spider diagrams for SLI contaminated samples	55
Figure 4.35 Downhole variation of δ^{34} S values in two drill holes	56
Figure 4.36 Binary diagram of εNd versus initial Sr _i of the SLI	57
Figure 4.37 Binary diagram of NiO versus % Fo in olivine from the UUZ and LUZ	58
Figure 5.1 Correlation of the lithological zones between two drill holes	61
Figure 5.2 Drill holes SL-17-18B and SL-19-026 chemotratigraphic and mineralogical	
percentage variations	62
Figure 5.3 Schematic representation of pooled early-formed cumulates	65
Figure 5.4 Simplified paragenetic sequence of crystallization for the SLI	68
Figure 5.5 Spider diagram showing the statistical average for each of the SLI zones and the	
Quetico metasedimentary rocks	72
Figure 5.6 Chondrite-normalized, whole-rock REE ratio for the SLI	73
Figure 5.7 Spider diagram showing the statistical average of contaminated samples from the C	ΞZ
and the MZ	74
Figure 5.8 Downhole variation of Nb/Nb*	76
Figure 5.9 Bivariate diagram of Ta/Yb versus Th/Yb	77
Figure 5.10 Binary diagram of εNd versus Sr _i for each zone of the SLI	79
Figure 5.11 Plot of δ34S for ten samples from the Marginal Zone	82
Figure 5.12 Bivariate diagram of S/Se ratios versus δ34S	84
Figure 5.13 Downhole S/Se ratios variation in two drill holes	85
Figure 5.14 Bivariate diagram of Ni/Cu versus MgO	87
Figure 5.15 Downhole range of values and average Fo% for two drill holes	91

Figure 5.16 Binary diagram of FeO and MgO to estimate the parental magma composition	93
Figure 5.17 Schematic model of a four-stage model (A) for the petrogenesis of the Sunday La	ıke
Intrusion	95
Figure 5.18 Schematic model of a four-stage model (B) for the petrogenesis of the Sunday	
Intrusion	97
Figure 5.19 Schematic model of a four-stage model (C) for the petrogenesis of the Sunday	
Intrusion	98
Figure 5.20 Schematic model of a four-stage model (D) for the petrogenesis of the Sunday	
Intrusion	99

List of abbreviations

Act Actinolite
Ap Apatite
Amp Amphibole

BSE Back-scattered electron

Bt Biotite

BZ Breccia zone
Cal Calcite
Cbn Cubanite
Ccp Chalcopyrite
Chl Chlorite
Chr Chromite
Cpx Clinopyroxene

Ep Epidote
GZ Gabbro Zone
Hbl Hornblende
Hem Hematite

HREE Heavy rare earth element

Ilm Ilmenite

ISS Intermediate solid solution

LA-ICP-MS Laser ablation inductively coupled plasma mass

spectrometry

LIP Large igneous province

LOI Lost on ignition

LREE Light rare earth element LUZ Lower Ultramafic Zone

Mag Magnetite

Mag. Sus. Magnetic susceptibility

Mch Michenerite

MDF Mass-dependent fractionation
MIF Mass-independent fractionation

MRS Midcontinent Rift System
Mtsd Metasedimentary rocks
MSS Monosulfide solid solution

Msl Maslovite
MZ Marginal Zone
OIB Ocean Island basalt

Ol Olivine Pd Palladium

PGE Platinum-group element

PGMs Platinum-group minerals

Pl Plagioclase Pn Pentlandite Po Pyrrhotite

PPL Plane polarized light

Py Pyrite

pXRF Portable x-ray fluorescence

Qz Quartz

Rbg Rustenburgite
REE Rare earth element

SEM Scanning electron microscopy

Ser Sericite

SLI Sunday Lake Intrusion

Sph Sphalerite
Spy Sperrylite
Srp Serpentine

UUZ Upper Ultramafic Zone TABS Te, As, Bi, Sn, Sb

TBNIC Thunder Bay North Intrusive Complex

Tlc Talc Troilite

XPL Cross polarized light

Chapter 1: Introduction

1.1 Background

Emerging technologies have dramatically increased the demand for "green-energy metals" to enhance energy efficiency and reduce greenhouse gasses emissions, as the transition to a low-carbon future requires a diversified supply of these critical resources (Hund et al, 2020). Platinum Group Elements (PGE) are part of these "green-metals" as they have high melting points, corrosion resistance and catalytic properties, which help decrease hydrocarbon, carbon monoxide and nitrous oxide emissions (Hughes et al., 2021). Similarly, nickel is widely used for the production of lithium-ion batteries, whereas copper is mainly used for electrical applications. As a result, these metals have become indispensable to various industrial applications, increasing the importance of magmatic sulfide deposits, which contain 96% of global PGE resources and 56% of global Ni resources (Mudd & Jowitt, 2022).

Magmatic Ni-Cu-PGE deposits are classified into two main types: i) sulfide-rich deposits, which contain relatively high concentrations of nickel and copper, and ii) sulfide-poor deposits, characterized by high PGE concentrations (Naldrett et al., 1990). According to Begg et al. (2010), the genesis of most Ni-Cu-PGE deposits is linked to mantle plumes that ascend to the base of the crust and migrate laterally along the base of the subcontinental lithospheric mantle (SCLM) towards cratonic margins, where the lithosphere is thinner. In these regions, decompression melting is induced by tectonic activity, creating lithospheric weak zones that serve as pathways for ascending magmatic plumes.

The formation of Ni-Cu-PGE deposits requires sulfur saturation of the magma, which leads to the precipitation of sulfide liquid. Sulfur saturation can occur through two primary processes: i) fractional crystallization, as the removal of Fe-rich minerals, such as olivine or magnetite, reduces sulfur solubility and triggers sulfide segregation (Li & Ripley, 2009; Smythe et al., 2017) and ii) through contamination (assimilation of crustal material into the magma), which increases sulfur abundance in the magma, initiating sulfur saturation and ultimately causing saturation (Hutchinson et al., 1990; Mungall, 2002; Ripley & Li, 2003; Naldrett, 2004; Begg et al., 2010; Mungall, 2014). Once sulfur saturation is achieved, sulfide droplets segregate from the silicate magma and accumulate at the base of the magma chamber through gravitational settling (Naldrett et al., 1990). Consequently, the highest concentrations of sulfides are typically found at the base of intrusions, forming a contact-type mineralization similar to other deposits in the region such as the Seagull and Thunder intrusions (Heggie, 2005; Zientek & Loferski, 2014; Trevisan, 2014). Following sulfide segregation, monosulfide solid solution (MSS) forms within a temperature range of 1190-900°C (Barnes et al., 2016; Mansur et al., 2021). During this process, metals such as Fe, Ni, Cu and PGE may partition into the MSS. As temperature decreases, MSS crystallizes pyrrhotite, whereas the remaining liquid, enriched in Cu, Au and palladium-type PGEs undergoes a second crystallization phase, forming an intermediate solid solution (ISS; Naldrett, 2004; Mansur et al., 2021). Below 650°C, pyrrhotite exsolves pentlandite and troilite, while ISS transforms into chalcopyrite and further exsolves cubanite (Naldrett et al., 1999; Fonseca et al., 2009).

The Midcontinent Rift System (MRS) is one of the world's largest Large Igneous

Provinces (LIP), extending over two thousand kilometers across what is now the Lake Superior

Region, from Lake Nipigon to Minnesota (Wold & Hinze, 1982; Woodruff et al., 2020). The MRS underwent prolonged magmatic activity, lasting ~30 million years, with voluminous eruptions and magmatic intrusions occurring between ~1112 Ma to ~1090 Ma (Heaman et al., 2007; Swanson-Hysell et al., 2014; Fairchild et al., 2017; Bleeker et al., 2020).

It is widely accepted that the MRS magmatism was driven by an upwelling mantle plume (Nicholson et al., 1997). This hypothesis explains the large volume mafic igneous rocks within the MRS, as well as their geochemical and isotopic characteristics, which support the existence of the mantle Keweenaw Plume (Nicholson & Shirey, 1990; Hutchinson et al., 1990, 1992; Cannon & Hinze, 1992). The Sunday Lake Intrusion, one of the early-phase MRS intrusions (1109.0±1.3 Ma), is a funnel-shaped intrusion that hosts Ni-Cu-PGE mineralization. This deposit hosts contact-type mineralization within a 20 meters thick zone with 2.11 g/t (grams per ton) platinum, 0.95 g/t palladium, 0.16 g/t gold, 0.26% copper and 0.11% nickel (Flank, 2017).

1.2 Objectives

The objectives of this project were to:

- Investigate the magmatic evolution of the Sunday Lake Intrusion
- Determine the parental magma composition
- Study possible sources of contamination and investigate the sulfur-saturation processes

To achieve this, characterization of textures and mineral assemblages was used to create a paragenesis and fractionation history for the Sunday Lake Intrusion (SLI). Sulfur isotopes were used to examine the source of S and the potential for externally derived sulfur. These two datasets are complemented by whole-rock geochemical data to further study the genesis, differentiation and contamination processes. The trace element chemistry of sulfides obtained via laser ablation Inductively Coupled Plasma Mass Spectrometry (ICP–MS) was used to characterize the distribution of metals within the sulfides and assess the degree of magmatic enrichment experienced by the sulfide liquid. Sulfur isotopes were used to determine the source of sulfur for the SLI and explore sulfur saturation processes. Olivine geochemistry was analyzed to determine parental magma composition and magma evolution. Isotopic Sm-Nd and Rb-Sr systems were used to determine the degree of interaction of magma with country rock.

Chapter 2: Regional and Local Geology

2.1 Superior Province

The Sunday Lake Intrusion (SLI) is located within the Superior Province, which extends from eastern Manitoba and northern Minnesota, through Ontario to Quebec (Percival et al., 2012). The Superior Province is surrounded by Proterozoic orogenic belts, bounded by the Grenville Province on the southeast, the Churchill Province on the east, north, and west; and to the south, by the Southern Province. It was created from several orogenic events during the Neoarchean, between 2.72 and 2.68 Ga (Percival et al., 2012). These orogenies are interpreted to have formed five broad periods during the accretion of the main tectonic blocks: The Northern Superior (2.71 Ga), Uchian (2.72-2.70 Ga), Central Superior (2.71-2.70 Ga), Shebandowanian (2.69 Ga), and Minnesotan (2.68 Ga) orogenies (Percival et al., 2006).

According to Card & Ciesielski (1986), the Superior Province can be divided into four types of subprovinces. These comprise four litho-tectonic groups: volcanic-plutonic, plutonic, metasedimentary, and high-grade gneissic subprovinces. The volcanic-plutonic subprovinces consist of supracrustal mafic to ultramafic volcanic rocks, granodiorite plutons, and metavolcanic rocks referred to as greenstone belts due to their greenschist metamorphic grade. Examples include the Wabigoon, North Caribou, and Wawa-Abititi subprovinces. Plutonic subprovinces include the Winnipeg River, Marmion, and North Caribou Core of the North Caribou subprovince, they consist of highly deformed tonalite and granitoid complexes. Metasedimentary belts are composed of turbiditic sediments, migmatites, and granitic equivalents; they are interpreted to have formed from detritus derived from boundary granite and

greenstone rocks (Card & Ciesielski, 1986; Williams & Currie, 1993). Examples include the English River, Quetico, and Pontiac Basins (Card & Ciesielski, 1986). The high-grade gneissic subprovinces include the Kapuskasing Structural Zone, which is composed of mafic, tonalitic, anorthositic, and metasedimentary gneisses from amphibolite and granulite facies rocks (Percival et al., 1992; Percival & Card, 1992; Mäder et al., 1994).

A reclassification by Stott et al. (2010) updated the Superior Province geology by incorporating new geochronologic, geochemical and isotopic syntheses. This classification presents terrane and domain boundaries across the Superior Craton to better address tectonic analysis (Fig. 2.1; Stott et al., 2010; Caglioti, 2023).

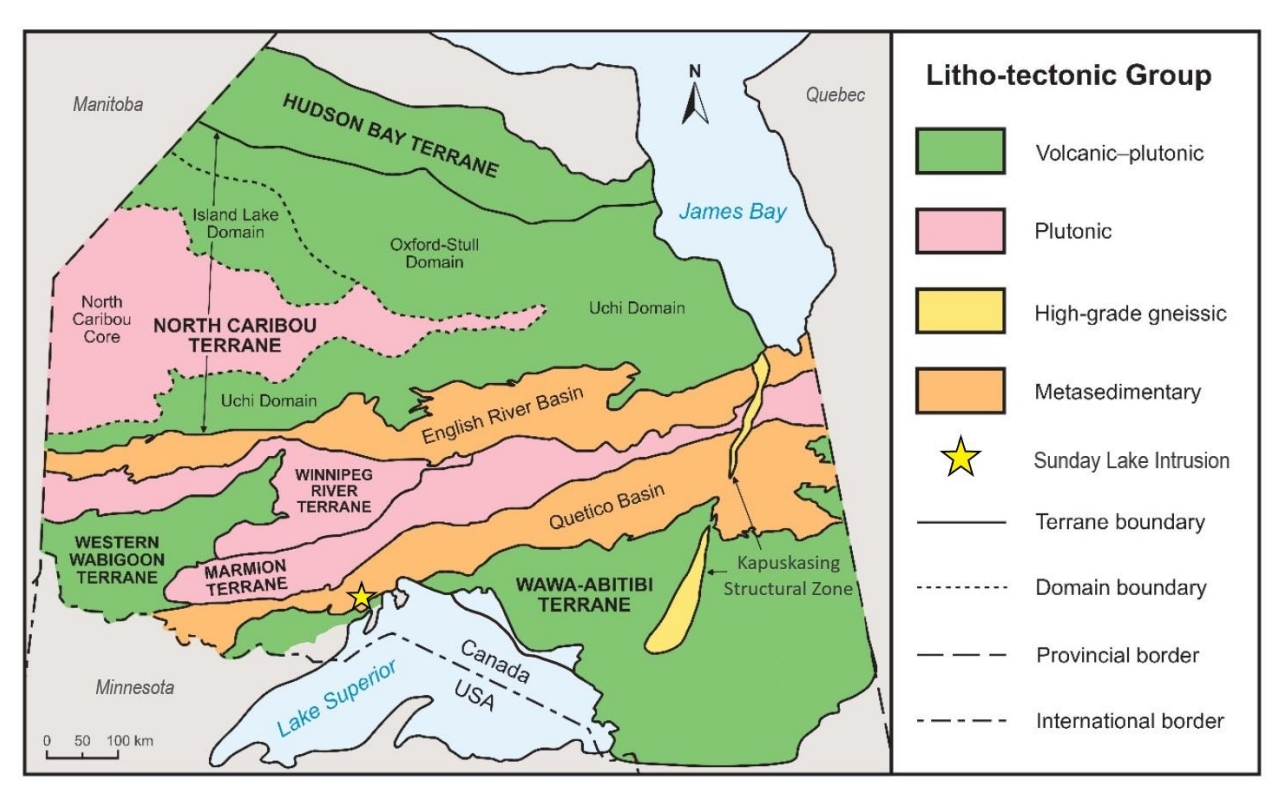


Figure 2.1. Terranes and domains of the Superior Province in Northwestern Ontario. After Stott (2011) and Caglioti (2023).

2.1.1 Quetico Basin

Country rocks of the SLI comprise the metasedimentary rocks of the Quetico Basin, which extends east-west for approximately 1200 km with a width of 10-100 km from northern Minnesota, across Ontario to the Kapuskasing Structural Zone (KSZ; Fig. 2.1; Percival, 2007). The northern boundary between the Quetico Basin and the Winnipeg River – Marmion – western Wabigoon terrane is defined by dextral faults such as the Seine River and the Rainy Lake Fault (SR-RL; Percival et al., 2006). The late transcurrent Quetico fault cuts the SR-RL fault and forms the Wabigoon-Quetico boundary to the east (Mackasey et al., 1974; Kehlenbeck, 1976). To the south, dextral transpressive faults mark the boundary with the Wawa-Abitibi Terrane (Percival et al., 1989; Williams, 1991; Corfu & Stott, 1996).

Rocks of the Quetico Basin include polydeformed greywacke and other minor metasedimentary rocks such as metamorphosed siltstone and conglomerate (Percival et al., 1989; Williams, 1991). Intrusive bodies are present throughout the basin occurring as granitoids, mafic-ultramafic bodies, paragneisses and migmatites (Percival et al., 1989; Williams, 1991). The sedimentation age of the Quetico Basin is constrained between 2698 and 2696 Ma (Davis et al., 1990). It has been suggested that sedimentation occurred syntectonically and that further deformation of the Quetico Basin happened during the collision between the Wabigoon and Wawa terranes (Percival et al., 2012). Wang et al. (2020) argued that subduction of oceanic lithosphere of the Wawa-Abitibi Terrane under the Wabigoon Terrane before ~2.7 Ga generated metasomatically enriched mantle and associated volcanic rocks. These volcanic edifices were

rapidly weathered and eroded to form immature rocks of the Quetico accretionary prism. (Percival et al., 1989).

2.1.2 Paleo-Mesoproterozoic Rocks

During the Penokean Orogeny, an oceanic arc collided with the southern margin of the Superior Craton at \sim 1830 Ma, resulting in back arc extension to form the Animikie Basin (Fralick et al., 2002). The Animikie Basin rocks are subdivided into the Gunflint Formation and Rove Formation in Ontario, whereas the US equivalents include the Mesabi Iron Range, Biwabik Iron Formation, Ironwood Iron Formation and Virginia Formation (McSwiggen & Morey, 2008). These Paleoproterozoic sedimentary rocks comprise the Animikie Group. In Ontario, the Animikie Group consists of Paleoproterozoic sedimentary rocks deposited between 1878.3 \pm 1.3 Ma to 1836 \pm 5 Ma (Fralick et al., 2002; Addison et al., 2005) including iron formation, chert and argillite and unconformably overlies Archean basement rocks.

Mesoproterozoic rocks of the Sibley Group overlie Archean basement rocks and the Paleoproterozoic Animikie Group. The Sibley Group is a ~950 m thick sequence divided into the Nipigon Bay Formation, Outan Island Formation, Pass Lake Formation, Rossport Formation and Kama Hill Formation (Rogala et al., 2007). The Sibley Group comprises sandstone, conglomerate, siltstone and dolostone originally deposited in an intercontinental basin in a lacustrine to aeolian environment sometime between 1537 + 10/-2 Ma and 1339±33 Ma (Davis et al., 1985; Fralick et al., 2002; Fralick & Pufahl, 2006).

2.2 Midcontinent Rift System

The 1.1 Ga Midcontinent Rift System (MRS) is one of the world's biggest Large Igneous Provinces (LIP) that extends around 2200 km from Kansas in the southwest, into the Lake Superior region and through lower Michigan (Fig. 2.2; Woodruff et al., 2020). MRS volcanism lasted ~30 million years with voluminous eruptions between ~1112 Ma to ~1090 Ma and other minor eruptions extending to ~1083 Ma (Bleeker et al., 2020; Fairchild et al., 2017; Heaman et al., 2007; Swanson-Hysell et al., 2014).

Different theories have been suggested to explain the rifting of North America at 1.1 Ga. The first theory involves a passive rifting model in response to far-field forces generated at distant plate boundaries or tectonic belts, presumably due to collision and subduction of the Grenville Orogeny (Donaldson & Irving, 1972; McWilliams & Dunlop, 1978; Gordon & Hempton, 1986). The second, and more widely accepted hypothesis, involves an upwelling mantle plume that spreads laterally beneath the lithosphere and causes crustal extension. This theory explains the large volume of MRS mafic igneous rocks, as well as their geochemical and isotopic characteristics, which have been used to argue for the existence of the mantle Keweenaw Plume (Nicholson & Shirey, 1990; Hutchinson et al., 1990, 1992; Cannon & Hinze, 1992).

Woodruff et al. (2020) have defined three main stages of rift development based on age, physical volcanology, magnetic polarity, and geochemistry. These are the Plateau Stage (~1112 to ~1105 Ma), Rift Stage (~1102 to ~1090 Ma), and Late-Rift Stage (~1090 to ~1083 Ma).

During the Plateau Stage, minor faulting, basalt flows erupted forming a ~10 km-thick volcanic plateau (Cannon et al., 1989). Diabase dike swarms occurred mainly in the northern part of the MRS (Halls & Pesonen, 1982). Intrusive rocks accompanied the volcanic eruptions, forming sills and plutons; these bodies intruded Proterozoic sedimentary rocks, volcanic rocks and Archean basement as early as 1113-1109 Ma (Bleeker et al., 2020). Intrusive bodies formed in this stage

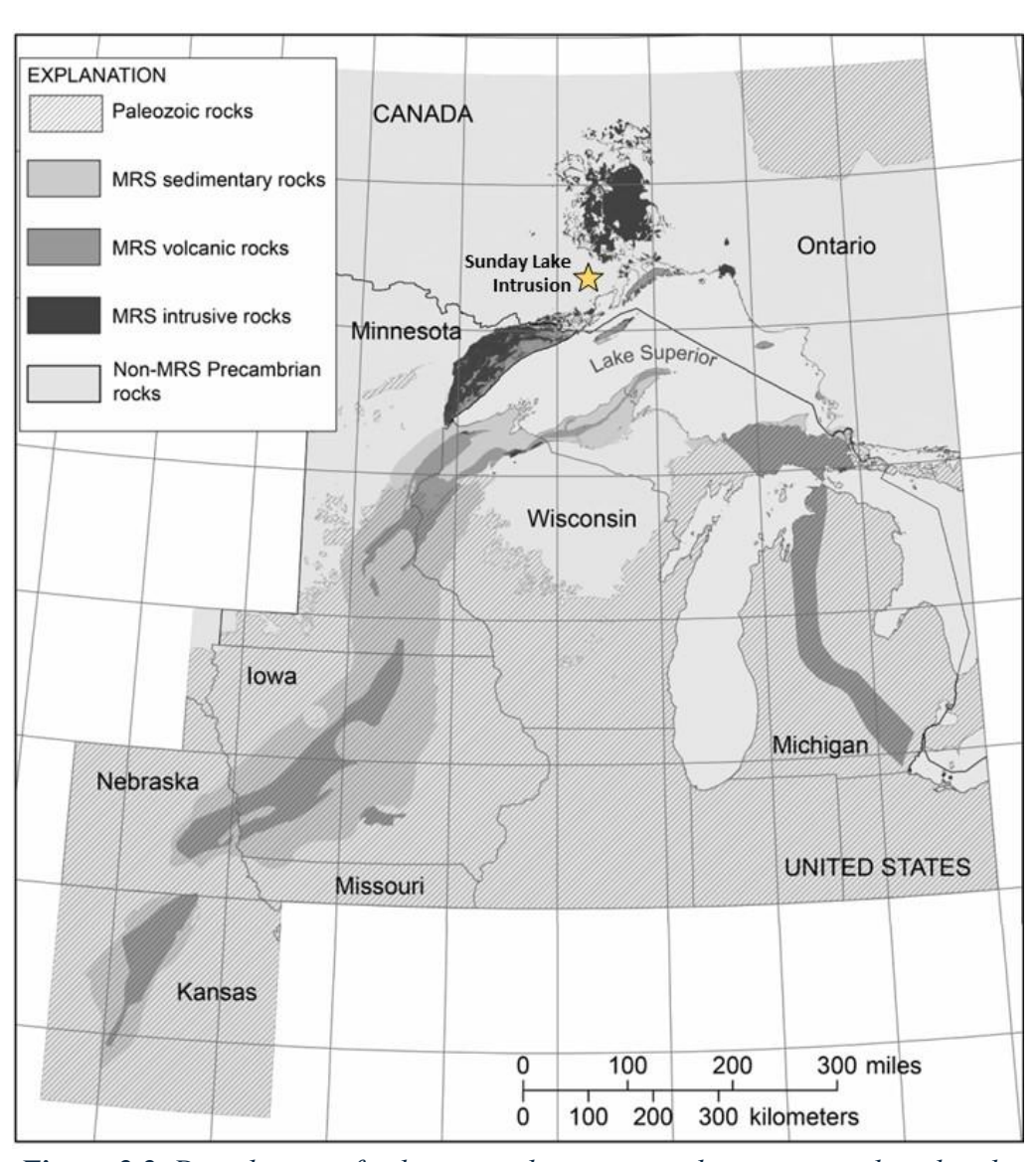


Figure 2.2. Distribution of volcanic, sedimentary and intrusive rocks related to the Midcontinent Rift System (MRS). Modified from Woodruff et al. (2020).

include the Sunday Lake Intrusion (1109.0 ± 1.3 Ma; Bleeker et al., 2020), alkaline intrusive rocks of the Coldwell Complex (1108 ± 1 Ma; Heaman & Machado, 1992), Logan Sills (1109 ± 4 Ma; Davis et al., 1985), the lower portion of the North Shore Volcanics (1108 ± 2 Ma; Davis & Green, 1997). Magmatic mineral deposits in the Plateau Stage include conduit-type Ni-Cu-PGE sulfide deposits, mafic and ultramafic tube-like intrusions, and dikes (Woodruff et al., 2020).

The Rift Stage is constrained between ~1105 and ~1090 Ma (Woodruff et al., 2020) and it is characterized by volcanic and intrusive activity with basalts filling basins of the central rift of what is now the Lake Superior basin, basalt composition changed from early Mg-rich to late Al-rich compositions over a period of ~30 m.y. from the Plateau Stage to the Rift Stage (Woodruff et al., 2020).

The Late-Rift Stage defines the end of the magmatic activity; it occurred from ~1090 to ~1083 Ma (Woodruff et al., 2020), during which subsidence of the central rift continued due to thermal relaxation (Cannon & Hinze, 1992). This period is characterized by the deposition of coarse conglomerates and red sandstones with a maximum thickness of ~2 km (Daniels, 1982). Minor magmatism also occurred, forming thin tholeitic basalt flows and local porphyritic intrusions (Richards & Spooner, 1989; Fairchild et al., 2017).

2.2.1 Intrusive complexes of the Thunder Bay area

Intrusive rocks in the northwest portion of Lake Superior, around Thunder Bay, have been extensively studied (Hollings et al., 2007b, 2010; Miller et al., 2013; Woodruff et al., 2020, 2020; Bleeker et al., 2020). The basement comprises Archean metasedimentary and granitic

rocks that are intruded by rocks of the MRS including sills and dykes. Intrusions in the area include the Sunday Lake, Thunder, Seagull, Eva-Kitto, Current Lake, and Escape intrusions (Fig. 2.3). These intrusions have an emplacement age between 1106.6±1.6 Ma and 1117.7±1.8 (Laarman, 2007; Hollings et al., 2007a; Heaman et al., 2007; Trevisan, 2014; Bleeker et al., 2020; Yahia, 2023). Intrusions in the Thunder Bay area include funnel- and tube-like to chonolith-shaped intrusions with variable levels of Ni-Cu-PGE mineralization. Studies of whole rock geochemistry and isotopic systems like Sm-Nd, Rb-Sr, and Re-Os have been used to argue for interaction of the ascending plume with the lithosphere and the mantle at the early stages of the MRS (Heggie, 2005; Laarman, 2007; Trevisan, 2014; Cundari et al., 2022; Brzozowski et al., 2023; Corredor, 2024). During this period, contributions from the ascending Keweenaw Plume melts, the Subcontinental Lithospheric Mantle (SCLM) and Archean crustal material were variable, leading to complex geochemical and isotopic variations masking the original compositions and characteristics of the source (Cundari et al., 2022; Brzozowski et al., 2023).

2.3 Sunday Lake Intrusion

The Sunday Lake Intrusion (SLI) has an age of 1109.0±1.3 Ma based on U/Pb from baddeleyite from a red monzogabbro at the top layers of the intrusion (Bleeker et al., 2020). It is one of the oldest differentiated intrusions in the northern part of the MRS located in Jacques Township, ~25 km north of Thunder Bay (Fig. 2.3). The intrusion is not exposed at surface and was first identified from airborne magnetic and gravity surveys (Flank, 2017). It hosts PGE-Cu-Ni mineralization, with one intersection of 42.9 m of 1.92 g/t Pt, 1.40 g/t Pd, 0.11 g/t Au, 0.44% Cu and 0.17% Ni in drill-hole 11SL0001 (Transition Metals Corp., 2015). Further drilling

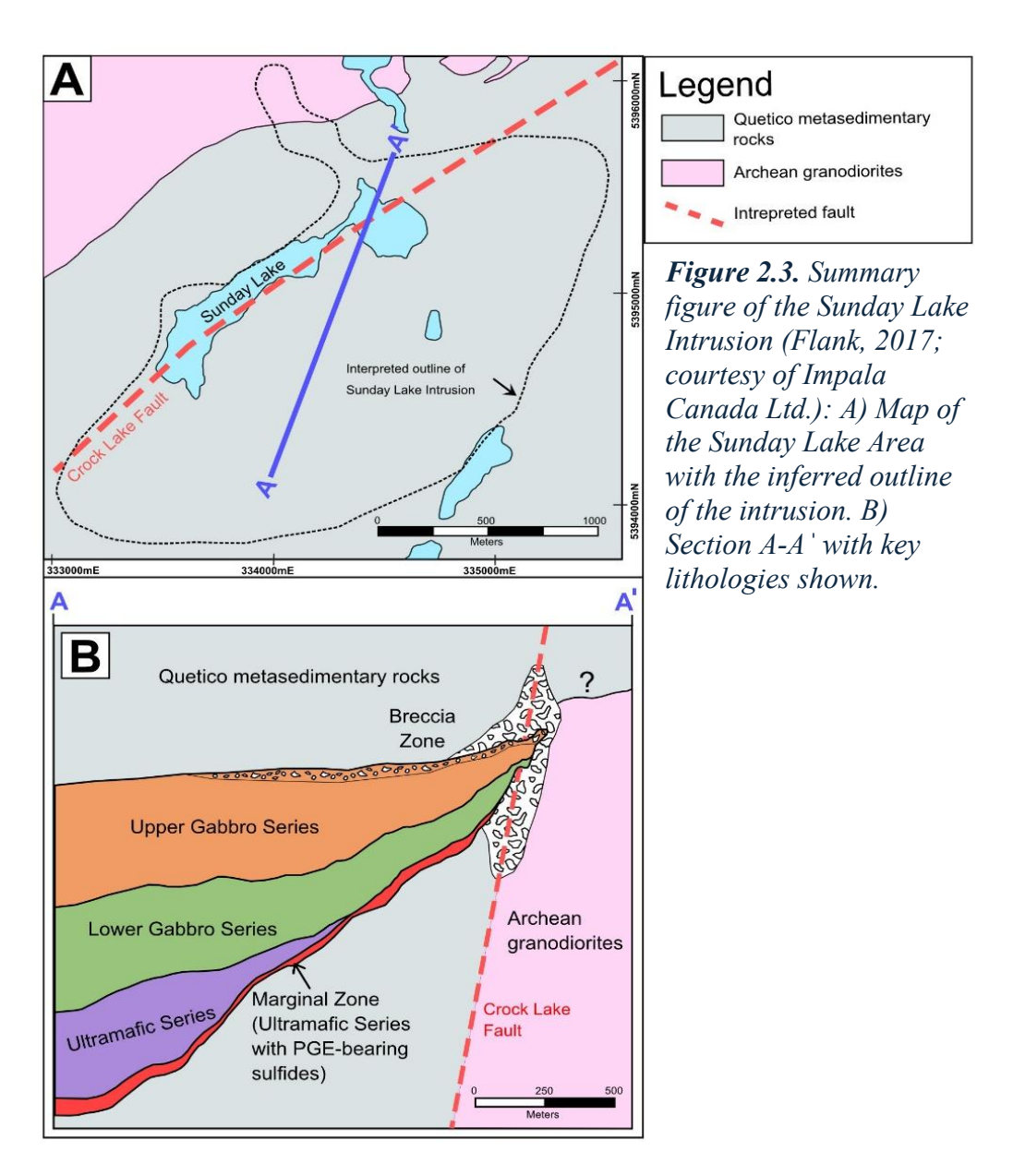
revealed a funnel/tabular-shaped intrusion buried beneath 400 m of Quetico metasedimentary rocks. The intrusion has a variable thickness of 350 m in the north and 990 m in the south (Fig. 2.3; Flank, 2017). The SLI is emplaced mainly in Quetico metasedimentary rocks but towards the NW, the intrusion cuts Archean granodiorite and metasedimentary rocks. The intrusion was emplaced along the Crock Lake Fault, a splay of the Quetico Fault, and has been divided into Upper Gabbro Series, Lower Gabbro Series and Ultramafic Series (Fig. 2.3; Flank, 2017).

The Upper Gabbro Series (UGS) comprises up to 348m at the southern portion of the intrusion and gradually decreases towards the Crock Lake Fault. The UGS has coarse-grained plagioclase orthocumulate and has been subdivided into four rock types: gabbro breccia, monzogabbro, oxide gabbro, and leucogabbro (Flank, 2017). A brecciated segment near the Crock Lake Fault and at the hanging wall contact of the intrusion consists of up to 45m with subangular quartz fragments and up to 15cm xenoliths of Quetico metasedimentary rocks, the brecciated segment is generally not mineralized but breccia-style mineralization has been found near the Crock Lake Fault (Flank, 2017). The UGS has a strong hematite-epidote-chlorite-potassic alteration with a deep red-to-green color with alteration intensity decreasing downwards (Flank, 2017). The UGS has a high magnetic susceptibility due to disseminated magnetite-ilmenite.

The Lower Gabbroic Series (LGS) is a 250m-thick layer (Fig. 2.3) comprising a clinopyroxene-phyric gabbro transitioning to a more primitive melagabbro/olivine melagabbro-peridotite towards the center of the intrusion. This layer is much less altered than the UGS but has weak selective chlorite-grunerite alteration of augite. Weak reef-style mineralization occurs

at the contact with the Ultramafic Series predominantly at the southern portion of the intrusion, with grades of approximately 1g/t Pt+Pd+Au (Flank, 2017).

The Ultramafic Series (UMS) includes gabbroic breccia, melagabbro, olivine melagabbro, peridotite and minor pyroxenite lithologies (Flank, 2017). The UMS has a variable thickness from 10m in the north to 120m in the south and has been divided into the Main Zone,



Breccia Zone, and Marginal Zone (Fig. 2.3; Flank, 2017). The Main Zone consists of serpentinized olivine melagabbro to plagioclase peridotite, it is 5m wide and is commonly mineralized with 1-5% blebby pyrrhotite-pyrite-chalcopyrite. PGE mineralization of up to 2 g/t Pt+Pd+Au and 0.3% Cu is associated with sulfides (Flank, 2017). The Breccia Zone (Fig. 2.3) occurs near the Crock Lake Fault and comprises dark green-black breccias with partially digested fragments of quartz-carbonate which are associated with sulfides, dominated by blebby and blocky textured pyrite-chalcopyrite.

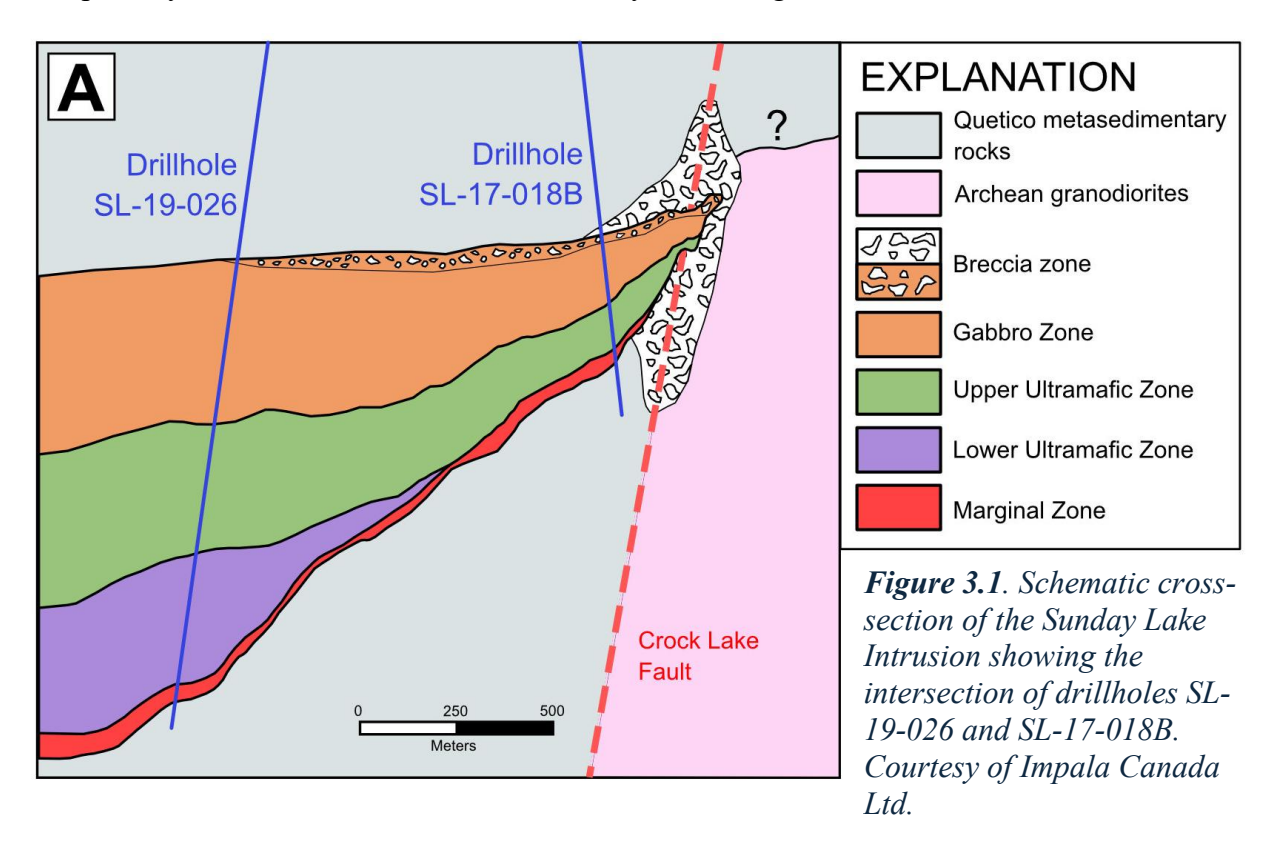
According to Flank (2017), the main host of the PGE-Cu-Ni mineralization in the Sunday Lake Intrusion is olivine melagabbro from the Marginal Zone, this zone hosts sulfide mineralization and is located at the basal contact of the Ultramafic Series. It contains 2-10% finely disseminated to blebby high PGE-tenor sulfides composed of chalcopyrite, pyrite, and pyrrhotite and occasional 1-3 cm-wide veins of pyrrhotite-chalcopyrite (Flank, 2017). This unit can be traced over a 1500 x 900 meter area, with a thickness of up to 43m at grades of 3-10 g/t Pt+Pd+Au, 0.22-0.74% Cu and 0.11-0.28% Ni (Flank, 2017). Overall, PGE-Cu-Ni mineralization occurs in three environments in the Sunday Lake Intrusion (Flank, 2017). 1) A relatively low grade (<1 ppm Pt+Pd+Au), high tenor (1200ppm Pt+Pd+Au) reef-style mineralization at the UMS/LGS contact. 2) The most volumetrically significant mineralization of the SLI, sulfide mineralization is disseminated with 3-10 g/t of Pt+Pd+Au and high Pd+Pt+Au tenors (Flank, 2017) at the Marginal Zone and 3) In the hanging wall breccias, near the Crock Lake Fault, low Cu-Ni and high Pt+Pd tenors have been found (Flank, 2017). Combining the different mineralized zones, has yielded an estimated resource of 20.4 Mt at 2.5 g/t Pt+Pd+Au (Flank, 2020).

Chapter 3: Methods

3.1 Sampling

Drill core sampling took place at the Impala Canada Ltd. facilities in Thunder Bay between October and November of 2023. Sampling was completed on two drillholes: SL-17-18B and SL-19-026. The two drillholes were selected due to their location, representative lithologies, presence of mineralization, and available data.

Hole SL-17-18B is located in the northern part of the intrusion with a total depth of 806 m, 310 meters of which was represented the intrusion. Portable XRF (pXRF) and magnetic susceptibility measurements were collected every 5m through the intrusion with the assistance of



Jami Brown from Impala. Hole SL-19-026 is located in the southwestern part of the intrusion; it has a total depth of 1492.00 m and an intrusion thickness of 980 meters (Fig. 3.1).

Drill core samples had a maximum length of 40 cm of NQ (47.6mm diameter) core with a total of 71 core samples collected. Samples for petrological work and mineral chemistry were selected based on lithological changes, magnetic properties, whole rock data, and pXRF data provided by Impala Canada Ltd. The drill core was split at Lakehead University with half the core retained for analysis.

3.2 Analytical methods

3.2.1 Portable X-Ray Fluorescence

A JITAI9201 Handheld X-ray fluorescence Analyzer spectrometer (pXRF) was used to analyze rock samples from two drill holes: SL-17-18B, for which readings were provided by Impala Canada Ltd, and SL-19-026, for which new measurements were taken. Analyses were conducted at approximately five-meter intervals along the drill core. For each analysis, readings were taken on drill core segments measuring from 40 to 70 cm in length. The pXRF was positioned along the selected interval, and a measurement was taken for approximately 60 seconds at each location. The instrument was calibrated using certified reference materials (CRMs) at the start of each work session.

3.2.2 Petrography

A total of thirty billets were sent to Precision Petrographics Ltd., Langley, British Columbia for the preparation of polished thin sections. Polished thin-section analysis was conducted using an Olympus BX2M Microscope with the Olympus SC180 camera at Lakehead University. Additionally, photomicrographs of polished thin sections were taken using a Zeiss Axioscope 5 with the Axiocam 305 color camera.

3.2.3 Whole Rock Geochemistry

Fifty-five samples were submitted to ALS Minerals in Thunder Bay, Ontario. Samples were crushed using a TM Engineering jaw crusher with chrome steel plates to > 70% passing 2 mm then riffle split to 250g. The split was then pulverized in a low chrome disc mill to better than 85% <75 μm. Major elements were analyzed by inductively-coupled atomic emission spectrometry (ICP-AES, ALS method ME-ICP06), following lithium borate fusion and HNO3 dissolution. Trace elements were analyzed by inductively coupled plasma mass spectrometry (ICP-MS, ALS method ME-MS81) following lithium borate fusion and HNO3 dissolution. Base metals were analyzed by ICP-AES using a mixed/sequential HF-HClO4-HCl-HNO3 digestion (ALS method ME-4ACD81). Sulfur was analyzed by combustion using a Leco infrared analyzer (ALS Method S-IR08).

In the Discussion chapter, the two downhole lithostratigraphic plots display Mg as elemental weight percent (Mg wt.%) rather than MgO wt.% to ensure consistency with the

original dataset provided by Impala Canada Ltd. This conversion was applied only where direct comparison with the database was necessary.

3.2.4 Scanning Electron Microscopy

Scanning Electron Microscopy was used to characterize sulfide mineral phases. The Scanning Electron Microscope EDX (SEM) Hitachi SU-70 Schottky Field Emission of Lakehead University Instrumentation Laboratory (LUIL) was used. This SEM is equipped with an Oxford Aztec 80mm/124eV Energy-dispersive X-ray spectrometer (EDS). The electron gun filament was operated using a voltage of 20 kV and a working distance of 15 mm, and the Z value (effectively stage height) was adjusted for each analysis. The EDS systems was calibrated using nickel sulfide standard and verified using an FeS₂ (pyrite) standard produced by Micro-Analysis Consultants Ltd. Analysis proceeded only if this check returned a total within ±0.5% of 100%. X-ray spectra were processed into elemental concentrations using "Ni-Sulfide" GL Standard from Carnegie Science Geophysical Laboratoy, Washington and for S and Ni and the "CuFeS₂-Chalcopyrite" standard from Micro-Analysis Consultants Ltd. for Fe and Cu. A default database standard was used for all other elements.

3.2.5 Sulfur isotopes

A total of ten samples were sent for S isotope studies at Queen's Facility for Isotope Research (QFIR) at Queen's University, Kingston. Hand drilling of sulfides was completed using a Powder Microdrill (Jobmate Rotary Drill) with a 2 mm "Diamond" drill bit. For each S isotope sample, a minimum of 1 mg of material was collected on single sulfide phases such as pyrrhotite

or chalcopyrite. Sample contamination was avoided by making use of fresh latex gloves, clean paper and cleaning the drill bit between each sample. Samples were weighed into tin capsules, and the sulfur isotopic composition was measured using a MAT 253 Stable Isotope Ratio Mass Spectrometer coupled to a Costech ECS 4010 Elemental Analyzer. δ^{34} S values were calculated by normalizing the 34 S/ 32 S ratios in the sample to the Vienna Canyon Diablo Troilite (VCDT) international standard. Values are reported using the delta (δ) notation in units of per mill (δ) and are reproducible to 0.3‰.

In situ sulfur isotopic ratios of sulfides (pyrrhotite and chalcopyrite) were conducted by LA-MC-ICP-MS at Nanjing FocuMS Technology Co. Ltd. An Australian Scientific Instruments RESOlution LR S-155 laser-ablation system (Canberra, Australia) and Nu Instruments Nu Plasma II MC-ICP-MS (Wrexham, Wales, UK) were combined for the experiments. Mediumresolution source slit of Nu Plasma II was applied to achieve resolving power better than 8000. The 193 nm ArF excimer laser, homogenized by a set of beam delivery systems, was focused on the surface with fluence of 2.5J/cm2. Each acquisition incorporated 30s background (gas blank), followed by spot diameter of 33 µm for pyrite, 40µm for pentlandite and chalcopyrite, 50µm for pyrrhotite for at 5 Hz repetition rate for 35 s. The Integration time of the Nu Plasma II was set to 0.3s (equating to 115 cycles during the 35s). Helium (400ml/min) was used as the carrier gas to efficiently transport aerosol out of the ablation cell and was mixed with argon (~0.95 L/min) via T-connector before entering ICP torch. Natural pyrite Wenshan ($\delta^{34/32}$ S= +1.2% V-CDT, inhouse standard) was primary standard for pyrite, pyrrhotite, pentlandite samples. Pyrrhotite Po-H $(\delta^{34/32}S = +6.0\% \text{ V-CDT}, \text{ unpublished data, from Institute of Geochemistry, Chinese Academy of})$ Sciences, Guiyang) was the secondary standard. Chalcopyrite GBW07268 ($\delta^{34/32}$ S= +0.2% V-

CDT, from National Research Center for Geoanalysis, China) were used as an external standard for every fourth chalcopyrite samples and natural chalcopyrite TC1725 ($\delta^{34/32}$ S=+12.8% V-CDT, https://doi.org/10.1039/d1ja00168j) were treated as the quality control. The long-term reproducibility of $\delta^{34/32}$ S is better than 0.5% (1 Standard Deviation).

3.2.6 Olivine compositional analyses

Quantitative analyses of olivine major element compositions were performed at the University of Manitoba using a Cameca SX-100 electron probe micro-analyzer (EPMA) equipped with five wavelength-dispersive spectrometers (WDS) and an energy-dispersive spectrometer (EDS). Analysis was performed using a 15 kV accelerating voltage, Ni was counted for 80 s in three EDS spectrometers, 150nA beam current and 5 μm electron beam width. The rest of the elements (Si, Ti, Al, Fe, Mn, Mg, Ca) were counted for 40 s, 20nA beam current and 5 μm electron beam width.

3.2.7 Strontium and Neodymium isotopes

Sixteen bulk-rock samples from the Sunday Lake Intrusion were analyzed for Sm-Nd isotopic compositions at the Isotope Geochronology and Geochemistry Research Centre (IGGRC) at Carleton University. Prior to dissolution in concentrated HF-HNO₃, each sample was spiked with a mixed ¹⁴⁸Nd tracer. The resulting residues were then dissolved in 1.5 mL of 2.5 N HCl in a chromatography. Isotopic measurements of Sr and Nd were conducted using a Thermo-Finnigan Neptune multi-collector ICP-MS. The Sr and Nd isotopic ratios were

standardized to 86 Sr/ 88 Sr = 0.1194 and 146 Nd/ 144 Nd = 0.7219. The measured 143 Nd/ 144 Nd ratios were corrected for instrumental drift by bracketing sample runs with JNdi-1 reference material, using an IGGRC Thermo-Finnigan Triton TIMS average JNdi-1 value of 0.512100. Final Sr and Nd isotope ratios are reported as initial values (Sr_i and ϵ Nd), recalculated to an age of 1109.0 Ma, the interpreted crystallization age of the Sunday Lake Intrusion (Bleeker et al., 2020).

Chapter 4: Results

The magmatic stratigraphy of the SLI can be separated into four distinct zones using petrography, magnetic susceptibility, portable XRF and whole-rock geochemistry.

4.1 Magnetic susceptibility and pXRF

Magnetic susceptibility measurements were taken to track the occurrence of Fe-Ti oxide throughout the SLI. The Gabbro Zone (GZ) has values ranging from 0 to 240 kappa. The upper part of the GZ in drillhole SL-17-18B corresponds to the breccia zone and is characterized by values close to 0 kappa. The bottom part of the GZ has kappa values ranging from 15 to 54. Magnetic susceptibility values for the Upper Ultramafic Zone (UUZ) have values ranging from 2 to 34 kappa, whereas the Lower Ultramafic Zone (LUZ) has magnetic susceptibility values from 3 to 126 kappa and the Marginal Zone has kappa values from 3 to 157 kappa (Fig. 4.1A-B).

A portable XRF analyzer was used to analyze Mg, Ca, Al and Cu throughout both drillholes and was useful for establishing the downhole boundaries of each zone. The GZ is characterized by an Mg average value of 37 218 ppm; Ca has an average value of 46 459 ppm, Al averages 56 548 ppm, and Cu averages 21 ppm. The UUZ is characterized by an Mg average abundance of 121 200 ppm; Ca averages 74 270 ppm, Al has an average value of 13 902 ppm and Cu averages 240 ppm. The LUZ comprises Mg average values of 196 243 ppm, Ca averages 28 739 ppm, Al has an average value of 11 907 ppm and Cu averages 231 ppm. The Marginal Zone (MZ) is characterized by an Mg average value of 124 226 ppm, a Ca average of 66 676 ppm, Al has averaged values of 16 179 ppm and a Cu average of 4 762 ppm. The host rock

Quetico metasedimentary rocks have a Mg average value of 20 423 ppm, Ca average of 20 562 ppm, Al an average value of 65 151 ppm and a Cu average of 520 ppm (Fig. 4.1A-B).

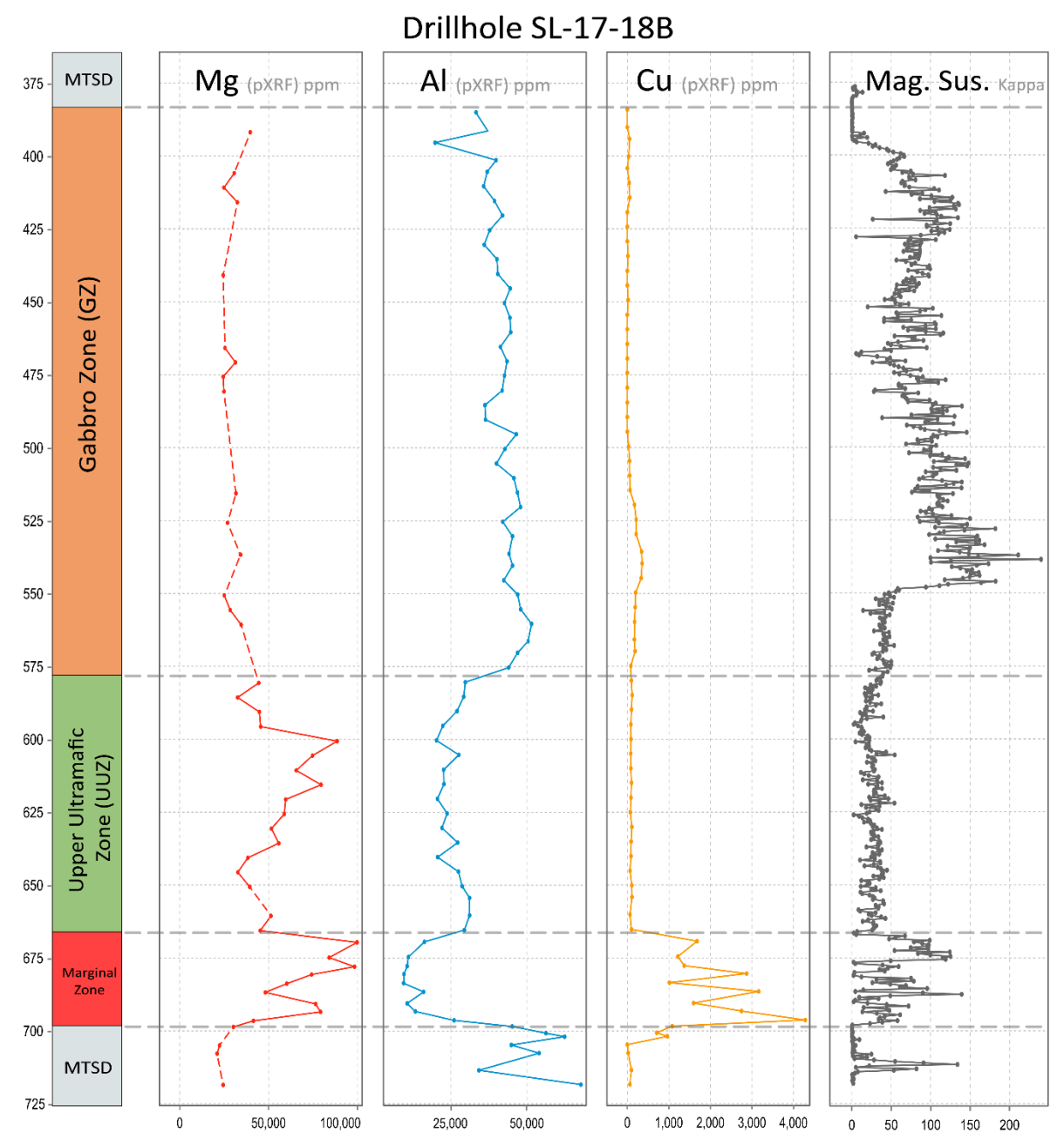


Figure 4.1A. Drill hole SL-17-18B chemostratigraphic variation in Mg, Al, Cu (pXRF) and Magnetic susceptibility (Mag. Sus.) readings.

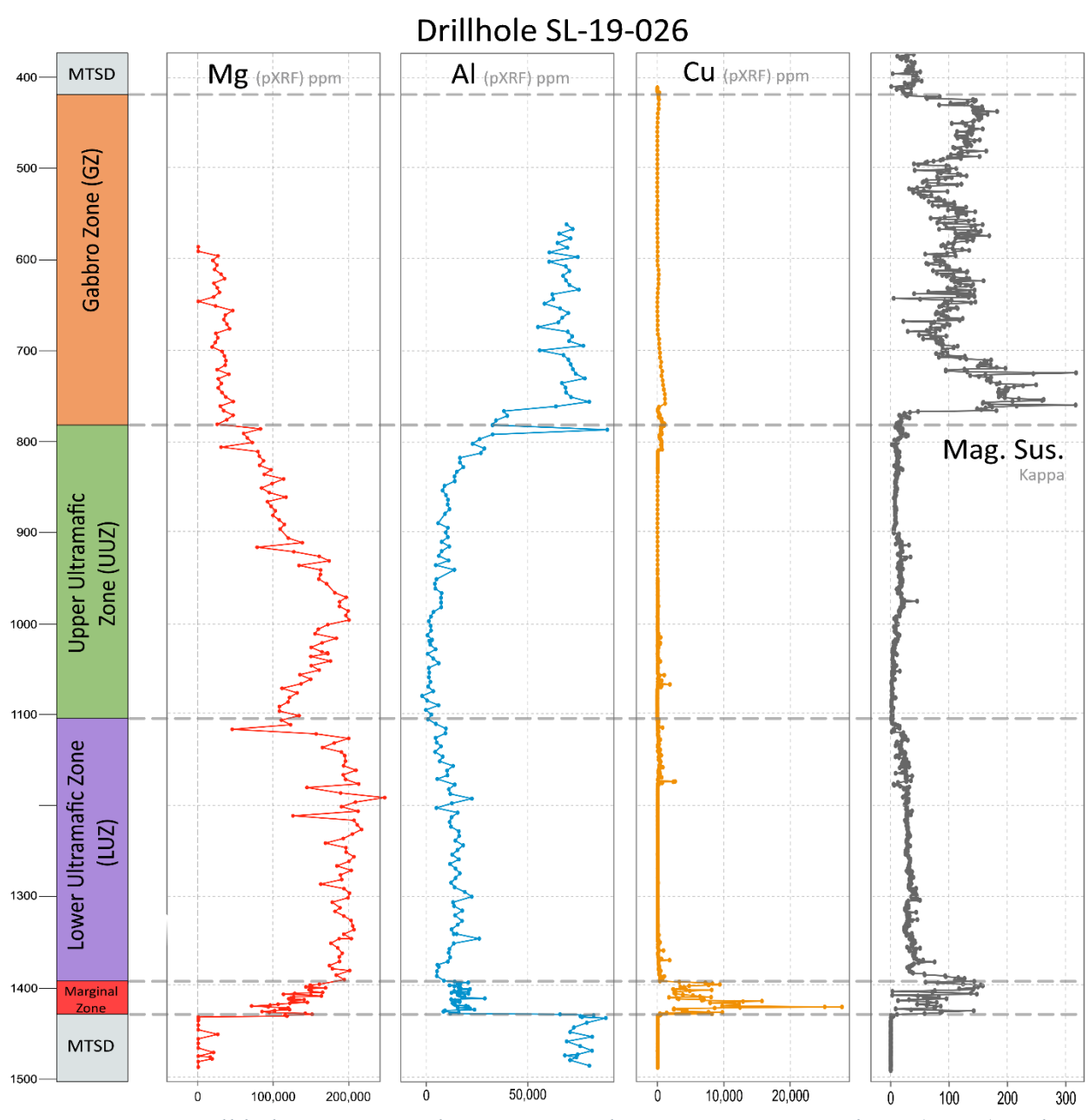


Figure 4.1B. Drill hole SL-17-18B chemostratigraphic variation in Mg, Al, Cu (pXRF) and Magnetic susceptibility (Mag. Sus.) readings.

4.2 Petrology and petrography

Petrographic descriptions of the country rock and mafic-ultramafic rocks of the Sunday Lake Intrusion were made from polished thin sections. Mafic and ultramafic rocks were classified using a plagioclase, clinopyroxene and olivine modal classification according to the Ternary Classification for mafic and ultramafic intrusive rocks of Miller et al. (2002). For rocks with mafic minerals less than 90%, classification was completed according to the IUGS Plutonic Rock Classification QAP by Le Maître et al. (2002). Grain sizes were defined as very fine-grained (<0.1 to 0.01 mm), fine-grained (0.01 to 1 mm), medium-grained (1 to 3 mm) and coarse-grained (> 3mm). Alteration intensities were defined as weak (0 to 30%), moderate (30% to 60%) and strong (60 to 100%) based on the modal abundance of secondary phases. Inclusion abundance was defined as low (1-30%), moderate (31-60%) and high (61-90%).

4.2.1 Gabbro Zone

The GZ forms the upper portion of the intrusion (Fig. 3.1), it is in contact with the country rock and is the more differentiated portion of the SLI based on its mineral assemblages. A total of ten samples were collected from this zone and based on mineral modal proportions, rock types for the Gabbro Zone are leucogabbro, gabbro, quartz monzonite and quartz gabbro (Fig. 4.2). The GZ is characterized by having the highest proportions of oxides compared to the rest of the intrusion, with 10 to 20%, resulting in the highest magnetic susceptibility values compared to the rest of the zones. It can be highly oxidized with a distinctive red-brick and greygreenish colour with moderate alteration increasing upwards (Fig. 4.3). The upper part of this layer often comprises a breccia that is more evident near the Crock Lake Fault. Gabbroic rocks

of this zone are among the least altered samples and are mainly distributed in drillhole SL-19-026, and at the lowermost part of the GZ. Gabbroic rocks are medium- to coarse-grained with a grey-greenish colour and phaneritic texture. Gabbros have a more mafic composition compared

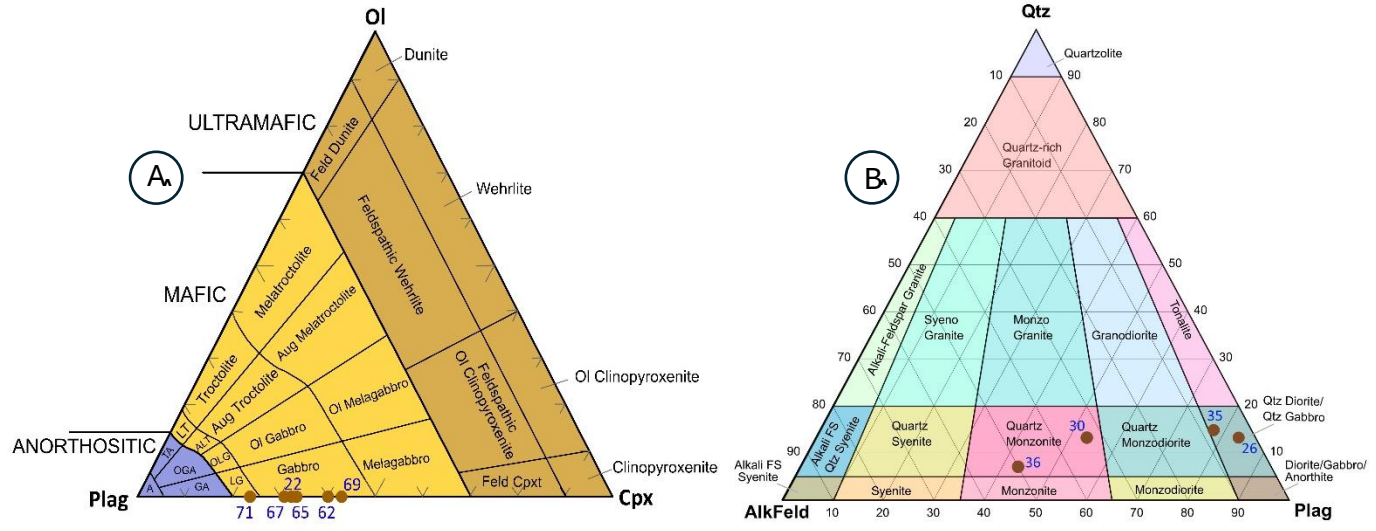


Figure 4.2. Classification for mafic and ultramafic intrusive rocks. A). Brown circles indicate modal abundances for samples of the GZ. Selection of appropriate diagram was based on the cutoff of greater than 90% of mafic minerals the Mafic-Ultramafic ternary classification diagram of Miller et al. (2002). B) IGZ Plutonic Rock Classification QAP (Lemaître et al., 2002). Abbreviations are LT: Leucotroctolite, ALT: Augite Leucotroctolite, OLG: Olivine Leucogabbro, LG: Leucogabbro, TA: Troctolitic anorthosite, OGA: Olivine gabbroic anorthosite, GA: Gabbroic anorthosite, A: Anorthosite.

to the rest of the samples of the GZ and are characterized by clinopyroxene comprising 20% to 30% of the rock (Fig. 4.3C). Quartz gabbros have the highest proportion of plagioclase compared to the rest of the zone, comprising up to 55% of the rock. Leucogabbro and quartz gabbros have porphyritic to glomeroporphyritic plagioclases, crystals are euhedral to subhedral mediumgrained and display weak to moderate alteration and hematization (Fig. 4.3B). Quartz monzonite rocks have the most felsic composition of the GZ, with alkali-feldspar abundance ranging from 30% to 35% of the rock, they are characterized by anhedral to subhedral plagioclase and granular

anhedral K-feldspar. The quartz monzonite is highly altered with chloritization of amphiboles, sericitization of feldspars and strong hematization (Fig. 4.3A).

The main minerals that comprise the GZ are plagioclase, clinopyroxene, and Fe-Ti oxide. Rocks of the GZ are coarse- to medium-grained, generally with grain-sizes from 2.5 mm to 6 mm, showing phaneritic, porphyritic, and glomeroporphyric textures. In the GZ, plagioclase ranges in modal abundance from 40% to 60%, and occurs as cumulate subhedral to euhedral crystals with variable grain sizes from medium- to coarse-grained oikocrysts with hornblende and oxides chadacrysts. Plagioclase is commonly tabular but can also be found as needle-like crystals in the breccia zone (Fig. 4.4). Plagioclase shows a moderate to strong alteration to sericite, chlorite, epidote, and calcite (Figs. 4.4 and 4.5). Moderate to strong zoned hematization is found predominantly in plagioclase (Fig. 4.5).

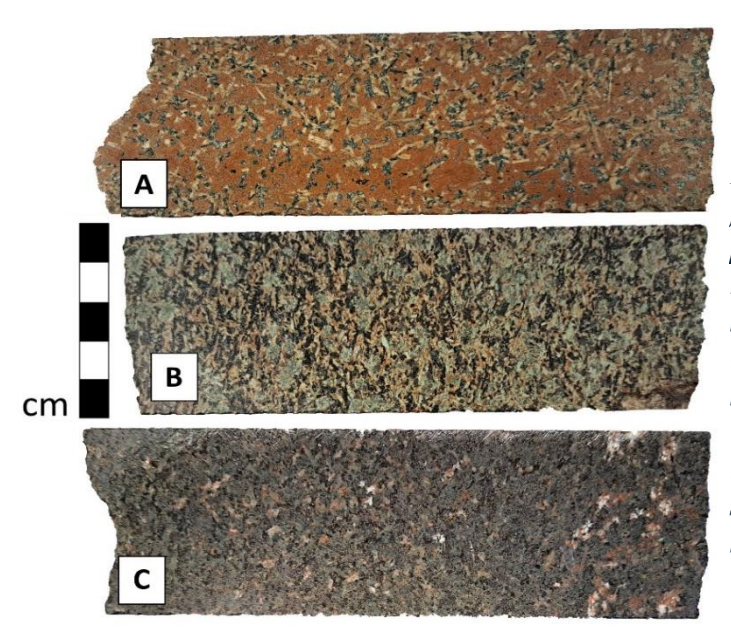


Figure 4.3. Representative core samples from the GZ. Sample SL23KM30 shows a porphyritic texture and the representative red-brick color (A). Sample SL23KM35 shows a porphyritic to glomeroporphyric texture (B). Sample SL23KM65 shows a phaneritic texture (C). Samples are organized based on their vertical position within the GZ, with sample A representing the upper GZ and Sample C representing the lower GZ.

Clinopyroxene ranges in abundance from 0% to 30%, occurring as medium- to coarse-grained subhedral to anhedral intercumulus. Clinopyroxene is commonly twinned and is rarely zoned, they are locally rounded and commonly have embayed textures (Fig. 4.6). Clinopyroxenes are moderately to completely altered to actinolite, chlorite, biotite and minor carbonates (Figs. 4.5 and 4.6). The clinopyroxene is most abundant in drillhole SL-19-026 where it comprises 20% to 30% of the rock, compared to drillhole SL-17-18B, where clinopyroxene ranges from 5% to absent.

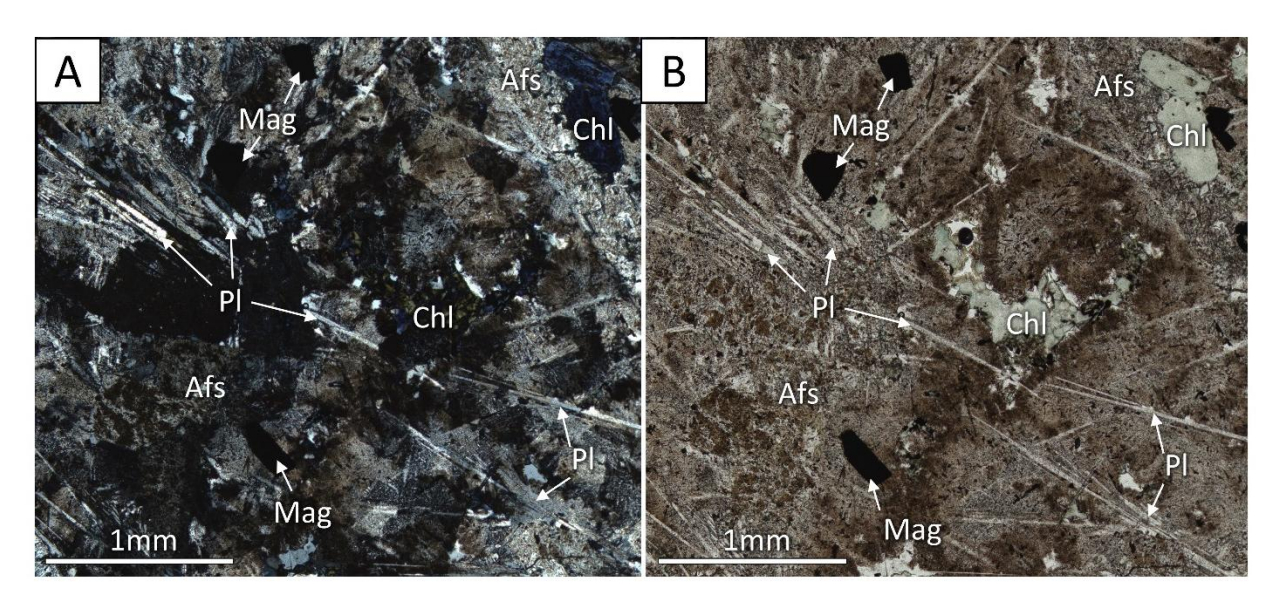


Figure 4.4. Photomicrographs of sample SL23KM30 (A - XPL, B - PPL in transmitted light) showing needle-like plagioclase. Abbreviations: Mag – magnetite, Pl – plagioclase, Chl – chlorite, Afs – alkali feldspar.

Iron-titanium oxides in the GZ are magnetite, ilmenite, and Cr-spinel, forming up to 15% of the rock (Fig. 4.6). Oxides occur in a range of sizes, textures and degrees of alteration.

Magnetite occurs as anhedral medium-grained blebs and subhedral skeletal crystals with common ilmenite exsolution lamellae (Fig. 4.6), and as well as being disseminated and as inclusions in amphiboles. Tabular-, skeletal- and needle-like fine- to medium-grained magnetite-

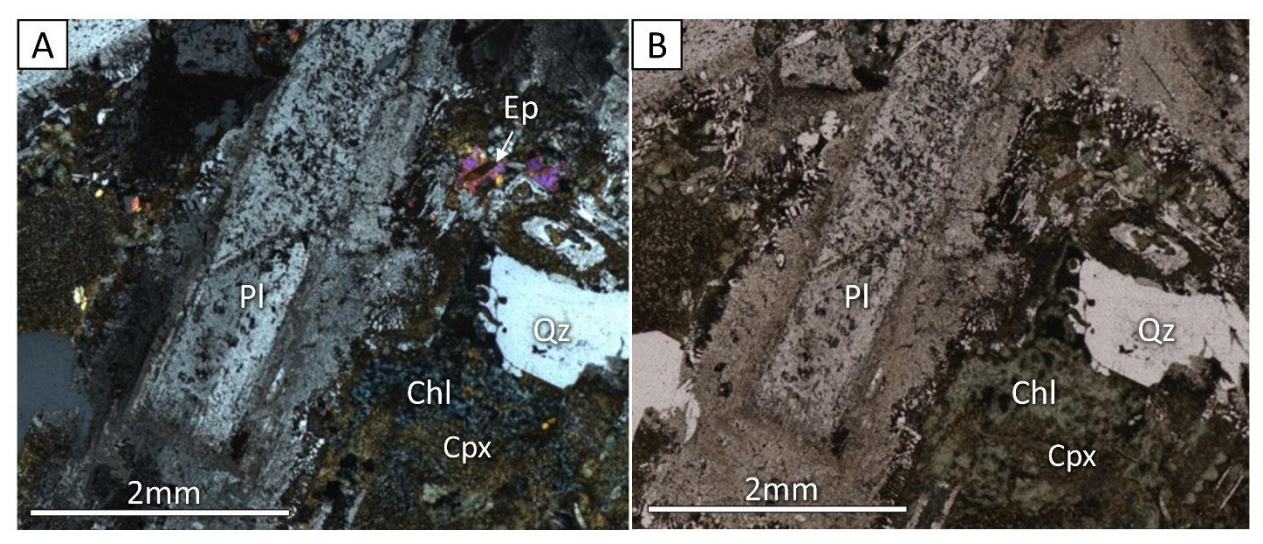


Figure 4.5. Photomicrographs of sample SL23KM69 (A-PPL, B-XPL in transmitted light) with sericite and epidote alteration with zoned hematization on plagioclase and chlorite alteration in clinopyroxenes. Abbreviations: Pl-plagioclase, Ep-epidote, Chl-chlorite, Cpx-clinopyroxene, Qz-quartz.

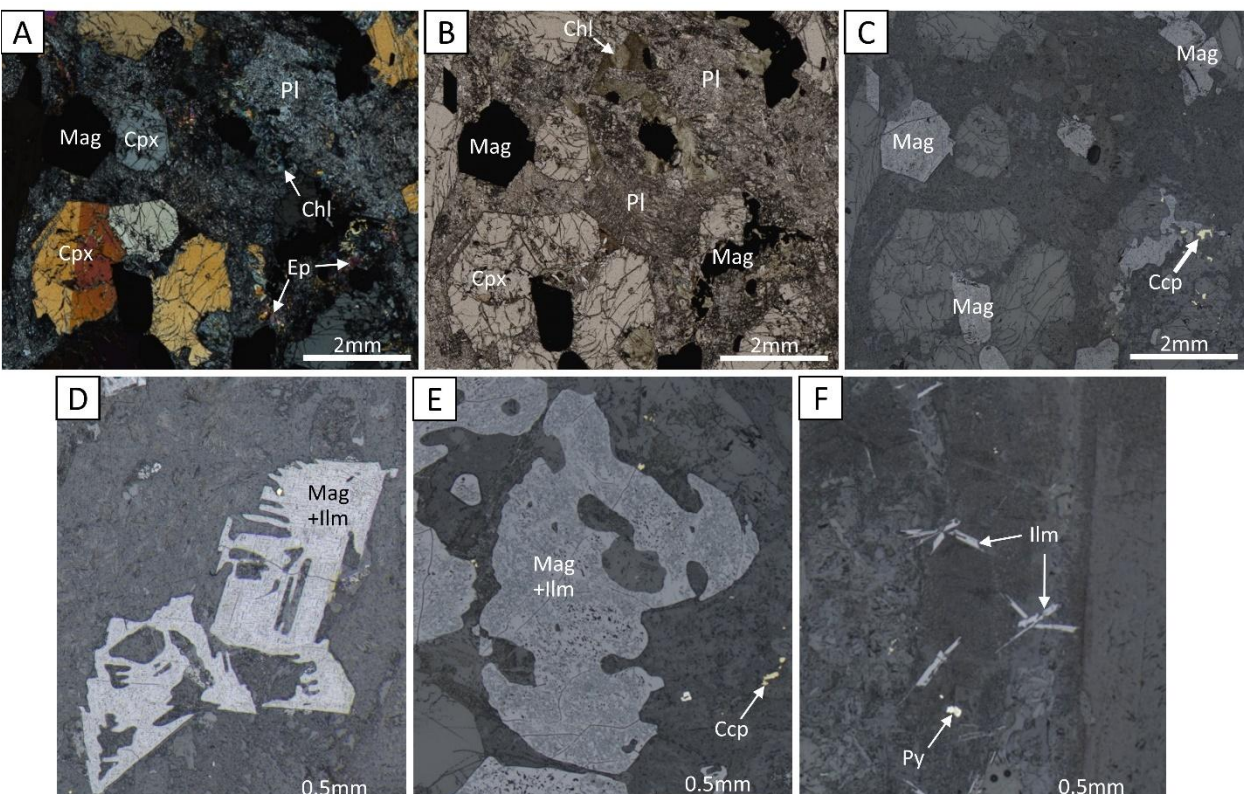


Figure 4.6. Photomicrographs of sample SL23KM62 (A – PPL, B - XPL in transmitted light and C – PPL in reflective light). Representative photomicrographs of different textured oxides taken in reflective light: subhedral skeletal magnetite crystals (Sample SL23KM71; D), magnetite blebs with ilmenite lamellae exsolution (Sample SL23KM65; E), ilmenite needle-like radial crystals (Sample SL23KM69; F). Abbreviations: Mag – magnetite, Ilm – ilmenite, Ccp – chalcopyrite, Py – pyrite.

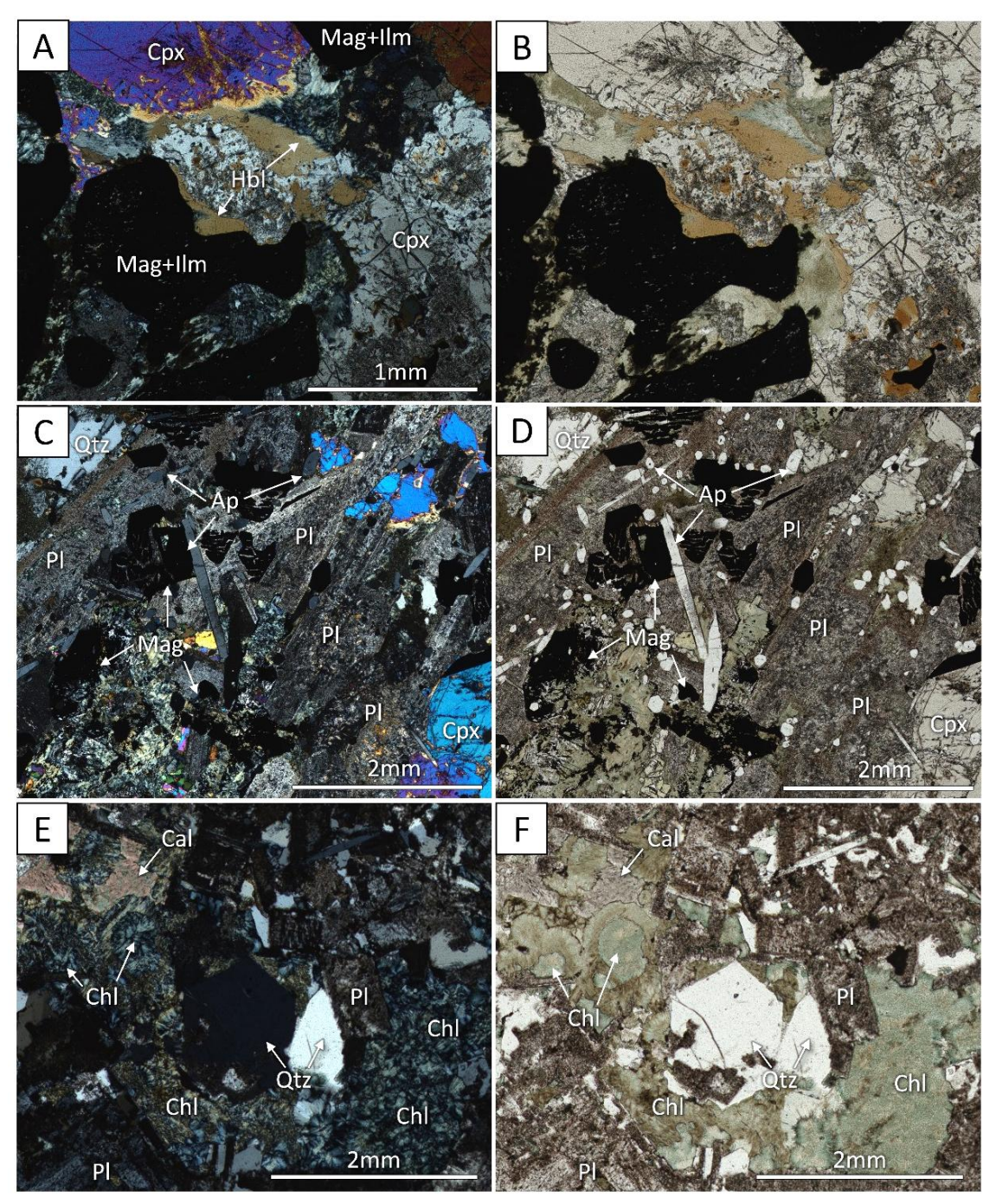


Figure 4.7. Photomicrographs of sample SL23KM65 showing hornblende between oxides and moderately altered to chlorite in (A-XPL, B-PPL) in transmitted light). Sample SL23KM67 is characterized as a gabbro and has disseminated subhedral apatites (C-XPL, B-PPL) in transmitted light). Sample SL23KM30 has subhedral interstitial and blebbly-like magnetite with associated chalcopyrite (E-PPL) in reflective light). Abbreviations: Mag-magnetite, Ccp-Chalcopyrite, Cpx-Clinopyroxene, Pl-plagioclase, Chl-chlorite, Hbl-Hornblende, Ol-Olivine.

ilmenite crystals are disseminated and form radial structures (Fig. 4.6 D-F). The red-brick colour of the quartz gabbros and red/pink patches on the gabbros are the result of hematization that occurs as microcrystalline to cryptocrystalline oxidation of plagioclase rims (Fig. 4.5).

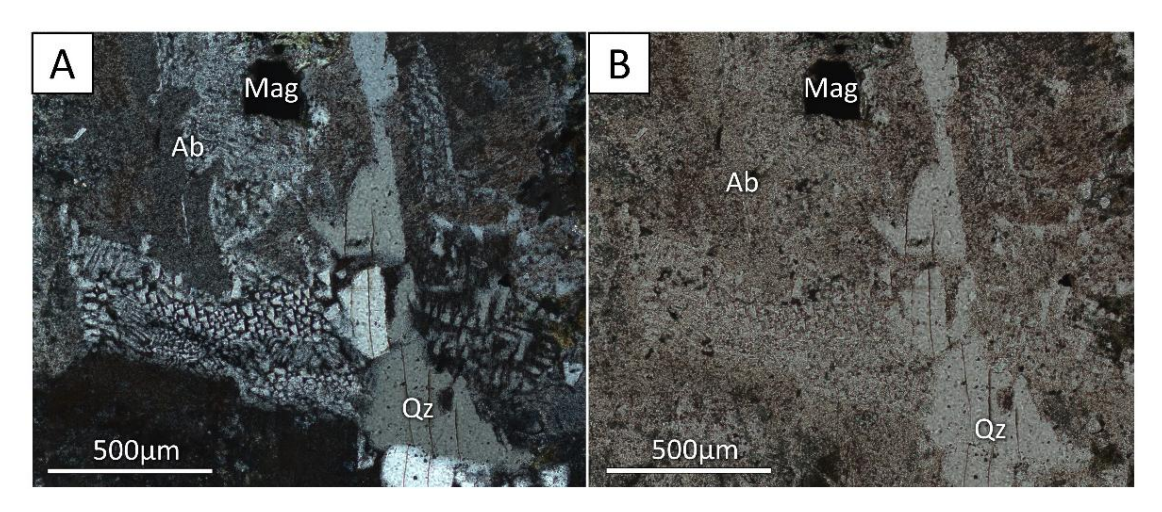


Figure 4.8. Photomicrograph of sample SL23KM30 (A - PPL, B - XPL in transmited light) showing graphic texture and very fine-grained disseminated hematite in albite.

Alkali-feldspar, quartz, hornblende and biotite are variably present in the GZ from absent to a few tens of percent. K-feldspar (0-35%) is found in the quartz monzonites as subhedral medium-grained prismatic crystals commonly with graphic texture, they are weakly to moderately altered to sericite forming radial spherules and show weak to moderate hematization (Figs. 4.7 and 4.8). Anhedral fine- to medium-grained quartz varies in abundance from 0% to 35% and occurs as an interstitial (intercumulous) phase, with common undulose extinction (Fig. 4.8). K-feldspars and quartz are more abundant towards the top in the uppermost units, for drillhole SL-17-18B (towards the northern portion of the intrusion) K-feldspar and quartz can comprise up to 40% of the rock, whereas in drillhole SL-19-26 they generally comprise 15% of

the rock. Hornblende and biotite generally occur as accessory minerals, occurring as anhedral to subhedral, fine- to very fine-grained interstitial crystals. Hornblende and biotite are closely related to oxides as they occur as inclusions and at crystal boundaries (Fig. 4.7A-B). Biotite shows a weak alteration to chlorite, whereas hornblende shows no alteration. Hornblende is interpreted as primary based on its subhedral habit and equilibrium textures with plagioclase and clinopyroxene. Other accessory minerals in the GZ are fine-grained prismatic euhedral apatite, which is generally found as traces along the GZ but has an increased abundance in samples SL23KM26 and SL23KM67 of 5-8% (Fig. 4.7C-D).

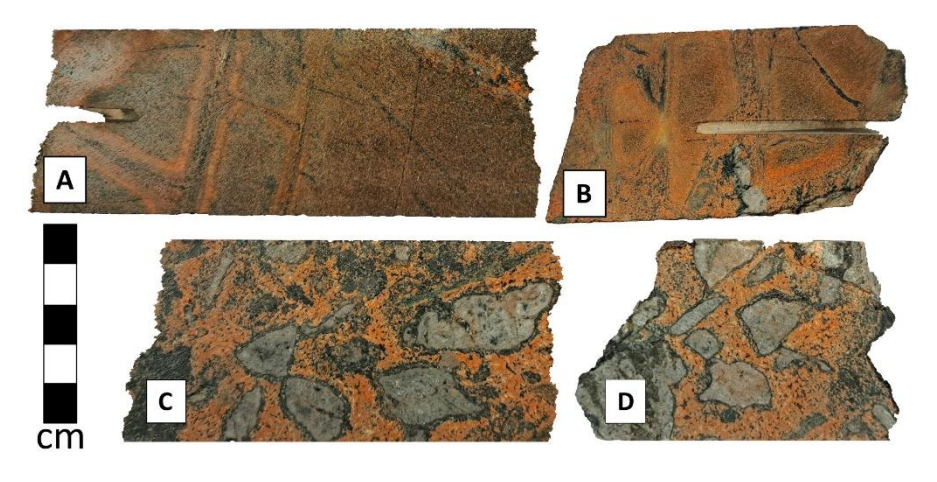


Figure 4.9.
Representative core
samples from the Breccia
Zone of the GZ. Sample
SL23KM39 shows a
crackle breccia with
zoned alteration around
fragments (A; B). Sample
SL23KM36 shows a
matrix-supported breccia
with gray Quetico
metasedimentary
rounded fragments (C;
D).

A breccia zone is present in hole SL-17-18B at the upper margin in the northern portion of the intrusion, it has an up to 20m wide zone with gradually increasing abundance of Quetico metasedimentary rocks fragments towards the hanging wall contact with the country rock (Fig. 3.1). The zone includes a variety of breccias, from a crackle breccia with moderate to strong zoned alteration and oxidation to hematite (Fig. 4.9A-B) at the top to a matrix-supported breccia with rounded gray xenoliths in a red-brick colour quartz monzonitic rock at the base (Fig. 4.9C-

D). Fragments are weakly to moderately altered to sericite and carbonates and have a reaction halo of chlorite-altered amphiboles, sericite and very fine-grained hematite (Fig. 4.10). Xenoliths

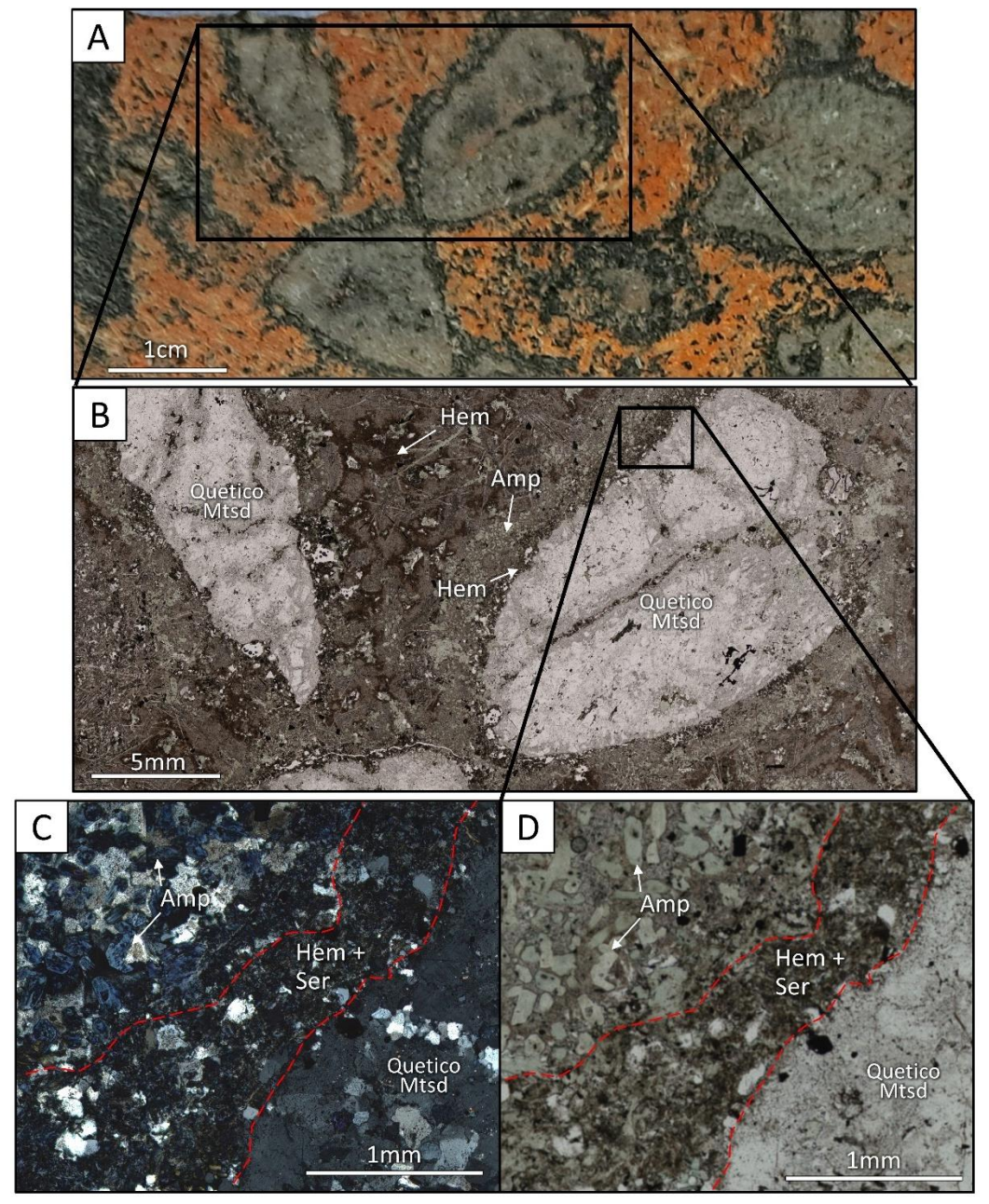


Figure 4.10. Sample SL23KM36 from drillcore (A) showing Quetico metasedimentary fragments with an amphibole reaction halo. Photomicrograph showing a closeup of the reaction halo of the metasedimentary fragments (B-PPL in transmitted light) with an amplified portion showing the outlined field of view. The reaction halo consists of hematite + sericite and chloritized amphiboles (C-XPL and D-PPL in transmitted light).

of the Quetico metasedimentary rocks have fine to very fine disseminated interstitial disseminated sulfides. The abundance of sulfides is generally around 3%, being pyrrhotite the dominant sulfide over chalcopyrite and pyrrhotite. The matrix has a gabbroic composition which is moderately altered and dominated by sericitization of plagioclase, completely chloritized amphiboles and strong oxidation of hematite. In the host rock, the angular breccia has red-brick and grey colour zoned fragments with minor matrix with 2-10% sulfide consisting of Ccp>Py>Po occurring at the contact of the fragments.

4.2.2 Upper Ultramafic Zone

The UUZ is the central unit of the SLI, thicknesses vary from 300 meters at the center of the intrusion to 50 meters in the northeast (Fig. 3.1). The UUZ is a clinopyroxene cumulate phase, with less plagioclase and oxides than the GZ. Plagioclase abundance ranges from 0% to 20%, whereas for the GZ it can be as high as 60%. A total of five thin sections were from the UUZ and are classified as olivine clinopyroxenite and feldspathic olivine clinopyroxenite (Fig. 4.11). Olivine clinopyroxenite is identified as clinopyroxene-rich samples ranging from 60% to

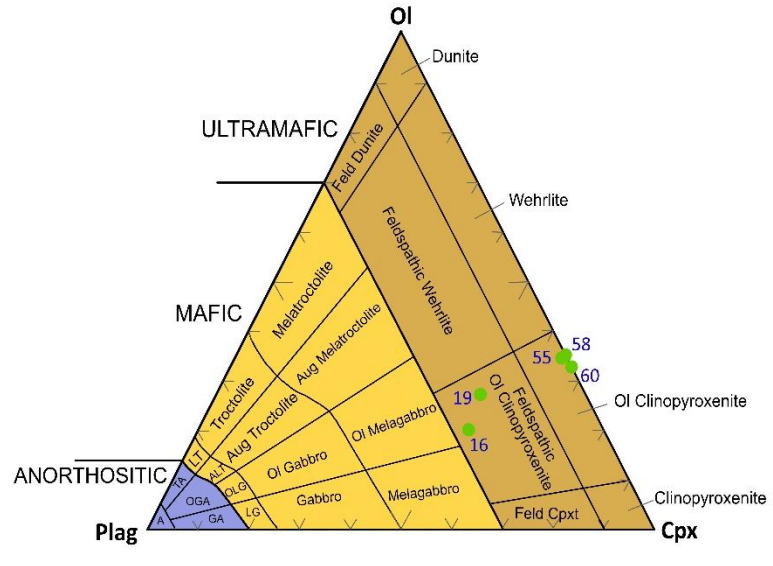


Figure 4.11. Ternary classification for mafic and ultramafic intrusive rocks (Miller et al., 2002). Green circles indicate modal mineral abundances for samples of the UUZ.

65% with no plagioclase, seriated and granular textures and weak alteration (Fig. 4.12). Olivine clinopyroxenite samples are only present in drillhole SL-19-026 and represent the most ultramafic composition in the UUZ (Fig. 4.12C). Feldspathic olivine clinopyroxenite samples were only found in drill hole SL-17-18B and have interstitial plagioclase ranging from 20% to 30% of the rock. The feldspathic olivine clinopyroxenite is fine- to very fine-grained with poikilitic textures and are moderately altered to chlorite, sericite, serpentine and calcite. Towards

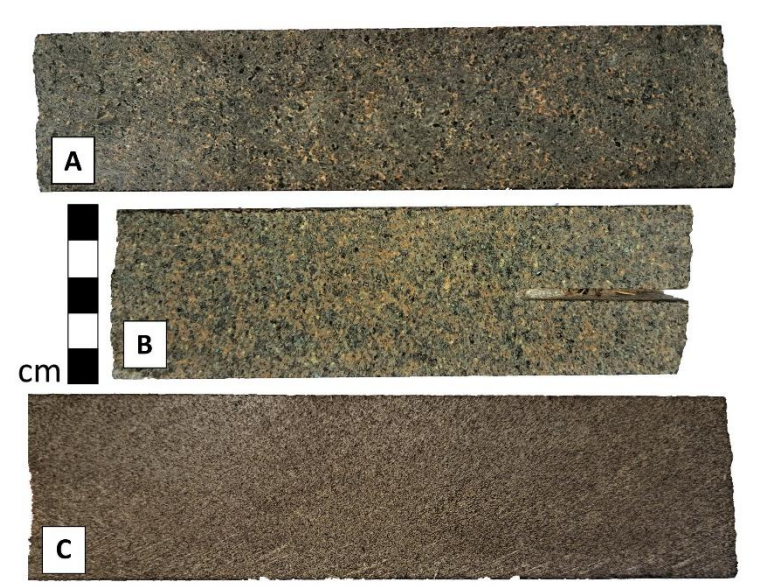


Figure 4.12. Representative core samples from the UUZ. Sample SL23KM20 (A) and sample SL23KM22 (B) have mediumgrained poikilitic to granular textures. Sample SL23KM55 (C) has a fine-grained texture.

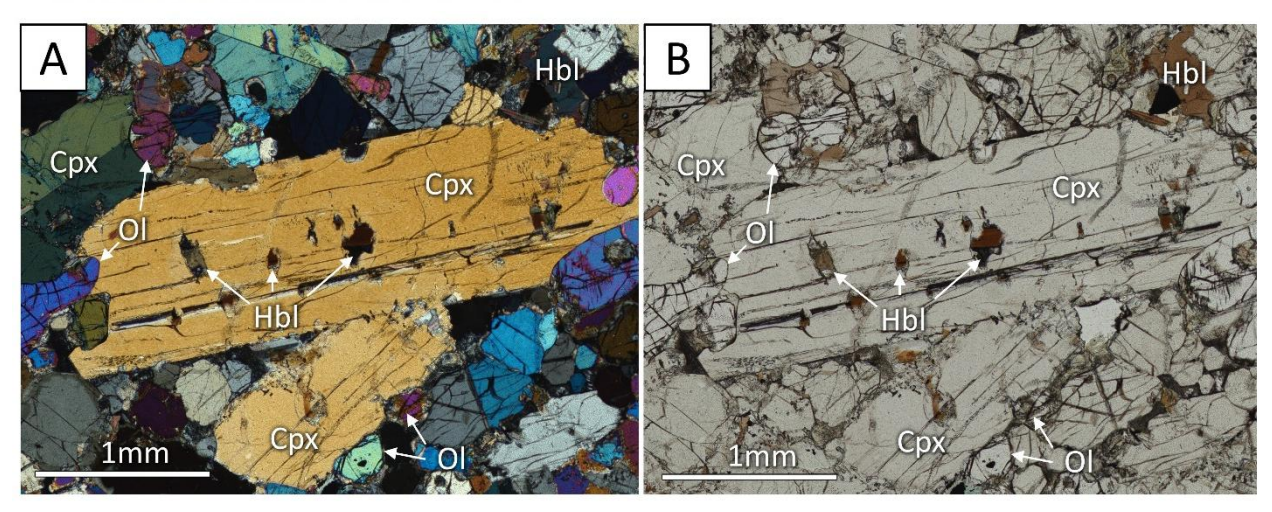


Figure 4.13. Photomicrograph of sample SL23KM60 (A-XPL, B-PPL in transmitted light) showing a clinopyroxene oikocrysts with fine-grained hornblende chadacrysts.

the bottom, in the UUZ, grain size decreases from 2 mm (medium-grained) to 0.75 mm (fine-grained; Fig. 4.12).

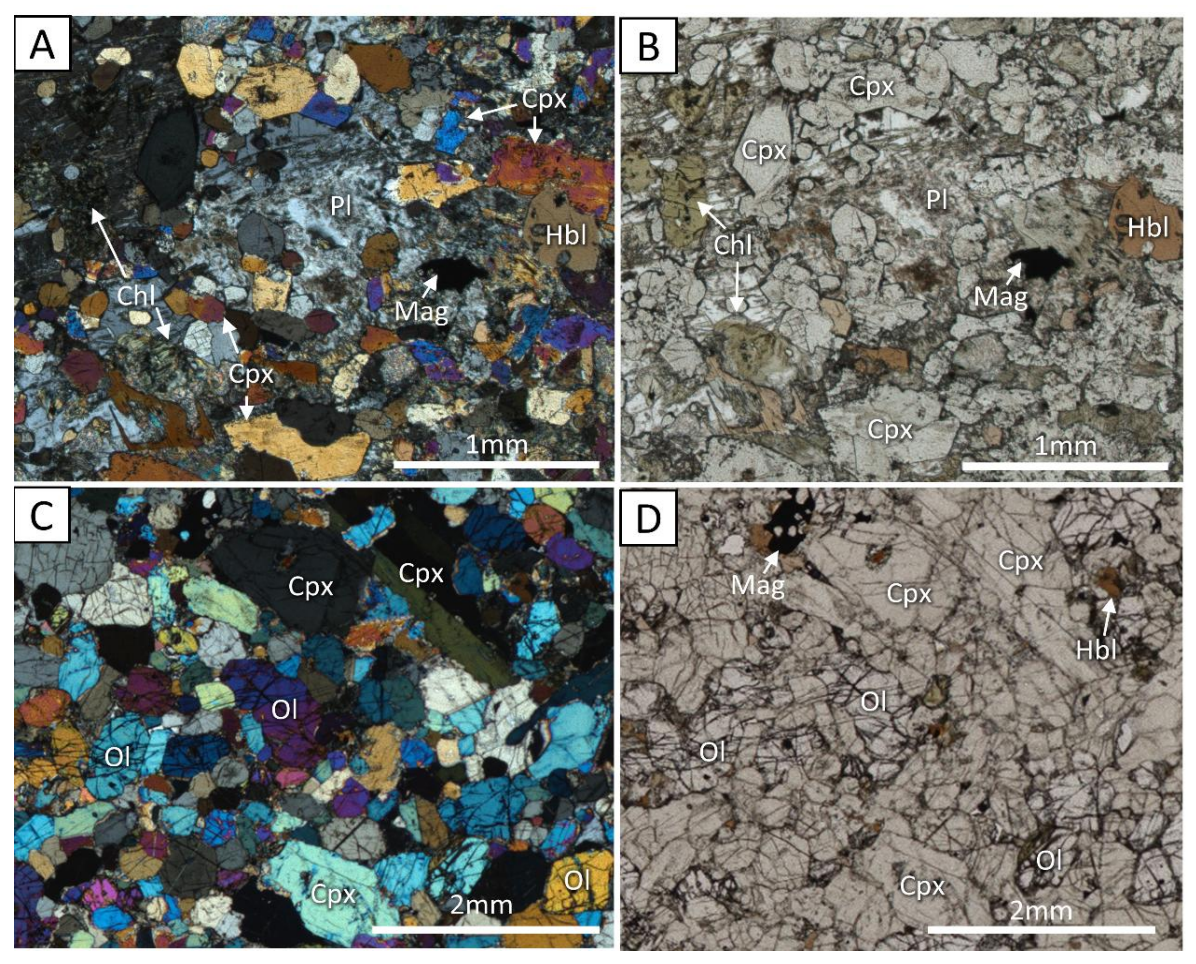


Figure 4.14. Photomicrographs of representative samples of the UUZ: Sample SL23KM19 (A-XPL, B-PPL) in transmitted light) classified as a feldspathic olivine clinopyroxenite with a poikilitic texture on plagioclase and subhedral clinopyroxene chadacrystals. Sample SL23KM60 classified as an olivine clinopyroxenite with granular seriate texture (C-XPL, B-PPL) in transmitted light). Abbreviations: Mag-magnetite, Cpx-Clinopyroxene, Pl-Plagioclase, Chl-chlorite, Chl-c

The main mineral assemblage for the UUZ is composed of clinopyroxene, olivine and plagioclase. Mafic mineral abundance generally increases downwards, with clinopyroxene and olivine increasing throughout the UUZ, from 35% to 65% and 0% to 35%, respectively. The

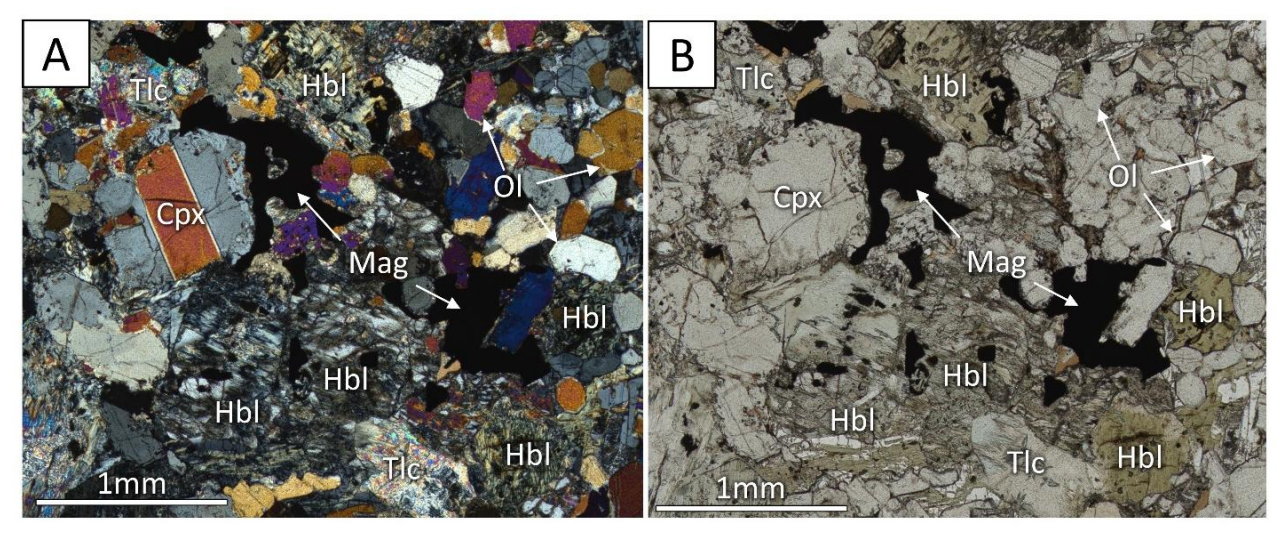


Figure 4.15. Photomicrograph of sample SL23KM19 (A-XPL, B - PPL in transmitted light) classified as a feldspathic olivine pyroxenite showing chloritized amphiboles.

UUZ is characterized by clinopyroxene varying in abundance from 35% to 65% occurring as subhedral to anhedral fine- to coarse-grained tabular and granular crystals. Clinopyroxene commonly has oxide and hornblende inclusions often occurring as oikocrysts (Fig. 4.13).

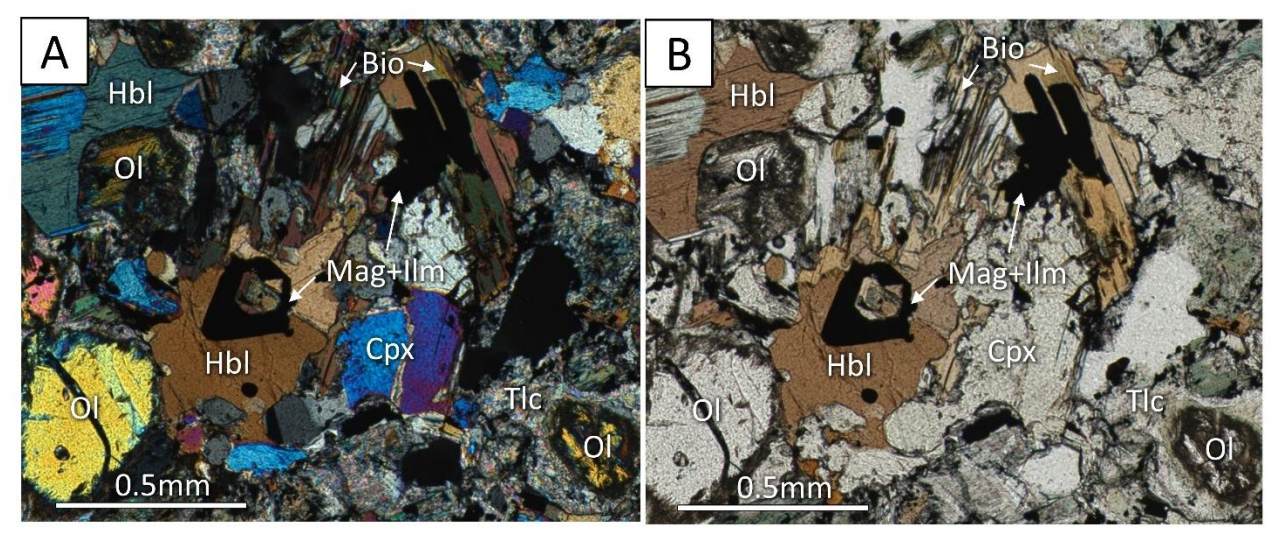


Figure 4.16. Photomicrograph of sample SL23KM16 (A-XPL, B-PPL in transmitted light) showing a biotite and hornblende with embedded magnetite and ilmenite.

Clinopyroxene crystals commonly show twinning with weak to moderate serpentinization and alteration to chlorite, sericite, biotite, epidote and minor carbonates (Fig. 4.14).

Olivine occurs as anhedral to subhedral fine- to medium-grained crystals with an abundance of 30% to 35%. Olivine crystals are weakly to strongly serpentinized and have magnetite/Cr-spinel inclusions, often as chadacrysts (Figs. 4.15 and 4.16). Plagioclase is subhedral medium- to coarse-grained and ranges from 0% to 35% in abundance, occurring as oikocrysts with moderate alteration to sericite and minor calcite. Anhedral fine-grained interstitial hornblende (1-10%) is found disseminated in the sample and is weakly to moderately altered to chlorite and often associated with oxides (Figs. 4.15 and 4.16). Fine- to medium-grained chlorite-actinolite spherules have replaced intensively altered amphiboles. Oxides in the UUZ comprise less than 5% of the total rock, and are characterized by subhedral fine-grained Cr-spinel, fine-grained tabular and needle-like ilmenite, and subhedral and blebby fine-grained interstitial magnetite with common ilmenite exsolution lamellae (Fig. 4.17). Sulfides occur as

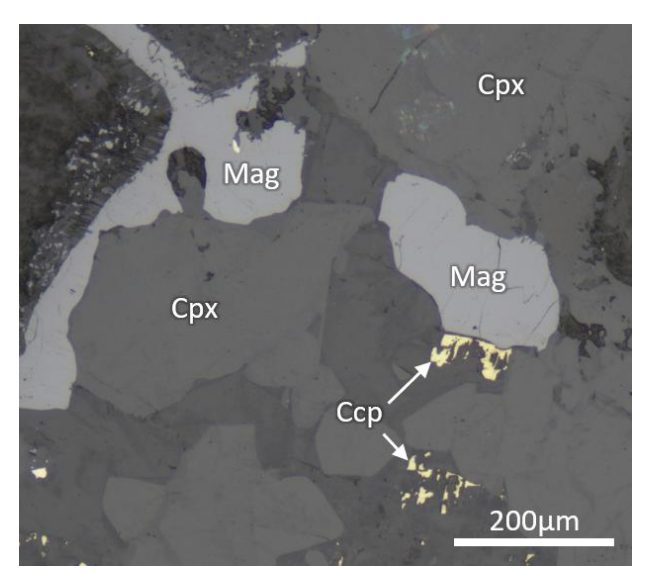
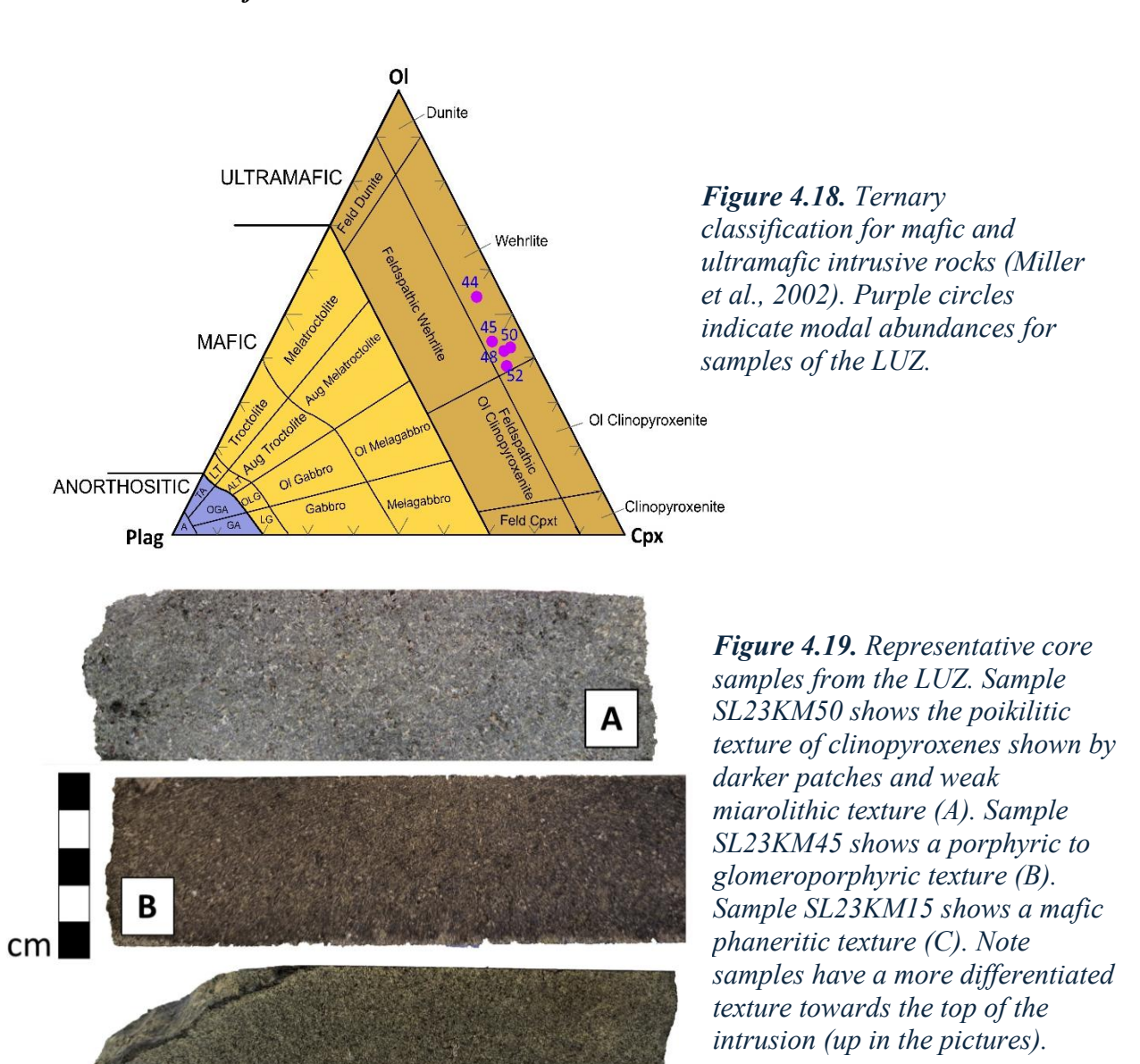


Figure 4.17. Subhedral interstitial and blebbly magnetite with associated chalcopyrite (E-PPL in reflective light).

Abbreviations: Cpx – Clinopyroxene, Mag – magnetite, Ccp – Chalcopyrite.

anhedral fine- to very fine-grained interstitial disseminated pyrrhotite>chalcopyrite in samples of the UUZ, sulfides have a variable abundance in the rocks from absent to up to 1%.

4.2.3 Lower Ultramafic Zone



The LUZ comprises the lower-most portion of the intrusion. It has an ultramafic composition and an increasing thickness from \sim 70 meters in the north, to \sim 250 meters towards the southern part of the intrusion (Fig. 3.1). A total of five thin sections were examined from the LUZ and were identified as wehrlite (Fig. 4.18). The main minerals that comprise the LUZ are

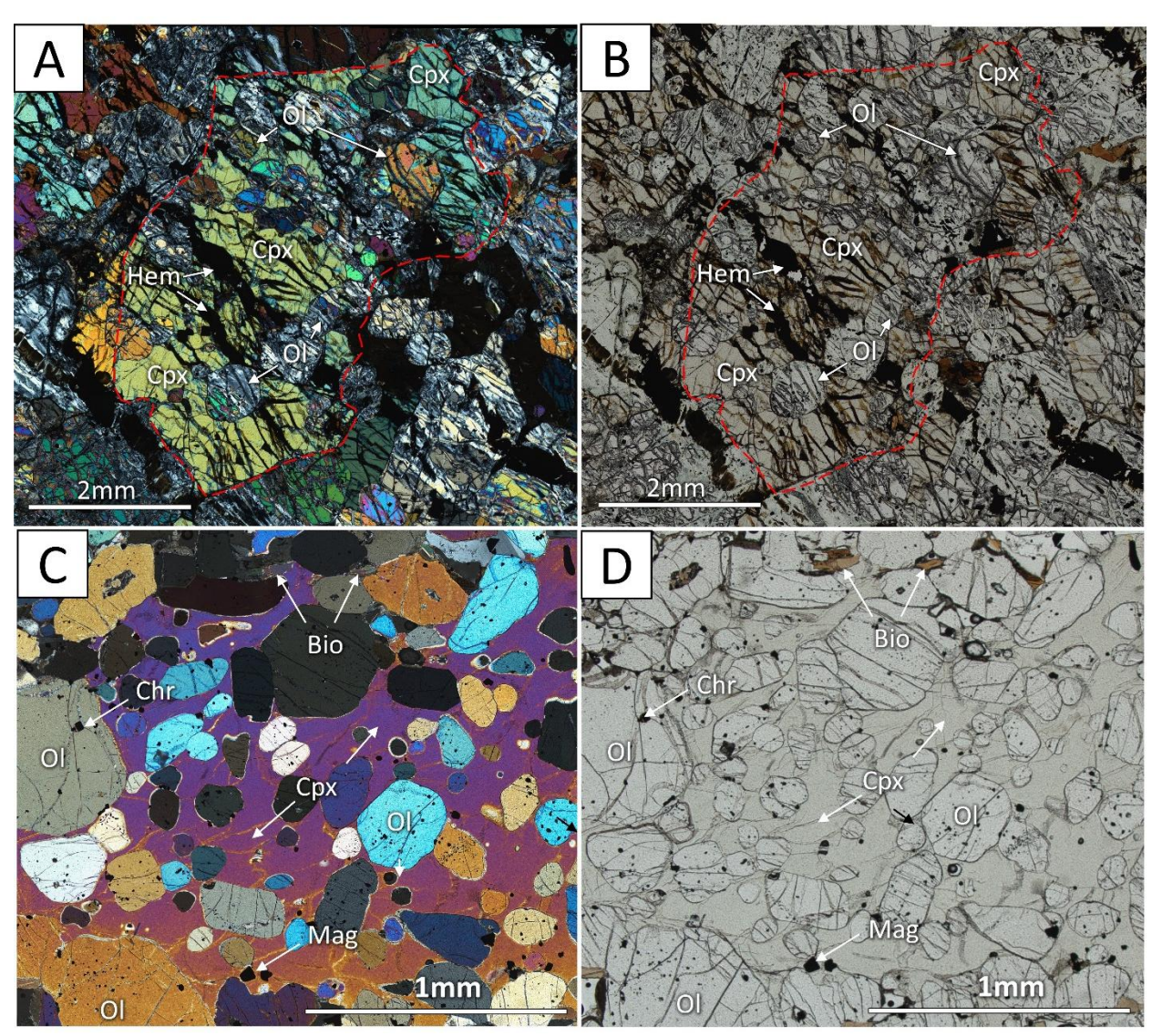


Figure 4.20. Photomicrographs of sample SL23KM44 (A-XPL, B-PPL in transmitted light) showing a clinopyroxene oikocryst with rounded subhedral olivine chadacryst with moderate to strong serpentinization. Sample SL23KM48 classified as a wehrlite with poikilitic texture (D-XPL, E-PPL in transmitted light), fine disseminated chromite inclusions occurring in olivine chadacrysts. Abbreviations: Mag – magnetite, Chr - Chromite, Cpx – Clinopyroxene, Bio – Biotite, Ol – Olivine, Hem – Hematite.

clinopyroxene, olivine and plagioclase. Rocks of the LUZ are fine- to medium-grained with a poikilitic texture formed by darker patches of clinopyroxene oikocrystals and miarolitic textures (Fig. 4.19). Weak to moderate serpentinization occurs throughout the LUZ.

Wehrlites of the LUZ are characterized by a clinopyroxene abundance from 30% to 50%, crystals are generally anhedral to euhedral, fine- to coarse-grained oikocrysts and chadacrysts. Clinopyroxenes are weakly altered to chlorite and serpentine with common oxide inclusions (Fig. 4.20). Olivines are subhedral medium- to fine-grained crystals and range in abundance from 30% to 45%. They are weakly to strongly serpentinized with moderate magnetite and chromite inclusions (Fig. 4.20). Olivine commonly occurs as chadacrysts in clinopyroxene and granular in groundmass (Fig. 4.20C-D). Plagioclase ranges in abundance from 5% to 10%, it occurs as anhedral, fine- to medium-grained crystals. Plagioclase is found as oikocrysts moderately to completely altered to sericite, chlorite and calcite. Anhedral to subhedral fine-grained hornblende (2-10%) is found interstitially and closely related to oxides (Fig. 4.21). Biotite (0-4%) is found as an accessory mineral in all the samples as fine-grained interstitial crystals weakly altered to

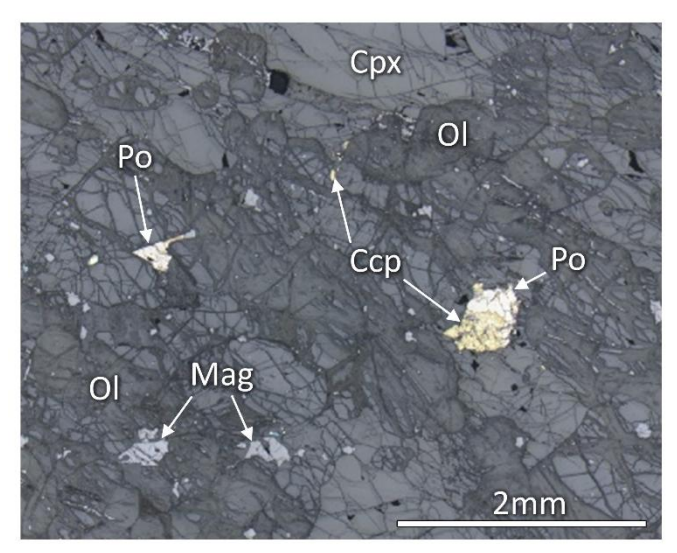
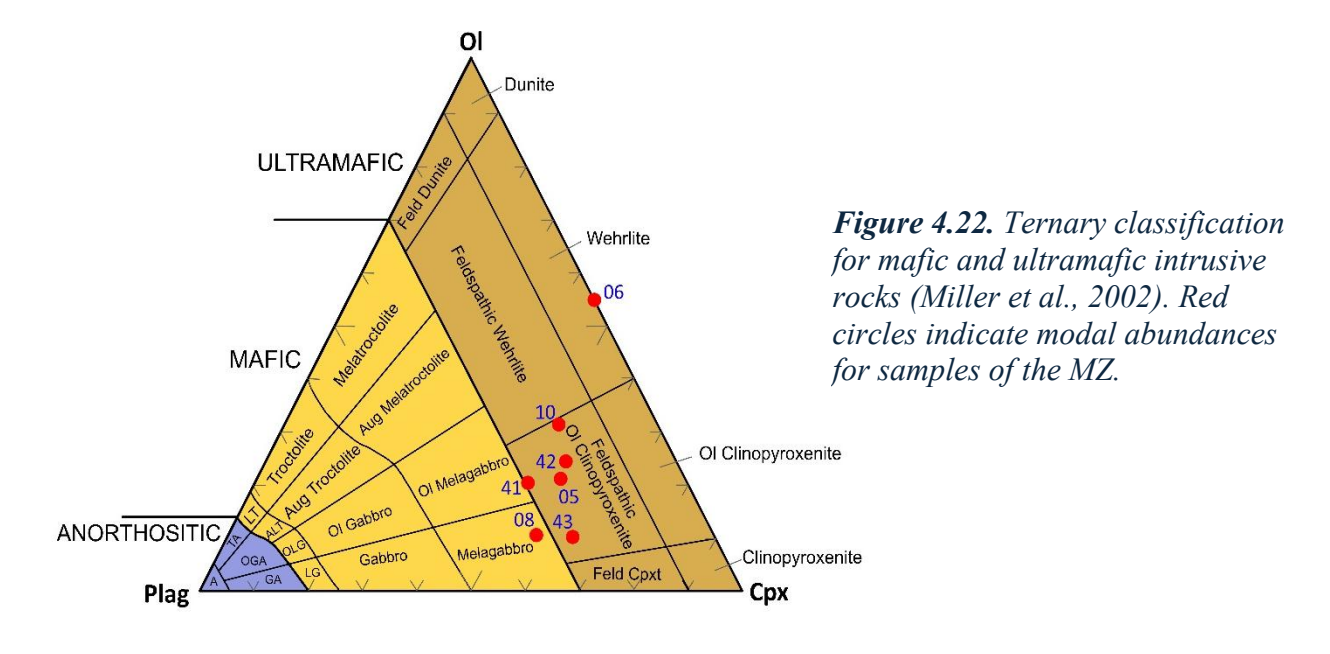


Figure 4.21. Photomicrograph of sample SL23KM44 showing interstitial oxides and sulfides. Abbreviations: Mag – magnetite, Po – Pyrrhotite, Ccp – Chalcopyrite, Cpx – Clinopyroxene, Ol – Olivine.

chlorite and closely related to hornblende and oxides (Fig. 4.20). Oxides are present in varying abundances, ranging from 1% to 7%. They consist of anhedral to euhedral fine- to very fine-grained magnetite with common ilmenite lamellae exsolutions (Fig. 4.20C-D and 4.21). Euhedral disseminated fine-grained Cr-spinel crystals are often found as inclusions in olivine (Fig. 4.20C-D). Generally, <2% sulfides are found as anhedral fine- to very fine-grained disseminated crystals which comprise 80% chalcopyrite, 18% pyrrhotite and 2% pentlandite (Fig. 4.21).

4.2.4 Marginal Zone

The Marginal Zone (MZ) is a subdivision of the Lower Ultramafic Zone (LUZ), it has a variable composition compared to the LUZ and is more heterogeneous. A total of seven samples were taken for thin sections from the MZ, which is characterized by sulfide abundances from 5% to 15%. The MZ occurs as the basal contact of the intrusion with the Quetico metasedimentary rocks (Fig. 3.1). The rock types in this zone are melagabbro, feldspathic olivine clinopyroxenite



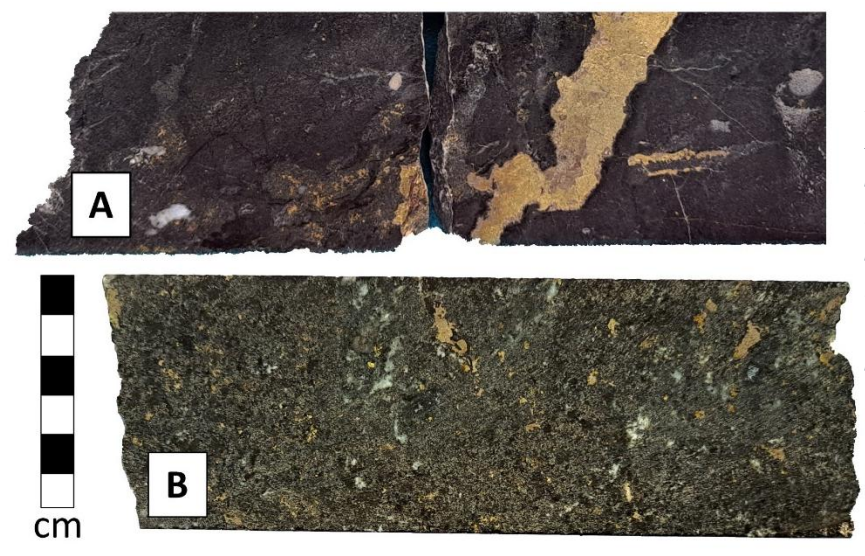


Figure 4.23.
Representative core
samples of the MZ. Sample
SL23KMMVZ shows a
sulfide vein (A). Sample
SL23KM04 shows
disseminated and blebby
sulfides (B).

and wehrlite (Fig. 4.22). The melagabbro sample is characterized by a plagioclase abundance of ~25% of the rock whereas the feldspathic olivine clinopyroxenite has 15 to 20% plagioclase abundance. One sample is a werhlite and has an increased olivine abundance of 35% of the rock whereas the rest of the samples have 10% to 25%. The Marginal Zone is generally dark grey with medium- to coarse-grained and granular, seriate and poikilitic textures (Fig. 4.23). The main

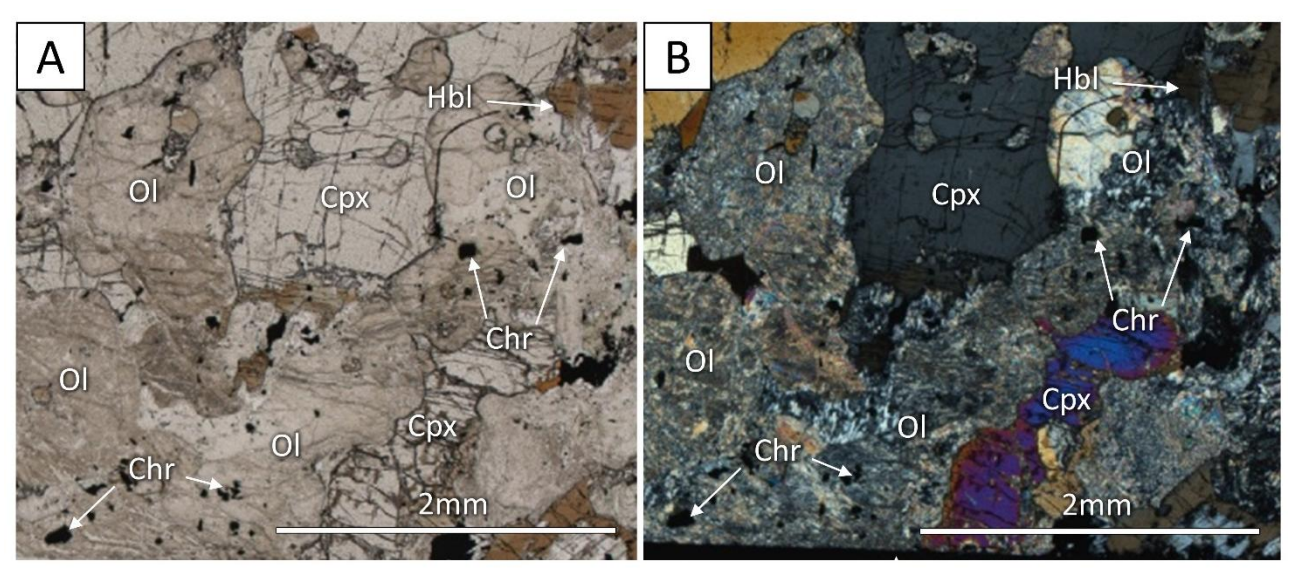


Figure 4.24. Photomicrographs showing chromite inclusions in strongly altered olivines. Sample SL23KM06. (A – PPL, B - XPL in transmitted light)

minerals in the MZ comprises clinopyroxene, plagioclase, olivine, and sulfide minerals such as pyrrhotite, chalcopyrite and pentlandite.

Clinopyroxene varies in abundance from 20% to 50%, occurring as anhedral to subhedral fine- to medium-grained crystals. Clinopyroxenes are weakly to moderately altered to sericite, calcite and biotite (Fig. 4.24). Olivine varies from absent to up to 30%, it occurs as rounded subhedral medium- to fine-grained crystals, that are moderately to strongly altered to talc, chlorite and serpentine, and commonly have very fine-grained Cr-spinel inclusions (Fig. 4.24). Anhedral to euhedral coarse- to medium-grained plagioclase ranges from 0% to 30% in abundance, it is moderately to strongly altered to sericite, calcite, and chlorite spherules (Fig. 4.25A-B). Plagioclase occurs as oikocrysts and as euhedral tabular crystals. Fine-grained anhedral biotite (0-10%) is found interstitially and often related to hornblende, oxides and sulfides as aggregates at the boundaries of oxides. Anhedral to euhedral tabular fine- to medium-grained hornblende ranges in abundance from 2% to 10%; it is found interstitially and associated with oxides.

Oxides are found in the silicate groundmass as fine, disseminated blebby and skeletal crystals of magnetite with trellis and sandwich exsolution. Fine disseminated needle- and tabular-like ilmenite crystals are also found (Fig. 4.25). Euhedral, very fine-grained disseminated Cr-spinel are found in the groundmass but are more commonly found in olivine as inclusions (Fig. 4.24). Mineralization in the Marginal Zone consists of disseminated, interstitial, blebby sulfides and 2-3 cm wide veins. The sulfide mineral assemblage consists of 55% pyrrhotite, 35% chalcopyrite, 8% pentlandite and 2% cubanite (Fig. 4.26). Pyrrhotite is the dominant phase of the

blebby and disseminated sulfides. Pyrrhotite commonly has troilite lamellae exsolution and pentlandite lamellae- and chain-like exsolution textures (Figs. 4.25 and 4.26). Chalcopyrite is found interstitially-disseminated and as blebs (Fig. 4.25), it frequently occurs surrounding

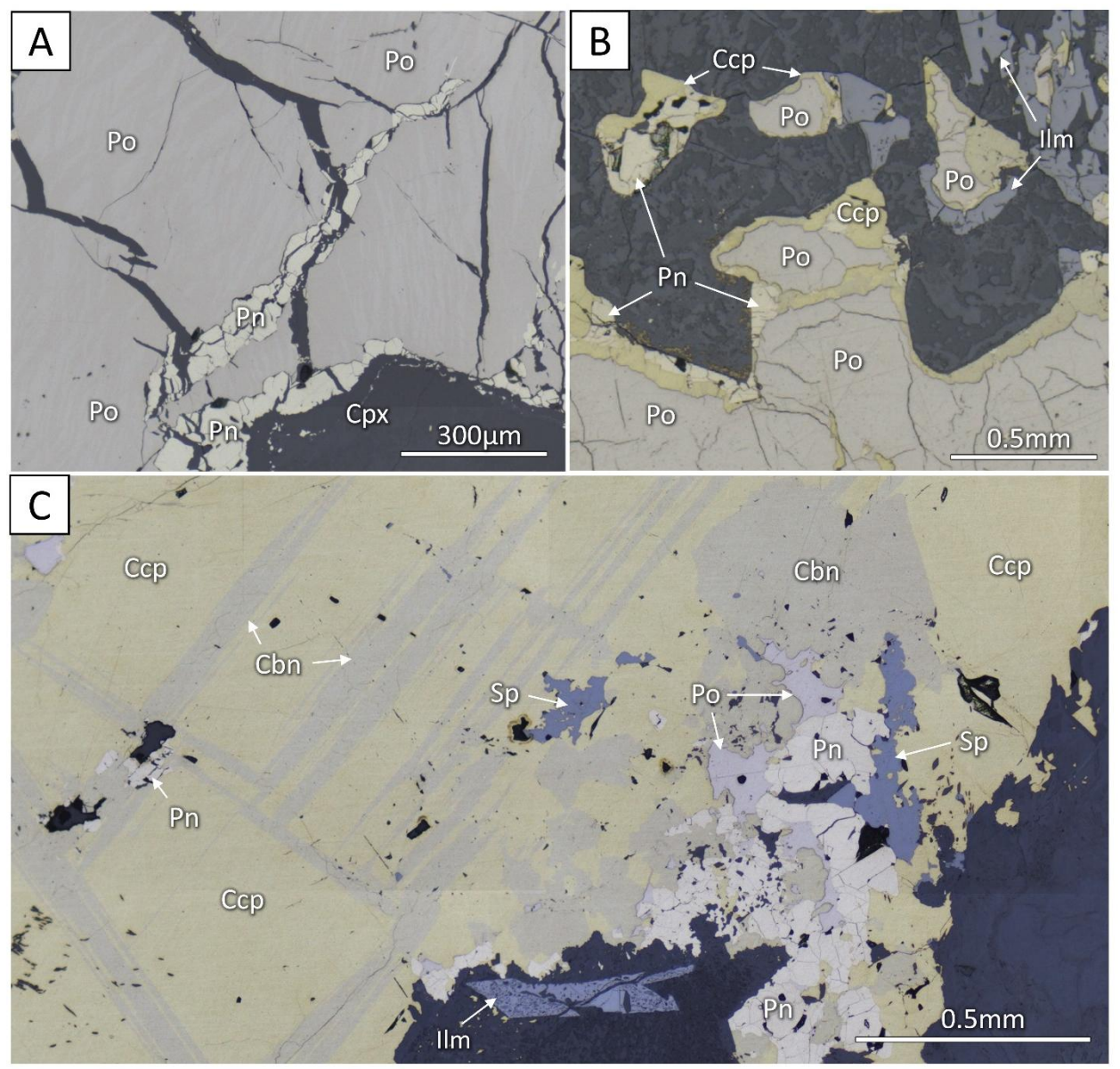


Figure 4.26. Photomicrographs of representative sulfide of the MZ. Sample SL23KM08 showing chain-like pentlandite exsolutions in pyrrhotite (A-PPL) in reflective light). Sample SL23KM41 shows chalcopyrite bounding sulfide blebs (B), cubanite exsolution in chalcopyrite, embedded sphalerite in chalcopyrite and other sulfides like pyrrhotite and pentlandite. (C-PPL) in reflective light). Abbreviations: (C-PPL) in cubanite, (C-PPL) in (C-PPL) in

pyrrhotite (Fig. 4.26B). Chalcopyrite has medium- to coarse-grained blebby textures with common cubanite lamellae exsolution (Fig. 4.26C). Minor fine-grained clusters of pentlandite are commonly found embedded in chalcopyrite (Fig. 4.26C). Traces of very fine-grained anhedral sphalerite occurs disseminated in chalcopyrite and often related to pentlandite (Fig. 4.26C). Oxides in the sulfide phases comprise wormy, blebby and anhedral aggregates of magnetite-ilmenite in chalcopyrite and pyrrhotite (Fig. 4.25).

4.2.5 Host rock – Quetico metasedimentary rocks

Quetico metasedimentary rocks are the dominant host rock to the Sunday Lake Intrusion. Three thin sections were produced to characterise the Quetico metasedimentary rocks. The host rock has foliated, gneissic and homogeneous textures. Quartz banding (Fig. 4.27A) is common in the northern portion of the intrusion, whereas the southern part shows a more homogeneous composition (Fig. 4.27B). It is characterized by anhedral fine-grained quartz with undulose extinction, fine-grained anhedral to anhedral K-feldspars with strong alteration to sericite (Fig. 4.28), fine- to very fine-grained biotite with weak alteration to chlorite. Very fine-grained subhedral needle- and lath-like ilmenite occur disseminated in the sample. Sulfides (<5%) occur



Figure 4.27. Representative core samples of the Quetico metasedimentary rocks. Sample SL23KM01 quartz banding (B). Sample SL23KM40 shows a granular homogeneous composition with a quartz veinlet (B).

as very fine- to fine-grained disseminated pyrrhotite, chalcopyrite and pyrite in modal proportions of 70%, 20% and 10%, respectively. Pyrrhotite is found as subhedral crystals with pyrite and chalcopyrite as anhedral aggregates (Fig. 4.28).

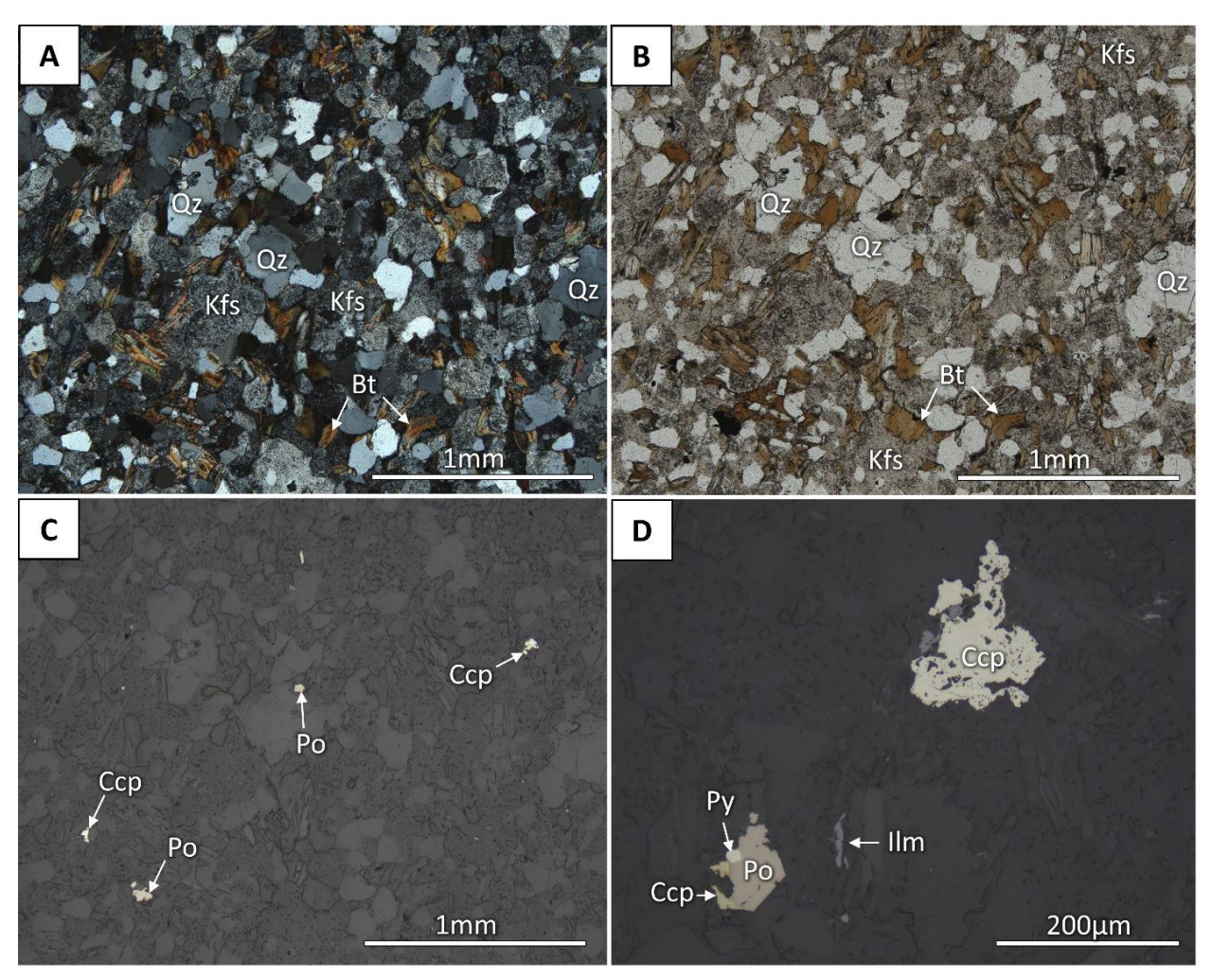


Figure 4.28. Photomicrographs of representative samples of the Quetico metasedimentary rocks: Sample SL23KM01 (A-XPL, B-PPL in transmitted light and C-PPL in reflective light) shows a fine grained homogeneous granular texture, a closeup of the very fine to fine grained sulfides are shown (D-PPL in reflective light). Abbreviations: Qz-quartz, Kfs-alkali feldspar, Bt-biotite, Po-Pyrrhotite, Ccp-chalcopyrite, Ilm-ilmenite, Py-Pyrite.

4.2.6 Platinum group minerals

A total of thirty-nine platinum-group minerals (PGMs), along with tellurides, sulfosalts, sulfides and native metals, were identified using SEM-EDS. The grain sizes range from 2 μ m to 20 μ m, and the PGMs characterized based on their elemental weight percent composition. The pie chart shows the relative abundance of PGMs, calculated by counting the frequency of occurrence crystals in the sample set (Fig. 4.29).

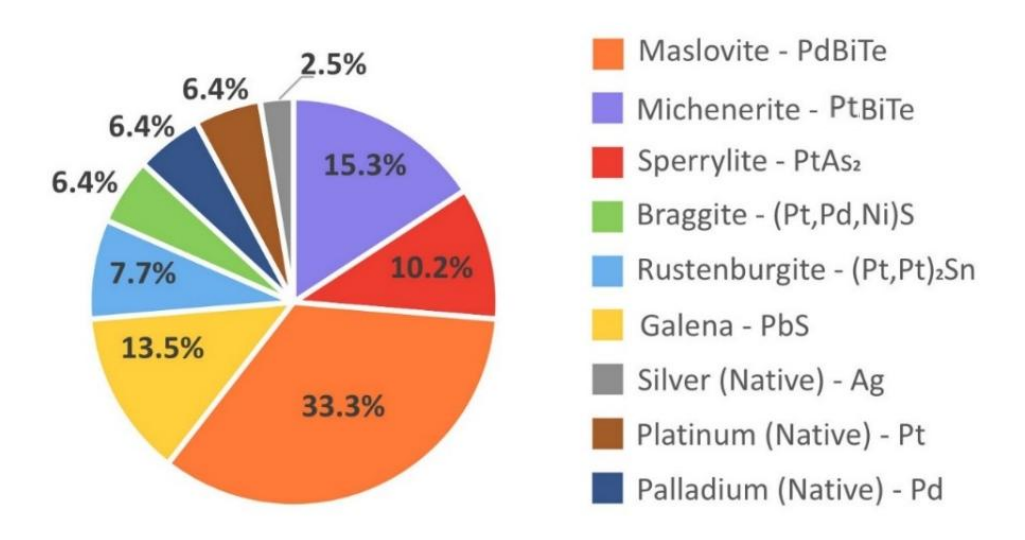


Figure 4.29. Pie chart of the PGM abundance percentages.

Michenerite, sperrylite and maslovite were the most common PGM identified. Maslovite is the most common telluride and occurs as very fine-grained elongated and rounded anhedral inclusions within sulfides, chalcopyrite is the most common host of maslovite but it was also found in pyrrhotite and pentlandite (Fig. 4.30A-B). The second most frequent PGM is sperrylite, which occurs as fine-grained, anhedral grains. It is found as inclusions within sulfide

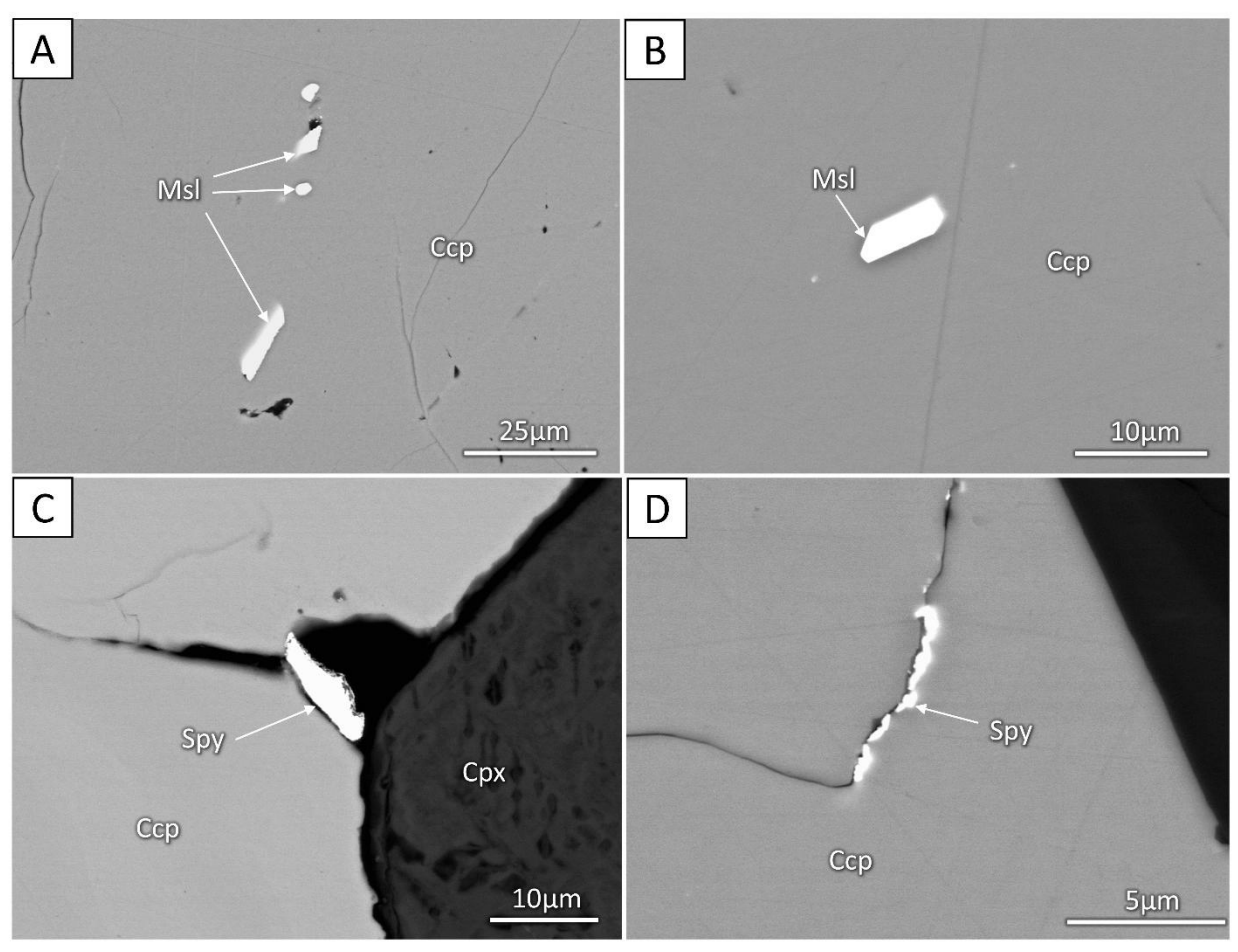


Figure 4.30. Back-scattered electron images of platinum group minerals and related minerals. A – very fine-grained elongated and rounded maslovite in chalcopyrite (sample SL23KM41). B – very fine-grained subhedral elongated maslovite (sample SL23KM10). C – very fine-grained anhedral sperrylite at the border of a chalcopyrite grain (sample SL23KM08). D - very fine-grained anhedral sperrylite at the fracture of chalcopyrite grain (sample SL23KM08). Abbreviations: Ccp – chalcopyrite, Msl – maslovite, Spy – sperrylite, Cpx – clinopyroxene.

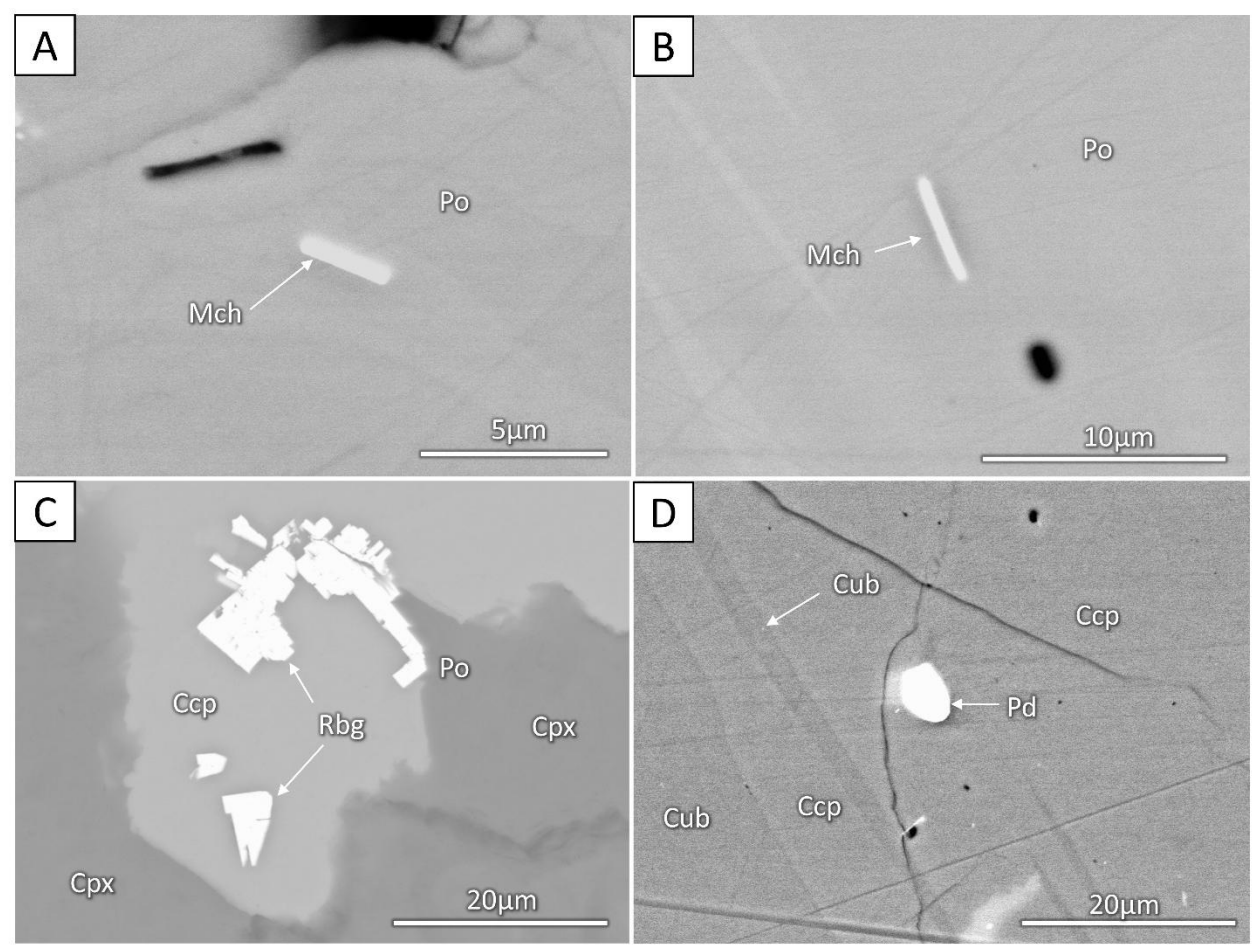


Figure 4.31. Back-scattered electron images of platinum group minerals and related minerals. A – very fine-grained elongated michenerite in pyrrhotite (sample SL23KM06). B – very fine-grained subhedral elongated michenerite in pyrrhotite (sample SL23KM08). C – very fine-grained equant/tabular rustenburgite in chalcopyrite (sample SL23KM41). D - very fine-grained rounded native palladium in pyrrhotite anhedral sperrylite at the fracture of chalcopyrite grain (sample SL23KM08). Abbreviations: Ccp – chalcopyrite, Po – pyrrhotite, Mch – michenerite, Rbg – rustenburgite, Cub – cubanite, Cpx – clinopyroxene, Pd – palladium (native).

fractures/cleavage and boundaries within chalcopyrite (Fig. 4.30C-D). Another important PGM found within sulfides is michenerite, it occurs as very fine-grained elongated crystals, they occur as inclusions in chalcopyrite, pyrrhotite and pentlandite (Fig. 31A-B).

Other PGM and related minerals such as rustenburgite, galena, silver, native palladium, native platinum and braggite were found in the sulfide phases. Rustenburgite occurred as very

fine-grained subhedral crystals, they have an equant/tabular habit which occurs in chalcopyrite and pentlandite (Fig. 4.31C). Native metals such as silver, native palladium and native platinum were found as anhedral very fine-grained rounded crystals found in pyrrhotite and chalcopyrite (Fig. 4.31D).

4.3 Whole-rock geochemistry

Geochemical rock composition within the two sampled drillholes (SL-17-18B and SL-19-026) revealed ranging values of major elements compositions for each zone of the SLI shown in Table 1.

Table 1. Summary chart of major elements compositions of the SLI.

	SiO ₂ (wt. %)	MgO (wt. %)	TiO ₂ (wt. %)
Gabbro Zone	44.70-61.32	4.25 to 7.01	1.45 to 4.88
Upper Ultramafic Zone	39.71-50.38	11.05-35.00	0.36 to 1.92
Lower Ultramafic Zone	38.29-46.57	25.52-38.69	0.27 to 0.57
Marginal Zone	41.43-47.76	12.11-22.79	0.71-1.28
Quetico metasedimentary rocks	61.28-65.29	2.77-6.09	0.55-0.75

The Gabbro Zone is characterized by Ni/Cu values of 0.04-4.32 with an average of 0.51, a La/Sm_n value of 2.56-3.17 (Fig. 4.32), Gd/Yb_n values of 3.02-4.66 and Nb/Nb* of 0.51-0.89. The Upper Ultramafic Zone has a value of Ni/Cu from 0.64 to 33.24 with an average of 8.90, La/Sm_n of 0.37-2.17, Gd/Yb_n varies from 3.47 to 4.29 and Nb/Nb* varies from 0.44 to 0.81. The Lower Ultramafic Zone has a Ni/Cu value of 0.45-27.87 with an average of 13.3, La/Sm_n of

1.41-2.62, Gd/Yb_n of 3.03-4.25 and Nb/Nb* of 0.66-0.97. Rocks of the Marginal Zone have a Ni/Cu value of 0.21-0.43 with an average of 0.32, La/Sm_n ranges from 1.46 to 2.35, Gd/Yb_n ranges from 3.34 to 4.04 and Nb/Nb* from 0.21 to 1.18. Quetico metasedimentary rocks have Ni/Cu values of 1.13 to 9.12 with an average of 3.77, La/Sm_n 4.07 to 4.53, Gd/Yb_n 1.59 to 2.49 and Nb/Nb* ranges from 0.08 to 0.18.

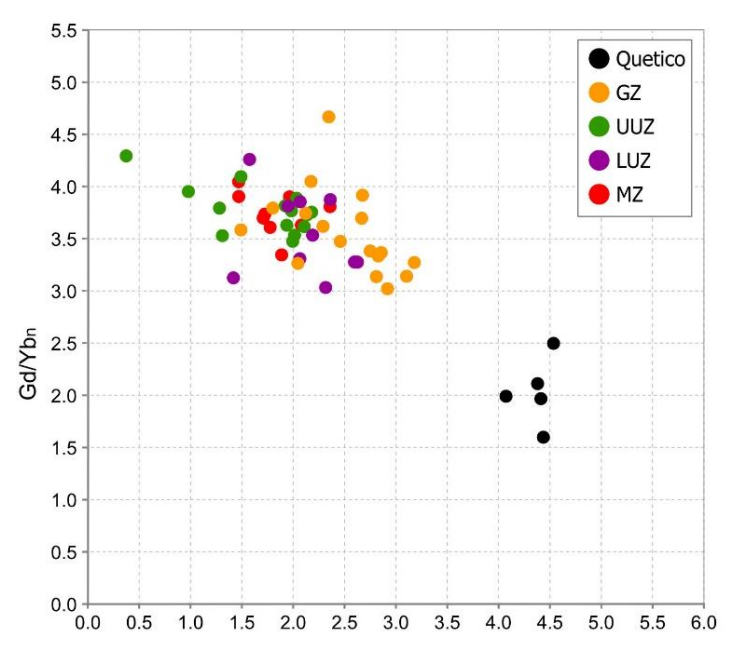
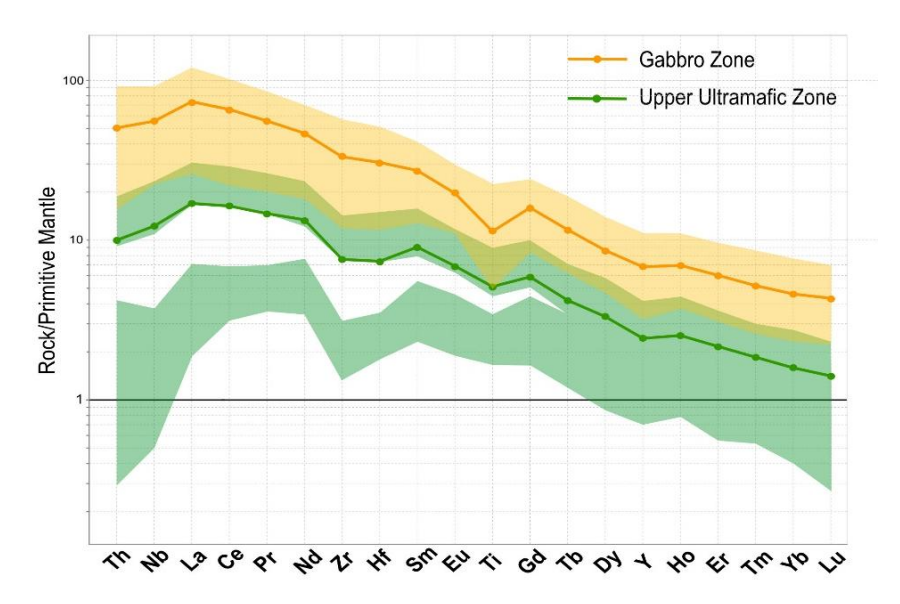


Figure 4.32. Chondrite-normalized, whole-rock trace-element variation diagram for the Sunday Lake Intrusion and country rocks. Normalizing values from Sun and McDonough (1989).



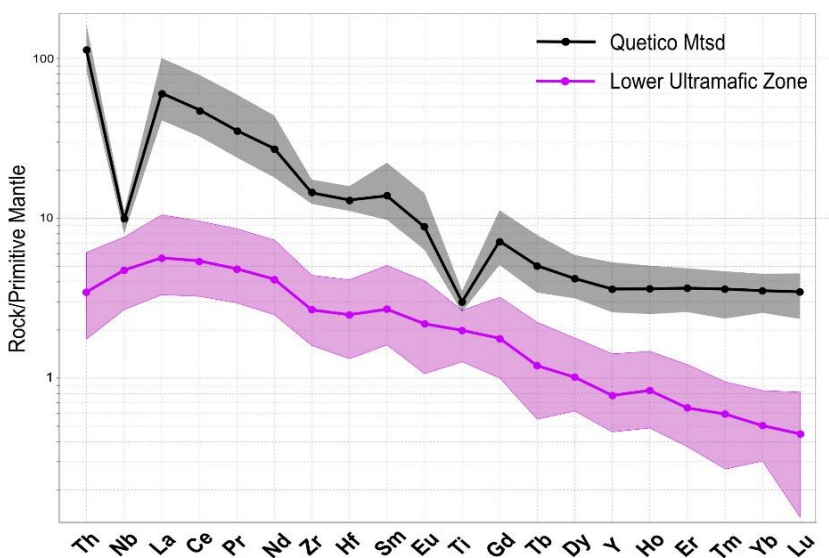
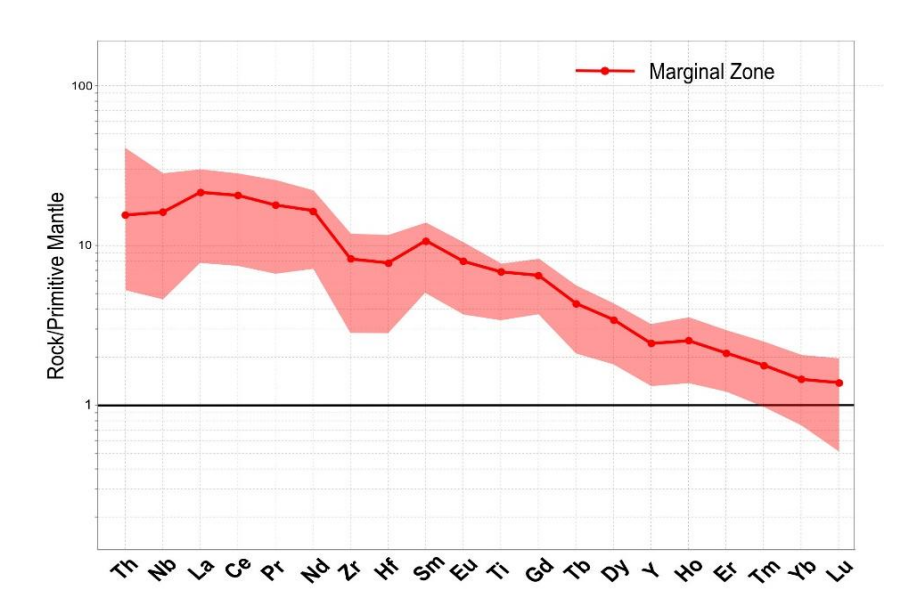


Figure 4.33. Primitive mantlenormalized spider diagram for each zone of the Sunday Lake Intrusion. Range of values are shown with a shaded polygons and solid lines represent the statistical average for each element. Normalizing values from Sun and McDonough (1989).



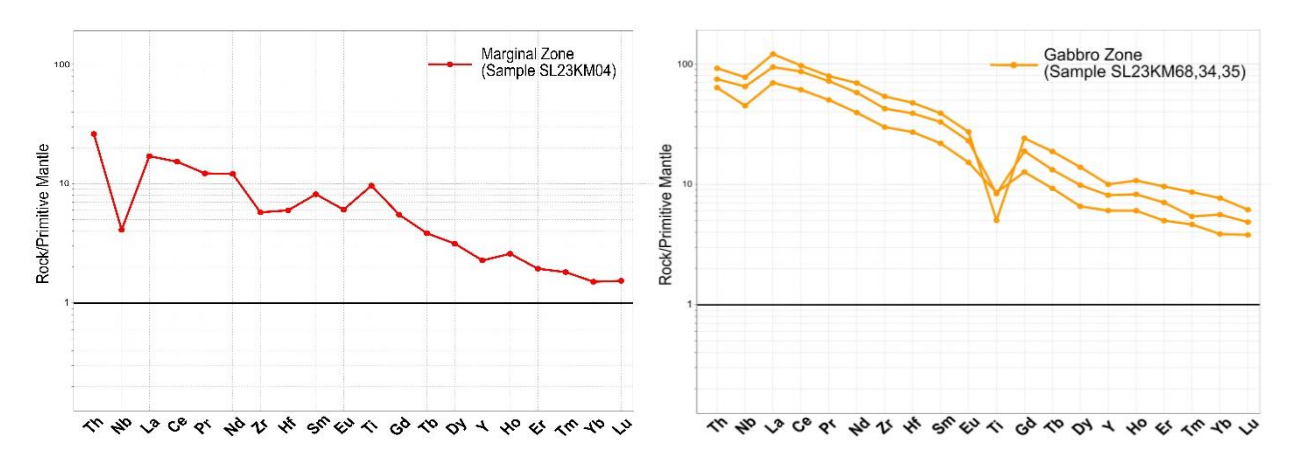


Figure 4.34. Primitive mantle normalized spider diagram for sample SL23KM04 from the Marginal Zone (Red) and samples SL23KM68,34 and 35 from the Gabbro Zone (Yellow). Normalizing values from Sun and McDonough (1989).

Primitive mantle normalized multi-element diagrams show a gently negative-sloping pattern similar to Ocean Island Basalts (OIB; Sun and McDonough, 1989). Generally, all zones of the SLI show an enrichment in light rare earth element (LREE) with slightly elevated Nb, La and Ce over Th (Figure 4.33). The only exceptions are sample SL23KM04 from the Marginal Zone and samples SL23KM68, 34 and 35, which have lower Nb values over Th (Fig. 4.34). Additionally set of samples from the UUZ show relatively depleted LREE compared to the average UUZ and GZ with notable Th and Nb depletions.

4.4 Stable isotopes

4.4.1 Sulfur isotopes

Two methods were used to analyze the sulfur isotope system. The first involved microdrilling of sulfide grains, with ten measurements taken from ten different samples obtained from pyrrhotite (and/or chalcopyrite). δ^{34} S values were obtained from the Marginal Zone of the

Sunday Lake Intrusion. The SLI sulfides have $\delta^{34}S$ ranging from -1.6 to -0.7‰ for drillhole SL-17-18B and from -1.3 to 0.3‰ for drillhole SL-19-026 with an average value of -0.97 for both drillholes (Fig. 4.35). The second method involved in-situ measurements on single sulfide phases from the MZ. Two samples were selected and a total of 30 analyses were performed on pyrrhotite and chalcopyrite. Pyrrhotite has ranging $\delta^{34}S$ values from -0.8 to 2.6 with an average of -1.8, whereas chalcopyrite has ranging $\delta^{34}S$ values from -0.3 to -1.4 with an averaging value of -0.7.

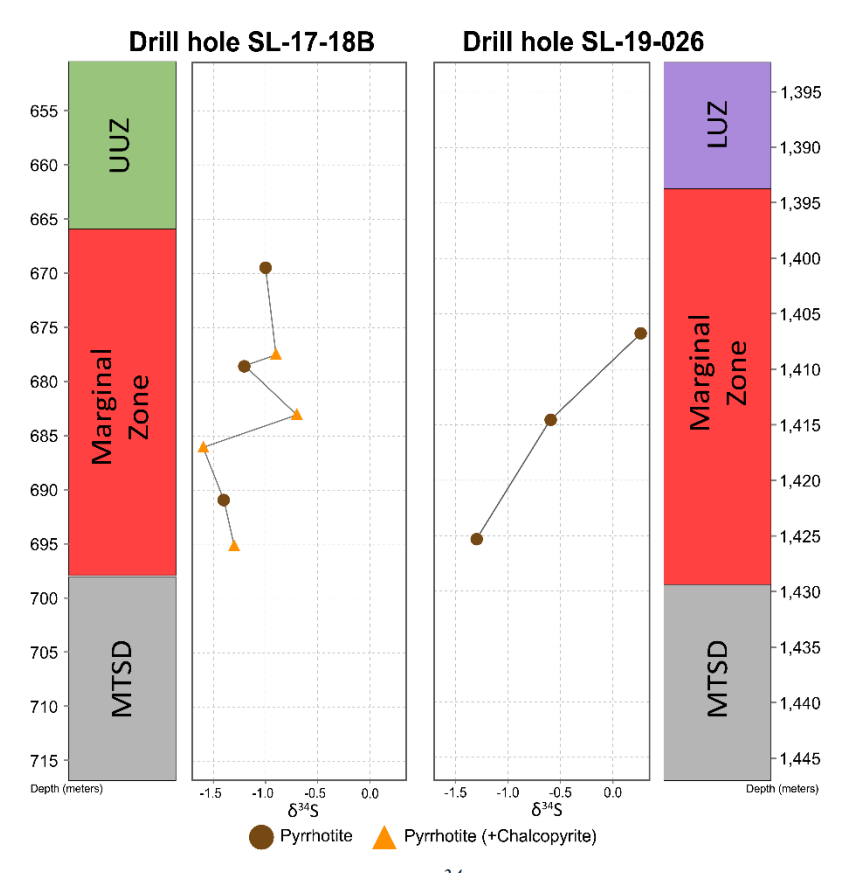


Figure 4.35. Downhole variation of $\delta^{34}S$ in drillholes SL-17-18B and SL-19-026 (sulfide microdrilling method).

4.5 Radiogenic isotopes

4.5.1 Strontium-Neodymium isotopes

Radiogenic isotopes of Sr and Nd were measured for fourteen samples throughout the different zones of the Sunday Lake Intrusion. Figure 4.36 illustrates the variation of εNd and initial ⁸⁷Sr/⁸⁶Sr ratios (Sr_i), recalculation was made at 1109.0 Ma. The SLI rock suite have values of εNd from 0.42 to -11.45, ¹⁴⁷Sm/¹⁴⁴Nd from 0.157 to 0.112, ¹⁴³Nd/¹⁴⁴Nd (initial) from 0.511227 to 0.511639, and ¹⁴³Nd/¹⁴⁴Nd (current) from 0.512373 to 0.511639 (recalculated at 1109.0 Ma). Additionally, SLI samples have values of Sr_i from 0.7025 to 0.7062 and ⁸⁷Sr/⁸⁶Sr (current) from 0.7286 to 0.7034. Two samples of radiogenic isotopes were also taken for the

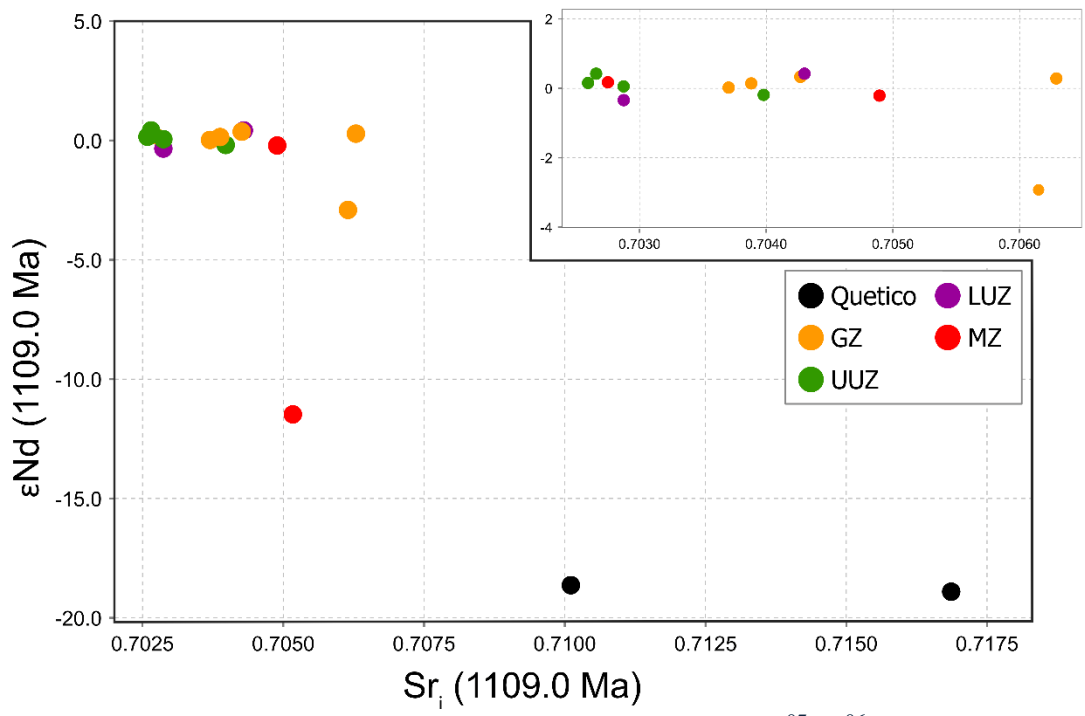


Figure 4.36. Binary diagram showing variation of εNd and initial ${}^{87}Sr/{}^{86}Sr$ (Sr_i) of the SLI suite and the Quetico metasedimentary rocks. The inset figure in the top right shows the same plot at a larger scale to better show the distribution of samples from the SLI suite samples.

Quetico metasedimentary rocks, which has values of ϵNd from -18.63 to -18.90, $^{147}Sm/^{144}Nd$ from 0.099 to 0.105, $^{143}Nd/^{144}Nd$ (initial) from 0.510239 to 0.510253 and $^{143}Nd/^{144}Nd$ (current) from 0.510964 to 0.511022. Additionally, the Quetico metasedimentary rocks have values of Sr_i from 0.7101 to 0.7168 and $^{87}Sr/^{86}Sr$ (current) from 0.7156 to 0.7342.

4.6 Mineral chemistry

4.6.1 Olivine chemistry

The compositional analyses of olivine were measured in eight samples from both drill holes SL-17-18B and SL-19-026. Multiple grains, and both core and rim were analyzed for each sample with a total of 238 spot analysis. The coarser and least altered olivine crystals were preferred for the analysis and included subhedral to euhedral grain habits occurring as

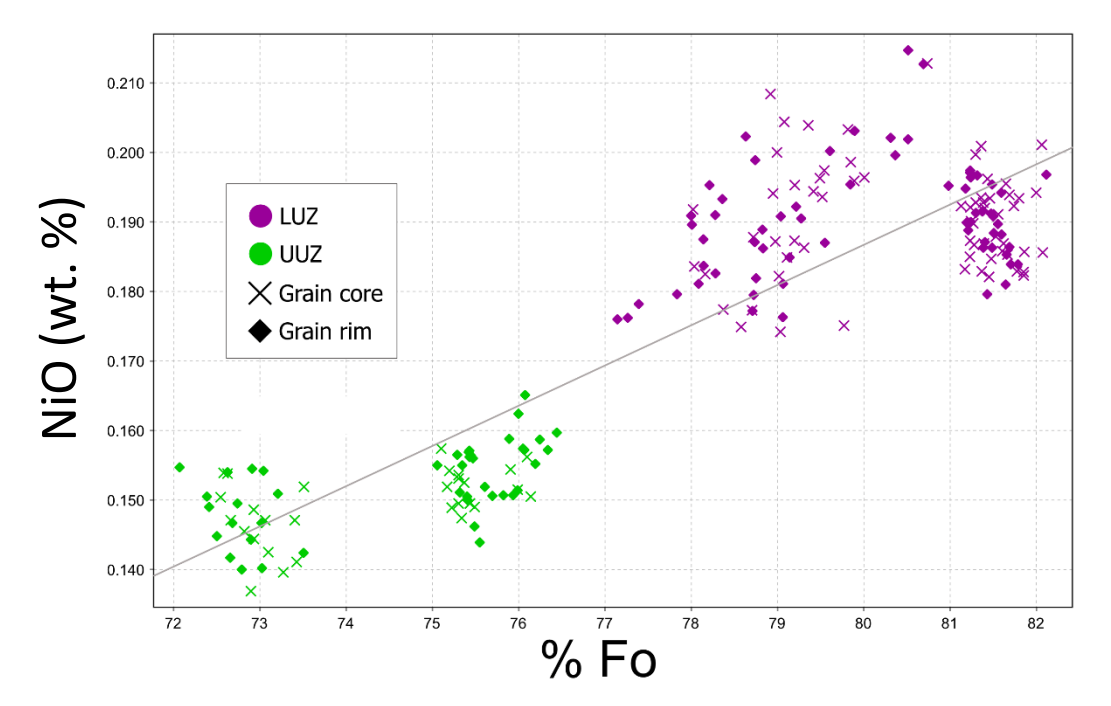


Figure 4.37. Plot of NiO (wt. %) versus % Fo olivine from the Upper and Lower Ultramafic Zone.

phenocrysts and chadacrysts. No fresh olivine was found in the Gabbro Zone and the Marginal Zone, restricting the analyses to rocks from the Upper and Lower Ultramafic Zones (LUZ and UUZ). Olivine forsterite compositions range from 72.0 to 82.1% Fo with an overall average of 74.3 % Fo for UUZ and 80.5 % Fo for the LUZ. There is little variation between core and rim measurements (typically < 0.8 % Fo). Plotting NiO versus Fo % exhibits a regression line with a R-squared value of 0.77 that shows a moderate positive relationship (Fig. 4.37).

Chapter 5: Discussion

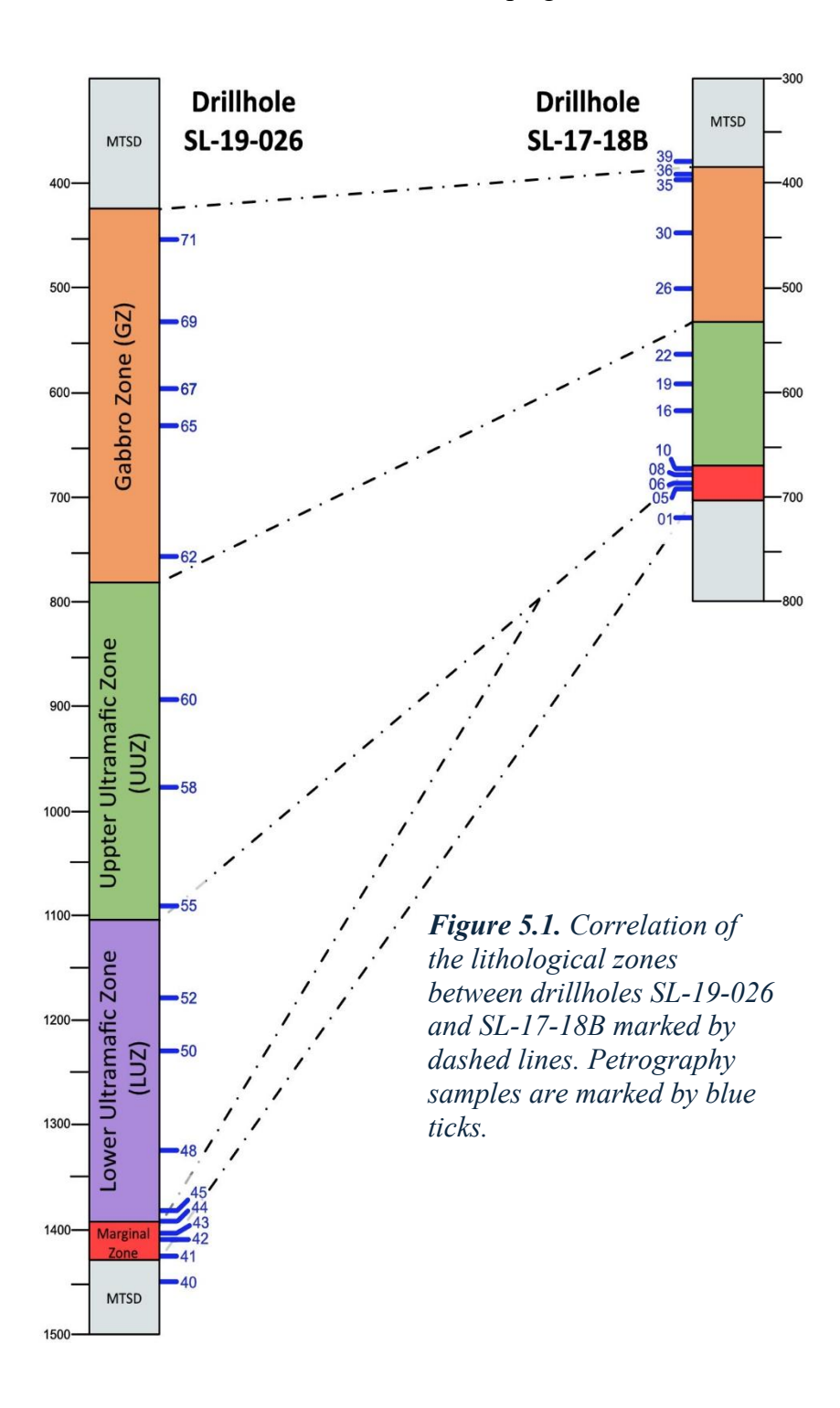
5.1 Lithostratigraphy

The Sunday Lake intrusion (SLI) is a differentiated funnel/tabular-shaped intrusion that can be subdivided into the Gabbro (GZ), Upper Ultramafic (UUZ) and Lower Ultramafic (LUZ) zones, all of which can be followed stratigraphically across the intrusion but vary in thickness. Petrological, physical and geochemical features can be used correlate between drill holes SL-17-18B and SL-19-026, which intersected ~305 m and ~1000 m of the intrusion, respectively (Fig. 5.1).

The ultramafic portion of the SLI (LUZ and UUZ) preserves olivine as phenocrysts, which suggests it was the earliest silicate mineral to segregate from the parental magma. Subsequently, as temperatures decreased, clinopyroxene oikocrysts enclosed the olivine chadacrysts. The occurrence of plagioclase in the ultramafic phase filling the remaining interstices indicates it was among the final silicate mineral to fractionate in this phase, followed by amphiboles and hornblende. The mafic phase (GZ) records the crystallization of a more differentiated magma, with fine- to medium-grained apatite, clinopyroxene and plagioclase being the first minerals to crystallize, as they occur as subhedral to euhedral phenocrysts. These minerals are followed by the interstitial crystallization of amphiboles and K-feldspar.

Aluminum values serve as a good proxy for plagioclase (Miller, 2020), aligning positively with the plagioclase cumulates in the GZ (Fig. 5.2). Similarly, high magnetic susceptibility values in the GZ are consistent with the accumulation of Fe-Ti oxides, except in

the 30 m Breccia Zone at the upper part of the GZ in drillhole SL-17-18B, where values are close to 0 kappa due to the absence of Fe-Ti oxide cumulates (Fig. 5.2). The sharp increase in pXRF Al values at the GZ-UUZ contact is consistent with the plagioclase cumulate zone in the GZ,



where it occurs as phenocrysts. In both drill holes, high Al pXRF values and plagioclase cumulates are followed by a sharp increase in magnetic susceptibility values and the appearance of Fe-Ti oxides. This transition is observed 25 meters above the GZ-UUZ contact in both drill holes (Fig. 5.2). The crystallization of plagioclase cumulates plays a key role in promoting the formation of titanomagnetite. As plagioclase crystallizes, it removes calcium and aluminium

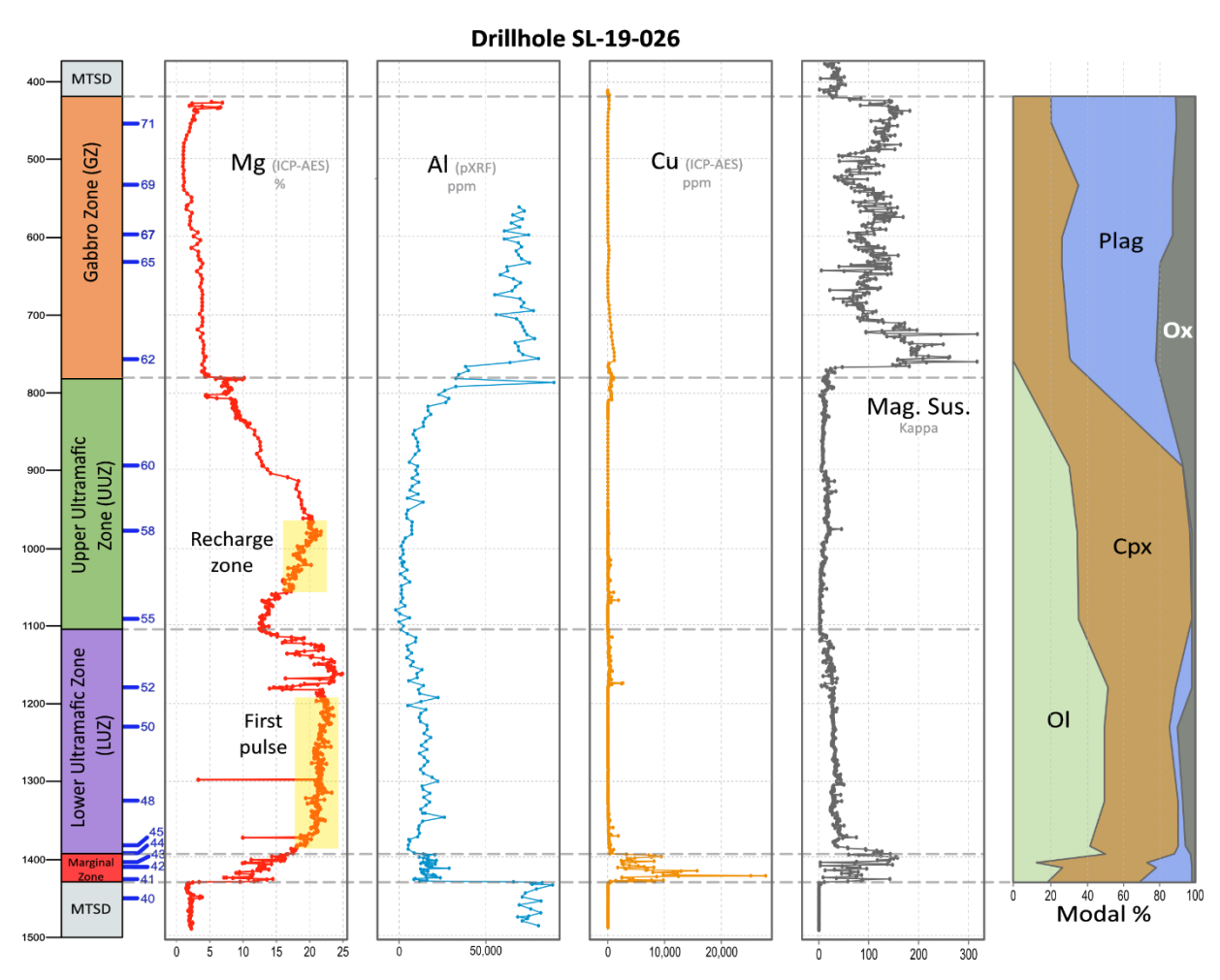


Figure 5.2A. Drillhole SL-19-026 chemostratigraphic variations in Mg wt. % and Cu (by ICP-AES), Al (by pXRF), magnetic susceptibility readings and mineralogical abundances. Whole rock Mg wt. % was calculated based on the MgO wt. % for consistency with additional data courtesy of Impala Canada Ltd.

from the liquid phase, saturating the titanium and iron content of the melt, promoting crystallization of titanomagnetite solid solution (Naldrett, 2004).

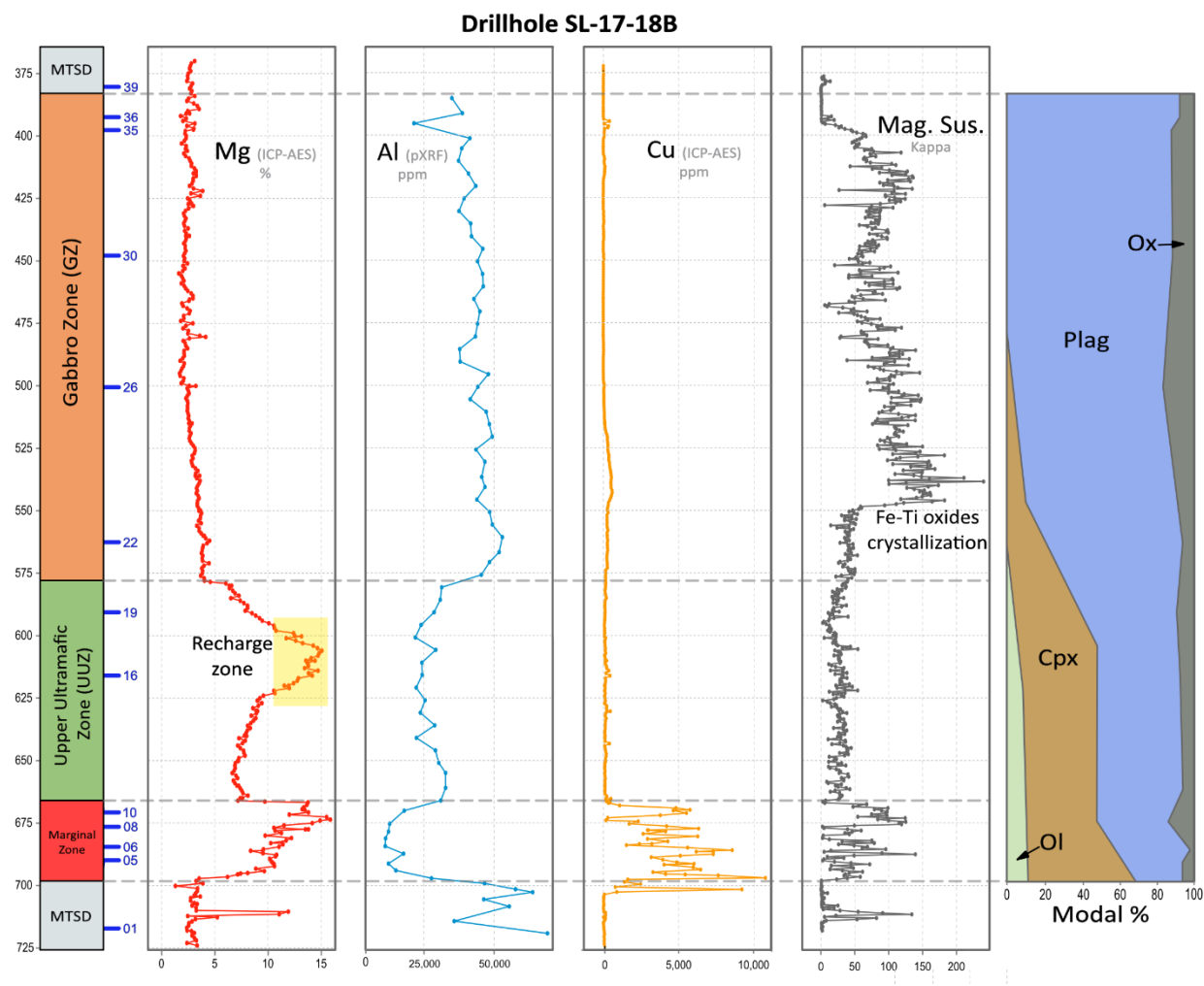


Figure 5.2B. Drillhole SL-17-18B chemostratigraphic variation in Mg wt. % and Cu (by ICP-AES), Al (by pXRF) and magnetic susceptibility readings and mineralogical abundances Whole rock Mg wt. % was calculated based on the MgO wt. % for consistency with additional data courtesy of Impala Canada Ltd.

The UUZ is characterized by cumulate Cpx>Ol, which corelates with a sharp downhole increase in Mg wt. % at the GZ-UUZ contact (Fig. 5.2). The Mg wt. % gradually increases and peaks at the center of the UUZ with 15.05 wt.% at 606 m in drillhole SL-17-18B and 21.7 wt. %

at 980 m for drillhole SL-19-026. After this peak, the Mg wt.% and Al ppm gradually decreases towards the lower contact with the LUZ. Similarly, the LUZ is characterized by relatively constant Mg wt. % values over 20 wt. % at depths from 1200 m to 1350 m. The LUZ Mg wt. % gradually decreases down to ~15 wt. % at the upper and lower contacts with the UUZ and MZ (Fig. 5.2B). These gradual changes in Mg wt. % and variations in cumulate mineral abundance are typical of magma recharge, followed by continuous fractionation. This process likely resulted from a recharge event that produced the Sunday Lake reservoir and supports previous observations of a two-pulse intrusion, as suggested by Flank (2017) and Miller (2020). The characteristic pattern of repeated element enrichment and depletion with depth has been observed in many layered intrusions and is similar to those in observed in the Seagull and Thunder intrusion, which are interpreted to be the result of cyclic units formed from single or multiple magmatic pulses (Jackson, 1961; Eales & Cawthorn, 1996; McCallum, 1996; Boudreau & McBirney, 1997; Heggie, 2005; Trevisan, 2014; Bain et al., 2024).

In drill hole SL-17-18B, there is no distinct pattern of consistently high Mg wt. % concentrations exceeding 20 wt. % below the UUZ. Instead, Mg wt. % values sharply transition to a range of 15 to 5 Mg wt. % (Fig. 5.2), similar to those values observed in drill hole SL-19-026 for the Marginal Zone and suggesting the absence of LUZ at the northern portion of the intrusion. Several maffector ultramaffic layered intrusions in the Thunder Bay area exhibit features of up section crystal fractionation and cumulate mineral layering (Heggie, 2005; Trevisan, 2014; O'Brien, 2018). These layers result from single or multiple magmatic pulses and are often associated with contact-type Ni-Cu-PGE sulfide deposits near the lower contact of the intrusions (Heggie, 2005; Zientek, 2012; Trevisan, 2014; Caglioti, 2023). Mineral layering forms as magma

becomes saturated during cooling, typically initiating the segregation and gravitational settling of early-crystallized cumulates at the base of the intrusion. The progressive removal of these dense cumulates from the melt decreases the melt density, promoting continued precipitation and accumulation of early-formed cumulates (Sparks et al., 1997). Given the concave-up shape of the SLI, it is reasonable to infer those early crystallized mafic minerals pooled in the deeper portions of the reservoir (Fig. 5.3). As a result, the residual melt became relatively depleted in early-crystallizing phases toward the shallower northern margins (Fig. 5.3). In other words, the settling cumulates effectively scavenged Mg-rich crystals from the melt, thus explaining their absence of the LUZ in the northern part of the chamber.

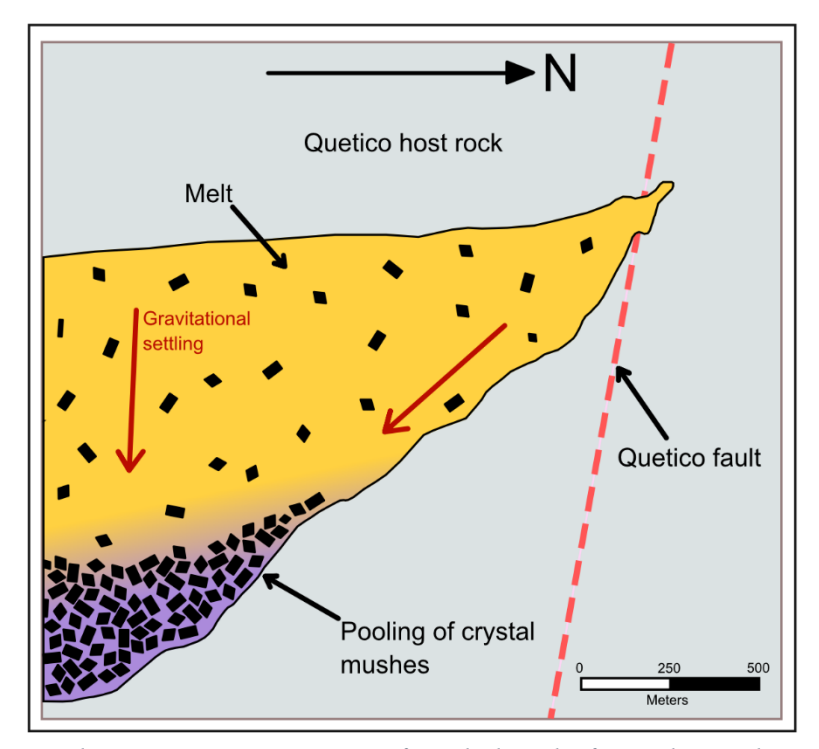


Figure 5.3. Schematic representation of pooled early-formed cumulates.

The Marginal Zone is mainly characterized by distinct Cu enrichment and an increase in magnetic susceptibility values (Fig. 5.2), which is directly linked to the presence of the weakly

magnetic pyrrhotite and chalcopyrite, typically at ~15% in abundance, and indicates the concentration of chalcophile elements (Cu, Ni, PGE) due to sulfide saturation in the cooling magma. The consistent medium- to fine-grained olivine through the MZ and LUZ, the absence of chilled margins (quenched textures) and the lower Fo content towards the MZ-LUZ contact compared to the central LUZ, suggests a relatively slow cooling at the base of the intrusion. This gradual cooling could have facilitated the re-equilibration of olivine to a more differentiated composition possibly due to the MZ interacting with the host rock (Barnes, 1986). The presence of a sulfide rich zone occurring mostly interstitially at the base of the intrusion suggests the settling of "trapped" sulfur-rich liquid contemporaneous with the crystallization of the cumulate phase (olivines) and subsequent crystallization of the segregated immiscible sulfide droplets forming the MZ. This mineral occurrence is comparable to other contact-type Ni-Cu-PGE deposits, where mineralization occurs at the basal contact of the intrusion with the host rock (Eales & Cawthorn, 1996; Miller et al., 2002; Heggie, 2005; Dare et al., 2014).

The Sunday Lake Intrusion not only displays a vertical fractionation but also shows evidence of lateral differentiation. This is supported by presence of olivine clinopyroxenite at the center and feldspathic olivine clinopyroxenite in the northern UUZ (Fig. 4.14). Additionally, this lateral fractionation is supported by an accumulation in the middle of the chamber due to the funnel-shaped geometry, leading to less trapped liquid and more latent heat release during crystallization. A similar pattern is observed in the GZ, where leucogabbros and gabbro contrasts with quartz monzonite and quartz gabbros found in the central and northern portions, respectively. Additionally, mineral grainsizes generally increase from fine- to medium-grained at the boundaries, to coarse-grained minerals towards the center, suggesting that the center of the

intrusion remained relatively isolated for a longer period of time compared to the outermost portions of the intrusion, allowing the development of coarser textures. Geochemical trends further reinforce this lateral differentiation in the UUZ, where a contrast between the maximum of ~20 wt.% magnesium at the center vs ~15 wt.% magnesium at the border of the intrusion also supports lateral fractionation. These patterns suggest that the progressive cooling accumulated high-Mg silicates at center of the intrusion compared to the boundaries, progressively cooling the intrusion from thinner sections toward thicker regions to the south, influencing the behaviour of the incompatible elements. These findings are consistent with the observations of Flank (2017), who first suggested a lateral fractionation in the Sunday Lake Intrusion, based on the olivine/pyroxene cumulate peridotites occurring within the center of the SLI, compared to the more felsic olivine melagabbro within the Lower Gabbroic Series (in this study: Upper Ultramafic Zone).

5.2 Sulfides and Fe-Ti oxides paragenesis

The complex textural relationships of the Sunday Lake Intrusion record magmatic processes related to the primary magmatic fractionation and mineral deposit formation. Using petrographic observations and integrating geochemical data, a paragenesis of the Sunday Lake Intrusion was developed. This is divided into three main phases: Silicate, sulfide and Fe-Ti oxide (Fig. 5.4). The silicate phases show downhole fractionation across all zones, recording key processes to interpret downhole lithostratigraphy, as discussed in the previous section. The sulfide phase comprises the early-segregated sulfide melt associated with the metal enrichment in

the MZ, whereas the Fe-Ti oxide phase mostly reflects late-stage magmatic crystallization of magnetite-ilmenite cumulates in the GZ.

Mineral	Primary phase	Mineralization phase
Silicate phase		
Olivine		
Clinopyroxene		
Plagioclase		
Apatite		
Oxide phase		
Chromite	?——	
Titano-magnetite		•
Ilmenite		
PGM-Sulfide phase		
Pyrrhotite		
Pentlandite		?———
Chalcopyrite		
Sphalerite		?——?
Platinum-group		?———
Troilite		
Cubanite		

Figure 5.4. Simplified paragenetic sequence of crystallization for the Sunday Lake Intrusion.

5.2.1 Sulfide phase

The Sunday Lake Intrusion displays interstitial and blebby textures of sulfide minerals with a distinct geometric distribution. Pyrrhotite usually predominates in the core of sulfide grains, chalcopyrite frequently forms a surrounding rim and pentlandite is occasionally found as an interface between these two, although it is sometimes found isolated in chalcopyrite (Fig. 4.26). This spatial arrangement suggests that pyrrhotite was an early-formed phase, with

chalcopyrite crystallizing afterwards. Additional textures found in the MZ, such as chain-like and flame exsolution pentlandite, and cubanite lamellae within chalcopyrite, are consistent with exsolution textures that occur at lower temperatures (Naldrett, 2004). In the MZ, the presence of tellurides, arsenides, Ni- and Pt-rich PGMs, and native metals both as rounded and elongated inclusions in all sulfide minerals or interstitial along sulfide fractures, suggests that the sulfide melt exsolved these phases during the final stages of crystallization possibly due to saturation of chalcophile elements in the residual melt. As the system cooled, sulfur fugacity increased and solubility limits of metals such as Pt, Pd and Ni were exceeded, nucleation of discrete telluride, arsenides and native-metals phases started to form within sulfides (Li & Ripley, 2005).

Moreover, the occurrence of sulfides interstitial to the high-temperature silicate minerals of the MZ implies that the sulfide melt segregated early at high temperatures but crystallization postdates the silicate phase in this zone.

In the Marginal Zone of the SLI, the observed sulfide assemblage and its textural relationships aligns with the crystallization history of an MSS-ISS system. In this model, originally described by Naldrett (2004), an immiscible sulfide liquid coexists with magma at high temperatures. Initially, as the magma cools from 1180 to 900°C, a monosulfide solid solution (MSS) forms, accommodating metals such as Fe, Ni, Cu, and PGE. With continued cooling, these elements further segregate into an intermediate sulfide solution (ISS; Naldrett, 2004; Holwell & McDonald, 2010; Chen et al., 2015; Mansur et al., 2021). In the MZ samples, the occurrence of pyrrhotite, pentlandite and chalcopyrite supports this two-stage crystallization sequence.

At high temperatures, MSS crystallization would generate pyrrhotite and pentlandite, depleting Fe and Ni and enriching Cu in the residual melt (Mungall, 2002). In the MZ, pentlandite occurs both occasionally on the interface between pyrrhotite and chalcopyrite, and as exsolutions in pyrrhotite, implying two crystallization stages. The pentlandite at the interphase suggests it was formed by a high-temperature peritectic reaction between MMS and ISS (Mansur et al., 2019), bridging the compositional gap between the Fe-Ni-rich pyrrhotite and the Cu-rich chalcopyrite. In contrast and upon further cooling to 650-350°C, chain- and flame-like pentlandite exsolutions, found within pyrrhotite at the MZ, record a secondary low-temperature stage of pentlandite growth (Mansur et al., 2021). At the same time, chalcopyrite likely crystallized from the Cu-rich ISS, whereas PGM-bearing minerals exsolved from both MSS and ISS. Subhedral elongated michenerite and rounded, elongated malsovite (comprising Bi-, Teand Pt-rich PGMs) occurring mostly in pyrrhotite and pentlandite at the MZ, suggest they crystallized from the MSS. Whereas grain-interstitial sperrylite, tabular rustenburgite and rounded braggite (As-, Sn- and Ni-rich PGM and TABS) in chalcopyrite reflect ISS-derived exsolutions (Mansur et al., 2021). Additionally, native Pt, Pd and Ag are found in both pyrrhotite and chalcopyrite. Finally, within the MZ sulfide assemblages, the occurrence of cubanite lamellae and discrete sphalerite in chalcopyrite, together with troilite lamellae in pyrrhotite, aligns with the latest stages of sulfide fractionation, where at around >210°C, cubanite and sphalerite exsolve from chalcopyrite and troilite exsolves from pyrrhotite (Mansur et al., 2021). The presence of exsolution mineral such as cubanite and troilite from chalcopyrite and pyrrhotite, along with the absence of pyrite, may indicate crystallization from a high metal/S sulfide melt, similar to the sulfide systems from Voisey's Bay (Naldrett, 1999)

5.2.2 Fe-Ti Oxides

Iron-titanium oxides are a good tool for recording processes such as oxygen fugacity, crystallization sequences and changes in temperature (Lindsley, 2018). In the ultramafic portion of the SLI (LUZ and UUZ), Cr-spinel is the dominant high-temperature oxide, occurring as inclusions in olivine and clinopyroxene. The high Cr/Fe ratios in olivine and the presence of Cr-spinel suggest a chromium-enriched magma, providing evidence for a Cr-saturated system during the earliest stages of the intrusion (Roeder & Emslie, 1970). In addition, Fe-Ti oxides in the LUZ commonly display interstitial textures, filling the spaces between cumulous olivine and clinopyroxene, which suggests that titanomagnetite crystallized late and that ilmenite exsolution subsequently occurred as the system cooled.

In the upper mafic zone of the SLI (GZ), Fe-Ti oxides gradually increase in abundance and transition from an intercumulate texture in the LUZ to a cumulate texture in the GZ (Fig. 5.2). In the GZ, the presence of primary skeletal titanomagnetite and ilmenite, along with magnetite exhibiting ilmenite exsolution crystallizing with plagioclase suggests higher oxygen fugacity than in the LUZ (Fig. 4.6; Lofgren, 1974). Furthermore, the occurrence of subhedral skeletal magnetite-ilmenite crystals and oxide blebs in the GZ, suggests a temperature ranging from 400 to 500°C, which aligns with the breakdown of an ulvöspinel-magnetite solid solution upon cooling (Lindsley, 2018). This is because, at temperatures within this range, ulvöspinel becomes unstable within the magnetite structure and begins to exsolve as discrete ilmenite lamellae or blebs. The unmixing of this solid solution is mainly driven by decreasing temperature, which

reduces solubility of Ti in magnetite, producing exsolution features (Bowles, 1977; Lindsley, 2018).

5.3 Tectonic setting and source

The Sunday Lake Intrusion dated at 1.1 Ga, is interpreted to be part of the MRS, as its age, composition, and location are typical of magmatism associated with the early stages of the MRS. The SLI is mainly characterized by negative-sloping REE patterns with small positive Nb, La and Ce anomalies over Th. This characteristic is shared by a number of intrusions in the Midcontinent Rift System and interpreted to be the result of primitive magmas derived from an ascending mantle plume (Hofmann, 1997; Hollings et al., 2007b, 2010). Most samples of the SLI show enriched LREE and HREE signatures compared to MORB and are similar to other MRS-

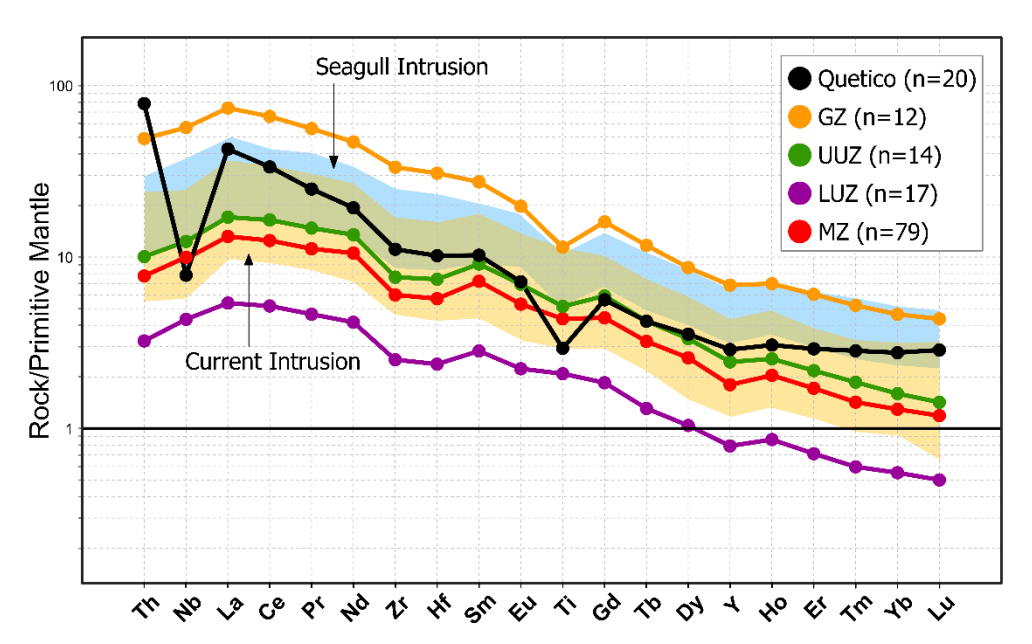


Figure 5.5. Spider diagram showing the statistical average for each zone of the SLI and the Quetico metasedimentary rocks. Sample fields for the Seagull and Current intrusions are shown in blue and yellow, respectively. Current and Seagull intrusion values were taken from Heggie (2005) and Corredor (2024). Normalizing values from Sun and McDonough (1989).

associated Ni-Cu-PGE mafic-ultramafic intrusions, such as the mafic-ultramafic rocks of the Seagull and Current intrusion (Fig. 5.5; Heggie, 2005; Corredor, 2024). Despite the broadly similar negative-sloping REE patterns, geochemical variations exist within the SLI. The Gabbro Zone exhibits a trace element pattern similar to the Lower Ultramafic Zone, but it has a notably higher overall trace element abundance (Fig. 5.5). This difference is attributed to the crystal fractionation of the parental melt during the formation of the Gabbro Zone. As the melt cooled, early-crystalizing minerals, such as olivine and pyroxene, incorporated compatible elements, thereby depleting them from the melt. Consequently, incompatible elements, including REEs, remained in the residual melt, leading to their gradual enrichment and enhancing the overall REE content as observed in the GZ.

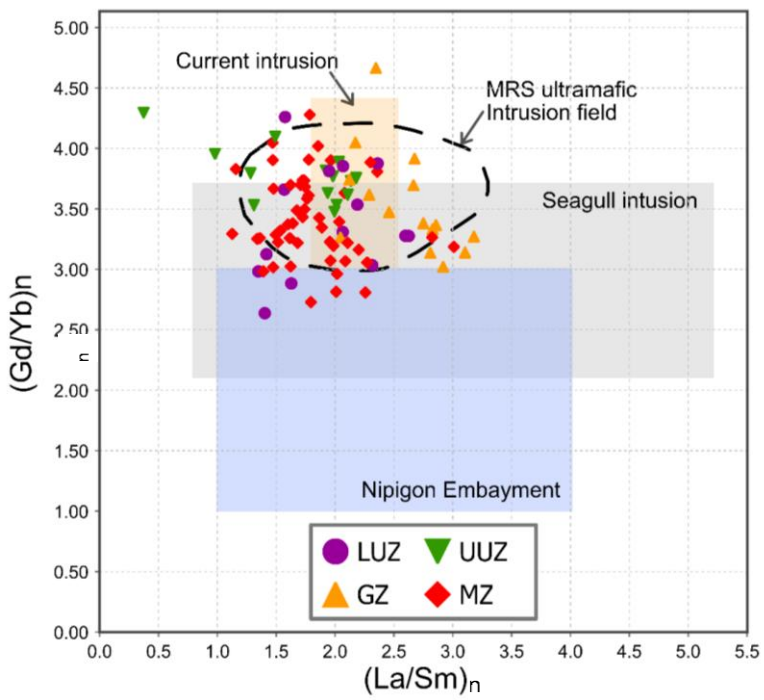


Figure 5.6. Chondrite-normalized, whole-rock REE ratio for Sunday Lake Intrusion. MRS ultramafic intrusion field by Hollings et al. (2007b). Nipigon Embayment, Seagull, Current intrusions values were taken from Heggie (2005), Hollings et al. (2007b), and Corredor (2024).

To further investigate the REE distribution, the Gd/Yb_n and La/Sm_n ratios were used to investigate indicators of HREE-LREE enrichment and partial melting processes, fractional crystallization and mantle differentiation (Fig. 5.6: Rollinson, 1993; Hollings, 2007a). The La/Sm_n values of the Sunday Lake Intrusion samples range from 1.0 to 3.2, similar to typical ratio of 2 to 3 observed in ocean-island basalts (OIB; Hart et al, 2006; Heaman et al. 2007). These are similar to the other MRS-related ultramafic intrusions, including the Seagull (0.78 to 5.21), Current (1.7 to 2.6) and Nipigon Embayment intrusions (1 to 4; Fig. 5.6; Heggie, 2005; Hollings et al., 2007b; Caglioti, 2023; Corredor, 2024). Similarly, the Gd/Yb_n values, which characterize the slope of the HREE, suggest contrasting mantle sources between the studied intrusions. The SLI shows values ranging from 2.6 to 4.3, suggesting a deep mantle source within the garnet stability field. The SLI Gd/Yb_n ratios are consistent with those observed in other MRS intrusions such as the Seagull (2.1 to 3.7) and Current (3.0 to 4.4) intrusions (Heggie, 2005; Corredor, 2024), reinforcing the interpretation that these magmas formed as a result of plume-related magmatism at greater depths.

5.4 Contamination

The possible contamination of the Sunday Lake Intrusion by assimilation of Quetico country rocks may be assessed through analyzing their LREE patterns and behaviour. Given that the LREE are relatively incompatible and are preferentially incorporated in the liquid phase, partial melt generated from Quetico country rocks will be enriched in LREE and therefore, reflected in the assimilating magma. The main marker of contamination in trace elements in the MRS intrusions is the enriched LREE with pronounced negative Nb anomaly (Hollings et al., 2007b;

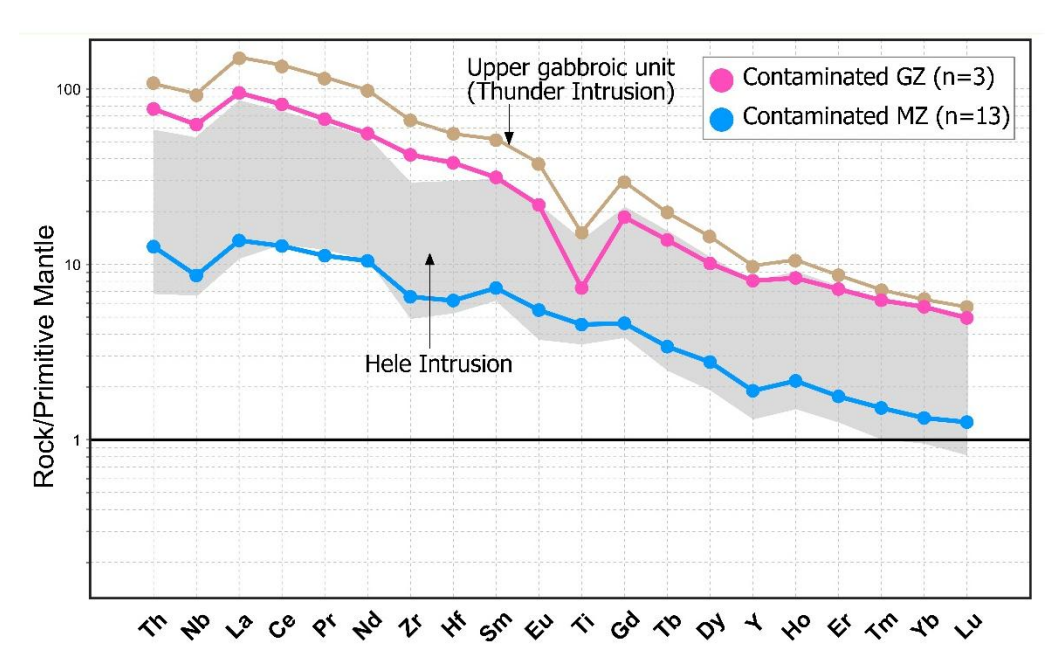
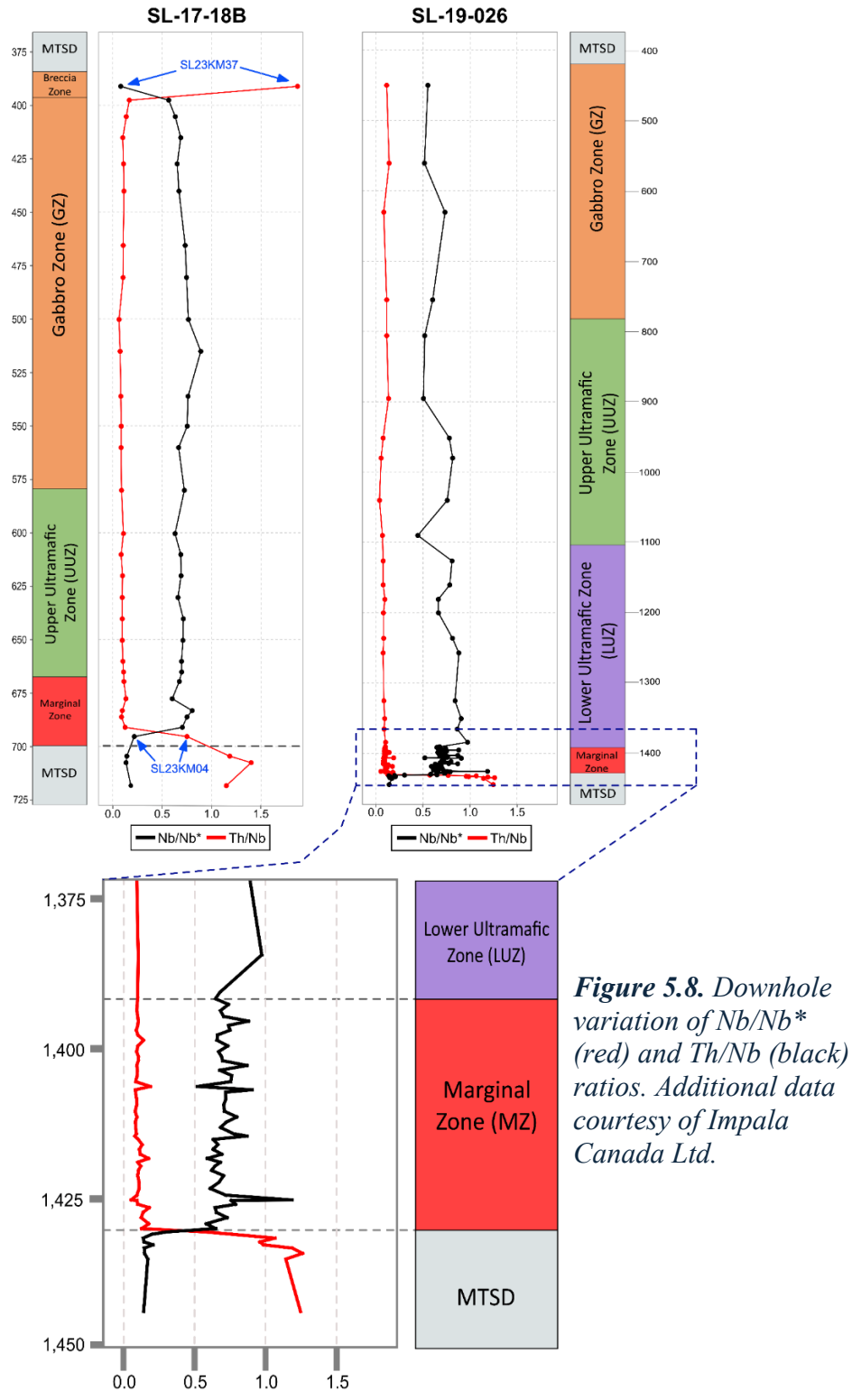


Figure 5.7. Spider diagram showing the statistical average for contaminated samples of the GZ and the MZ. Thunder Intrusion data from Trevisan (2014) and Hele Intrusion from Hollings et al. (2007a). Normalizing values from Sun and McDonough (1989).

see Quetico metasedimentary rocks in Fig. 5.5). Partial melting of Archean Quetico metasedimentary rocks are the main potential source that can cause relatively enriched Th with Nb negative anomalies, as well as moderate abundances of large-ion lithophile elements (LILE) and LREE (Hollings et al., 2007a). The majority of samples from the SLI zones show positive Nb values compared to Th, indicating they have not assimilated significant amounts of the Quetico host rock. However, a small group of samples from the Gabbro Zone (n=3) and the MZ (n=13) display a small negative Nb anomaly relative to Th, La and Ce values, which suggests small degrees of assimilation of the Quetico host rock (Fig. 5.7). The slightly depleted Nb values over Th, La and Ce are comparable to the Upper gabbroic unit of the Thunder Intrusion and the range of values of the Hele Intrusion, both of which are interpreted to have been contaminated by older crustal material (Fig. 5.6; Trevisan, 2014; Hollings et al., 2007a).

To better evaluate the extent of crustal contamination, Nb/Nb* ratios can be used to quantify the Nb negative anomaly, as Archean metasedimentary rocks are typically depleted in high field



strength elements like Nb, producing a distinctive negative Nb signature when assimilated (Cundari, 2012). Th/Nb behaves inversely, increasing where Nb is depleted (Fig. 5.8). Downhole Nb/Nb* and Th/Nb in both drill holes remain relatively consistent, with only two exceptions. The first is observed the Breccia Zone in sample SL23KM37, at the uppermost part of drill hole SL-17-18B, where Nb/Nb* drops to 0.08 and Th/Nb increases to 1.87 due to the presence of up to 80% Quetico fragments, supporting mixing of the GZ with country rock and producing a negative Nb anomaly (Fig. 5.7). The second exception is in the Marginal Zone (sample SL23KM04), where Nb/Nb* decreases to 0.21, similar to that of the Quetico host rock (~0.2; Fig. 5.7), suggesting significant crustal assimilation in this sample. Although these specific samples record contamination, the generally consistent Nb/Nb* and Th/Nb values downhole

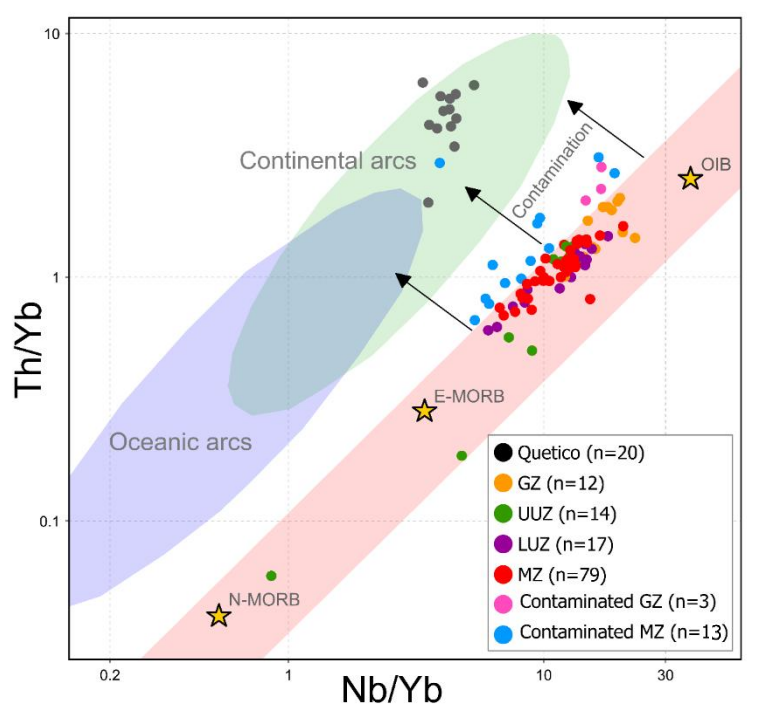


Figure 5.9. Ta/Yb vs Th/Yb distribution diagram (Pearce, 2014) for the zones of the Sunday Lake Intrusion, including the contaminated MZ and GZ in blue and pink, respectively. Additional data courtesy of Impala Canada Ltd. N-MORB, E-MORB and OIB values are from Sun & McDonough (1989). Tectonic discrimination fields are from Pearce (2008).

suggests one of two possibilities: either crustal assimilation was generally limited throughout the intrusion, or small amounts of contamination do not significantly affect Nb/Nb* ratios. The interpretation of limited assimilation throughout the intrusion is further supported by the fact that, of the 138 samples of the SLI (including samples courtesy of Impala Canada Ltd.), only 16 "Contaminated GZ and MZ" samples identified in Figure 5.6 show negative Nb anomalies. Additionally, the absence of orthopyroxene also suggests limited assimilation of silica-rich material, which is typically promotes orthopyroxene stability in mafic magmas, supporting a weak interaction with the crust (Irvine, 1975; Ripley & Li, 2011)

On a Th/Yb versus Ta/Yb diagram (Fig. 5.9), most of the SLI samples fall within the mantle array, between an OIB and E-MORB signature. In contrast, the 16 contaminated GZ and MZ (in pink and blue on Fig. 5.9) samples show pronounced negative Nb anomalies (relative to Th) and also show slight lower Th/Yb ratios (Fig 5.8). Rather than plotting in the mantle field, these anomalous samples plot between the mantle array and the continental arc array. This drift toward the arc field provides further evidence that assimilation of country rocks modified their mantle-derived geochemical signature.

5.4.1 Radiogenic isotopes

The ε Nd (1109.0 Ma) values of most samples of the Sunday Lake Intrusion range from +0.42 to -0.33, clustering near the chondritic value (ε Nd \approx 0; Fig. 5.10). This near-zero values suggest a mantle source similar to primitive mantle values at 1100 Ma (Nicholson & Shirey, 1990). At 1.1 Ga, a depleted mantle source would exhibit ε Nd values around +5.8 (Shirey & Hanson, 1986;

Puchtel et al., 2018), whereas an enriched subcontinental lithospheric mantle (SCLM) would have εNd of -4.27 (Steiner, 2014) and a depleted SCLM εNd of +4 (Rooney et al., 2022). The near-zero εNd values of the SLI are most consistent with a primitive mantle, plume-derived or OIB-like melt, whose end-member εNd values are typically close to zero and have been attributed to the Keweenaw plume (Sun & McDonough, 1989; Shirey et al., 1994; Rooney et al., 2022). Compared to the rest of intrusions in the Thunder Bay area, similar chondritic εNd values have been reported in other Midcontinent Rift magmas such as the Thunder Intrusion and Logan sills (Nicholson & Shirey, 1990; Shirey et al., 1994; Hollings et al., 2012; Trevisan, 2014; Rooney et al., 2022; Brzozowski et al., 2023).

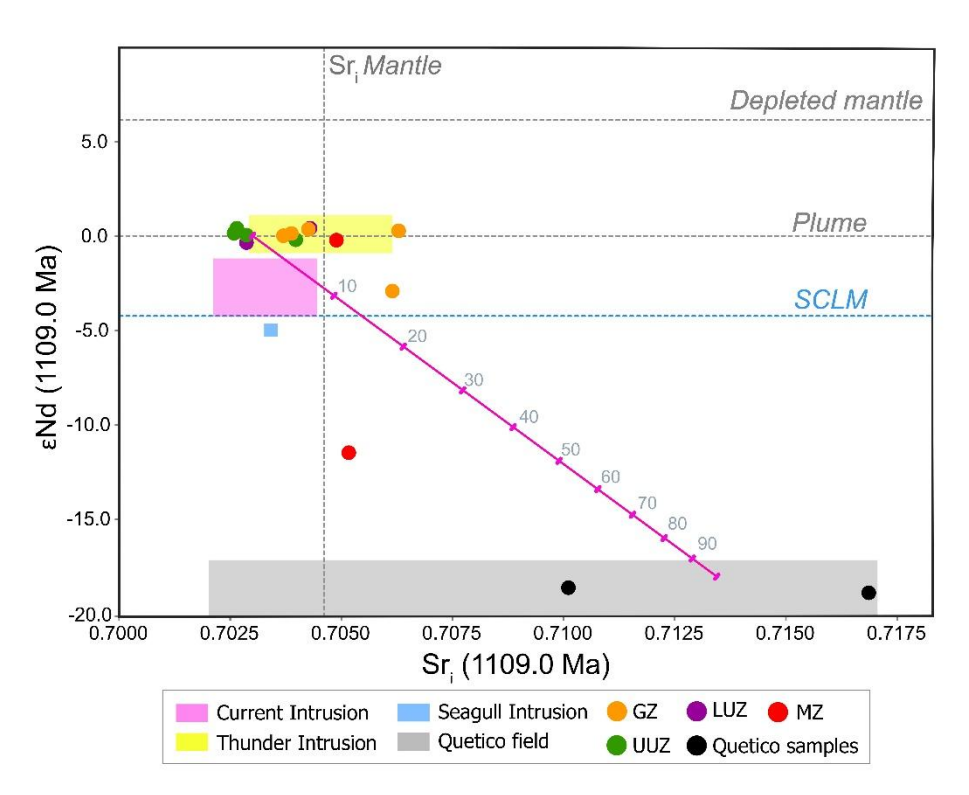


Figure 5.10. Binary diagram ε Nd versus Sr_i for each zone of the Sunday Lake Intrusion. Mantle and Quetico country rocks values were taken from Hergt et al. (1989) and Caro & Bourdon (2010). Current, Thunder and Seagull intrusions data were taken from Heggie (2005) and Trevisan (2014). Ultramafic zones of the SLI and Quetico country rocks (pink line) represents hybrid melt end-members.

The ${}^{87}\text{Sr}/{}^{86}\text{Sr}$ ratios of the SLI samples (Sr_i= 0.7025-0.7062) align with the typical values of the mantle source at 1100 Ma, which has a composition of 0.703 to 0.705 (Hergt et al., 1989; Nicholson & Shirey, 1990). However, one sample from the GZ that plot above 0.705 may suggest interaction with an enriched SCLM (Fig. 5.10; Caro & Bourdon, 2010). Notably, two samples (SL23KM09 and SL23KM68) plot within the chondrite ε Nd field while exhibiting negative Nb anomalies (Fig. 5.10). This pattern of negative Nb but chondritic εNd is consistent with ancient subduction-related metasomatism of the SCLM (Shirey et al., 1994). Subduction can introduce slab-derived material into the overlying mantle wedge, which triggers changes in the SCLM composition (Shirey et al., 1994). This slab-derived material can be enriched in large ion lithophile elements (LILE) but poor in high field strength elements (HFSE) such as Nb, Ta and Ti. Although this suggests some SCLM influence, the εNd values of these samples remain unmodified and plot within typical plume-like values. This likely reflects the similar geochemical behaviour of Sm and Nd, which are both rare earth elements and thus less affected by subduction-related fluids compared to the HFSE (Steiner, 2014). As a result, the Sm/Nd ratio (and consequently the εNd value) of the metasomatized SCLM can remain relatively unchanged and plot within the mantle range, explaining the chondritic-like ENd values despite Nb depletion. It is possible that only these two samples preserve the subtle SCLM signal because they crystallized from the very first melt pulse, which underwent interaction with the SCLM. A subsequent, purely primitive melt recharge event possibly flushed the chamber with fresh plumederived magma through magma outflow from the chamber. Resulting on the SLI having a more dominant primitive signature with minor SCLM contribution.

Brzozowski et al. (2023) demonstrated that plume-derived magmas of the MRS underwent variable degrees of interaction with the SCLM by comparing trace element patterns and isotopic compositions. They emphasised negative Nb-Ta anomalies and LILE enrichments as indicators of SCLM involvement, supported by Re-Os and εNd-Sr isotopic mixing models. In the Seagull and Current intrusions, where SCLM interaction was more significant, the magmas display slightly negative εNd signature (-1.18 to -4.0; Heggie, 2005; Corredor, 2024). In contrast, the SLI and Thunder intrusions may record more limited SCLM interaction. Trevisan (2014) reported that although the εNd values (~0.51) in the Thunder intrusion are close to zero and indicate a dominant plume-like signature, additionally, interpretations of subtle SCLM interaction were still proposed based on the presence of Nb depletions, major and trace element patterns. This highlights that even near chondritic εNd values do not exclude minor SCLM contributions (Trevisan, 2014).

Two Sunday Lake Intrusion samples with more negative εNd values (at -2.91 and -11.45) and more positive Sr_i values (~0.7060) suggest localized contamination by the Quetico metasedimentary rocks (Fig. 5.10). The country rocks are characterized by εNd values averaging -18.76 and Sr_i values ranging from 0.701 to 0.717 (Henry et al., 1998). The combined negative εNd values and Nb negative anomalies for these samples from the GZ and MZ support localized but significant assimilation of Quetico metasedimentary rocks, likely involving less than 30% Quetico-derived melt (Fig. 5.10).

5.5 Sulfur isotopes and trace elements

5.5.1 Microdrilling vs in-situ Laser Ablation

Hand-microdrilling sulfides (Po \pm Ccp) isolates discrete grains for $\delta^{34}S$ analysis, but the small sample size is limited by the method's robustness. Despite careful targeting of pyrrhotite, the 1 mm drill tip that was used can incorporate minor chalcopyrite, pentlandite and sphalerite, as these phases coexist as fine-grained inclusions or exsolution intergrowths within MZ sulfide grains. These microscale heterogeneities can influence $\delta^{34}S$ values, causing variability in measurements and potentially masking localized isotopic variations. In contrast, in situ laser ablation sulfur isotope analysis provides high spatial resolution, allowing analyses of individual

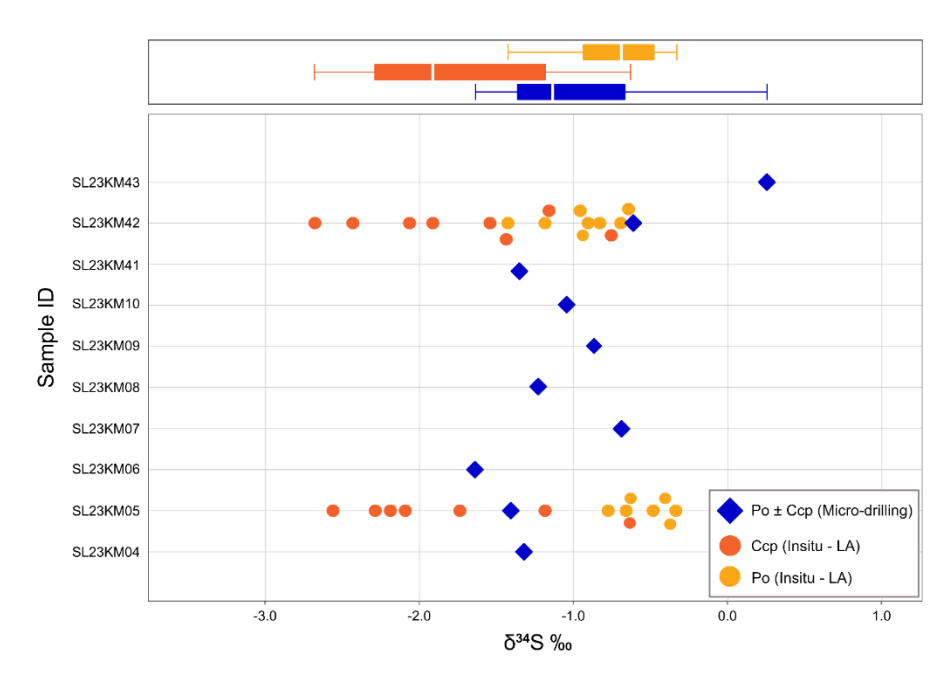


Figure 5.11. Plot of $\delta^{34}S$ for 10 samples from the Marginal Zone. In-situ (LA-ICPMS) samples are shown in orange and yellow dots showing the $\delta^{34}S$ value for pyrrhotite and chalcopyrite, respectively. Blue diamonds show the micro drilled pyrrhotite (±chalcopyrite) $\delta^{34}S$ values. Box-and-whisker plots of $\delta^{34}S$ values are overlaid on the diagrams to illustrate data distributions.

mineral grains and phases. This results in more precise $\delta^{34}S$ values independent of mineral mixing effects.

Microdrilled samples show an average δ^{34} S value of -1.0%, whereas in situ analyses record -1.8% for pyrrhotite and -0.7% for chalcopyrite (Fig. 5.11). The average micro drilled value suggests that this technique may have integrated sulfides from both mineral phases, reflecting micro-scale heterogeneity within the sulfide assemblage. However, micro drilled pyrrhotite SL23KM43 and SL23KM42 samples exhibit the most positive δ^{34} S values of the dataset, at 0.3% and -0.6%, respectively. These values may represent the contribution of additional PGM's or sulfur-bearing phases with higher δ^{34} S values compared to the range of values for chalcopyrite and pyrrhotite. One possible explanation is the incorporation of micro-scale sphalerite within chalcopyrite. This low-temperature zinc sulfide is occasionally found as inclusions in chalcopyrite at the MZ and can be exsolved during the late stages of sulfide crystallization (Rickard & Luther, 2007). Sphalerite tends to incorporate more ³⁴S due to equilibrium fractionation at lower temperatures, typically resulting in the highest δ^{34} S values among sulfides and contrasting with chalcopyrite, which usually has the lowest δ^{34} S values (Seal, 2006). Given the variability in the δ^{34} S values among sulfide phases in the SLI, obtaining a homogenous sample from fine- to medium-grained sulfides is challenging as microscale sulfide heterogeneities can significantly influence bulk δ^{34} S measurements. While micro drilling provides a useful broad-scale value, for more precise characterization of sulfur isotopic variability, in situ laser ablation analysis is recommended.

5.5.2 Sulfur enrichment

Ni-Cu-PGE deposits in the MRS are commonly attributed to an upwelling mantle plume.

These high-degree mantle melts ascend rapidly and may assimilate crustal rocks, potentially triggering sulfur saturation (Hutchinson et al., 1990; Mungall, 2002, 2014; Naldrett, 2004; Begg

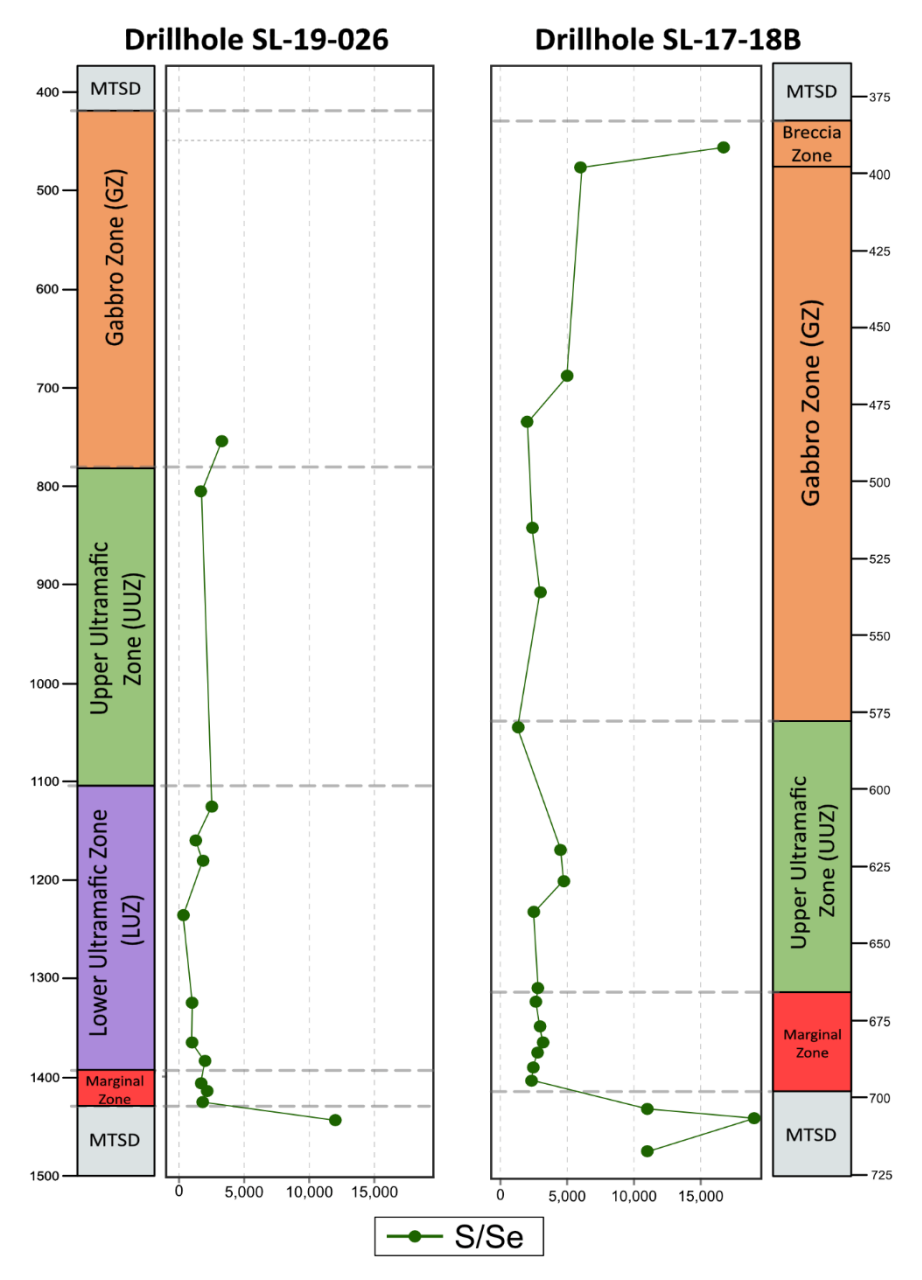


Figure 5.13. Downhole whole-rock S/Se ratios variation for drillholes SL-19-026 (left) and SL-17-18B (right).

et al., 2010). Sulfur saturation, considered a key factor in ore formation, is often initiated by a assimilation of S- and silica- rich rocks, which increases sulfur content and reduces the melts ability to dissolve sulfur in melt (Ripley & Li, 2003; Naldrett, 2004). Understanding the extent of these processes in the Sunday Lake Intrusion requires integration of trace element and isotopic data.

The relative abundance of S-isotopes is based on mass differences in each isotope system, the general process that creates this dependency is determined as mass-dependent-fractionation (MDF; Farquhar & Wing, 2003). However, sediments from the Archean (Quetico metasedimentary rocks) record values of mass-independent fractionation (MIF), as bacterial

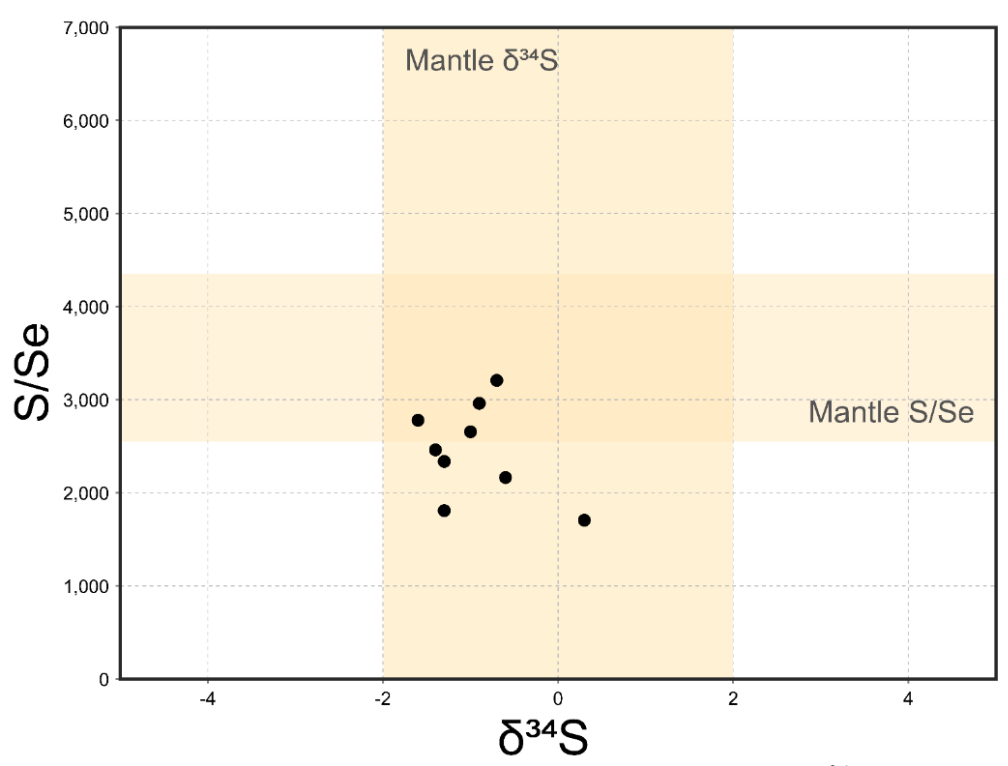


Figure 5.12. Bivariate diagram of whole rock S/Se versus sulfide δ^{34} S showing sample from the Marginal Zone. Mantle δ^{34} S values were taken Ripley & Li (2003). Mantle S/Se values were taken from Eckstrand & Hulbert (1987) and Palme & O'Neill (2014).

sulfate needed to recycle and overprint these signals with a MDF signature, was not active at the time (Halevy et al., 2010). Therefore, if the SLI records a S-rich source that records a MIF signal, the intrusion could have assimilated large quantities of host rock. In the SLI, sulfide δ^{34} S values (Fig. 5.12; -1.6 to 0.3) fall within mantle range (0 ± 2‰) established by Ripley & Li (2003). On the other hand, sulfides of the Quetico metasedimentary host rocks in the Thunder Bay area, have δ^{34} S values ranging from -2.0 to 3.8‰ (Heggie, 2005; Trevisan, 2014; O'Brien, 2018; Caglioti, 2023). Therefore, as both the SLI and the Quetico metasedimentary rocks produce δ^{34} S values that resemble that of the mantle values range, the detection of crustal sulfur addition becomes impossible.

Sulfur/Se ratios are also helpful in tracking the addition of externally derived sulfur (Figs. 5.12 and 5.13). The S/Se mantle ratios have been estimated to the range from 2632 to 4350 (Eckstrand & Hulbert, 1987; Palme & O'Neill, 2014). Therefore, the S/Se ratios higher than mantle values are interpreted to reflect the addition of sulfur to the magma, by contrast, lower values are interpreted to reflect loss of sulfur (Maier et al., 2010). The SLI samples have S/Se ratios of 1700 to 3200 partially falling within the mantle array, suggesting that δ³⁴S values are likely due a mantle origin rather than from assimilation of host rock (Fig. 5.12). However, the S/Se ratios plotting under the limit of the mantle field may reflect hydrothermal loss of sulfur, supported by low S/Se for given PGE tenors (Queffurus & Barnes, 2015), or alternatively degassing or early saturation and precipitation of sulfides. This occurs as sulfur could partition into a gas phase (SO₂ or H₂S) and liberate from the system through magma outflow, scavenging S from the intrusion and decreasing the S/Se ratio (Wallace & Edmonds, 2011; Wang & Becker, 2013). Alternatively, S could be scavenged by early sulfur saturation, leading to the formation of

immiscible sulfide liquid, partitioning sulfur into that sulfide and removing it from the silicate melt and increasing Se, resulting in decreased S/Se ratios (Li & Ripley, 2009).

In both cases the residual melt may show low S/Se ratios not necessarily due to Se addition, but rather due to S depletion in the system. The contrasting downhole S/Se ratios of the SLI only show interaction with the Quetico metasedimentary rocks at the breccia zone, where ratios (>10 000) are explained by the occurrence of Quetico fragments in the breccia zone (Fig. 5.13). Other than that, the S/Se ratios and δ^{34} S values of the SLI do not show evidence for significant sulfur addition. Taken together, δ^{34} S and S/Se values suggest a dominantly mantle-derived sulfur signature, however, this interpretation contrasts with radiogenic isotope data (ϵ Nd and Sr_i signatures), which show evidence for crustal contamination. Two scenarios could explain these contrasting observations in the SLI.

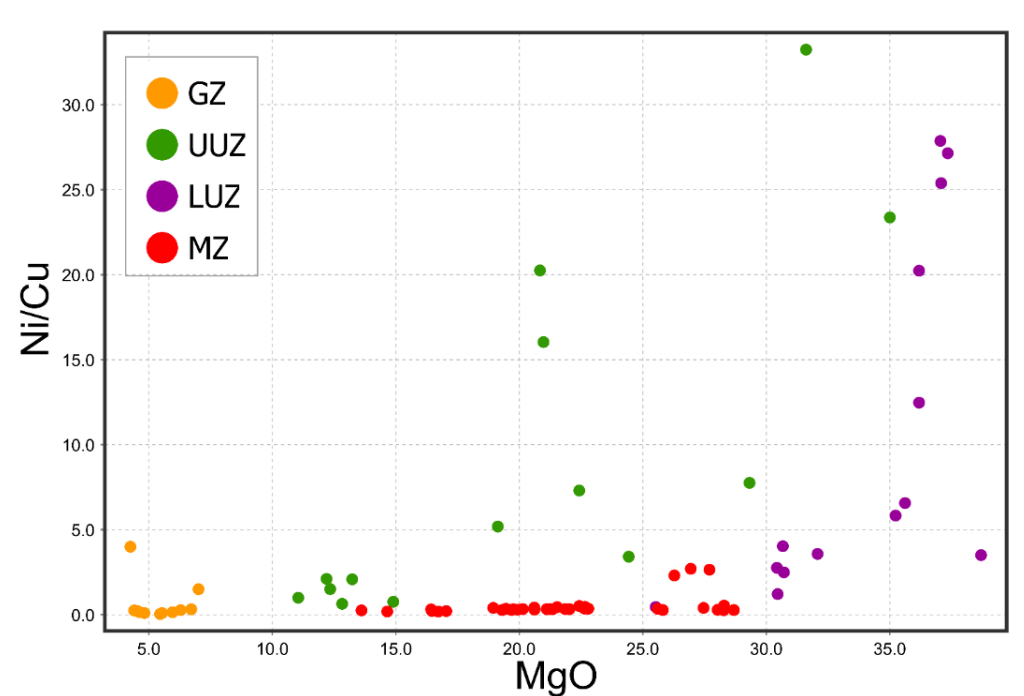


Figure 5.14. Bivariate diagram of whole rock Ni/Cu versus MgO wt. %.

In scenario 1, the sulfide saturation occurred early in a relatively closed magmatic system, prior to significant contamination. In this case, sulfur saturation was controlled by the magma source itself, and it is important to assess if the magma held enough sulfur to achieve sulfide precipitation. Evidence for this model includes visible sulfide blebs up to ~1.0 % in the LUZ (the most primitive zone of the SLI), suggesting that early sulfur saturation could have occurred. The saturation of mantle-derived sulfur is supported by δ^{34} S values plotting within the mantle averages and S/Se ratios within the lower-mantle array. Ni/Cu ratios have been used to define the behaviour of chalcophile elements to investigate the sulfur saturation processes in a mafic system (Naldrett, 2004; Li & Ripley, 2009; Barnes et al., 2016). In the SLI, elevated whole-rock Ni/Cu ratios occur in the most primitive samples (LUZ and some samples from UUZ; Fig. 5.14), implying that the Ni + Cu concentration exceeded the sulfide-saturation threshold defined by sulfur-solubility models for mafic magmas (Mavrogenes & O'Neill, 1999). Under these conditions, sulfide droplets could have started exsolving early before significant olivine crystallization, scavenging Ni and Cu from the melt. As olivine continued to crystallize, it preferentially removed Mg and Fe, leaving the sulfide liquid enriched in Ni. This two-stage process depleted Ni throughout the LUZ and UUZ and produced a high metal tenor, where Nirich sulfides settled at the base of the intrusion (MZ; Fig. 5.14). Electron-microprobe analyses of olivine from the UUZ and LUZ plot in a relatively narrow NiO range (~0.14 to 0.21 wt.%; Fig. 4.37), consistent with the fact that olivine grew in a sulfide-saturated melt where Ni addition was constrained at the saturation point (Fleet & MacRae, 1988). Additionally, in this scenario, radiogenic isotope data resulted in contamination primarily in the GZ and MZ. However, this

contamination was limited and occurred late in the magmatic history, having minimal impact on the sulfur system and having no significant role in the sulfur saturation process.

In the second scenario, early assimilation of sulfur from Quetico metasedimentary rocks triggered the melt to sulfide saturation, either by increasing sulfur concentration above the immiscibility threshold or by lowering sulfur solubility through added silica. The upwardconcave shaped chamber, combined with gravitational settling, accumulated the exsolved sulfide melt intro topographic irregularities along the floor and walls, which served as natural traps that could have formed by country-rock breakdown. Subsequently, the isotopic evidence for mantlederived sulfur (δ^{34} S values) could have been overprinted by the subsequent recharge event involving fresh, mantle-like magma. This recharge event likely introduced a significant volume of uncontaminated melt that interacted with preexisting sulfide phases, leading to re-equilibration of sulfides, as supported by a purely OIB-like trace element signature in the UUZ. The interaction between crustal-derived sulfur and more primitive magma may have reset sulfur isotope signatures toward mantle values. At the same time, this process could have increased the Se content of sulfides (lowering the S/Se value), diluting the contamination signature as suggested by sulfur ratios and stable sulfur isotopes (Queffurus & Barnes, 2015). This would explain why the isotopic system and S/Se ratios does not reflect strong evidence for contamination, despite the potential interaction with the Quetico host rock. Importantly, radiogenic isotopes (εNd and Sr_i values) retained both their crustal and mantle signature even after the recharge event, as this radiogenic isotopic system is less mobile and more resistant to re-equilibration (Dickin, 2018). This scenario, suggests a more complex, open-system magmatic

evolution involving stages of contamination, sulfide saturation and later recharge, with the latter masking early sulfur contamination.

Although the first scenario can explain some features of the SLI, the second model provides a more complex scenario to account for the high tenor mineralization of the SLI. About ~10% of the samples show Nb negative anomalies relative to Th, and two radiogenic isotopes analyzes show deviations from mantle-derived signatures, evidence of limited crustal contamination at the GZ and MZ. However, it is plausible that country-rock assimilation was more significant during the initial emplacement. The subsequent mafic recharge pulse could have flushed or "upflowed" a stronger contamination signature, replacing it with a more primitive melt while preserving the early-formed sulfide melt. The second scenario is considered the most plausible and comprehensive model for explaining the formation and distribution of sulfide mineralization at the SLI. This second interpretation is characterized by an early stage of wall-rock interaction, followed by sulfide saturation, possible recharge-driven flushing, and subsequent sulfur isotope resetting, thereby providing the most robust framework for understanding the genesis of sulfides and associated metal enrichment in the system.

5.6 Olivine chemistry and parental magma composition

The forsterite content of olivine and the Mg# from a mineral phase or the parental liquid, is commonly used to assess the degree of differentiation and estimate the composition of the parental melt (Roeder & Emslie, 1970; Irvine & Baragar, 1971). Olivine Fo compositions for the central LUZ and the UUZ reveal an evolutionary trend, decreasing from a range of ~81-82 % in

the wehrlite and olivine clinopyroxenite (at the LUZ) to ~75-76.5% in the feldspathic olivine clinopyroxenite (at the UUZ: Fig. 5.15). This decrease in Fo % may be the result of differentiation within the SLI or by a slight fractionation of a deeper magma feeder and a subsequent recharge event into the SLI, which introduced more evolved melt, iron-enriched olivines with lower Fo content (Fig. 5.15).

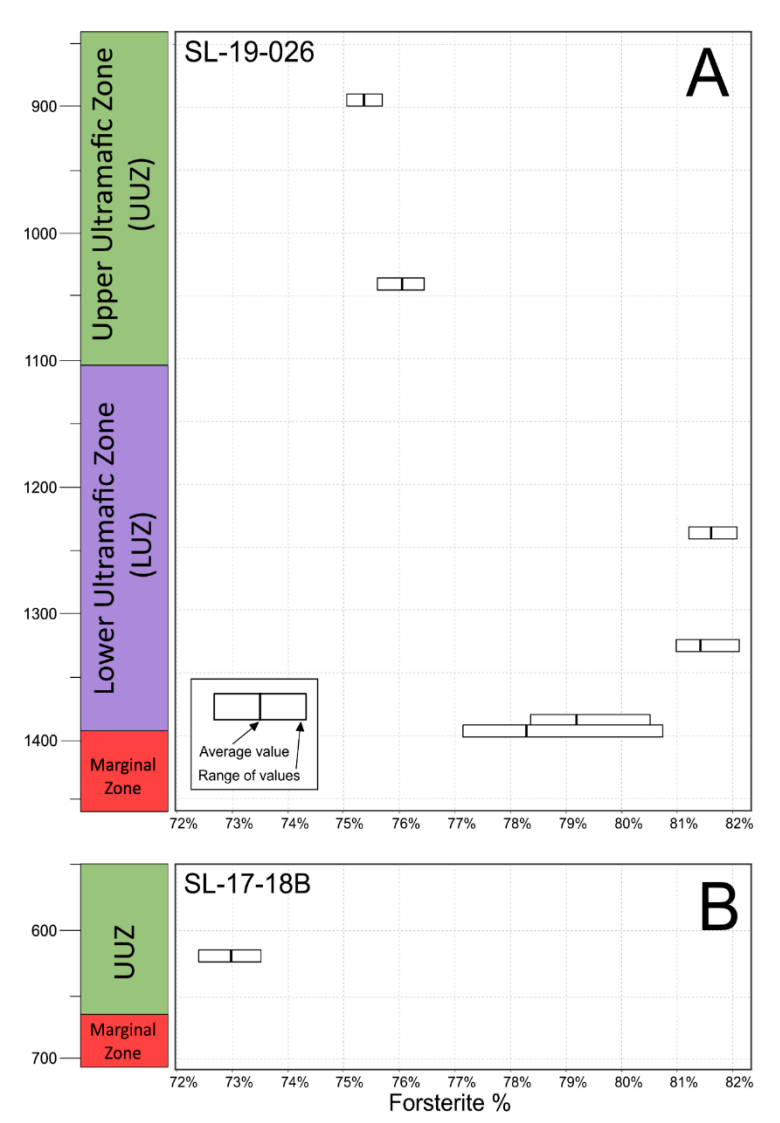


Figure 5.15. Downhole range of values and average Fo % for drill hole SL-19-026 (A) and drill hole SL-17-18B (B).

The slightly lower and wider range of Fo % values towards the LUZ-MZ contact (~77 to 81) compared to the central LUZ (~81 to 82) may reflect a different process than fractionation (Fig. 5.14). This decrease towards the LUZ-MZ contact suggests poor olivine re-equilibration and incomplete assimilation at the basal portions of the intrusion. The magma may have been contaminated by the host rock during transport and/or emplacement, lowering the Mg/Fe ratio and reducing olivine Fo values at the LUZ-MZ contact. This evidence for limited assimilation of crustal material is supported by trace elements and radiogenic isotopic data of the Marginal Zone, where only some samples have negative Nb anomalies relative to Th (Fig. 5.6). Additionally, thermal low-grade metamorphism (TLM) may have altered primary mineral compositions, further contributing to the observed Fo % (Smith, 2024). This process of olivine grain re-equilibration has been proposed to be a common feature in slow-cooling systems, where changes in the geochemistry of the melt can directly influence olivine composition (Barnes, 1986; Goldner, 2011). This low Fo % composition at the basal contact of the intrusion is similar to that observed in the Seagull intrusion, which decreases from an overall Fo 83 % in the ultramafic layers to values ranging from Fo 78 to Fo 81 % at the mineralized contact. In the Seagull Intrusion, contamination of magma by wall rock, lowered the Mg/Fe ratio of the magma, resulting in crystallization of more Fe-rich olivine with a lower Fo composition (Heggie, 2005).

The parental magma composition can be indirectly calculated by estimating the melt composition from which olivine equilibrated. The olivine-liquid partitioning method of Chai and Naldrett (1991) was reproduced for the Sunday Lake Intrusion, the parent magma composition can be calculated using the equilibrium partitioning of Mg and Fe between olivine. In the SLI, this equilibrium partitioning is defined by the slope 0.57, based on the calculated liquid Mg# for

which Fo 82 olivine is in equilibrium. The MgO / (MgO + FeO) = 0.57 reflects the olivine-liquid equilibrium under typical upper mantle conditions and is shown in Figure 5.15 as a red line. A second blue linear regression was fitted using the ultramafic whole-rock compositions for the LUZ and UUZ (Fig. 5.16). The intercept of these two regression lines representing the ultramafic rocks of the SLI with the regression line with a value of 0.57, can be used to estimate the MgO and FeO contents of the parental magma. The intercept of both lines is indicated by a black circle in Figure 5.16 and yields a parental magma composition of approximately 11.15 wt.% FeO and 19.5 wt. % MgO. From these abundances, molar Mg+Fe of the parental magma was calculated to estimate the Mg# of the parental magma liquid, which is estimated to be about 75 using the

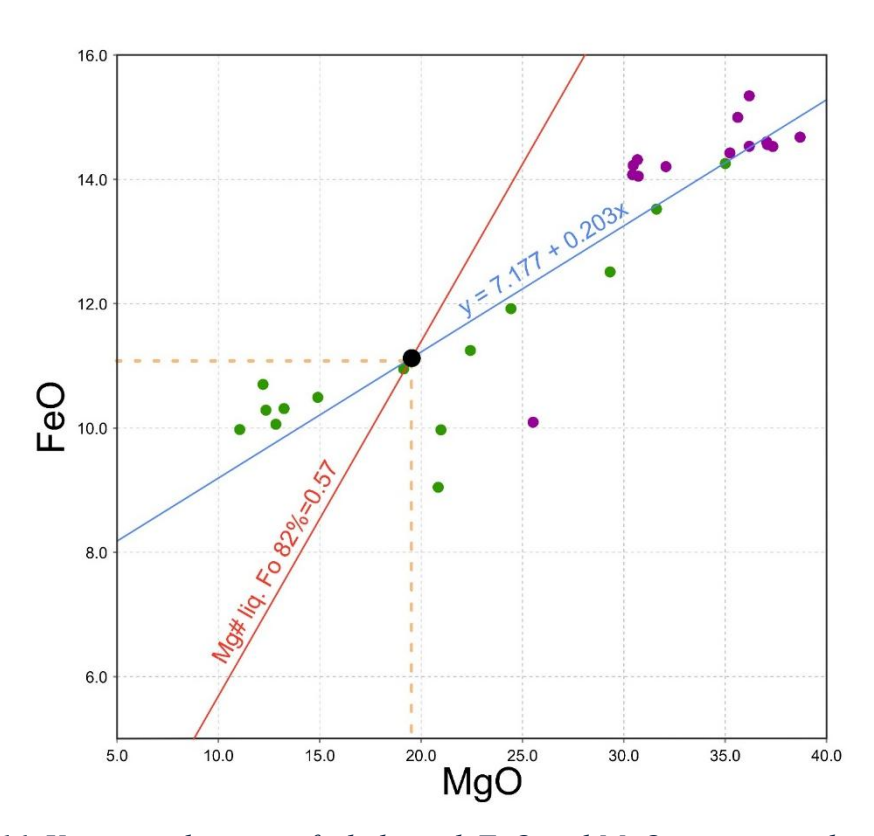


Figure 5.16. Variation diagram of whole-rock FeO and MgO to estimate the composition of the Sunday Lake Intrusion parental magma. The primary magma has an MgO 19.5 wt. % content and 11.15 wt. % FeO.

equation Mg# = (Mg / (Mg + Fe)) *100. The calculated 19.5 wt. % MgO indicates that the parental magma was a high-MgO basalt, according to Chai & Naldrett (1991). It is acknowledged that the MgO content (19.5 wt. %) inferred for olivine with 82 mol. % Fo may be overestimated, possible due to alteration or Thermal Low-Grade Metamorphism effects as observed in other settings such as in Mount Ayliff (Smith, 2024).

A calculated olivine Fo of 82 for the Sunday Lake Intrusion is higher than Fo ~75 reported for the Crystal Lake Intrusion (O'Brien, 2018), and the calculated Mg# of 75 for the SLI exceeds the Mg #57 inferred for the Thunder intrusion (Trevisan, 2014). Both the Crystal Lake and Thunder intrusions are interpreted to have undergone significant fractionation prior to emplacement from an Early-MRS phase (Trevisan, 2014; O'Brien, 2018). In contrast, the SLI parental magma's Mg# of 75 broadly matches values for Midcontinent Rift System lavas (Mg# 60 to 72), and is comparable to the calculated value for the Tamarack Intrusion (Mg# 70-74) as well as the upper range of MRS-related basalt lavas, such as the Mamainse Point Formation lavas and the Osler Volcanic Group (Mg# 60-72; Goldner, 2011). This suggests that the SLI rocks were high-MgO tholeiites, comparable to other early primitive MRS basalts (Goldner, 2011).

5.7 Petrogenetic model of the Sunday Lake Intrusion

The Sunday Lake Intrusion crystallization history can be divided into four main stages according to a synthesis of petrographic observations, whole-rock major and trace-element geochemistry, mineral chemistry and radiogenic isotope systematics: (A) initial plume melt

ascent, limited mantle/SCLM/crust interaction and sulfur saturation, (B) paused melt feeder, progressive crystallization and sulfide accumulation, (C) melt recharge and conduit outflow, subsequent crystallization and silicates accumulation, and (D) final magma chamber fractionation.

5.7.1 Stage A

The SLI was formed from high-Mg basaltic melt derived from a mantle plume with a mixed composition between depleted mantle and the subcontinental lithospheric mantle (SCLM). This interpretation is supported by radiogenic isotopes (ϵ Nd ranging from 0.42 to -0.33; Sr_i from

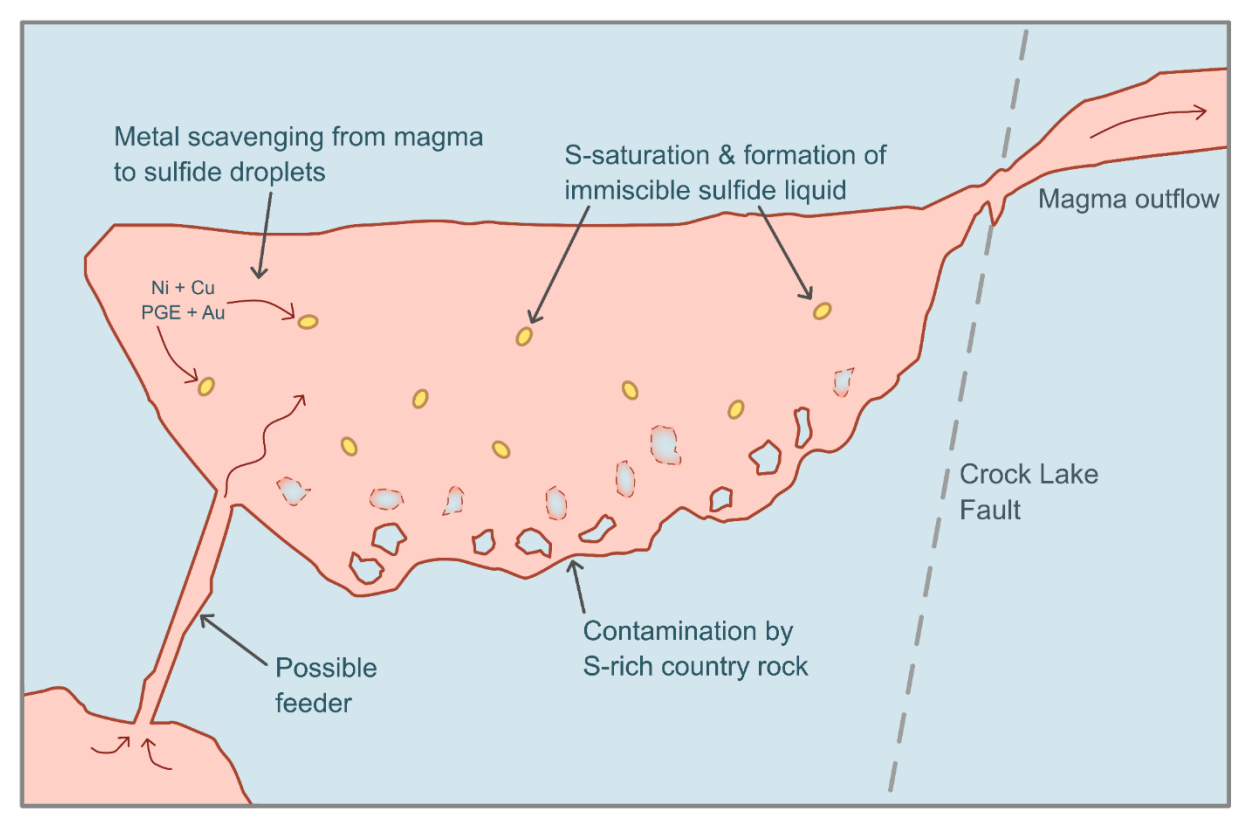


Figure 5.17. Schematic model of stage A showing magma emplacement from a deeper source, assimilation of country rocks and segregation of sulfide melt through sulfur saturation (yellow ovals).

0.7025 to 0.7062) and OIB-like trace element patterns, indicating a mantle origin with limited crustal influence. Interaction with the Quetico metasedimentary rocks is suggested by radiogenic isotope deviations (ϵ Nd -2.91 and -11.45; $Sr_i \sim$ 0.7060), suggesting that the emplaced magma underwent early but restricted crustal assimilation.

Sulfur saturation was an important process in this stage. As the magma interacted with the host rock, slight re-equilibration of olivine (demonstrated by decreased forsterite content at the LUZ-MZ margin compared to the rest of the LUZ) indicates high-temperature interaction and early assimilation of country rocks. This interaction likely enhanced the sulfur content in the magma, triggering in-situ sulfur saturation. Once sulfur saturation was reached, immiscible sulfide droplets formed, separating from the silicate melt and initiation the early accumulation of sulfide phases (Fig. 5.17).

5.7.2 Stage B

Following initial emplacement and host rock interaction, the SLI underwent a period of relative stability marked by inactivity of the melt feeder. This pause allowed progressive crystallization, leading to the formation of high-temperature silicate minerals (in a sequence of olivine > clinopyroxene > plagioclase) and high-temperature sulfide melt, accumulating 2-10% sulfides within the MZ and gradually depleting sulfur from the residual melt.

As the system cooled, crystallization continued, with the formation of the UUZ, where high-temperature silicates continued to crystallize. The sulfide content in this zone is lower <1% due to the previous segregation of sulfides from the residual melt. The whole-rock MgO content

peaked at approximately 23 wt. % in the LUZ, then gradually decreased toward the UUZ contact, suggesting a pause in the input of magma and a slight differentiation within the LUZ (Fig. 5.18). During this stage, whole-rock S/Se ratios of the early-formed silicates would have been like that of the Quetico metasedimentary rocks (>8 000) and the δ^{34} S values of sulfides would suggest interaction with the host rock.

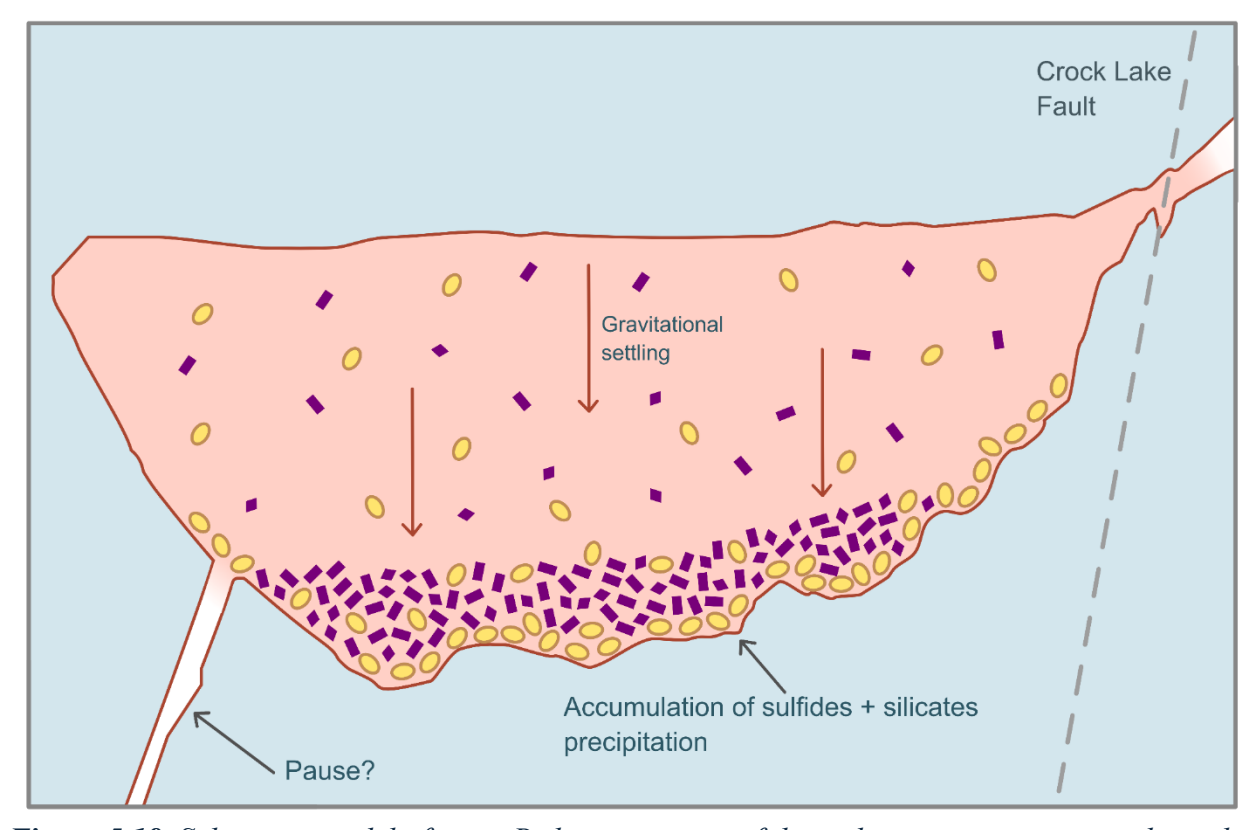


Figure 5.18. Schematic model of stage B showing pause of the melt input, precipitation through gravitational settling of sulfides at the base of the intrusion and silicates forming the Lower Ultramafic Zone (in purple).

5.7.3 Stage C

The intrusions magmatic history became more dynamic in this stage due to a significant melt recharge event. Fresh, high-MgO melt was injected into the chamber causing a distinct increase

in whole-rock MgO content (~22%) in the UUZ. This new influx triggered the crystallization of silicates in the general abundance of clinopyroxene > olivine > plagioclase. The decrease in forsterite content from 81.5 in the LUZ to ~75.5 in the UUZ reflects a chemical change in the incoming melt, which may have originated from a deeper, slightly differentiated intrusive source. This evolution likely led to the variation in forsterite content between the initial melt emplacement and the recharge event. The sulfur system was also affected during this stage. The fresh sulfur introduced by the recharge melt altered the pre-existing sulfur isotope signatures and whole rock S/Se ratios, possibly overprinting the earlier crustal sulfur signal with a mantle-derived sulfur signature. This change is evidenced by a shift in δ^{34} S values toward a composition

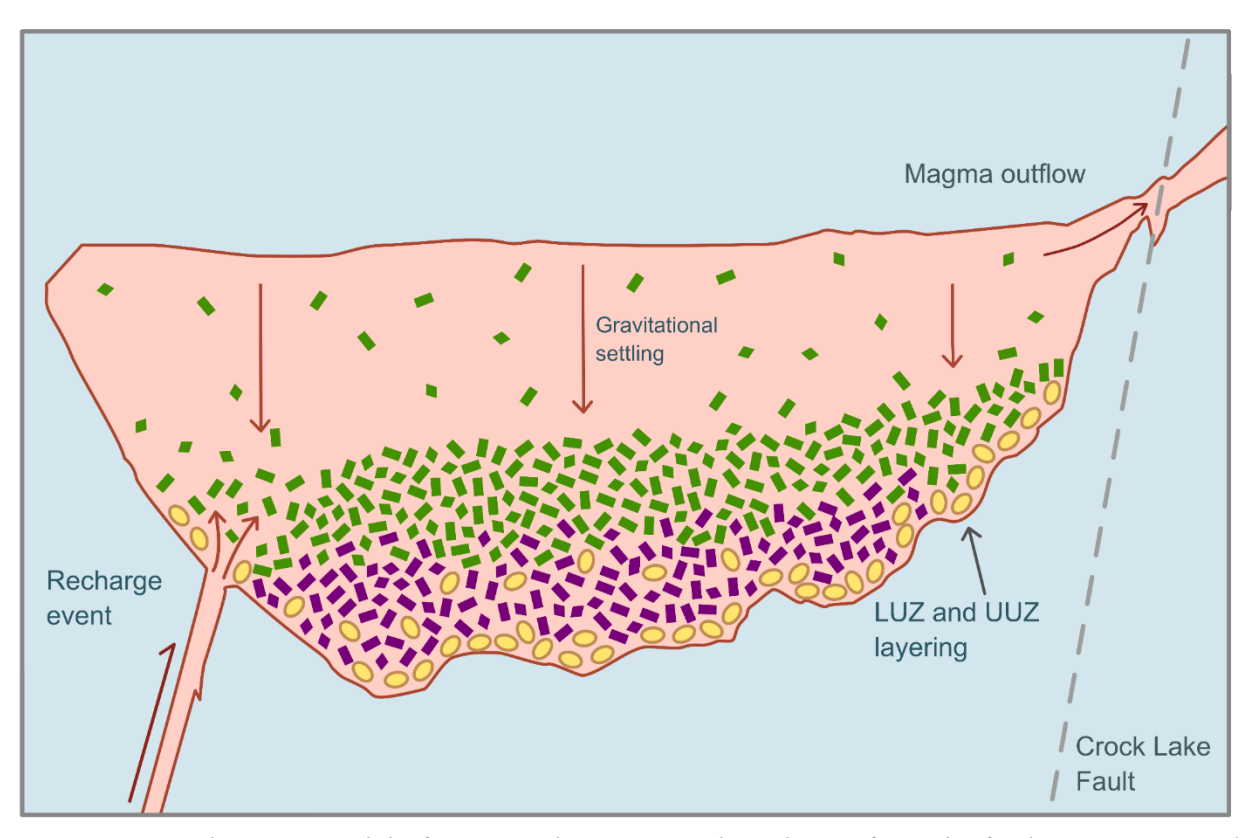


Figure 5.19. Schematic model of stage C showing a melt recharge from the feeder structure and a magma outflow at the right portion of the intrusion. Precipitation of minerals forming the Upper Ultramafic Zone are colored in green.

consistent with mantle sulfur. Additionally, the pressure generated by the recharge event likely caused magma to escape through the northern conduit across the Crock Lake Fault (Fig. 5.19).

5.7.4 Stage D

The feeder structure eventually ceased to introduce melt into the system, as evidenced by a gradual decrease in whole-rock MgO content and increase in SiO₂ wt.%, alongside an enrichment in incompatible elements within the residual melt. This transition reflects the progressive depletion of mafic minerals and the accumulation of residual, more evolved melt in the upper portion of the SLI (GZ: Fig 5.20). As the SLI system continued to cool, the crystallization of high-Mg silicates (such as olivine and clinopyroxene) diminished, giving way

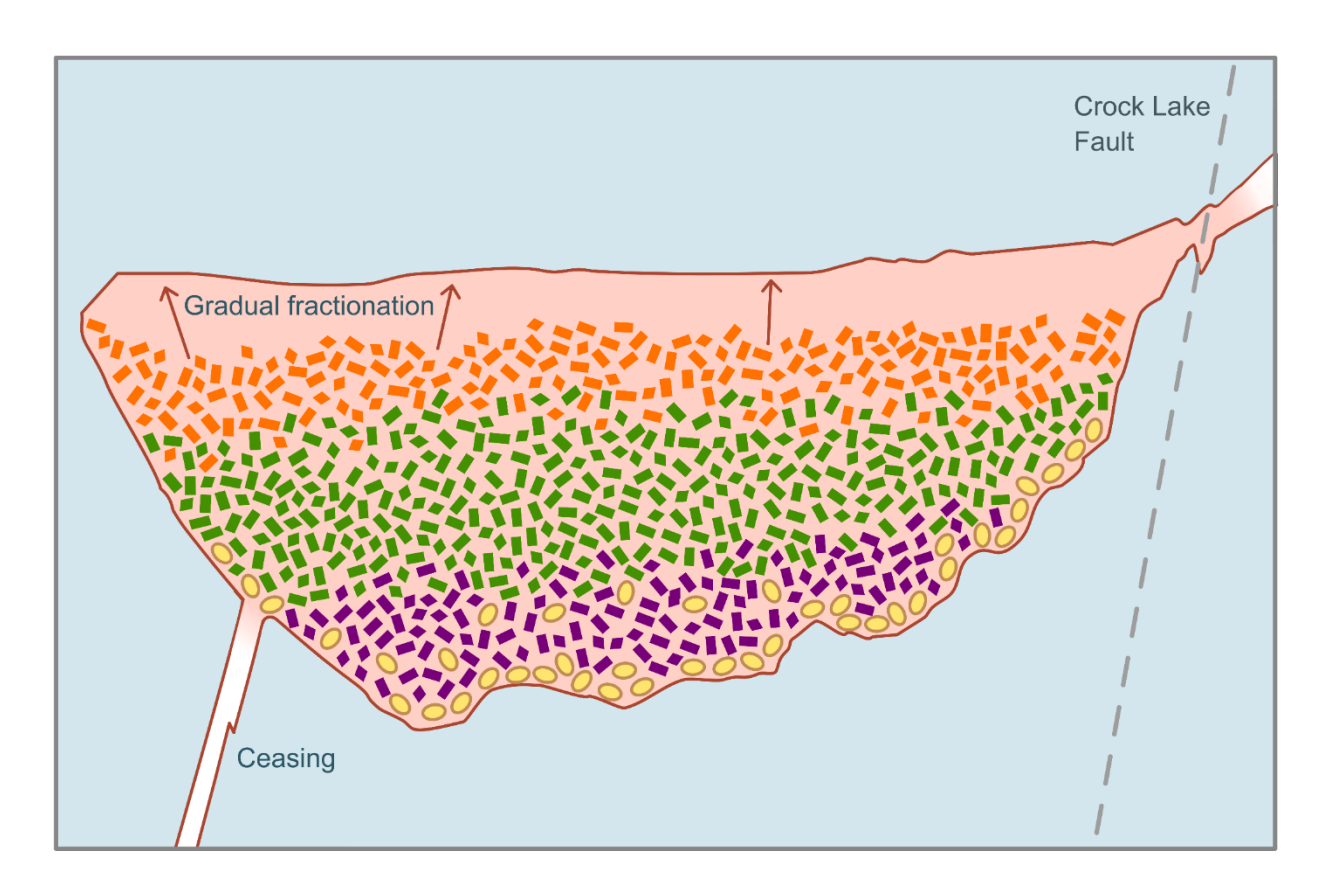


Figure 5.20. Schematic model stage D showing a ceasing on the melt feeder and a gradual fractionation of the residual melt that formed the Gabbro Zone.

to the formation of Fe-Ti oxides and plagioclase cumulates. These final crystallization products in the GZ exhibit a mineral assemblage dominated by plagioclase > clinopyroxene > Fe-Ti oxides. This mineral assemblage is consistent with fractional crystallization of the residual melt under conditions of increased oxygen fugacity compared to the ultramafic zones. Notably, radiogenic isotope ratios remain largely buffered by the silicate cumulates without significant changes compared to the rest of the intrusion.

Chapter 6: Conclusions

The Sunday Lake Intrusion is related to the Midcontinent Rift System and consists of a mafic-ultramafic intrusion that hosts contact-type PGE-Cu-Ni magmatic mineralization along its lower contact. The main objectives were addressed: 1) to investigate the magmatic evolution of the SLI, 2) to determine the composition of the parental magma, 3) to evaluate the roles of crustal contamination and sulfur saturation that triggered the formation of immiscible sulfide melt.

The SLI is a well-defined, layered intrusion that comprises wehrlite, olivine clinopyroxenite, feldspathic olivine clinopyroxenite, melagabbro, gabbro, leucogabbro, quartz monzonite and quartz gabbro, based on petrographic and major element data. Variations in whole-rock MgO (wt. %) and forsterite content of olivine suggest that the SLI was formed from at least two discrete, distinct magma pulses.

Lithostratigraphy of the SLI indicates that in the MZ, early formed sulfide-silicate immiscible melts sank into structural traps or embayments created by breakdown of country rock. Similarly, upon a slight cooling of the chamber, the most volumetric silicate liquid ponded at the deeper portions of the chamber, accumulating cumulate mushes and forming the LUZ. Overall, both vertical and lateral trends in fractional crystallization are apparent, with the highest degrees of fractionation toward the upper stratigraphy and the intrusion margins.

Trace element and radiogenic data are similar to ocean island basalts (OIB), and together with olivine compositions, indicates a basaltic parental magma that was derived from a mantle plume and is likely related to the Keweenaw Plume. Mass-balance calculations yield a calculated parental magma composition on ~11.15% FeO and ~19.5% MgO, consistent with a high-Mg tholeiitic basaltic magma. The varying olivine forsterite content between the Lower Ultramafic and Upper Ultramafic zones, suggest some degree of differentiation that occurred within a mid-crust staging or feeder chamber prior to the recharge event. This mid-crust differentiation of the feeder subtly depleted the primitive melt in Mg and increased the Fe content, resulting in a slightly decreased forsterite content in olivine of the UUZ compared to the LUZ.

Although most samples exhibit ɛNd and Sr_i isotopic ratios similar to the primitive mantle, some samples within this array display a negative Nb anomaly, suggesting that the parental magma underwent limited interaction with an enriched SCLM. Country rock assimilation is largely absent throughout the intrusion, with the exception of localized assimilation of Quetico metasedimentary country rocks at the Gabbro and Marginal zones being recorded by trace element and radiogenic isotope data. Some samples from these zones display negative ɛNd values and negative Nb anomalies compared to Th, consistent with a limited and localized country rock assimilation by the parental magma. Additionally, olivine equilibration at the LUZ-MZ contact, marked by decreased forsterite content in olivine, suggests that assimilation of country rocks occurred during the magma emplacement in the first episode of melt emplacement. During the intrusion emplacement and country rock assimilation, the sulfur isotopic system could have been produced a country rock-like signature, however, the subsequent recharge event

injected fresh, primitive melt that overprinted this signal, yielding near-mantle sulfur isotope values.

Petrographic evidence suggests early formation of euhedral fine-grained chromite, followed by medium- to coarse- grained olivine that crystallized and enclosed the chromite grains. As the magmatic system cooled further, clinopyroxene oikocrysts grew to enclose olivine. Plagioclase and titanomagnetite occur interstitially within the ultramafic zones but appear as phenocrysts in the Gabbro Zone, indicating an increasingly cumulate nature upwards through the intrusion.

Trace element signatures, petrographic observations, low Ni content in olivine and decreasing S/Se ratios suggest that the magmatic system initially carried sufficient sulfur and could have achieved sulfur saturation, but this process was enhanced by early assimilation of country rocks, leading to segregation of sulfide immiscible droplets upon sulfur saturation, comprising 2 to 10 vol. % of the crystallizing assemblage and subsequent precipitation.

Sulfide melt formed early in the melt ceased crystallizing at the latest stages of the magma crystallization, with a progressive sulfide crystallization of pyrrhotite, pentlandite, chalcopyrite, cubanite, troilite, cubanite and sphalerite. Platinum group minerals, such as maslovite, michenerite, sperrylite and native metals (silver, platinum and palladium), likely exsolved from the sulfide melt during the final stages of crystallization.

Future work in the SLI should prioritize identifying the feeder zone, specially within the less explored portion of the intrusion at the south. This area may host important sulfide-rich

mineralization and could represent a target for future exploration and a better understanding of metal distribution within the intrusion.

Chapter 7: References

- Addison, W. D., Brumpton, G. R., Vallini, D. A., McNaughton, N. J., Davis, D. W., Kissin, S. A., et al. (2005). Discovery of distal ejecta from the 1850 Ma Sudbury impact event. *Geology*, *33*(3), 193–196. https://doi.org/10.1130/G21048.1
- Bain, W. M., Hollings, P., Djon, L. M., Brzozowski, M. J., Layton-Matthews, D., & Dobosz, A. (2024). The geology, geochemistry, and magmatic evolution of the Legris Lake mafic—ultramafic complex, Ontario, Canada. *Mineralium Deposita*, *59*(1), 85–108. https://doi.org/10.1007/s00126-023-01183-x
- Barnes, S. J. (1986). The effect of trapped liquid crystallization on cumulus mineral compositions in layered intrusions. *Contributions to Mineralogy and Petrology*, *93*(4), 524–531. https://doi.org/10.1007/BF00371722
- Barnes, S. J., Cruden, A. R., Arndt, N., & Saumur, B. M. (2016). The mineral system approach applied to magmatic Ni–Cu–PGE sulphide deposits. *Ore Geology Reviews*, *76*, 296–316. https://doi.org/10.1016/j.oregeorev.2015.06.012
- Begg, G. C., Hronsky, J. A. M., Arndt, N. T., Griffin, W. L., O'Reilly, S. Y., & Hayward, N. (2010). Lithospheric, Cratonic, and Geodynamic Setting of Ni-Cu-PGE Sulfide Deposits. *Economic Geology*, 105(6), 1057–1070. https://doi.org/10.2113/econgeo.105.6.1057
- Bleeker, W., Smith, J., Hamilton, M., Kamo, S., Liikane, D., Hollings, P., et al. (2020). *The Midcontinent Rift and its mineral systems: overview and temporal constraints of Ni-Cu-PGE mineralized intrusions* (No. 8722) (p. 8722). https://doi.org/10.4095/326880
- Boudreau, A. E., & McBirney, A. R. (1997). The Skaergaard Layered Series. Part III. Non-dynamic Layering. *Journal of Petrology*, *38*(8), 1003–1020. https://doi.org/10.1093/petroj/38.8.1003
- Bowles, J. F. W. (1977). A method of tracing the temperature and oxygen-fugacity histories of complex magnetite-ilmenite grains. *Mineralogical Magazine*, *41*(317), 103–109. https://doi.org/10.1180/minmag.1977.041.317.15
- Brzozowski, M., Hollings, P., Heggie, G., MacTavish, A., Wilton, D., & Evans-Lamswood, D. (2023a). Characterizing the supra- and subsolidus processes that generated the Current PGE–Cu–Ni deposit, Thunder Bay North Intrusive Complex, Canada: insights from trace

- elements and multiple S isotopes of sulfides. *Mineralium Deposita*, *58*(8), 1559–1581. https://doi.org/10.1007/s00126-023-01193-9
- Brzozowski, M. J., Hollings, P., Zhu, J.-J., & Creaser, R. A. (2023b). Osmium isotopes record a complex magmatic history during the early stages of formation of the North American Midcontinent Rift Implications for rift initiation. *Lithos*, 436–437, 106966. https://doi.org/10.1016/j.lithos.2022.106966
- Caglioti, C. (2023). PGE-Cu-Ni Sulfide Mineralization of the Mesoproterozoic Escape Intrusion, Northwestern Ontario. Lakehead University.
- Cannon, W. F., Green, A. G., Hutchinson, D. R., Lee, M., Milkereit, B., Behrendt, J. C., et al. (1989). The North American Midcontinent Rift beneath Lake Superior from Glimpce seismic reflection profiling. *Tectonics*, 8(2), 305–332. https://doi.org/10.1029/TC008i002p00305
- Cannon, W. F. & Hinze, W.J. (1992). Speculations on the origin of the North American Midcontinent rift. *Tectonophysics*, 213(1–2), 49–55. https://doi.org/10.1016/0040-1951(92)90251-Z
- Card, K. D., & Ciesielski, A. (1986). DNAG #1. Subdivisions of the Superior Province of the Canadian Shield. *Geoscience Canada*. Retrieved from https://journals.lib.unb.ca/index.php/GC/article/view/3439
- Caro, G., & Bourdon, B. (2010). Non-chondritic Sm/Nd ratio in the terrestrial planets:

 Consequences for the geochemical evolution of the mantle–crust system. *Geochimica et Cosmochimica Acta*, 74(11), 3333–3349. https://doi.org/10.1016/j.gca.2010.02.025
- Chai, G., & Naldrett, A. J. (1991, April). Jinchuan Ultramafic Intrusion: Cumulate of a High-Mg Basaltic Magma | Journal of Petrology | Oxford Academic. Retrieved April 15, 2025, from https://academic.oup.com/petrology/article-abstract/33/2/277/1497381
- Chen, L.-M., Song, X.-Y., Danyushevsky, L. V., Wang, Y.-S., Tian, Y.-L., & Xiao, J.-F. (2015). A laser ablation ICP-MS study of platinum-group and chalcophile elements in base metal sulfide minerals of the Jinchuan Ni–Cu sulfide deposit, NW China. *Ore Geology Reviews*, 65, 955–967. https://doi.org/10.1016/j.oregeorev.2014.07.011

- Corfu, F., & Stott, G. M. (1996). Hf isotopic composition and age constraints on the evolution of the Archean central Uchi Subprovince, Ontario, Canada. *Precambrian Research*, 78(1), 53–63. https://doi.org/10.1016/0301-9268(95)00068-2
- Corredor, A. P. (2024). Magmatic and hydrothermal evolution of the Mesoproterozoic Current *PGE-Cu-Ni* deposit within the Thunder Bay North Intrusive Complex: Insights from trace element geochemistry and Nd, Sr, O, and H isotopes.
- Cundari, R. (2012). Geology and geochemistry of Midcontinent Rift-related igneous rocks.
- Cundari, R., Hollings, P., Smyk, M., & Carl, C. (2022). The geochemical evolution of the Logan Igneous Suite, Ontario, Canada: new insights from the Logan Basin and implications for the genesis of the Mesoproterozoic Midcontinent Rift System. In R. K. Srivastava, R. E. Ernst, K. L. Buchan, & M. de Kock (Eds.), *Large Igneous Provinces and their Plumbing Systems* (p. 0). Geological Society of London. https://doi.org/10.1144/SP518-2021-6
- Daniels, P. A., Jr. (1982). 7C: Upper Precambrian sedimentary rocks: Oronto Group, Michigan-Wisconsin. In Richard J. Wold & W. J. Hinze (Eds.), *Geology and Tectonics of the Lake Superior Basin* (Vol. 156, p. 0). Geological Society of America. https://doi.org/10.1130/MEM156-p107
- Dare, S. A. S., Barnes, S.-J., Prichard, H. M., & Fisher, P. C. (2014). Mineralogy and Geochemistry of Cu-Rich Ores from the McCreedy East Ni-Cu-PGE Deposit (Sudbury, Canada): Implications for the Behavior of Platinum Group and Chalcophile Elements at the End of Crystallization of a Sulfide Liquid*. *Economic Geology*, 109(2), 343–366. https://doi.org/10.2113/econgeo.109.2.343
- Davis, D. W., & Green, J. C. (1997). Geochronology of the North American Midcontinent rift in western Lake Superior and implications for its geodynamic evolution. *Canadian Journal of Earth Sciences*, 34(4), 476–488. https://doi.org/10.1139/e17-039
- Davis, D. W., Krogh, T. E., Hinzer, J., & Nakamura, E. (1985). Zircon dating of polycyclic volcanism at Sturgeon Lake and implications for base metal mineralization. *Economic Geology*, 80(7), 1942–1952. https://doi.org/10.2113/gsecongeo.80.7.1942
- Davis, D. W., Pezzutto, F., & Ojakangas, R. W. (1990). The age and provenance of metasedimentary rocks in the Quetico Subprovince, Ontario, from single zircon analyses: implications for Archean sedimentation and tectonics in the Superior Province. *Earth and*

- Planetary Science Letters, 99(3), 195–205. https://doi.org/10.1016/0012-821X(90)90110-J
- Dickin, A. P. (2018). Radiogenic Isotope Geology. Cambridge University Press.
- Donaldson, J. A., & Irving, E. (1972). Grenville Front and Rifting of the Canadian Shield.

 Nature Physical Science, 237(78), 139–140. https://doi.org/10.1038/physci237139a0
- Eales, H. V., & Cawthorn, R. G. (1996). The Bushveld Complex. In R. G. Cawthorn (Ed.), Developments in Petrology (Vol. 15, pp. 181–229). Elsevier. https://doi.org/10.1016/S0167-2894(96)80008-X
- Eckstrand, O. R., & Hulbert, L. J. (1987). Selenium and the source of sulfur in magmatic nickel and platinum deposits. In *Geol Assoc Can-Mineral Assoc Can Program Abstr* (Vol. 12, p. 40).
- Fairchild, L. M., Swanson-Hysell, N. L., Ramezani, J., Sprain, C. J., & Bowring, S. A. (2017). The end of Midcontinent Rift magmatism and the paleogeography of Laurentia. *Lithosphere*, 9(1), 117–133. https://doi.org/10.1130/L580.1
- Farquhar, J., & Wing, B. A. (2003). Multiple sulfur isotopes and the evolution of the atmosphere. *Earth and Planetary Science Letters*, 213(1), 1–13. https://doi.org/10.1016/S0012-821X(03)00296-6
- Flank, S. (2017). The Petrography, Geochemistry and Stratigraphy of the Sunday Lake Intrusion, Jacques Township, Ontario.
- Fleet, M. E., & MacRae, N. D. (1988). Partition of Ni between olivine and sulfide: equilibria with sulfide-oxide liquids. *Contributions to Mineralogy and Petrology*, 100(4), 462–469. https://doi.org/10.1007/BF00371375
- Fonseca, R. O., Campbell, I. H., O'Neill, H. S. C., & Allen, C. M. (2009). Solubility of Pt in sulphide mattes: Implications for the genesis of PGE-rich horizons in layered intrusions. *Geochimica et Cosmochimica Acta*, 73(19), 5764-5777.
- Fralick, P., & Pufahl, P. K. (2006). Iron Formation in Neoarchean Deltaic Successions and the Microbially Mediated Deposition of Transgressive Systems Tracts. *Journal of Sedimentary Research*, 76(9), 1057–1066. https://doi.org/10.2110/jsr.2006.095

- Fralick, P., Davis, D. W., & Kissin, S. A. (2002). The age of the Gunflint Formation, Ontario, Canada: single zircon U– Pb age determinations from reworked volcanic ash. *Canadian Journal of Earth Sciences*, 39(7), 1085–1091. https://doi.org/10.1139/e02-028
- Halevy, I., Johnston, D. T., & Schrag, D. P. (2010). Explaining the Structure of the Archean Mass-Independent Sulfur Isotope Record. *Science*, 329(5988), 204–207. https://doi.org/10.1126/science.1190298
- Halls, H. C., & Pesonen, L. J. (1982). Paleomagnetism of Keweenawan rocks.
- Hart, S. R., & Gaetani, G. A. (2006). Mantle Pb paradoxes: the sulfide solution. *Contributions to Mineralogy and Petrology*, 152(3), 295-308.
- Heaman, L. M., & Machado, N. (1992). Timing and origin of midcontinent rift alkaline magmatism, North America: evidence from the Coldwell Complex. *Contributions to Mineralogy and Petrology*, 110(2), 289–303. https://doi.org/10.1007/BF00310744
- Heaman, L. M., Easton, R. M., Hart, T. R., Hollings, P., MacDonald, C. A., & Smyk, M. (2007).
 Further refinement to the timing of Mesoproterozoic magmatism, Lake Nipigon region,
 Ontario. Canadian Journal of Earth Sciences, 44(8), 1055–1086.
 https://doi.org/10.1139/e06-117
- Heggie, G. (2005). Whole rock geochemistry, mineral chemistry, petrology and Pt, Pd mineralization of the Seagull Intrusion, Northwestern Ontario.
- Hergt, J. M., Chappell, B. W., Faure, G., Mensing, T. M., & McDougall, I. (1989). The geochemistry of Jurassic dolerites from Portal Peak, Antarctica. *Contributions to Mineralogy and Petrology*, 102, 298–305. https://doi.org/10.1007/BF00373722
- Henry, P., Stevenson, R. K., & Gariépy, C. (1998). Late Archean Mantle Composition and Crustal Growth in the Western Superior Province of Canada: Neodymium and Lead Isotopic Evidence from the Wawa, Quetico, and Wabigoon Subprovinces. *Geochimica et Cosmochimica Acta*, 62(1), 143–157. https://doi.org/10.1016/S0016-7037(97)00324-4
- Hofmann, A. W. (1997). Mantle geochemistry: the message from oceanic volcanism. *Nature*, 385(6613), 219–229. https://doi.org/10.1038/385219a0
- Hollings, P., Fralick, P., & Cousens, B. (2007a). Early history of the Midcontinent Rift inferred from geochemistry and sedimentology of the Mesoproterozoic Osler Group, northwestern

- Ontario. *Canadian Journal of Earth Sciences*, 44(3), 389–412. https://doi.org/10.1139/e06-084
- Hollings, P., Richardson, A., Creaser, R. A., & Franklin, J. M. (2007b). Radiogenic isotope characteristics of the Mesoproterozoic intrusive rocks of the Nipigon Embayment, northwestern Ontario. *Canadian Journal of Earth Sciences*, 44(8), 1111–1129. https://doi.org/10.1139/e06-128
- Hollings, P., Smyk, M., Heaman, L. M., & Halls, H. (2010). The geochemistry, geochronology and paleomagnetism of dikes and sills associated with the Mesoproterozoic Midcontinent Rift near Thunder Bay, Ontario, Canada. *Precambrian Research*, 183(3), 553–571. https://doi.org/10.1016/j.precamres.2010.01.012
- Hollings, P., Smyk, M., & Cousens, B. (2012). The radiogenic isotope characteristics of dikes and sills associated with the Mesoproterozoic Midcontinent Rift near Thunder Bay, Ontario, Canada. *Precambrian Research*, 214–215, 269–279. https://doi.org/10.1016/j.precamres.2011.11.006
- Holwell, B. D. A., & McDonald, I. (2010). A Review of the Behaviour of Platinum Group Elements within Natural Magmatic Sulfide Ore Systems. *Platinum Metals Review*, *54*(1), 26–36. https://doi.org/10.1595/147106709X480913
- Hughes, A. E., Haque, N., Northey, S. A., & Giddey, S. (2021). Platinum Group Metals: A
 Review of Resources, Production and Usage with a Focus on Catalysts. *Resources*, 10(9),
 93. https://doi.org/10.3390/resources10090093
- Hund, K. (2023, May 24). Minerals for Climate Action.
- Hutchinson, D. R., White, R. S., Cannon, W. F., & Schulz, K. J. (1990). Keweenaw hot spot:

 Geophysical evidence for a 1.1 Ga mantle plume beneath the Midcontinent Rift System. *Journal of Geophysical Research: Solid Earth*, 95(B7), 10869–10884.

 https://doi.org/10.1029/JB095iB07p10869
- Hutchinson, D. R., Lee, M. W., Behrendt, J., Cannon, W. F., & Green, A. G. (1992). Variations in the reflectivity of the moho transition zone beneath the Midcontinent Rift System of North America: Results from true amplitude analysis of GLIMPCE data. *Journal of Geophysical Research: Solid Earth*, 97(B4), 4721–4737.
 https://doi.org/10.1029/91JB02572

- Irvine, T. N., & Baragar, W. R. A. (1971). A Guide to the Chemical Classification of the Common Volcanic Rocks. *Canadian Journal of Earth Sciences*, 8(5), 523–548. https://doi.org/10.1139/e71-055
- Irvine, T. N. (1975). Crystallization sequences in the Muskox intrusion and other layered intrusions II. Origin of chromitite layers and similar deposits of other magmatic ores. Geochimica et Cosmochimica Acta, 39, 991–1020. https://doi.org/10.1016/0016-7037(75)90043-5
- Jackson, E. D. (1961). Primary Textures and Mineral Associations in the Ultramafic Zone of the Stillwater Complex, Montana. *Geological Survey Professional*, 358.
- Kehlenbeck, M. M. (1976). Nature of the Quetico–Wabigoon boundary in the de Courcey Smiley Lakes area, northwestern Ontario. *Canadian Journal of Earth Sciences*, *13*(6), 737–748. https://doi.org/10.1139/e76-078
- Laarman, J. E. (2007). Geochemistry and PGE mineralization of the Kitto Intrusion: A product of Mesoproterozoic plume magmatism through fault bounded Archean crust, east Nipigon Embayment, northern Ontario (Thesis). Lakehead University.
- Le Maitre, R.W., (2002). Igneous Rocks: A Classification and Glossary of Terms:

 Recommendations of the International Union of Geological Sciences Subcommission on the Systematics of Igneous Rocks. 2nd edition. Cambridge University Press.
- Li, C., & Ripley, E. M. (2005). Empirical equations to predict the sulfur content of mafic magmas at sulfide saturation and applications to magmatic sulfide deposits. Retrieved May 28, 2025, from https://link.springer.com/article/10.1007/s00126-005-0478-8
- Li, C., & Ripley, E. M. (2009). Sulfur Contents at Sulfide-Liquid or Anhydrite Saturation in Silicate Melts: Empirical Equations and Example Applications. *Economic Geology*, 104(3), 405–412. https://doi.org/10.2113/gsecongeo.104.3.405
- Li, C. & Ripley, E. M. (2011). The giant Jinchuan Ni-Cu-(PGE) deposit: Tectonic setting, magma evolution, ore genesis, and exploration implications. In Magmatic Ni-Cu and PGE deposits: Geology, Geochemistry, and genesis (Reviews in Economic Geology, Vol. 17, pp. 163-180). Society of Economic Geologists. https://doi.org/10.5382/Rev.17.06
- Lindsley, D. H. (2018). *Oxide Minerals: Petrologic and Magnetic Significance*. Walter de Gruyter GmbH & Co KG.

- Lofgren, G. (1974). An experimental study of plagioclase crystal morphology; isothermal crystallization. *American journal of Science*, 274(3), 243-273.
- Mäder, U. K., Percival, J. A., & Berman, R. G. (1994). Thermobarometry of garnet—clinopyroxene—hornblende granulites from the Kapuskasing structural zone. *Canadian Journal of Earth Sciences*, *31*(7), 1134–1145. https://doi.org/10.1139/e94-101
- Maier, W. D., Barnes, S.-J., Sarkar, A., Ripley, E., Li, C., & Livesey, T. (2010). The Kabanga Ni sulfide deposit, Tanzania: I. Geology, petrography, silicate rock geochemistry, and sulfur and oxygen isotopes. *Mineralium Deposita*, 45(5), 419–441. https://doi.org/10.1007/s00126-010-0280-0
- Mansur, E. T., Barnes, S. J., Fiorentini, M. L., Miller, J., & Hronsky, J. (2019). Sulfur isotope signatures in komatiite-hosted Ni–Cu–PGE deposits: Evidence for crustal contamination and sulfur addition. *Ore Geology Reviews*, 107, 107–133. https://doi.org/10.1016/j.oregeorev.2019.01.013
- Mansur, E. T., Barnes, S.-J., & Duran, C. J. (2021). An overview of chalcophile element contents of pyrrhotite, pentlandite, chalcopyrite, and pyrite from magmatic Ni-Cu-PGE sulfide deposits. *Mineralium Deposita*, 56(1), 179–204. https://doi.org/10.1007/s00126-020-01014-3
- Goldner, B. D. (2011). Igneous petrology of the Ni–Cu–PGE mineralized Tamarack intrusion, Aitkin and Carlton Counties, Minnesota. *University of Minnesota Conservancy*.
- Gordon, M. B., & Hempton, M. R. (1986). Collision-induced rifting: The Grenville Orogeny and the Keweenawan Rift of North America. *Tectonophysics*, *127*(1–2), 1–25. https://doi.org/10.1016/0040-1951(86)90076-4
- Mackasey, W.O., Blackburn, C.E., & Trowell, N.F. (1974). A regional approach to the Wabigoon-Quetico belts and its bearing on exploration in northwestern Ontario. *Ontario Division of Mines. Miscellaneous Paper*, 58.
- Mavrogenes, J. A., & O'Neill, H. St. C. (1999). The relative effects of pressure, temperature and oxygen fugacity on the solubility of sulfide in mafic magmas. *Geochimica et Cosmochimica Acta*, 63(7), 1173–1180. https://doi.org/10.1016/S0016-7037(98)00289-0

- McCallum, I. S. (1996). The Stillwater Complex. In R. G. Cawthorn (Ed.), *Developments in Petrology* (Vol. 15, pp. 441–483). Elsevier. https://doi.org/10.1016/S0167-2894(96)80015-7
- McSwiggen, P. L. & Morey, G.B. (2008). Overview of the mineralogy of the Biwabik Iron Formation, Mesabi Iron Range, northern Minnesota. *Regulatory Toxicology and Pharmacology*, *52*(1), S11–S25. https://doi.org/10.1016/j.yrtph.2007.09.010
- McWilliams, M.O. & Dunlop, D.J. (1978). Grenville paleomagnetism and tectonics. Retrieved October 22, 2024, from https://cdnsciencepub.com/doi/abs/10.1139/e78-076
- Miller, J. (2020). Report on the Petrography, Geochemistry, and Lithostratigraphy of DDH SL19-026 from the Southern Sunday Lake Intrusion.
- Miller, James D., Green, J. C., Severson, M. J., Chandler, V. W., Hauck, S. A., Peterson, D. M., & Wahl, T. E. (2002). RI-58 Geology and mineral potential of the Duluth Complex and related rocks of northeastern Minnesota. Retrieved from http://purl.umn.edu/58804
- Miller, J.D., Nicholson, S. W., Easton, R. M., Ripley, E., & Feinberg, J. (2013). The Geology and Mineral Deposits of the 1.1Ga Midcontinent Rift in the Lake Superior Region An Overview. *Field Guide to the Copper-Nickel-Platinum Group Element Deposits of the Lake Superior Region*, 1, 1–50.
- Mudd, G. M., & Jowitt, S. M. (2022). The New Century for Nickel Resources, Reserves, and Mining: Reassessing the Sustainability of the Devil's Metal. *Economic Geology*, 117(8), 1961–1983. https://doi.org/10.5382/econgeo.4950
- Mungall, J. E. (2002). Kinetic Controls on the Partitioning of Trace Elements Between Silicate and Sulfide Liquids. *Journal of Petrology*, *43*(5), 749–768. https://doi.org/10.1093/petrology/43.5.749
- Mungall, J. E. (2014). Geochemistry of Magmatic Ore Deposits. In *Treatise on Geochemistry* (pp. 195–218). Elsevier. https://doi.org/10.1016/B978-0-08-095975-7.01108-6
- Naldrett, A. J. (2004). *Magmatic Sulfide Deposits*. Berlin, Heidelberg: Springer. https://doi.org/10.1007/978-3-662-08444-1
- Naldrett, A. J., Bruegmann, G. E., & Wilson, A. H. (1990). Models for the concentration of PGE in layered intrusions. *The Canadian Mineralogist*, 28(3), 389–408.

- Naldrett, A. J. (1999), World-class Ni-Cu-PGE deposits: key factors in their genesis. Mineralium deposita, 34(3), 227-240.
- Nicholson, S. W., & Shirey, S. B. (1990). Midcontinent rift volcanism in the Lake Superior Region: Sr, Nd, and Pb isotopic evidence for a mantle plume origin. *Journal of Geophysical Research: Solid Earth*, 95(B7), 10851–10868. https://doi.org/10.1029/JB095iB07p10851
- Nicholson, S. W., Schulz, K. J., Shirey, S. B., & Green, J. C. (1997). Rift-wide correlation of 1.1 Ga Midcontinent rift system basalts: implications for multiple mantle sources during rift development. *Canadian Journal of Earth Sciences*, *34*(4), 504–520. https://doi.org/10.1139/e17-041
- O'Brien, S. (2018). Petrology of the Crystal Lake Gabbro and the Mount Mollie Dyke,

 Midcontinent Rift, Northwest Ontario (Thesis). Retrieved from

 https://knowledgecommons.lakeheadu.ca/handle/2453/4177
- Palme, H., & O'Neill, H. St. C. (2014). 3.1 Cosmochemical Estimates of Mantle Composition. In H. D. Holland & K. K. Turekian (Eds.), *Treatise on Geochemistry (Second Edition)* (pp. 1–39). Oxford: Elsevier. https://doi.org/10.1016/B978-0-08-095975-7.00201-1
- Pearce, J. A. (2008). Geochemical fingerprinting of oceanic basalts with applications to ophiolite classification and the search for Archean oceanic crust. *Lithos*, *100*(1–4), 14–48. https://doi.org/10.1016/j.lithos.2007.06.016
- Pearce, J. A. (2012). Geochemical fingerprinting of the Earth's oldest rocks. *Geology*, 40(6), 535–536. https://doi.org/10.1130/focus062012.1
- Percival, J., Skulski, T., Sanborn-Barrie, M., Stott, G., Leclair, A., Corkery, T., & Boily, M. (2012). *Geology and tectonic evolution of the Superior Province, Canada; in Tectonic Styles in Canada: The Lithoprobe Perspective*.
- Percival, J. A., & Card, K. D. (1992). Vizien greenstone belt and adjacent high-grade domains of the Minto block, Ungava Peninsula, Quebec. *Current Research, Geol. Surv. Can. Pap*, 69–80.
- Percival, J. A., Green, A. G., Milkereit, B., Cook, F. A., Geis, W., & West, G. F. (1989). Seismic reflection profiles across deep continental crust exposed in the Kapuskasing uplift structure. *Nature*, *342*(6248), 416–420.

- Percival, J. A., Mortensen, J. K., Stern, R. A., Card, K. D., & Bégin, N. J. (1992). Giant granulite terranes of northeastern Superior Province: the Ashuanipi complex and Minto block. *Canadian Journal of Earth Sciences*, 29(10), 2287–2308. https://doi.org/10.1139/e92-179
- Percival, J A, Sanborn-Barrie, M., Skulski, T., Stott, G. M., Helmstaedt, H., & White, D. J. (2006). Tectonic evolution of the western Superior Province from NATMAP and Lithoprobe studies. *Canadian Journal of Earth Sciences*, 43(7), 1085–1117. https://doi.org/10.1139/e06-062
- Percival, John A. (2007). Geology and metallogeny of the Superior Province, Canada.
- Puchtel, I. S., Blichert-Toft, J., Touboul, M., & Walker, R. J. (2018). 182W and HSE constraints from 2.7 Ga komatiites on the heterogeneous nature of the Archean mantle. *Geochimica et Cosmochimica Acta*, 228, 1–26. https://doi.org/10.1016/j.gca.2018.02.030
- Queffurus, M., & Barnes, S.-J. (2015). A review of sulfur to selenium ratios in magmatic nickel–copper and platinum-group element deposits. *Ore Geology Reviews*, *69*, 301–324. https://doi.org/10.1016/j.oregeorev.2015.02.019
- Richards, J. P., & Spooner, E. T. C. (1989). Evidence for Cu-(Ag) mineralization by magmatic-meteoric fluid mixing in Keweenawan fissure veins, Mamainse Point, Ontario. *Economic Geology*, 84(2), 360–385. https://doi.org/10.2113/gsecongeo.84.2.360
- Rickard, D., & Luther, G. (2007). Chemistry of Iron Sulfides. Retrieved May 9, 2025, from https://pubs.acs.org/doi/full/10.1021/cr0503658?casa_token=8pYbcVvI9zcAAAAA:nCK nEaXAzN7Ks4Hfuo-1P6cs2CLE6wow6t6ABt9PxA9iHarY4yLCxoR04YqmE_LRRIBh6pbV-FOMvQ&casa_token=idmPlRczHRgAAAAA:AV6JiH5Wp33xwlDUTNOHLrd0PVNZ KrjbXWyzNjfkevGVZGM_U08ZUOLLlozyQ9nz0e1JUoTKLEsomA
- Ripley, E. M., & Li, C. (2003). Sulfur isotope exchange and metal enrichment in the formation of magmatic Cu-Ni-(PGE) deposits. *Economic Geology*, *98*(3), 635–641. https://doi.org/10.2113/gsecongeo.98.3.635
- Roeder, P. L., & Emslie, R. F. (1970). Olivine-liquid equilibrium. *Contributions to Mineralogy* and *Petrology*, 29(4), 275–289. https://doi.org/10.1007/BF00371276

- Rogala, B., Fralick, P. W., Heaman, L. M., & Metsaranta, R. (2007). Lithostratigraphy and chemostratigraphy of the Mesoproterozoic Sibley Group, northwestern Ontario, Canada1. *Canadian Journal of Earth Sciences*, *44*(8), 1131–1149. https://doi.org/10.1139/e07-027
- Rollinson, H. (1993). Using Geochemical Data: Evolution, Presentation, Interpretation.

 Retrieved February 19, 2025, from

 https://www.researchgate.net/publication/49180506_Using_Geochemical_Data_Evolutio

 n Presentation Interpretation
- Rooney, T. O., Konter, J. G., Finlayson, V. A., LaVigne, A., Brown, E. L., Stein, C. A., et al. (2022). Constraining the isotopic endmembers contributing to 1.1 Ga Keweenawan large igneous province magmatism. *Contributions to Mineralogy and Petrology*, 177(4), 49. https://doi.org/10.1007/s00410-022-01907-8
- Seal, R. R., II. (2006). Sulfur Isotope Geochemistry of Sulfide Minerals. *Reviews in Mineralogy and Geochemistry*, 61(1), 633–677. https://doi.org/10.2138/rmg.2006.61.12
- Shirey, S. B., & Hanson, G. N. (1986). Mantle heterogeneity and crustal recycling in Archean granite-greenstone belts: Evidence from Nd isotopes and trace elements in the Rainy Lake area, Superior Province, Ontario, Canada. *Geochimica et Cosmochimica Acta*, 50(12), 2631–2651. https://doi.org/10.1016/0016-7037(86)90215-2
- Shirey, S. B., klewin, K. W., Berg, J. H., & Carlson, R. W. (1994). Temporal changes in the sources of flood basalts: Isotopic and trace element evidence from the 1100 Ma old Keweenawan Mamainse Point Formation, Ontario, Canada. *Geochimica et Cosmochimica Acta*, 58(20), 4475–4490. https://doi.org/10.1016/0016-7037(94)90349-2
- Smith, W.D., Albrechtsen, B., Maier, W.D., & Mungall, J. E. (2024). Petrogenesis and Ni-Cu-(PGE) prospectivity of the Mount Ayliff Complex in the Karoo Igneous Province: new insights from the Ingeli and Horseshoe lobes. *Geological Society, London, Special Publications*, 551(1), SP552-2023.
- Smythe, D. J., Woof, B. J., & Kiseeva, E. S. (2017). The S content of silicate melts at sulfide saturation: New experiments and a model incorporating the effects of sulfide composition. Retrieved July 24, 2025, from https://www.degruyterbrill.com/document/doi/10.2138/am-2017-5800CCBY/html

- Sparks, R. S. J., Huppert, H. E., Turner, J. S., Sakuyama, M., O'Hara, M. J., Moorbath, S. E., et al. (1997). The fluid dynamics of evolving magma chambers. *Philosophical Transactions of the Royal Society of London. Series A, Mathematical and Physical Sciences*, 310(1514), 511–534. https://doi.org/10.1098/rsta.1984.0006
- Steiner, R. A. (2014). Genesis of sulfide mineralization within the granite footwall of the Maturi deposit of the South Kawishiwi Intrusion, Duluth Complex, NE Minnesota. Retrieved May 8, 2025, from https://www.proquest.com/openview/9d8ecfbd1e2d76dccb0da3475e16dc3b/1?cbl=18750 &pq-origsite=gscholar
- Steven Flank. (2020). Sunday Lake Project Overview.
- Stott, G. M., Corkery, M. T., Percival, J. A., Simard, M., & Goutier, J. (2010). 20. Project Units 98-006 and 98-007. A Revised Terrane Subdivision of the Superior Province.
- Sun, S. & McDonough, W. F. (1989). Chemical and isotopic systematics of oceanic basalts: implications for mantle composition and processes. *Geological Society, London, Special Publications*, 42(1), 313–345. https://doi.org/10.1144/GSL.SP.1989.042.01.19
- Swanson-Hysell, N. L., Burgess, S. D., Maloof, A. C., & Bowring, S. A. (2014). Magmatic activity and plate motion during the latent stage of Midcontinent Rift development. *Geology*, 42(6), 475–478. https://doi.org/10.1130/G35271.1
- Transition Metals Corp. (2015). Detailed Log Report of Hole Number SL-15-013 [Data set].
- Trevisan, B. E. (2014). The petrology, mineralization and regional context of the Thunder mafic to ultramafic intrusion, Midcontinent Rift, Thunder Bay, Ontario.
- Wallace, P. J., & Edmonds, M. (2011). The Sulfur Budget in Magmas: Evidence from Melt Inclusions, Submarine Glasses, and Volcanic Gas Emissions. *Reviews in Mineralogy and Geochemistry*, 73(1), 215–246. https://doi.org/10.2138/rmg.2011.73.8
- Wang, S., Kuzmich, B., Hollings, P., Zhou, T., & Wang, F. (2020). Petrogenesis of the Dog Lake Granite Chain, Quetico Basin, Superior Province, Canada: Implications for Neoarchean crustal growth. *Precambrian Research*, *346*, 105828. https://doi.org/10.1016/j.precamres.2020.105828

- Wang, Z., & Becker, H. (2013). Ratios of S, Se and Te in the silicate Earth require a volatile-rich late veneer | Nature. Retrieved April 22, 2025, from https://www.nature.com/articles/nature12285
- Williams, H. R. (1991). Quetico subprovince. *Geology of Ontario. Ontario Geological Survey Special*, 4(Part 1).
- Williams, P. R., & Currie, K. L. (1993). Character and regional implications of the sheared Archaean granite-greenstone contact near Leonora, Western Australia. *Precambrian Research*, 62(3), 343–365. https://doi.org/10.1016/0301-9268(93)90029-2
- Wold, Richard John, & Hinze, W. J. (1982). *Geology and Tectonics of the Lake Superior Basin*. Geological Society of America.
- Woodruff, L. G., Schulz, K. J., Nicholson, S. W., & Dicken, C. L. (2020). Mineral deposits of the Mesoproterozoic Midcontinent Rift system in the Lake Superior region A space and time classification. *Ore Geology Reviews*, *126*, 103716. https://doi.org/10.1016/j.oregeorev.2020.103716
- Yahia, K. (2023). Geochemistry, petrography, geochronology, and radiogenic isotopes of the weakly mineralized intrusions in Thunder Bay North Igneous Complex (Thesis).

 Lakehead University. Retrieved from https://knowledgecommons.lakeheadu.ca/handle/2453/5283
- Zientek, M. L. (2012). USGS Open-File Report 2012-1010: Magmatic Ore Deposits in Layered Intrusions—Descriptive Model for Reef-Type PGE and Contact-Type Cu-Ni-PGE Deposits. Retrieved February 12, 2025, from https://pubs.usgs.gov/of/2012/1010/
- Zientek, Michael L., & Loferski, P. J. (2014). *Platinum-group elements: So many excellent properties* (No. 2014–3064). *Fact Sheet*. U.S. Geological Survey. https://doi.org/10.3133/fs20143064

Appendix one - Sample information

Mineral and lithostratigraphic abbreviations

Act Actinolite Ap Apatite Amphibole Amp Bt **Biotite** Calcite Cal Cubanite Cbn Chalcopyrite Ccp Chl Chlorite Chromite Chr Cpx Clinopyroxene

Ep Epidote
GZ Gabbro Zone
Hbl Hornblende
Hem Hematite
Ilm Ilmenite

LUZ Lower Ultramafic Zone

Mag Magnetite
Mch Michenerite

Mtsd Metasedimentary rocks

Msl Maslovite MZ Marginal Zone

Olivine Ol Pd Palladium **P**1 Plagioclase Pn Pentlandite Po Pyrrhotite Py **Pyrite** Qz Quartz Sericite Ser Sphalerite Sph Srp Serpentine

UUZ Upper Ultramafic Zone

Tlc Talc Troilite

Hole ID	Sample ID	From	То	Lithology	Methods
SL-17-18B	SL23KM01	718.2	718.45	Meta-greywacke	Petrography, whole-rock,
					TIMS
SL-17-18B	SL23KM02	707.38	707.75	Meta-greywacke	Whole-rock
SL-17-18B	SL23KM03	704.38	704.7	Meta-greywacke	Whole-rock
SL-17-18B	SL23KM04	695.2	695.5	Olivine melagabbro	Whole-rock, sulfide micro-
					drilling, TIMS
SL-17-18B	SL23KM05	690.9	691.2	Feldspathic olivine	Petrography, whole-rock,
				clinopyroxenite	sulfide micro-drilling, LA-
					ICPMS
SL-17-18B	SL23KM06	686.05	686.35	Wehrlite	Petrography, whole-rock,
					sulfide micro-drilling
SL-17-18B	SL23KM07	683.05	683.4	Olivine melagabbro	Whole-rock, sulfide micro-
					drilling
SL-17-18B	SL23KM08	678.50	678.85	Melagabbro	Petrography, sulfide micro-
					drilling
SL-17-18B	SL23KM09	677.5	677.8	Olivine melagabbro	Whole-rock, sulfide micro-
					drilling, TIMS
SL-17-18B	SL23KM10	669.45	669.75	Feldspathic olivine	Petrography, whole-rock,
				clinopyroxenite	sulfide micro-drilling
SL-17-18B	SL23KM11	665	665.3	Melagabbro	Whole-rock
SL-17-18B	SL23KM12	660	660.35	Melagabbro	Whole-rock
SL-17-18B	SL23KM13	650.2	650.5	Melagabbro	Whole-rock
SL-17-18B	SL23KM14	640.15	640.45	Melagabbro	Whole-rock
SL-17-18B	SL23KM15	630.15	630.45	Melagabbro	Whole-rock
SL-17-18B	SL23KM16	620	620.25	Feldspathic olivine	Petrography, whole-rock,
				clinopyroxenite	EPMA
SL-17-18B	SL23KM17	610	610.35	Peridotite	Whole-rock
SL-17-18B	SL23KM18	600.25	600.55	Olivine melagabbro	Whole-rock
SL-17-18B	SL23KM19	590.00	590.30	Feldspathic olivine	-
				clinopyroxenite	
SL-17-18B	SL23KM20	580	580.3	Gabbro	Whole-rock
SL-17-18B	SL23KM21	570.55	570.80	Oxide gabbro	-
SL-17-18B	SL23KM22	560	560.3	Gabbro	Petrography, whole-rock,
					TIMS
SL-17-18B	SL23KM23	550	550.25	Gabbro	Whole-rock
SL-17-18B	SL23KM24	536	536.28	Oxide gabbro	Whole-rock
SL-17-18B	SL23KM25	515	515.25	Oxide gabbro	Whole-rock
SL-17-18B	SL23KM26	500.05	500.35	Gabbro	Petrography, whole-rock
·					

SL-17-18B	SL23KM27	480.45	480.7	Oxide monzogabbro	Whole-rock
SL-17-18B	SL23KM28	472.20	472.45	Oxide monzogabbro	-
SL-17-18B	SL23KM29	465.45	465.7	Oxide monzogabbro	Whole-rock
SL-17-18B	SL23KM30	447.00	447.30	Monzonite	Petrography
SL-17-18B	SL23KM31	440	440.3	Monzogabbro	Whole-rock, TIMS
SL-17-18B	SL23KM32	427.25	427.55	Monzogabbro	Whole-rock
SL-17-18B	SL23KM33	415	415.3	Monzogabbro	Whole-rock
SL-17-18B	SL23KM34	405.15	405.45	Monzogabbro	Whole-rock
SL-17-18B	SL23KM35	397.5	397.75	Quartz gabbro	Petrography, whole-rock,
SL-17-18B	SL23KM36	395.75	396.00	Quartz monzonito	TIMS
				Quartz monzonite	Petrography Whole-rock
SL-17-18B	SL23KM37	391	391.25	Matrix supported breccia	whole-rock
SL-17-18B	SL23KM38	382.70	383.00	Crackle breccia	-
SL-17-18B	SL23KM39	377.00	377.30	Meta-greywacke	Petrography
SL-19-026	SL23KM40	1444.18	1444.45	Meta-greywacke	Petrography, whole-rock, TIMS
SL-19-026	SL23KM41	1425.3	1425.65	Feldspathic olivine	Petrography, whole-rock,
31-19-020	3LZ3KIVI41	1423.3	1423.03	clinopyroxenite	sulfide micro-drilling
SL-19-026	SL23KM42	1414.6	1414.9	Feldspathic olivine	Petrography, whole-rock,
JL 13 020	JLZJKIVITZ	1414.0	1717.5	clinopyroxenite	sulfide micro-drilling, LA-
				emopyroxemee	ICPMS
SL-19-026	SL23KM43	1406.75	1407	Feldspathic olivine	Petrography, whole-rock,
				clinopyroxenite	sulfide micro-drilling, TIMS
SL-19-026	SL23KM44	1392.00	1392.32	Wehrlite	Petrography, EPMA
SL-19-026	SL23KM45	1384	1384.25	Wehrlite	Petrography, EPMA, whole-
					rock
SL-19-026	SL23KM46	1365.25	1365.55	Peridotite	Whole-rock
SL-19-026	SL23KM47	1350.35	1350.6	Peridotite	Whole-rock
SL-19-026	SL23KM48	1325	1325.3	Wehrlite	Petrography, EPMA, whole-
					rock, TIMS
SL-19-026	SL23KM49	1257	1257.35	Peridotite	Whole-rock
SL-19-026	SL23KM50	1236.1	1236.4	Wehrlite	Petrography, EPMA, whole- rock
SL-19-026	SL23KM51	1200.05	1200.35	Peridotite	Whole-rock, TIMS
					·
SL-19-026	SL23KM52	1180.85	1181.15	Wehrlite	Petrography, whole-rock
SL-19-026	SL23KM53	1160.3	1160.6	Peridotite	Whole-rock
SL-19-026	SL23KM54	1126.25	1126.5	Peridotite	Whole-rock

SL-19-026	SL23KM55	1090	1090.3	Olivine	Petrography, whole-rock
				clinopyroxenite	
SL-19-026	SL23KM56	1040	1040.35	Peridotite	EPMA, whole-rock, TIMS
SL-19-026	SL23KM57	1012.00	1012.25	Peridotite	-
SL-19-026	SL23KM58	980	980.35	Olivine	Petrography, whole-rock
				clinopyroxenite	
SL-19-026	SL23KM59	951.6	951.75	Peridotite	Whole-rock, TIMS
SL-19-026	SL23KM60	895.25	895.6	Olivine	Petrography, EPMA, whole-
				clinopyroxenite	rock, TIMS
SL-19-026	SL23KM61	806	806.35	Melagabbro	Whole-rock
SL-19-026	SL23KM62	755	755.35	Gabbro	Petrography, whole-rock
SL-19-026	SL23KM63	711.00	711.20	Gabbro	-
SL-19-026	SL23KM64	669.00	669.15	Gabbro	-
SL-19-026	SL23KM65	630.35	630.8	Gabbro	Petrography, whole-rock,
					TIMS
SL-19-026	SL23KM66	615.65	616.00	Oxide gabbro	-
SL-19-026	SL23KM67	595.00	595.30	Gabbro	Petrography
SL-19-026	SL23KM68	560.7	561	Oxide gabbro	Whole-rock, TIMS
SL-19-026	SL23KM69	534.00	534.20	Gabbro	Petrography
SL-19-026	SL23KM70	500.88	501.00	Oxide monzogabbro	-
SL-19-026	SL23KM71	450	450.3	Leucogabbro	Petrography, whole-rock,
					TIMS

Appendix two - Petrographic descriptions

Sample ID: SL23KN Drillhole: SL-17-18	-	oth: 718.20 m	Zone: Footwall		Rock type: Meta- greywacke
Mineral	Abundance	Habit	Grain size		Comments
Quartz	40%	Subgranular anhedral	Coarse	forme elonga ha	artz occurs as bands d of anhedral granular ated grains. Boundaries ve suture textures. ndulose extinction.
K-feldspar	30%	Anhedral granular	Fine	sam bands	ns are oriented in the ne way as the quartz . Feldspars are strongly altered to sericite.
Biotite	25%	Subhedral	Fine	or mo chlori	e occur interstitially an iented. Crystals are oderately altered to te. Fine-grained oxides sions are common in biotite.
Oxides	<1%	Subhedral	Very fine	as inclu	occur interstitially and usions in biotite. Traces magnetite and rare longated ilmenite.
Sulfides	5%	Subhedral	Fine	dissem forms aggre rhomb chalce	Py>Ccp>Po grained sulfides occur linated and as blebs. Py sanhedral subgranular egates and subhedral ohedral crystals. Minor opyrite and pyrrhotite Is occur disseminated.

Comments: Sample has as very fine-grained foliated texture with two main phases: quartz bands and the feldspar/biotite groundmass. Sample has an overall moderate alteration. K-feldspars are strongly altered to sericite and biotite has a moderate alteration to chlorite. Sulfides occur disseminated and forming pyrite granular aggregates. Oxides and sulfides occur disseminated.

Sample ID: SL23KM05		Depth	: 690.90 m	Zo	ne: M	Z	Rock type: Feldspathic
Drillhole: SL-17-18B							Olivine
							Clinopyroxenite
Mineral Ab		ındance	Habit	Grain si	ize		Comments

Clinopyroxene	40%	Anhedral to subhedral	Fine to medium	Crystals show a granular texture. They have weak alteration to chlorite to no alteration. Twinning is common.
Olivine	15%	Anhedral	Fine to medium	Crystals are highly fractured. Moderate alteration to serpentine and talc. Rare oxide rim is formed at grains.
Plagioclase	15%	Anhedral	Fine	Plagioclases are moderately to strongly altered to chlorite, sericite, calcite and actinolite. Crystals occur interstitially.
Biotite	5%	Anhedral	Fine	Crystals occur interstitially. Forms anhedral aggregates which are often related to hornblende.
Amphibole	8%	Subhedral	Fine	Occurs as an interstitial phase and frequently found at oxides boundaries.
Oxides	3%	Subhedral	Fine to very fine	Mag>Ilm Oxides occur as anhedral grains and as lath-like crystals of magnetite with ilmenite sandwich exsolution. They frequently occur as alteration patches.
Pyrrhotite	<7%	Anhedral	Medium to fine	Occurs interstitially with chalcopyrite and granular pentlandite. It has very weak pentlandite exsolution flames
Chalcopyrite	<5%	Anhedral	Medium to fine	Occurs Interstitially. Some grains have weak cubanite exsolution and are closely related to pyrrhotite and pyrite
Pentlandite	<2%	Anhedral	Fine	Granular pentlandite occurs at the sulfide boundaries and occur embedded in chalcopyrite.

Comments: Sample has a granular-subpoikilitic texture. Strong altered patches of chlorite, sericite, talc, actinolite and calcite often occur interstitially. Oxides occur disseminated preferentially in the alteration patches and in fine sized crystals. Sulfides occur interstitially (Po>Ccp>Pn), pyrrhotite and chalcopyrite form irregular granular texture and pentlandite occurs as an interphase between Ccp and Po.

Sample ID: SL23KN Drillhole: SL-17-18		h: 686.29 m	Zone: M	Z Rock type: Wehrlite	
Mineral	Abundance	Habit	Grain size		Comments
Clinopyroxene	25%	Subhedral	Medium to coarse	Crystals occur interstitially and often enclosing olivine. Weakly altered to biotite, actinolite and chlorite. Crystals often have twinning	
Olivine	35 %	Subhedral to euhedral	Medium	co serper gr	ne are equant and are impletely altered to atine and talc. Very fineained hematite and etite occur from olivine.
Biotite	5%	Subhedral	Fine		interstitially and closely lated to amphibole
Amphibole	10%	Anhedral	Fine to medium	Amphibole occurs interstitially and frequently related to oxides at the crystal boundaries.	
Oxides	1%	Subhedral to anhedral	Fine	skele with Ilmenit fine need	Ilm>Mag. les occur as blebs and etal magnetite crystals ilmenite exsolutions. te occurs as fine- to very e-grained as lath- and ile-like crystals. Oxides at sulfide boundaries.
Pyrrhotite	15%	Anhedral	Fine to coarse	surrou occi irreg cleav lan exsolu	rrhotite is commonly inded by chalcopyrite. It urs as blebby-like and ular aggregates. Weak vage is present. Po has nellae and chain-like tions of pentlandite and lae troilite exsolutions.
Chalcopyrite	<10%	Anhedral	Fine to medium	Chalcopyrite occurs partially enclosing Po at the exterior of the sulfide blebs. Chalcopyrite is found interstitially.	
Pentlandite	<1%	Anhedral	Fine	Pei	ntlandite occurs as a lar interphase between Po and Ccp.

Comments: Sample has a granular-subpoikilitic texture. Sample is moderately altered to serpentine, talc, chlorite, actinolite and biotite. Oxides occur related to olivine but are also interstitially disseminated. Sulfide occurs interstitially as aggregates are disseminated but a 1 cm

sulfide bleb was present. Pyrrhotite usually forms the core of sulfides, followed by pentlandite and chalcopyrite at the rims.

Sample ID: SL23KM		n: 678.50 m	Zone: MZ	, · · · · · · · · · · · · · · · · · · ·	
Drillhole: SL-17-18I	3			Melagabbro	
Mineral	Abundance	Habit	Grain size		Comments
Clinopyroxene	<30%	Subhedral	Coarse to fine	Crysta	Is comprise a cumulate
		to		phase.	Clinopyroxenes are very
		euhedral		weakly	to unaltered. Decrease
				of gra	insize is visible towards
					he sulfide veinlet.
Plagioclase	<20%	Anhedral	Medium to fine	_	clase occurs interstitially
				fori	ming a subpoikilitical
				tex	ture. It is strongly to
				compl	etely altered to sericite
					and calcite.
Olivine	<5%	anhedral	Medium	Diss	seminated olivine are
				со	mpletely altered to
					serpentine
Biotite	<1%	Anhedral	Fine	Occ	urs interstitially often
				relate	d to sulfides and oxides
Amphibole	10%	Euhedral	Medium	Hornblende crystals are weakly	
				alter	ed to chlorite and is a
					cumulate phase.
Oxides	<10%	Subhedral	Fine	Magne	etite occurs interstitially
				and o	ften as skeletal crystals
				wit	th common ilmenite
				sand	wich-like exsolutions.
				The	y are often related to
					sulfides.
Pyrrhotite	20%	Anhedral	Medium to	Pyrrho	tite occurs as a vein-like
		Vein-like	coarse	struc	ture with chalcopyrite
				being	the outermost phase of
				the st	ructure. Pyrrhotite has
				pe	ntlandite exsolution
				occurr	ing as flames and chain-
				like g	rains. Troilite lamellae
				exsc	olutions are common.
Chalcopyrite	<10%	Anhedral	Fine to medium	0	ccurs mostly at the
				outern	nost part of the vein-like
				stru	cture. Ccp also occurs
				interst	itially disseminated and
				ass	ociated with oxides.

Pentlandite	2%	Anhedral	Fine	Occur disseminated as part of
				sulfide blebs with Po and/or
				Сср.

Comments: The sample has a subpoikilitical to phaneritic texture. Alteration occurs as a sericite-chlorite assemblage on plagioclase and serpentine in olivine. A 10 mm veinlet-like structure occurs towards the center of the sample, it has diffuse boundaries with a gradual increase of silicates the boundaries. At the left of the vein, euhedral hornblende crystals are common. At the right, coarse grained clinopyroxenes are the dominant mineral.

Sample ID: SL23KN Drillhole: SL-17-18	•	n: 669.45 m	Zone: MZ		Rock type: Feldspathic Olivine Clinopyroxenite
Mineral	Abundance	Habit	Grain size		Comments
Clinopyroxene	25%	Granular	Medium to fine	Clinop	yroxenes are weakly to
		anhedral		со	mpletely altered to
				actino	lite, calcite and biotite.
				So	me 5 mm actinolite
				alterat	ion patches occur in the
				samp	ole. Twinning occurs in
					some crystals.
Plagioclase	20%	Subhedral	Coarse to	_	clase occurs interstitially
		to	medium		oikocrystals. Pl has a
		anhedral			dral tabular habit with
					eletal structure. It is
					ately altered to chlorite
				and	sericite mostly at the
					crystal core.
Olivine	20%	Subhedral	Fine		rs disseminated and as
					acrystals in plagioclase
					nopyroxene. Olivines are
					y fractured and occur
					alteration to talc and
					onates, weak oxidation
				occui	rs mainly at the crystal
					rims.
Amphibole	2%	Anhedral	Fine		boles occur interstitially
				1	osely related to oxides.
Oxides	3%	Subhedral	Fine	_	netite-ilmenite crystals
					disseminated. Blebby
					d skeletal crystals of
				1	gnetite with ilmenite
					ution. Isolated needle-
					l lath- like crystals of
				ilmer	nite occur interstitially.

Pyrrhotite	10%	Anhedral	Medium to fine	Pyrrhotite is commonly
				enclosed by Ccp. Po frequently
				has silicate vein-like structures
				with Ccp at the boundaries of
				these fractures. Po has chain-
				like and lamellae pentlandite
				exsolutions.
Chalcopyrite	<20%	Anhedral	Coarse to fine	Ccp encloses silicate minerals.
				Ccp commonly has cubanite
				exsolutions and also encloses
				pentlandite grains.
Pentlandite	3%	Anhedral	Fine	Pentlandite occurs isolated
				enclosed in Ccp and frequently
				occurs as an interphase
				between Ccp and Po

Comments: Sample has a poikilitic texture. Sericite alteration occurs in plagioclase whereas patches of actinolite-calcite-chlorite alteration occur in clinopyroxenes and different levels of this alterations occurs along the thin section. Sulfide has a blebby texture with suture textures at the boundaries of sulfides.

Sample ID: SL23KM Drillhole: SL-17-18		Depth	: 620.00 m	Zone: UL	ΙZ	Rock type: Felspathic Olivine Clinopyroxenite	
Mineral	Ab	undance	Habit	Grain size		Comments	
Clinopyroxene		45%	Anhedral to subhedral	Fine		ar twinned crystals with alteration to actinolite and biotite.	
Plagioclase		<25%	Anhedral	Fine	int subpo are s	Plagioclase crystals occur interstitially forming a subpoikilitical texture. They are strongly to completely altered to sericite and calcite	
Olivine		<20%	Subhedral to euhedral	Fine	frac Inclusio	Olivines are moderately fractured with Cr-spinel Inclusions. Moderate to strong alteration occurs forming talcand oxide rims.	
Biotite		<3%	Subhedral	Very fine	Occurs interstitially and as product of Cpx alteration and closely related to oxides and sulfides		
Amphibole		5%	Anhedral	Fine	Amphiboles occur interstitially and moderately altered to actinolite		

Oxides	5%	Anhedral	Fine to very fine	Occurs as an interstitial phase.
		to		Magnetite occurs as embayed
		euhedral		blebs and euhedral crystals.
				Magnetite has ilmenite
				exsolution. Cr-Spinel euhedral
				crystals occur disseminated
				but also often in olivine as
				inclusions.
Sulfides	2%	Anhedral	Fine	Po>Ccp
				Sulfides occur interstitially and
				finely disseminated in the
				sample. Pyrrhotite rarely
				occurs as inclusions in oxides.

Comments: Sample has a poikilitic texture. Alteration occurs mainly in the interstitial phase as chlorite-actinolite-calcite-epidote and talc in olivine crystals, other alteration to biotite and actinolite occurs in Cpx and amphibole. Sulfides and oxides are equally distributed in the sample. Oxides occur as inclusions in olivine crystals and sulfides often occur as inclusions at the borders of the crystals.

Sample ID: SL23KN Drillhole: SL-17-18	-	th: 590.00 m	Zone: LG	S	Rock type: Felspathic Olivine Clinopyroxenite
Mineral	Abundance	e Habit	Grain size		Comments
Clinopyroxene	30%	Subhedral to euhedral	Fine to medium	Crystals have variable size. Twinning is common and the commonly have embayed textures. Weak alteration to amphiboles occurs. In the leucocratic dykelet, Cpx are anhedral, fine-grained and with moderate chlorite and	
Plagioclase	15%	Subhedral to anhedral	Medium to coarse	Crysta coars with ser Plag leuco equ crystal seri	epidote alteration. als occur as medium- to be-grained oikocrystals moderate alteration to icite and serpentine. ioclase crystals in the ocratic dykelet occur as ant medium- grained is moderately altered to cite, chlorite, calcite.
Olivine	20%	Subhedral	Fine to medium	talc comm	is completely altered to and serpentine. They only have Cr-spinel and agnetite inclusions.

	1	1		1
Amphibole	5-10%	Anhedral	Fine	Occur as an alteration from Cpx but it also occurs disseminated in the sample weakly altered to chlorite. In the leucocratic dykelet amphiboles are mainly subhedral needle-like fine
				grained crystals.
Quartz	0-5%	Anhedral	Fine	Only found in the leucocratic dykelet. It occurs as interstitial fine-grained crystals.
K feldspar	0-60%	Subhedral	Medium	Anhedral to subhedral crystals moderately altered to sericite occur in the leucocratic dykelet.
Oxides	5%	Subhedral to anhedral	Fine	Blebby to suhedral magnetite crystals with ilmenite exsolutions. Often related to hornblende. They occur with sandwich-like exsolution or usually the core are ilmenite crystals. Oxides in the leucocratic dykelet occur interstitially and often as needle/lath-like ilmenite crystals are common.
Chalcopyrite	<1%	Anhedral	Very fine	Traces of anhedral disseminated cpy occur in the rock.

Comments: The sample occurs a poikilitic texture with a K-feldspar bearing (leucocratic) dykelet 1cm thick. Alteration of the groundmass is moderate with chlorite-serpentine-hornblende-sericite-calcite alteration. The veinlet occurs a felsic composition as K-feldspars and quartz. Oxides occur in the groundmass as Mag-Ilm while the leucocratic veinlet has only fine needle-like ilmenite.

Sample ID: SL23KN	122 De	pth: 560.00 m		Zone: GZ		Rock type: Gabbro
Drillhole: SL-17-18	3B					
Mineral	Abundan	ce Habit	Gro	ain size	Comments	
Clinopyroxene	30%	Subhedral	Co	arse to	Cpx have moderate to strongly	
			me	edium	alteration to chlorite	
					spheru	les, epidote, calcite and
						hornblende.

Plagioclase	<65%	Subhedral	Coarse to medium	Crystals are strongly to completely altered to sericite and calcite.
Biotite	1%	Anhedral	Fine	Disseminated interstitial biotite occurs in the sample
Oxides	5%	Blebby- like and anhedral	Fine	Oxides occur as blebby to interstitial anhedral magnetite with ilmenite exsolution. Oxides frequently occur as inclusions in Cpx and olivines.
Sulfides	1%	Anhedral	Fine	Anhedral interstitial Ccp>Po occur disseminated and rarely seen together.

Comments: Sample has a phaneritic texture. Strong to moderate alteration of sericite-chlorite-epidote-calcite. Plagioclase occur moderate disseminated cryptocrystalline hematite with pinkish patches visible in hand sample. Oxides occur as anhedral fine-grained blebby oxides. Weakly disseminated Ccp>Po occur.

Sample ID: SL23KN	126 Depth	n: 500.05 m	Zone: Gz	7_	Rock type: Quartz
Drillhole: SL-17-18	BB			Gabbro	
Mineral	Abundance	Habit	Grain size		Comments
Clinopyroxene	5%	Anhedral	Fine to medium	Срх	is strongly altered to
				chlori	te, calcite and epidote.
Plagioclase	50%	Subhedral	Medium		gioclase crystals are
				_	ly to moderately altered
					cite, chlorite and calcite.
				Crysta	Is have oxide inclusions
				at t	he outermost part of
					s forming a pinkish band
				that a	are more easily seen in
					hand sample.
Apatite	7%	Euhedral	Fine	Disseminated apatite have an	
				elongated hexagonal shape.	
K-feldspar	2%	Anhedral	Fine	Poss	sibly sanidine? and K-
				feldspar with graphic textures.	
Amphibole	20%	Subhedral	Fine to medium	Occur	s completely chloritized
				w	ith frequent strong
				n	nagnetite-ilmenite
				replacement occurring as	
				worm-like blebs.	
Quartz	<10%	Anhedral	Fine	Occur interstitially with	
				en	nbayed borders and
				undulose extinction	
Oxides	10%	Anhedral	Fine	Very fine-grained magnetite	
				occur	s in the sample. Mostly

				occur as inclusions or altering amphiboles. Crystals have skeletal and worm-like textures
Sulfides	<1%	Anhedral	Very fine	Traces of disseminated ccp>py occur interstitially in the
				sample

Comments: Sample has a subphaneritic texture. Shows strong sericite-calcite-epidote-chlorite altered patches. Oxides are mainly replacing strongly altered amphiboles. Forming blebs and worm-like textures. Traces of Cpp> occur disseminated in the sample

Sample ID: SL23KM		th: 447.00 m	Zone: Gz	<u>'</u>	Rock type: Quartz	
Drillhole: SL-17-18		1		I	Monzonite	
Mineral	Abundance		Grain size		Comments	
Quartz	10%	Anhedral	Fine	pha	Quartz occurs as an interstitial phase. Crystals have an undulose extinction	
Plagioclase	40%	Subhedral to euhedral	Coarse to fine grained	Plagioclase crystals occur in two grainsize populations: Firstly, as coarse-grained crystals in a cumulate texture, these are moderately altered to sericite, calcite and chlorite, with microcrystalline disseminated hematite. Secondly, as an intercumulus phase, they are fine-grained crystals and are strongly altered to chlorite and sericite.		
K-feldspar	25%	Anhedral to subhedral	Fine	with they of texture with the are	crystals occur associated the second phase of Pl. commonly have graphic es, are strongly oxidized nematite inclusions and moderately altered to sericite.	
Amphibole	20%	Subhedral to anhedral	Fine to medium	compl sphe crypto	rs as elongated crystals etely altered to chlorite rules and fine-grained calcite. Hematite crystalline inclusions are mon in these crystals.	
Oxides	5%	Anhedral to euhedral	Very fine to medium	fine- subhe	es occur as very fine- to grained anhedral and dral magnetite crystals. edle-like fine grained	

				ilmenite occurs disseminated
				in the sample.
Sulfides	<1%	Anhedral	Fine to very fine	Sulfides occur finely
				disseminated as traces of
				ру>ро

Comments: Sample has a glomero-porphyritic to porphyritic texture of plagioclases and amphiboles. Sample occur two different phases. The first occurs as glomerates of coarse-grained plagioclase and amphiboles cumulates, with interstitial fine-grained plagioclases + K-feldspars. This first cumulate phase has moderate alteration to chlorite, sericite and calcite with moderate oxidation disseminated in plagioclases. The second residual phase of fine-grained plagioclases + quartz + K-felspars occurs strongly altered with strong hematite oxidation. In hand sample this last phase shows pinkish oxides patches.

Sample ID: SL23KN Drillhole: SL-17-18	<u> </u>	h: 397.50 m	Zone: G	Z	Rock type: Quartz Gabbro
Mineral	Abundance	Habit	Grain size		Comments
Quartz	10%	Anhedral	Fine	inters	uartz crystals occur titially. Crystals have an ndulose extinction.
Plagioclase	<55%	Subhedral to anhedral	Coarse to fine	undulose extinction. Plagioclase crystals occur in two manners. The first is as coarse-grained plagioclases with a porphyritic texture, these are moderately to strongly altered to sericite, chlorite and calcite, rare microcrystalline disseminated hematite. The second phase occurs interstitially as finegrained plagioclase crystals associated with quartz and K-felspars, this phase has strongly altered PI to chlorite and sericite and has microcrystalline hematite inclusions.	
K-feldspar	5%	Anhedral	Very fine	These crystals are highly altered to sericite and occur a subgraphic texture. K-feldspars occur in the second phase along with fine grained plagioclases.	
Amphibole	25%	Subhedral	Medium	altere	hiboles are completely ed to chlorite with blue ingence color. Medium

				grained cubic magnetite crystals commonly occur in
				these crystals.
Oxides	<10%	Subhedral	Fine to medium	Cubic skeletal magnetite
				medium grained crystals are
				altered. Common subhedral
				octahedral and cubic
				magnetite crystals with
				ilmenite sandwich and trigonal
				exsolutions occurs as
				inclusions in amphiboles.
				Other magnetite subhedral
				and ilmenite needle-like
				crystals occur disseminated in
				the sample.
Sulfides	<1%	Anhedral	Very fine	Ccp <pn<po< td=""></pn<po<>
				Sulfides occur finely
				disseminated in the sample as
				isolated grains.

Comments: Sample has a porphyritic-glomeroporphyric texture of plagioclase and amphibole.

Phenocrysts occur moderate alteration to sericite-chlorite-calcite, hematite inclusions occur in Pl.

The matrix is characterized by fine-grained Pl, quartz and K-felspars, matrix has disseminated microcrystalline hematite.

Sample ID: SL23KM Drillhole: SL-17-18	-	n: 395.75 m	Zone: GZ	Rock type: Quartz Monzonite	
Mineral	Abundance	Habit	Grain size		Comments
	Breccia fr	agments (Qu	etico Mtsd; 40% of	sample)	
Quartz	<80%	Anhedral Granular	Fine to medium	Quartz occurs as elongated granular crystals with weak foliation and variable grainsizes. Undulose extinction. Sulfides inclusions	
Biotite	15%	Anhedral elongated	Fine to medium	to chlo	are rare. s are completely altered rite spherules. It is hard fine what chlorite has altered
Sulfides	<5%	Anhedral	Very fine to fine	di	ne to fine disseminated Py>Ccp usually as sseminated crystals
	IV	lagmatic mat	rix (60% of sample)	
Plagioclase	30%	Subhedral	Medium to fine	textu	oclases form a seriate re. Pl occurs as needle- id tabular crystals. They

				are moderately altered to sericite. Strong hematization occur as microcrystalline minerals
K-feldspars	35%	Subhedral	Medium to fine	Tabular and radial textured minerals moderately altered to sericite
Quartz	5%	Anhedral	Fine	Crystals occur interstitially, granular and with undulous extinction
Amphibole	30	Subhedral	Medium to fine	Crystals are completely altered to chlorite and calcite. Magnetite is common in this mineral
Oxide	2%	Subhedral to anhedral	Fine to medium	Magnetite with sandwich-like and ilmenite lamellae exsolution are common. Magnetite-ilmenite and needle-like ilmenite crystals occur disseminated in the sample
Sulfides	3%	Anhedral	Fine	Ccp>Py is disseminated.

Comments: Sample occur a brecciated texture. Fragments are rounded Quetico meta-greywacke. Fragments are moderately altered and have an alteration halo characterized to have an altered amphibole reaction halo, these fragments have weak disseminated pyrrhotite and chalcopyrite. The matrix has an intermediate composition and a phaneritic texture. Alteration is moderate defined by sericitization in plagioclase and completely altered amphibole. Strong hematization occur as cryptocrystalline to microcrystalline disseminated hematite. Sulfides occur as weak disseminated chalcopyrite and pyrite.

Sample ID: SL23KM	139	Depth: 377.00 m		Zone: Hangin	gwall Rock type: Meta-		
Drillhole: SL-17-18	3B					greywacke	
Mineral	Ab	undance	Habit	Grain size		Comments	
Quartz	3	0-40%	Anhedral	Medium to fine	Cry	stals have a granular	
			granular		texture	e, crystals show foliation	
					and a	n undulose extinction.	
K-feldspar	3	0-35%	Anhedral	Fine to medium	Crystals	s are moderately altered	
			granular		to se	ricite. They occur with	
					mode	rate to strong oxidation	
					with m	icrocrystalline hematite.	
Biotite		10%	Anhedral	Fine	Crystal	s occur interstitially and	
					comp	completely chloritized with	
					relat	ed magnetite crystals	
Amphibole		15%	Subhedral	Fine to medium	Tabulai	r crystals are completely	
					altered	d to chlorite and calcite.	

				They become more frequent at
				the boundaries of the blocky
				textured breccia.
Oxides	1%	Anhedral	Very fine to fine	Magnetite crystals with
		to		ilmenite trigonal exsolution
		subhedral		crystals occur disseminated
				and associated with sulfides.
				Other single ilmenite crystals
				also occur in the sample.
Sulfides	2-10%	Anhedral	Medium to fine	Ccp>Pn>Po
				Sulfides occur disseminated in
				the sample but they form a
				highly disseminated to a
				veinlet-like structure at the
				boundaries of the blocky-like
				texture.

Comments: Sample is a breccia with a blocky texture. Fragments have alteration haloes, with oxidation at the fragment borders and at the contact. Sulfides occur at the fragment contacts.

Sample ID: SL23KN	140 Dep	th: 1444.18m	Zone: Foots	wall	Rock type: Meta-
Drillhole: SL-19-02	26				greywacke
Mineral	Abundance	Habit	Grain size		Comments
Quartz	40%	Granular,	Medium to very	Cryst	als have variable grain
		anhedral	fine	sizes. T	hey have anhedral habit
				а	nd suture borders.
K-Feldspar	35%	Anhedral	Fine grained	Moder	ate alteration to sericite
					and calcite.
Biotite	23%	Subhedral	Fine grained	Interstitial with very weak	
					oxidation.
Sulfides	2%	Various	Fine to very fine		Py>Po>Ccp
				Pyrite	grains are subhedral to
				а	nhedral and occur
				inte	rstitially, pyrrhotite is
				sul	phedral to anhedral,
				anhe	edral chalcopyrite. Po
				cor	nmonly encloses Py.
Comments: San	nple is fine g	ained. It is wea	kly to moderately a	altered to	sericite and calcite.

Sample ID: SL23KM41 Depth		Depth: 1425.30m		Zone: MZ		Rock type:	
Drillhole: SL-19-026							Feldspathic Olivine
							Clinopyroxenite
Mineral	Ab	undance	Habit		Grain size		Comments
Clinopyroxene		35%	Anhedral to	F	ine to medium	Twinni	ng common. Moderate
			subhedral			altera	ntion occurs as fine- to
						mediu	ım-grained amphibole,

				very fine-grained sericite and patches of actinolite, epidote
				and calcite.
Plagioclase	15%	Subhedral	Medium to	Occurs interstitially and as
			coarse	oikocrysts, moderate to
				strong alteration to sericite.
Olivine	10%	Subhedral	Medium	Crystals are strongly to
				completely altered to talc and
				frequently have oxide rims.
Biotite	2%	Subhedral	Very fine	Occurs interstitially.
Amphibole	5-10%	Subhedral	Fine	Fractured crystals occur
				embayed texture.
Oxides	1%	Lath-like,	Fine	Ilm>Mag.
		anhedral,		Magnetite occurs as anhedral
		minor blebs		interstitial grains with
				ilmenite exsolution. Ilmenite
				occurs as tabular needle-like
				crystals disseminated.
Pyrrhotite	~10%	Anhedral,	Medium	Pyrrhotite has weak
		semi		exsolutions to pentlandite in
		massive		weakness planes. Pn
				commonly occurs as an
				interface with Po and Ccp.
Chalcopyrite	~5%	Anhedral	Medium	Ccp has anhedral sphalerite
				inclusions. It occurs cubanite
				exsolution lamellae.
Pentlandite	~2%	Anhedral to	Fine	Mostly occur as an interface
		subhedral		between pyrrhotite and
				chalcopyrite.

Comments: Sample has a poikilitic texture with semi-massive, disseminated interstitial and blebby Sulfides. Moderately altered, sericite-calcite-actinolite alteration occurs in patches. Sulfides are semi massive and occurs as pyrrhotite at the core of sulfide blebs.

Sample ID: SL23KN	Sample ID: SL23KM42 Dept		Depth: 1414.60m		Zone: MZ		Rock type: Felspathic
Drillhole: SL-19-0	26						Olivine
							Clinopyroxenite
Mineral	Αbι	ındance	Habit		Grain size		Comments
Olivine		20%	Rounded	١	Medium to fine	Oliv	ine are chadacrystals
			subhedral			embe	dded in clinopyroxene.
						Olivir	ne has fine-grained Cr-
						!	spinel inclusions.
Clinopyroxene		40%	Subhedral,	١	Medium to fine	Срх а	re weakly to moderate
			subpoikilitic			alte	red at fractures and
						cleavag	ge planes. Weak sericite
						an	d calcite alteration.

Plagioclase	15%	Subhedral interstitial	Medium	Occurs weakly to moderately altered to sericite.
Hornblende	15%	Anhedral to subhedral	Medium to fine	Closely related to fine biotite crystals at the borders of biotite.
Oxides	1%	Lath-like, blebby, interstitial	Fine to very fine	Ilmenite>magnetite crystals occur disseminated in the rock and related to sulfides, these oxides have skeletal-caries texture.
Sulfides	<10%	Anhedral, blebby		Ccp>Po>Pn>Py Ccp is anhedral with annealing-like borders and oxides often included. Po is embedded in Ccp and common Ccp vein-like structures in Po. Po has weak exsolusion Pn flames. Fine grained aggregates in sulfides.

Comments: Seriate granular texture with interstitial disseminated and blebby sulfides. Lath-like oxides are only in the groundmass while only anhedral oxides are in sulfides. Ccp quickly tarnishes to blue-pink-brown colors.

Sample ID: SL23KM Drillhole: SL-19-02	•	th: 1406.75m	Zone: M	1Z	Rock type: Felspathic Olivine Clinopyroxenite
Mineral	Abundance	Habit	Grain size		Comments
Clinopyroxene	50%	Subhedral	Coarse to	Fract	ured crystals with low
		to anhedral	medium	fine	-grained hornblende
				cl	nadacrystals. Weak
				alte	eration to actinolite.
Plagioclase	20%	Anhedral	Coarse to	Strong	ly to completely altered
			medium	to	sericite, calcite and
				chlori	te. Alteration occurs as
				radia	Il actinolite spherules.
Olivine	10%	Anhedral	Medium		stals are completely
				alter	ed to talc and calcite.
Amphiboles	<10%	Subhedral	Fine	Cryst	als are associated with
				oxide	s and biotite occurring
				at	the borders. Occurs
					interstitially.
Oxides	2%	Subhedral	Fine	Mag	netite-ilmenite occur
		blebs		with	blebby and embayed
				textu	res. Ilmenite elongated
				round	ed crystals are common

				and include fine-grained silicates inclusions.
Sulfides	<10%	Interstitially, blebs, Anhedral	Coarse to fine	Ccp>>Py Chalcopyrite occurs as an interstitial phase with silicates, it has cubanite exsolution lamellae. Ccp replaces plagioclase. Pyrrhotite occur fully enclosed by Ccp crystals

Comments: Granular subpoikiitic texture medium to coarse grained. Moderately altered to sericite, calcite, talc. Sulfides and oxides have granular, prismatic and blebby-like textures.

Sample ID: SL23KM Drillhole: SL-19-02	-	n: 1392.00m	Zone: LU	Z Rock type: Wehrlit	
Mineral	Abundance	Habit	Grain size		Comments
Olivine	40%	Subhedral	Medium to fine	Mo	derately to strongly
				serper	ntinized, often occurs as
				chadac	crystals in clinopyroxene
					oikocrystals.
Clinopyroxene	30%	Anhedral	Medium	Cpx h	ave a poikilitic texture,
		to		th	ney are moderately
		subhedral			serpentinized.
Plagioclase	5%	Anhedral	Medium	Occurs as oikocrystals. Strongly	
				altered to sericite.	
Amphibole	10%	Anhedral	Fine	Related to very fine-grained	
					and opaque minerals at
					orders of the crystals.
Hematite	10%	Anhedral	Medium	Occurs	as oriented dark brown
				S	tringer structures.
Oxides	5%	Anhedral	Fine		Mag>Ilm
				Magne	etite has worm-like and
				intersti	tial texture. Some occur
					ded in olivine crystals.
				Oxides form subhedral	
				round	ed blebs and annealing
					texture?

Comments: Granular subpoikilitic texture. Strongly to moderate serpentinization. Moderate to strong serpentinization occurs a trend also marked by the hematite stringers.

Sample ID: SL23KM45 Dep		Depth	Depth: 1384.00m		<u>Z</u>	Rock type: Wehrlite
Drillhole: SL-19-02	26					
Mineral	Ab	undance	Habit	Grain size	Comments	
Olivine		40%	Subhedral	Medium to fine	Roun	ided crystals with very
					we	eak serpentinization

				occurring as chadacrystals
				enclosed by clinopyroxenes
				oikocrysts.
Clinopyroxene	45%	Anhedral	Medium to	Cpx occurs as medium to
		and	coarse	coarse grained oikocrysts. Cpx
		subhedral		have. Has finely disseminated
				magnetite crystals.
Plagioclase	<10%	Anhedral	Fine	Interstitial isolated crystals,
				moderately altered to sericite
				and chlorite.
Biotite	2%	Subhedral	Fine	Occurs disseminated related to
				amphibole crystals.
Hornblende	2%	Anhedral	Fine	Occurs disseminated and
				interstitially.
Oxides	2%	Subhedral	Fine	Magnetite and Cr-spinel
				inclusions occur in olivines and
				clinopyroxenes.
Sulfides	<1%	Anhedral	Fine	Ccp>Po>Py
				Sulfides occur interstitially and
				as very fine-grained blebs.

Comments: Sample has poikilitic and seriate texture with weak serpentinization on clinopyroxene and olivine borders. Weak miarolitic texture. Cr-spinel and magnetite inclusions in Cpx and Ol.

Sample ID: SL23KM Drillhole: SL-19-02		n: 1325.00m	Zone: LU	Z Rock type: Wehrlite	
Mineral	Abundance	Habit	Grain size		Comments
Olivine	<35%	Subhedral rounded	Fine to medium	with fr	occurs as chadacrystals requent magnetite and r-spinel inclusions.
Clinopyroxene	45%	Anhedral to euhedral	Coarse to fine	medi	rals occur as anhedral um to coarse grained ysts. Weakly altered to chlorite
Plagioclase	10%	Anhedral	Coarse to medium		curs as oikocrystals ately altered to chlorite and sericite
Biotite	<5%	Anhedral	Fine		rs interstitially, closely d to sulfides and oxides
Hornblende	<5%	Anhedral	Fine		urs interstitially often d to oxides and sulfides
Oxides	<5%	Euhedral to anhedral	Very fine	Cr-spinel inclusions mostly occur disseminated interstitially and as inclusions in silicates.	
Sulfides	1%	Anhedral	Fine	Interst	titial fine blebs Ccp>Po

Comments: Sample has poikilitic and seriate texture with weak serpentinization on clinopyroxene and olivine borders. Cr-spinel and magnetite inclusions in Cpx and Ol.

Drillhole: SL-19-026	0 Depth	: 1236.10m	Zone: LU	Z Rock type: Wehrli	
Drillinole: 3L-19-026					
Mineral	Abundance	Habit	Grain size		Comments
Olivine	45%	Subhedral	Fine to medium	Frequ	uent oxides inclusions.
		to		Occur a	as oikocrysts. Very weak
		euhedral			serpentinization.
Clinopyroxene	35%	Subhedral	Medium to fine	Seriate	texture occurring both
				as m	edium-coarse grained
				oikocr	ystals and fine-medium
				grain	ed chadacrystals with
				(oxides inclusions.
Plagioclase	5%	Anhedral	Medium to fine	Occurs as oikocrysts,	
		poikilitic		moderately altered to chlorite	
					and sericite.
Biotite +	<5%	Anhedral	Fine	These o	crystals commonly occur
Hornblende		to		toge	ther, interstitially and
		subhedral		ass	ociated with oxides.
Oxides	<10%	Subhedral	Fine	Cr-spii	nel occurs as inclusions
		rounded		in silic	ates and interstitially in
					oikocrystals.
				Mino	or ilmenite-magnetite
				occui	only interstitially and
				ofte	n related to sulfides.
Sulfides	<1%	Anhedral	Very fine	Inte	erstitial fine-grained
				chal	copyrite occurs in the
					sample.

Comments: Poikilitic texture with very weak serpentine alteration in pyroxenes and olivine. Weak sericite alteration of plagioclase.

Sample ID: SL23KM		Depth	: 1180.85m	Zone: LU	Z	Rock type: Wehrlite
Drillhole: SL-19-02	26					
Mineral	Ab	undance	Habit	Grain size		Comments
Olivine		<50%	Subhedral	Medium to fine	C	Crystals have weak
					serpen	tinization and embayed
						texture.
Clinopyroxene		35%	Subhedral	Medium to fine	Twinin	g in some crystals. Very
			to		weak	serpentinization. Weak
			anhedral		corrosion texture	
Plagioclase		5%	Anhedral	Medium to fine	Occurs as oikocrystals,	
					moderately altered to clay-	
						sericite

Biotite +	5%	Anhedral	Fine	Occur together and frequently
horblende		interstitial		related to oxides and sulfides
Oxides	<1%	Anhedral,	Fine	Ilm>Mag
		elongated		Occurring as inclusions in
		blebs		silicates and as well
				interstitially
Sulfides	<10%	Anhedral	Medium to fine	Ccp>Po>Py
		blebs		Occurs as an interstitial phase

Comments: Sample has a poikiliic texture, weak serpentinization in olivines and pyroxenes. Weak to moderate alteration of plagioclases. Miarolitic texture is common.

55 Depth	: 1090.00m	Zone: UU	Z Rock type: Olivine	
6				Clinopyroxenite
Abundance	Habit	Grain size		Comments
35%	Subhedral	Very fine to fine	Very	weak serpentinization
			with gr	anular textures. Crystals
			ar	e weekly altered to
				serpentine.
65%	Subhedral	Fine to very fine	Crystals are commonly	
	granular		twinned and rounded. Crystals	
			are v	weekly serpentinized.
<1%	Anhedral	Very fine	Very f	inely disseminated and
			О	ccurs interstitially.
-	Subhedral	Very fine	Traces of Cr-spinel occurs as	
			inclusions in olivine and traces	
			of magnetite-ilmenite occur	
				interstitially.
	Abundance 35% 65%	Abundance Habit 35% Subhedral 65% Subhedral granular <1% Anhedral	Abundance Habit Grain size 35% Subhedral Very fine to fine 65% Subhedral granular <1% Anhedral Very fine	Abundance Habit Grain size 35% Subhedral Very fine to fine Very with granular 65% Subhedral Fine to very fine Cry twinned are very fine <1% Anhedral Very fine Very fine - Subhedral Very fine Trace inclusion

Comments: Seriate fine to very fine-grained texture. Very weak serpentinization of olivine and clinopyroxenes.

Sample ID: SL23KN	158	Depth	n: 980.00m	Zone: UU	Z	Rock type: Olivine	
Drillhole: SL-19-02	26					Clinopyroxenite	
Mineral	Ab	undance	Habit	Grain size		Comments	
Olivine		<35%	Subhedral	Medium to fine	Com	mon oxide inclusions.	
Clinopyroxene		60%	Subhedral	Medium to fine	Gran	ular twinned rounded	
						crystals.	
Plagioclase		1%	Anhedral	Fine	Occur	interstitially forming a	
					subpoi	kilitic texture. Moderate	
					to stro	ongly altered to sericite	
						and chlorite.	
Biotite +		1%	Anhedral	Fine	Ver	finely disseminated	
Hornblende			interstitial		interst	interstitially related to oxides.	
Oxides		1%	Euhedral	Fine	Cr-sp	Cr-spinel/magnetite? occur	
			to		interst	itially and as inclusions	
			anhedral		in sil	icates. Minor ilmenite	

				exsolution in magnetite crystals.					
Sulfides	<1%	Anhedral	Fine	Occur interstitially in					
	oikocrystals								
Comments: Sub	noikilitic toytur	o Vory work	corportinization w	yeak to moderate chlorite and					

Comments: Subpoikilitic texture. Very weak serpentinization, weak to moderate chlorite and sericite alteration in plagioclase.

Sample ID: SL23KI Drillhole: SL-19-0		Depth: 895.25m		Zone: UL	JZ	Rock type: Olivine Clinopyroxenite.
Mineral	Abui	ndance	Habit	Grain size		Comments
Olivine	3	80%	Anhedral to	Fine to		kly oxidized crystals.
			subhedral	medium		Seriate texture.
Clinopyroxene	6	52%	Subhedral to	Medium to	Elor	ngated and granular
			anhedral	coarse grained	crysta	lls, common twinning
					and c	rystals display a weak
					magr	matic foliation. Weak
					alter	ation to clay, chlorite
					а	nd sericite at the
						boundaries.
Biotite +	;	3%	Anhedral	Fine	0	ccurs interstitially.
Hornblende						
Oxides	<	:5%	Euhedral	Fine	Cr-s	pinel and magnetite
			rhombohedral		occur i	nterstitially. Elongated
					il	menite. Cr-spinel
					СС	mmonly occur as
					ine	clusions in olivine.
Sulfides		1%	Anhedral	Fine	Ir	nterstitial Po>Ccp

Comments: Granular seriate texture with a weak magmatic foliation indicated by elongated clinopyroxenes. Weak alteration of Cpx to clay, sericite and chlorite.

Sample ID: SL23KM Drillhole: SL-19-02		Depth: 755.00m		Zone: G	Z	Rock type: Gabbro	
Mineral	Abun	dance	Habit	Grain size		Comments	
Clinopyroxene	30	0%	Subhedral to anhedral	Coarse	spine crysta chad altered	Occurs with fine-grained Cr- spinel inclusions. Embayed crystals. Cpx has amphibole chadacrystals. Moderately altered to serpentine, chlorite, biotite and minor carbonates.	
Plagioclase	45	5%	Anhedral to subhedral	Medium to coarse	to sei	Strongly to completely altered to sericite, chlorite, epidote and minor calcite.	
Amphibole	2	!%	Anhedral	Fine		Occurs as chadacrystals in Cpx. Weakly altered to chlorite	

Oxides	20%	Elongated	Medium to fine	Magnetite blebs occur
		blebs		disseminated in the sample,
				common ilmenite exsolution
				with interstitial disseminated
				ilmenite twinned crystals.
				Disseminated rounded Cr-
				Spinel occurs related to oxides.
Sulfides	<5%	Anhedral	Very Fine	Ccp>Po
				Sulfides occur interstitially and
				often closely related to oxides

Comments: Phaneritic texture. Moderately to strongly alteration to sericite, chlorite, epidote, biotite and calcite. Oxides occur as blebs of magnetite-ilmenite with minor sulfides related. Traces of disseminated hexagonal prismatic apatite.

Sample ID: SL23KN Drillhole: SL-19-02		Depth: 630.35m		Zone: G	7	Rock type: Gabbro		
Mineral	Abundar	се	Habit	Grain size		Comments		
Clinopyroxene	25%		Subhedral	Medium to	Moder	ately to strongly altered		
			to	coarse	to chlo	rite, biotite, sericite and		
			anhedral		acti	inolite. Crystals have		
					ε	embayed textures.		
Plagioclase	50%		Anhedral	Medium to	Stroi	ngly to fully altered to		
			to	coarse	serici	te, chlorite and minor		
			subhedral			epidote.		
Clay	5%		Anhedral	Fine	Fibr	ous sericite-chlorite-		
					actin	olite patches occur at		
					clir	nopyroxene clusters.		
Amphiboles	1%		Anhedral	Fine	Occu	ır as alteration of Cpx.		
					They	also occur interstitially		
					and a	ssociated with oxides.		
Oxides	<20%		Blebs	Medium	Magne	tite-ilmenite blebs form		
					trigo	nal and sandwich-like		
					exs	solutions. Cr-spinel?		
					Commo	only occurs as inclusions		
						in silicates.		
Sulfides	1%		Anhedral	Fine	Po>Cc	p occur disseminated in		
					the sa	ample interstitially and		
					ofte	en related to oxides.		

Comments: Sample has a phaneritic texture. Strongly altered sample with sericite, chlorite, epidote and secondary biotite. Oxides have a blebby/worm-like texture, they have a dirty appearance with Cr-spinel and silicate Inclusions. Traces of disseminated hexagonal prismatic apatite. In hand sample pinkish bands in plagioclases are visible in thin section, moderate oxidation occurs at plagioclase rims.

Sample ID: SL23KN Drillhole: SL-19-02	Depth	n: 695.00m	Zone: G	Z	Rock type: Gabbro		
Mineral	undance	Habit	Grain size		Comments		
Amphibole	<15%	Prismatic subhedral	Medium	crystal chlori to str forn needle	Elongated prismatic rounded crystals. Completely altered to chlorite, they have moderate to strong oxide inclusions in form on single grains and needle-like oxides. They have a black border reaction.		
Clinopyroxene	20%	Subhedral	Medium	chlo commo glom	Occurs moderately altered to chlorite and biotite. Cpx commonly has hornblende and oxides inclusions. They form a subglomeroporphyric texture. Crystals have embayed textures.		
Plagioclase	45%	Subhedral to anhedral	Medium	chlorit	g alteration to sericite, te and epidote. Crystals ve an oxidation rim.		
Apatite	<10%	Euhedral	Fine to medium	and a occu	natic hexagonal crystals patite aggregates. They r disseminated and as clusions in silicates.		
Quartz	2%	Anhedral	Fine to medium	С	occurs interstitially.		
Oxides	10%	Subhedral and blebby- like	Medium	Mag ilr sandv comn embay Oxides at the	Magnetite with common ilmenite trigonal and sandwich-like exsolutions is common. Oxides occur with embayed and skeletal textures. Oxides have annealing textures at the boundaries. Cr-spinel inclusions are common in silicates.		
Sulfides	1%	Anhedral	Fine		Po>Ccp Occur interstitially minated as fine-grained blebs.		

Comments: Sample has a phaneritic texture with a weak magmatic foliation. Alteration is moderate to strong with common sericite-chlorite-epidote-calcite alteration minerals.

Sample ID: SL23KN Drillhole: SL-19-02		Depth: 534.00m		Zone: GZ	7	Rock type: Gabbro
Mineral	Abundar	nce	Habit	Grain size		Comments

Clinopyroxene	30%	Subhedral	Coarse	Occurs completely altered to
, ,				chlorite, calcite and epidote.
				Crystals have embayed rims. It
				has replacement to biotite in
				the core.
Plagioclase	40%	Subhedral	Medium to	Rectangular and rhombohedral
		to	coarse	shapes. Moderately altered to
		euhedral		sericite and chlorite. Moderate
				oxidation corona.
K-feldspar	15%	Subhedral	Medium	Crystals have a graphic texture
				with weak to moderate
				alteration to sericite and
				oxides inclusions.
Quartz	5%	Anhedral	Medium	Occurs interstitially.
Oxides	10%	Subhedral	Medium	Fine to medium grained blebby
				crystals of magnetite with
				ilmenite exsolutions with
				caries-skeletal textures, these
				crystals might have an
				annealing texture at the
				borders. Fine-grained needle-
				like ilmenite crystals form a
				radial habit.
Sulfides	1%	Anhedral	Very fine	Traces of interstitial
				disseminated Po>Ccp>Pn.

Comments: Sample has a phaneritic texture. Moderate to strong alteration, plagioclases occur moderate alteration to sericite and oxidation haloes at the rims and Cpx is strongly to completely altered to chlorite, calcite and epidote. Oxides occur as subhedral skeletal and blebby textures.

Sample ID: SL23KM		Depth: 450.00m		Zone: GZ	7_	Rock type:
Drillhole: SL-19-02	26		1		ı	Leucogabbro
Mineral	Abι	ındance	Habit	Grain size		Comments
Clinopyroxene		20%	Anhedral	Medium to fine	An	hedral sub poikilitic
			to		clino	pyroxene. Moderately
			subhedral		altered	d to calcite, sericite and
						chlorite.
Plagioclase		65%	Subhedral	Medium to fine	Moderately altered to chlorite	
					and s	sericite with moderate
						oxidation haloes.
Quartz		5%	Anhedral	Fine to medium	I	nterstitial quartz.
Oxides		10%	Anhedral	Medium to fine	O	kides are present in
			to		sub	hedral cubic skeletal
			subhedral		cryst	als of magnetite with
					ilmenite exsolution and single	
					ilmen	ite needle-like crystals.

				Cr-Spinel occurs finely
				disseminated.
Sulfides	<1%	Anhedral	Very fine	Traces of disseminated
				Po>Ccp.

Comments: Moderate to strong sericite, biotite and chlorite alteration. Oxides occur as subhedral cubic and rhombohedral skeletal magnetite-ilmenite crystals. Ilmenite needle-lath-like crystals.

Appendix three – whole-rock geochemistry

Sample ID	SL23KM01	SL23KM02	SL23KM03	SL23KM04	SL23KM05	SL23KM06	SL23KM07
SiO ₂ (wt. %)	63.90	59.90	61.50	46.90	46.40	43.70	45.80
Al_2O_3	15.20	16.25	16.00	6.91	4.04	4.33	3.92
Fe ₂ O ₃	7.02	8.40	7.76	17.45	14.45	15.80	15.45
CaO	0.77	0.51	0.56	11.00	13.40	13.90	12.85
MgO	4.64	5.53	6.01	12.30	17.30	15.75	18.80
Na ₂ O	2.70	3.87	3.93	1.46	0.56	0.55	0.62
K_2O	3.37	2.24	1.80	0.60	0.28	0.18	0.18
Cr_2O_3	0.03	0.04	0.04	0.13	0.24	0.32	0.26
TiO ₂	0.61	0.74	0.71	2.03	0.97	1.01	1.06
MnO	0.06	0.05	0.08	0.19	0.18	0.18	0.19
P_2O_5	0.18	0.17	0.17	0.06	0.07	0.12	0.06
SrO	0.03	0.02	0.02	0.02	0.01	0.01	0.02
BaO	0.09	0.02	0.02	0.01	0.01		0.01
LOI	2.61	3.31	3.13	2.05	2.31	3.21	2.56
Total	101.21	101.05	101.73	101.11	100.22	99.06	101.78
	·	·			·		

Sample ID	SL23KM09	SL23KM10	SL23KM11	SL23KM12	SL23KM13	SL23KM14	SL23KM15
SiO ₂ (wt. %)	42.70	40.10	48.70	48.40	47.80	49.30	48.90
Al_2O_3	2.03	3.71	7.17	8.00	7.34	7.05	6.39
Fe_2O_3	14.95	20.50	12.20	13.00	12.30	12.75	13.00
CaO	11.20	7.44	12.85	11.90	12.65	13.45	13.35
MgO	22.40	21.90	12.60	12.00	11.95	13.25	14.95
Na ₂ O	0.36	0.68	1.99	2.23	2.26	1.71	1.28
K_2O	0.08	0.23	0.55	0.59	0.33	0.47	0.49
Cr_2O_3	0.36	0.32	0.18	0.14	0.14	0.17	0.20
TiO ₂	0.60	0.87	1.56	1.69	1.64	1.58	1.42
MnO	0.18	0.21	0.18	0.18	0.19	0.18	0.18
P_2O_5	0.04	0.09	0.17	0.18	0.17	0.16	0.13
SrO	0.01	0.02	0.04	0.04	0.04	0.04	0.04
BaO		0.01	0.02	0.02	0.01	0.01	0.01
LOI	3.20	5.31	1.62	1.96	1.95	1.42	1.62
Total	98.11	101.39	99.83	100.33	98.77	101.54	101.96

Sample ID	SL23KM16	SL23KM17	SL23KM18	SL23KM20	SL23KM22	SL23KM23	SL23KM24
SiO ₂ (wt. %)	47.10	44.00	45.50	49.70	50.00	47.60	46.00
Al_2O_3	5.28	4.52	3.64	8.16	14.45	14.85	13.40
Fe ₂ O ₃	13.50	14.40	13.50	12.15	10.45	11.40	17.05
CaO	11.40	8.03	10.30	12.25	10.25	9.78	9.64
MgO	19.10	23.90	21.80	10.90	6.63	6.06	5.92
Na ₂ O	1.03	0.82	0.50	2.36	4.11	3.76	3.32
K_2O	0.60	0.49	0.42	0.69	0.55	0.60	0.37
Cr_2O_3	0.25	0.30	0.29	0.07	0.01	0.00	
TiO ₂	1.18	1.02	0.94	1.92	1.80	1.85	3.08
MnO	0.19	0.20	0.20	0.22	0.16	0.16	0.21
P_2O_5	0.13	0.09	0.07	0.16	0.19	0.18	0.20
SrO	0.05	0.04	0.03	0.03	0.08	0.09	0.06
BaO	0.02	0.01	0.01	0.03	0.01	0.02	0.01
LOI	1.68	2.81	2.59	1.58	2.71	2.86	2.61
Total	101.51	100.63	99.79	100.22	101.40	99.21	101.87
Sample ID	SL23KM25	SL23KM26	SL23KM27	SL23KM29	SL23KM31	SL23KM32	SL23KM33
SiO ₂ (wt. %)	48.60	46.30	58.70	60.40	55.60	55.10	52.40
AI_2O_3	13.55	12.20	14.00	13.55	13.65	13.65	12.95
Fe ₂ O ₃	14.35	18.55	9.60	9.76	11.20	12.45	13.40
CaO	7.64	5.49	1.00	1.12	1.45	2.51	3.47
MgO	4.74	5.32	6.85	4.34	4.33	4.14	5.37
Na₂O	3.87	4.09	3.71	4.68	4.61	4.54	3.94
K_2O	0.79	0.50	1.86	2.66	2.55	2.19	1.80
Cr_2O_3							
TiO ₂	4.17	3.39	1.42	1.47	1.58	1.96	2.90
MnO	0.27	0.40	0.10	0.06	0.07	0.12	0.24
P_2O_5	0.26	1.16	0.38	0.39	0.52	0.54	0.45
SrO	0.06	0.04	0.01	0.01	0.01	0.02	0.02
BaO	0.01	0.01	0.03	0.05	0.05	0.06	0.06
LOI	2.60	2.70	3.52	2.61	2.94	2.58	3.29
Total	100.91	100.15	101.18	101.10	98.56	99.86	100.29
Sample ID	SL23KM34	SL23KM35	SL23KM37	SL23KM40	SL23KM41	SL23KM42	SL23KM43
SiO ₂ (wt. %)	60.40	54.40	58.20	64.60	45.40	42.80	46.10
Al_2O_3	13.65	14.60	13.70	14.70	5.09	4.84	4.91
							149

Fe_2O_3	9.44	8.98	6.21	6.43	17.45	17.75	12.95
CaO	1.96	2.52	2.87	2.21	14.30	8.62	13.15
MgO	3.70	4.95	4.37	2.72	11.80	20.10	16.45
Na₂O	4.45	4.59	3.95	4.65	1.27	1.18	0.91
K_2O	2.93	2.52	3.51	1.84	0.35	0.34	0.20
Cr ₂ O ₃		0.01	0.03	0.02	0.19	0.32	0.29
TiO ₂	1.80	1.76	0.55	0.55	1.22	1.20	1.24
MnO	0.08	0.09	0.06	0.07	0.18	0.20	0.19
P_2O_5	0.52	0.32	0.23	0.13	0.09	0.09	0.09
SrO	0.01	0.01	0.02	0.06	0.03	0.04	0.02
BaO	0.07	0.04	0.08	0.05	0.02	0.01	0.01
LOI	2.81	4.16	7.06	2.08	2.98	1.96	3.23
Total	101.82	98.95	100.84	100.11	100.37	99.45	99.74

Sample ID	SL23KM45	SL23KM46	SL23KM47	SL23KM48	SL23KM49	SL23KM50	SL23KM51
SiO ₂ (wt. %)	41.40	38.90	38.10	40.20	40.40	38.90	40.00
AI_2O_3	1.32	1.69	1.95	2.07	1.68	1.66	1.76
Fe ₂ O ₃	17.50	18.25	18.85	18.25	18.45	17.75	18.35
CaO	6.01	2.75	2.60	2.24	2.00	1.96	2.08
MgO	32.00	35.10	36.00	36.80	38.40	36.60	37.70
Na₂O	0.26	0.33	0.43	0.56	0.45	0.39	0.38
K_2O	0.06	0.12	0.15	0.12	0.11	0.13	0.13
Cr_2O_3	0.55	0.63	0.63	0.69	0.63	0.61	0.63
TiO ₂	0.41	0.49	0.47	0.47	0.42	0.42	0.43
MnO	0.23	0.23	0.24	0.23	0.24	0.24	0.24
P_2O_5	0.02	0.04	0.04	0.04	0.04	0.04	0.04
SrO	0.01	0.01	0.01	0.01	0.01	0.01	0.01
BaO			0.01	0.01			0.01
LOI	0.07	0.50	0.23	-0.82	-1.06	-0.21	-0.11
Total	99.84	99.04	99.71	100.87	101.77	98.50	101.65

Sample ID	SL23KM52	SL23KM53	SL23KM54	SL23KM55	SL23KM56	SL23KM58	SL23KM59
SiO ₂ (wt. %)	46.90	39.90	40.50	47.70	44.20	39.60	41.80
Al_2O_3	2.68	1.00	1.34	1.60	1.28	1.30	1.52
Fe ₂ O ₃	12.55	18.55	18.25	11.15	15.65	17.55	16.85
CaO	10.80	1.86	4.68	17.20	9.06	4.96	7.30
MgO	25.70	39.60	36.10	20.80	29.70	34.90	31.90

Na₂O	0.74	0.22	0.32	0.28	0.28	0.21	0.35
K₂O	0.18	0.07	0.08	0.01	0.04	0.08	0.08
Cr_2O_3	0.30	0.59	0.55	0.30	0.41	0.47	0.43
TiO ₂	0.58	0.28	0.36	0.56	0.42	0.36	0.42
MnO	0.18	0.24	0.24	0.19	0.22	0.23	0.22
P_2O_5	0.05	0.03	0.03	0.01	0.02	0.03	0.03
SrO	0.02		0.01	0.01	0.01	0.01	0.01
BaO	0.01						
LOI	0.07	-0.86	-1.08	-0.34	-0.71	-0.40	-0.73
Total	100.76	101.48	101.38	99.47	100.58	99.30	100.18

Sample ID	SL23KM60	SL23KM61	SL23KM62	SL23KM65	SL23KM68	SL23KM71
SiO ₂ (wt. %)	48.40	49.10	42.80	44.40	61.20	48.40
Al_2O_3	2.54	15.55	12.35	12.70	14.20	12.85
Fe ₂ O ₃	12.50	6.97	18.80	17.15	9.95	15.65
CaO	14.85	13.95	12.30	9.87	1.41	8.42
MgO	21.30	7.97	7.28	5.92	2.51	4.56
Na₂O	0.57	2.46	2.30	3.55	5.46	3.91
K_2O	0.10	0.69	0.47	0.47	2.71	0.86
Cr_2O_3	0.28	0.03				
TiO ₂	0.76	0.89	2.98	4.85	1.08	3.27
MnO	0.19	0.10	0.16	0.21	0.18	0.32
P_2O_5	0.03	0.05	0.05	0.13	0.26	0.27
SrO	0.01	0.10	0.09	0.05	0.02	0.02
BaO		0.02	0.02	0.01	0.06	0.02
LOI	0.36	1.75	1.69	2.08	1.44	2.34
Total	101.89	99.63	101.29	101.39	100.48	100.89

Sample ID	SL23KM01	SL23KM02	SL23KM03	SL23KM04	SL23KM05	SL23KM06	SL23KM07
C (ppm)	0.02	0.02	0.02	0.19	0.15	0.15	0.19
S	0.22	0.38	0.22	1.75	1.38	2.17	0.99
Ва	808.00	202.00	151.50	128.00	86.70	30.40	70.30
Ce	57.20	88.40	73.30	26.00	24.70	29.10	18.70
Cr	234.00	313.00	276.00	1015.00	1900.00	2440.00	2020.00
Cs	7.70	8.21	8.31	2.81	1.84	3.06	1.96
Dy	2.26	3.09	3.11	2.24	2.27	2.37	1.81
Er	1.21	1.82	1.94	0.90	0.86	1.02	0.75
Eu	1.04	1.55	1.22	0.98	1.07	1.15	0.89
							151

Ga	17.30	21.10	20.30	10.80	6.60	7.10	7.20
Gd	2.96	4.52	3.69	3.16	3.13	3.36	2.71
Ge	0.80	0.80	1.00	1.40	2.00	1.60	1.90
Hf	3.65	4.75	3.59	1.78	1.80	1.80	1.38
Но	0.40	0.61	0.61	0.41	0.34	0.42	0.32
La	27.60	42.80	36.10	11.20	9.80	11.70	7.20
Lu	0.22	0.26	0.27	0.11	0.09	0.11	0.07
Nb	6.56	7.49	6.80	2.82	7.35	9.48	5.98
Nd	25.80	40.00	32.30	15.70	16.20	18.60	13.10
Pr	6.46	9.94	8.46	3.23	3.35	4.01	2.76
Rb	111.00	86.10	80.60	23.10	10.00	9.90	6.70
Sm	4.38	6.27	5.26	3.48	3.71	4.26	2.70
Sn	1.10	1.40	1.40	1.30	1.70	0.80	0.90
Sr	294.00	179.00	148.00	209.00	136.00	88.80	184.00
Та	0.40	2.50	0.40	0.40	0.30	0.40	0.30
Tb	0.36	0.55	0.48	0.40	0.39	0.44	0.35
Th	7.55	10.50	8.06	2.12	0.92	0.85	0.58
Tm	0.20	0.30	0.29	0.13	0.14	0.13	0.09
U	2.18	3.39	2.57	0.64	0.35	0.28	0.22
V	119.00	142.00	139.00	321.00	180.00	163.00	191.00
W	1.60	2.20	2.30	1.40	1.10		1.00
Υ	11.40	16.20	15.90	10.00	9.90	11.30	8.40
Yb	1.23	1.90	1.91	0.72	0.70	0.77	0.60
Zr	151.00	189.00	149.00	62.00	72.00	75.00	55.00
As	0.40	0.10	0.20	0.40	0.30		0.20
Bi	0.28	0.30	0.18	1.08	0.57	0.90	0.51
Hg							
In	0.03	0.02	0.03	0.03	0.05	0.03	0.02
Re	0.00	0.00	0.00	0.00	0.00	0.01	0.00
Sb							
Se	0.20	0.20	0.20	7.50	5.60	7.80	3.10
Te	0.03	0.05	0.01	1.73	2.55	1.88	0.49
TI	0.37	0.24	0.26	0.99	0.19	0.39	0.10
Ag				3.70	3.60	2.90	1.20
Cd				0.70		0.50	
Со	23.00	31.00	28.00	149.00	130.00	163.00	131.00
Cu	68.00	36.00	21.00	5430.00	6020.00	6160.00	2400.00
Li	110.00	100.00	90.00	40.00	30.00	30.00	20.00
Mo	3.00	3.00	2.00				
Ni	81.00	98.00	99.00	1840.00	1455.00	1920.00	962.00
Pb	2.00	4.00		11.00	5.00	7.00	

Sc	12.00	16.00	15.00	32.00	40.00	35.00	36.00
Zn	21.00	20.00	26.00	97.00	76.00	65.00	79.00

Sample ID	SL23KM09	SL23KM10	SL23KM11	SL23KM12	SL23KM13	SL23KM14	SL23KM15
C (ppm)	0.19	0.11	0.12	0.12	0.10	0.06	0.09
S	0.95	2.15	0.14	0.08	0.08	0.05	0.19
Ва	26.70	83.80	147.50	168.50	98.30	108.00	86.30
Ce	9.90	21.00	46.80	48.20	45.50	42.90	37.80
Cr	2780.00	2440.00	1380.00	1110.00	1105.00	1290.00	1565.00
Cs	1.14	0.79	2.28	1.70	0.66	1.64	3.15
Dy	1.20	1.86	3.40	3.54	3.55	3.23	3.08
Er	0.55	0.74	1.56	1.46	1.42	1.40	1.22
Eu	0.51	0.91	1.72	1.73	1.59	1.55	1.51
Ga	3.90	6.30	11.90	12.30	12.20	11.60	10.50
Gd	1.81	2.50	5.04	5.07	5.05	4.79	4.19
Ge	1.60	1.30	1.80	1.80	2.00	2.00	2.00
Hf	0.74	1.62	3.32	3.46	3.43	3.22	2.60
Но	0.21	0.27	0.60	0.56	0.60	0.55	0.49
La	4.00	8.60	19.00	19.70	18.60	17.50	15.70
Lu	0.04	0.08	0.16	0.15	0.14	0.13	0.12
Nb	2.61	6.37	14.45	15.05	14.50	13.70	11.55
Nd	7.30	12.80	27.00	29.00	27.40	26.00	23.40
Pr	1.40	2.81	6.12	6.64	6.01	5.93	5.24
Rb	2.70	6.10	18.00	17.10	9.20	14.50	17.30
Sm	1.76	2.83	6.10	6.04	5.63	5.67	5.12
Sn	0.50	1.00	0.80	1.10	1.00	0.80	0.90
Sr	86.40	198.50	394.00	399.00	304.00	381.00	359.00
Ta		0.30	0.90	0.80	0.80	0.70	0.60
Tb	0.20	0.31	0.66	0.68	0.61	0.60	0.54
Th	0.35	0.72	1.58	1.55	1.40	1.32	1.11
Tm	0.07	0.10	0.19	0.21	0.21	0.18	0.17
U	0.13	0.25	0.48	0.44	0.43	0.41	0.32
V	115.00	145.00	253.00	258.00	263.00	265.00	241.00
W	0.80	0.60	0.70	0.60	0.80	0.50	12.70
Υ	5.60	7.30	15.00	15.80	15.20	15.40	14.10
Yb	0.37	0.53	1.18	1.16	1.12	1.14	0.92
Zr	27.00	59.00	135.00	142.00	130.00	128.00	104.00
As		0.30	0.10		0.20	0.30	0.20
Bi	0.43	0.67	0.07	0.06	0.05	0.03	0.08
Hg							
In	0.02	0.05	0.01			0.01	0.01
							1.50

Re	0.00	0.01			0.00		0.00
Sb							
Se	3.20	8.10	0.50			0.20	0.40
Te	0.58	1.03	0.03	0.01	0.01	0.01	0.09
TI	0.06	0.07	0.11	0.05	0.03	0.05	0.14
Ag	1.70	3.60	0.60				
Cd		0.70					
Co	155.00	218.00	72.00	70.00	68.00	72.00	80.00
Cu	2930.00	5750.00	503.00	109.00	151.00	115.00	471.00
Li	10.00	10.00	20.00	20.00	10.00	20.00	10.00
Мо							
Ni	1270.00	2070.00	323.00	230.00	228.00	240.00	358.00
Pb		3.00	11.00				
Sc	33.00	23.00	38.00	34.00	38.00	38.00	37.00
Zn	88.00	109.00	91.00	76.00	72.00	83.00	80.00

Sample ID	SL23KM16	SL23KM17	SL23KM18	SL23KM20	SL23KM22	SL23KM23	SL23KM24
C (ppm)	0.11	0.15	0.19	0.05	0.06	0.07	0.03
S	0.09	0.04	0.06	0.04	0.09	0.09	0.12
Ва	190.00	133.50	126.00	263.00	115.00	170.50	58.00
Ce	34.30	28.00	27.80	51.00	50.60	53.10	59.20
Cr	1990.00	2310.00	2220.00	496.00	78.00	46.00	6.00
Cs	3.39	4.33	2.69	0.36	0.18	0.23	0.16
Dy	2.67	1.99	2.26	4.25	3.54	3.33	3.90
Er	1.12	0.90	1.01	1.72	1.49	1.45	1.78
Eu	1.30	1.12	1.03	1.95	1.94	2.08	2.23
Ga	8.90	6.30	6.10	11.80	15.80	17.00	18.70
Gd	4.06	2.95	3.29	5.88	4.90	5.16	6.07
Ge	1.90	1.60	1.80	2.00	1.60	1.60	1.60
Hf	2.52	2.27	2.50	4.57	3.93	4.46	4.92
Но	0.41	0.37	0.41	0.72	0.61	0.62	0.70
La	13.80	11.60	11.20	20.80	21.30	21.50	23.90
Lu	0.13	0.10	0.12	0.17	0.17	0.16	0.20
Nb	10.30	8.88	7.64	16.50	16.05	17.60	19.75
Nd	21.50	16.20	17.30	31.30	30.10	30.30	35.30
Pr	4.66	3.92	3.92	7.18	7.09	7.24	8.30
Rb	18.50	17.20	12.80	21.40	10.60	14.00	7.60
Sm	4.64	3.44	3.56	6.94	6.01	6.55	7.11
Sn	0.80	0.50	0.70	1.20	1.10	1.40	1.40
Sr	410.00	354.00	254.00	290.00	721.00	783.00	596.00
Та	0.50	0.60	0.50	1.00	1.00	1.20	1.20

Tb	0.51	0.36	0.43	0.76	0.66	0.69	0.75
Th	1.02	0.76	0.83	1.48	1.36	1.52	1.62
Tm	0.15	0.12	0.13	0.22	0.19	0.20	0.23
U	0.27	0.21	0.24	0.42	0.39	0.41	0.55
V	196.00	182.00	209.00	328.00	269.00	303.00	659.00
W		0.70	4.50	1.20	0.70	1.70	0.70
Υ	12.00	9.50	10.90	18.80	16.90	16.60	18.60
Yb	0.88	0.65	0.70	1.34	1.12	1.14	1.24
Zr	92.00	83.00	92.00	158.00	145.00	158.00	179.00
As		0.30	0.10	0.10		0.20	0.10
Bi	0.03	0.04	0.02	0.02	0.03	0.03	0.04
Hg							
In	0.01	0.01	0.01	0.01	0.01	0.02	0.03
Re							
Sb							
Se	0.20			0.30			0.40
Te	0.01	0.02	0.01	0.01	0.01		0.02
TI	0.10	0.06	0.08	0.04			
Ag							
Cd							
Со	99.00	127.00	115.00	60.00	48.00	49.00	68.00
Cu	95.00	224.00	79.00	148.00	268.00	292.00	513.00
Li	20.00	20.00	20.00	20.00	20.00	20.00	20.00
Мо							
Ni	493.00	765.00	577.00	148.00	87.00	78.00	75.00
Pb	2.00			3.00		9.00	3.00
Sc	34.00	24.00	32.00	42.00	25.00	23.00	26.00
Zn	90.00	95.00	94.00	91.00	90.00	101.00	120.00

Sample ID	SL23KM25	SL23KM26	SL23KM27	SL23KM29	SL23KM31	SL23KM32	SL23KM33
C (ppm)	0.04	0.10	0.02	0.11	0.14	0.09	0.16
S	0.12	0.20	0.04	0.10	0.11	0.12	0.03
Ва	122.50	92.30	320.00	441.00	450.00	549.00	508.00
Ce	75.10	144.00	173.50	170.00	166.00	159.50	123.50
Cr	5.00		5.00		6.00		
Cs	0.16	0.54	0.96	0.49	0.35	0.59	0.67
Dy	4.62	7.18	9.15	7.67	8.11	8.06	6.91
Er	2.05	3.13	4.28	3.66	3.81	3.57	3.09
Eu	2.69	4.23	4.81	3.81	4.02	4.03	3.39
Ga	18.40	17.20	23.80	19.60	21.30	20.00	17.70
Gd	6.51	12.30	13.70	11.25	12.25	11.65	10.10

Ge	1.60	1.50	1.90	1.60	1.50	1.70	1.60
Hf	6.54	7.89	15.40	15.00	13.95	12.60	10.15
Но	0.80	1.26	1.74	1.40	1.46	1.40	1.21
La	31.50	59.00	75.10	72.70	71.30	68.50	52.80
Lu	0.23	0.34	0.50	0.41	0.46	0.42	0.32
Nb	31.60	49.70	65.20	61.20	55.10	51.50	41.70
Nd	41.90	84.00	90.30	85.40	87.20	86.20	66.30
Pr	10.30	19.80	22.60	21.90	21.70	20.90	16.30
Rb	14.50	10.60	39.20	52.40	52.60	47.40	38.70
Sm	8.28	16.25	17.65	16.10	16.40	15.65	12.80
Sn	1.80	2.10	3.10	3.50	3.90	3.70	2.80
Sr	537.00	394.00	134.50	117.50	117.00	221.00	212.00
Ta	2.00	2.90	3.60	3.50	3.30	3.10	2.50
Tb	0.91	1.48	1.80	1.49	1.58	1.64	1.28
Th	2.37	3.16	6.85	6.51	6.27	5.61	4.26
Tm	0.27	0.41	0.57	0.51	0.53	0.48	0.41
U	0.70	0.93	2.14	1.82	1.84	1.63	1.25
V	414.00	225.00	19.00	24.00	44.00	103.00	240.00
W	0.70	1.00	2.20	1.50	3.20	2.30	1.60
Υ	21.40	35.90	48.90	39.00	40.60	39.90	32.40
Yb	1.55	2.18	3.35	3.08	3.23	2.89	2.26
Zr	245.00	324.00	617.00	588.00	558.00	505.00	387.00
As	0.40						0.10
Bi	0.02	0.04	0.02	0.04	0.02	0.02	0.02
Hg	0.01		0.01	0.01			
In	0.03	0.02	0.04	0.06	0.08	0.07	0.05
Re	0.00	0.00	0.00			0.00	0.00
Sb							
Se	0.50		0.20	0.20			
Te		0.01		0.01	0.01	0.01	
TI		0.02		0.03	0.03	0.03	0.02
Ag			0.50				
Cd							
Со	56.00	52.00	15.00	17.00	21.00	22.00	35.00
Cu	102.00	73.00	2.00	4.00	18.00	1.00	92.00
Li	20.00	30.00	60.00	40.00	60.00	50.00	60.00
Mo	1.00	1.00	1.00	2.00	2.00	2.00	1.00
Ni	10.00	3.00	3.00	1.00	4.00	4.00	9.00
Pb	7.00	12.00			3.00		3.00
Sc	21.00	11.00	9.00	9.00	9.00	11.00	16.00
Zn	107.00	141.00	99.00	65.00	81.00	78.00	95.00
				<u> </u>		<u> </u>	156
							150

Sample ID	SL23KM34	SL23KM35	SL23KM37	SL23KM40	SL23KM41	SL23KM42	SL23KM43
C (ppm)	0.22	0.41	0.11	0.11	0.17	0.13	0.34
S	0.09	0.18	2.34	0.24	4.10	1.88	1.14
Ва	618.00	343.00	733.00	422.00	179.50	113.00	63.80
Ce	149.50	104.00	131.00	56.70	25.70	31.00	31.80
Cr		85.00	197.00	157.00	1435.00	2510.00	2190.00
Cs	0.59	0.57	0.43	2.77	2.13	0.79	1.86
Dy	7.07	4.64	4.04	2.32	2.53	2.05	2.57
Er	3.30	2.30	2.17	1.27	1.13	0.95	1.19
Eu	3.75	2.45	2.24	1.04	1.14	1.08	1.26
Ga	18.40	18.80	14.70	15.40	7.20	7.60	7.00
Gd	10.95	7.24	6.22	3.14	3.54	2.90	3.64
Ge	1.40	1.30	0.70	1.00	1.60	1.40	1.80
Hf	11.70	8.05	4.02	3.36	2.15	2.39	2.56
Но	1.32	0.95	0.77	0.45	0.48	0.36	0.42
La	63.00	45.90	64.70	28.80	9.60	13.10	12.50
Lu	0.35	0.27	0.31	0.17	0.13	0.11	0.12
Nb	45.10	30.80	6.92	5.56	11.40	12.90	11.95
Nd	76.30	51.20	55.50	23.90	17.60	16.50	19.50
Pr	19.35	13.30	15.35	6.64	3.80	4.10	4.53
Rb	60.50	53.60	69.60	60.20	9.40	7.70	7.90
Sm	14.25	9.33	9.22	4.25	4.22	3.59	4.28
Sn	3.20	2.20	1.00	0.80	2.10	1.20	1.30
Sr	133.50	109.50	136.00	502.00	277.00	364.00	155.00
Та	2.70	1.90	0.60	0.40	0.50	0.70	0.70
Tb	1.39	0.96	0.79	0.43	0.45	0.39	0.47
Th	6.19	5.18	12.95	6.93	0.61	1.02	0.99
Tm	0.39	0.33	0.32	0.17	0.16	0.10	0.15
U	1.90	1.46	3.55	1.92	0.14	0.33	0.32
V	76.00	225.00	118.00	119.00	227.00	213.00	206.00
W	2.20	2.20	3.70	1.60	1.40	0.60	1.10
Υ	36.00	26.40	22.40	12.70	12.00	9.80	12.20
Yb	2.69	1.83	2.06	1.23	0.75	0.63	0.90
Zr	464.00	321.00	154.00	135.00	78.00	95.00	94.00
As			0.90	0.10	1.00	0.30	0.30
Bi	0.06	0.05	0.31	0.19	3.33	1.30	0.95
Hg					0.01	0.01	0.01
In	0.06	0.04	0.04	0.03	0.10	0.04	0.05
Re		0.00	0.00	0.00	0.01	0.00	0.00
Sb				0.19	0.05		

Se		0.30	1.40	0.20	22.70	8.70	6.70
Te		0.03	0.07	0.01	6.60	3.34	1.38
TI	0.07	0.05	0.02	0.32	0.13	0.07	0.21
Ag					12.90	6.60	5.50
Cd					2.30	0.70	
Со	19.00	24.00	26.00	23.00	179.00	175.00	124.00
Cu	3.00	306.00	8.00	56.00	27800.00	8100.00	8170.00
Li	40.00	50.00	50.00	50.00	20.00	10.00	40.00
Mo	2.00	1.00	2.00	1.00	1.00		
Ni		49.00	73.00	62.00	3390.00	2410.00	1740.00
Pb			2.00	16.00	16.00	12.00	8.00
Sc	10.00	14.00	10.00	13.00	36.00	23.00	37.00
Zn	42.00	65.00	33.00	91.00	140.00	104.00	112.00

Sample ID	SL23KM45	SL23KM46	SL23KM47	SL23KM48	SL23KM49	SL23KM50	SL23KM51
C (ppm)	0.10	0.19	0.25	0.15	0.11	0.24	0.14
S	0.08	0.03	0.01	0.02	0.01	0.01	
Ва	19.80	35.90	55.60	45.60	37.20	40.60	48.60
Ce	7.00	8.90	10.30	10.40	9.90	9.30	9.70
Cr	4160.00	4880.00	4960.00	5240.00	4710.00	4650.00	4770.00
Cs	0.05	0.10	0.20	0.05	0.06	0.08	0.35
Dy	0.84	0.74	0.71	0.77	0.62	0.73	0.66
Er	0.39	0.29	0.41	0.27	0.22	0.23	0.27
Eu	0.36	0.33	0.42	0.37	0.31	0.35	0.37
Ga	3.00	3.50	3.80	3.50	3.10	3.00	3.20
Gd	1.02	1.06	1.10	1.03	0.99	0.89	0.94
Ge	1.50	1.20	1.20	1.20	1.10	1.20	1.30
Hf	0.61	0.77	0.94	0.83	0.78	0.81	0.71
Но	0.15	0.13	0.16	0.12	0.12	0.12	0.13
La	2.50	3.50	4.30	4.30	3.90	3.80	4.20
Lu	0.04	0.04	0.04	0.03	0.02	0.03	0.03
Nb	2.33	3.19	4.36	4.01	3.63	3.39	3.24
Nd	4.80	5.50	5.70	5.80	5.20	5.50	5.50
Pr	1.08	1.24	1.36	1.45	1.30	1.28	1.32
Rb	1.30	3.00	4.00	2.60	2.30	2.70	3.40
Sm	1.14	1.16	1.20	1.07	0.96	1.04	1.24
Sn							
Sr	63.30	97.40	112.00	122.00	96.40	96.20	124.00
Та	0.20	0.20	0.30	0.30	0.20	0.20	0.20
Tb	0.10	0.13	0.15	0.13	0.12	0.10	0.12
Th	0.24	0.28	0.41	0.34	0.28	0.28	0.26

Tm	0.04	0.04	0.05	0.05	0.04	0.04	0.05
U	0.07	0.07	0.17	0.14	0.06		0.05
V	110.00	112.00	111.00	99.00	88.00	89.00	97.00
W	0.50		0.80	0.70	1.60	0.60	1.70
Υ	3.50	3.30	3.60	3.70	3.10	3.10	3.30
Yb	0.27	0.23	0.30	0.26	0.25	0.19	0.22
Zr	20.00	28.00	38.00	33.00	30.00	31.00	30.00
As		0.10	0.10	0.10			0.20
Bi	0.04	0.02	0.05	0.02	0.01	0.01	0.01
Hg			0.01				
In	0.01	0.01	0.01	0.02	0.01	0.01	0.01
Re	0.00	0.00		0.00			0.00
Sb							
Se	0.40	0.30		0.20		0.30	
Te	0.13	0.05	0.08	0.01		0.02	0.02
TI		0.03	0.02	0.03			0.03
Ag							
Cd							
Со	174.00	191.00	181.00	188.00	196.00	196.00	199.00
Cu	327.00	207.00	101.00	64.00	49.00	52.00	47.00
Li	10.00	10.00	10.00	10.00	10.00	10.00	10.00
Mo							
Ni	1170.00	1360.00	1260.00	1295.00	1330.00	1320.00	1310.00
Pb							
Sc	20.00	11.00	10.00	9.00	8.00	9.00	9.00
Zn	109.00	120.00	119.00	112.00	113.00	118.00	126.00

Sample ID	SL23KM52	SL23KM53	SL23KM54	SL23KM55	SL23KM56	SL23KM58	SL23KM59
C (ppm)	0.15	0.05	0.05	0.04	0.05	0.06	0.06
S	0.37	0.09	0.05	0.01	0.03	0.02	0.02
Ва	60.60	22.50	25.30	3.10	14.20	15.00	24.10
Ce	17.00	5.80	7.90	5.60	6.30	7.00	8.60
Cr	2330.00	4440.00	4290.00	2380.00	3180.00	3660.00	3390.00
Cs	0.11	0.10	0.05	0.02	0.06	0.21	0.05
Dy	1.31	0.46	0.61	1.52	0.92	0.64	0.92
Er	0.58	0.18	0.27	0.66	0.43	0.27	0.40
Eu	0.68	0.18	0.30	0.59	0.41	0.32	0.47
Ga	4.00	2.30	2.70	3.70	2.80	2.70	3.00
Gd	1.91	0.60	1.03	2.18	1.29	0.99	1.28
Ge	1.80	1.30	1.40	2.20	1.70	1.40	1.50
Hf	1.27	0.41	0.57	0.73	0.56	0.59	0.72

11-	0.24	0.00	0.12	0.27	0.16	0.42	0.16
Но	0.24	0.08	0.12	0.27	0.16	0.13	0.16
La	7.20	2.30	2.90	1.30	2.00	2.40	3.00
Lu	0.06	0.01	0.03	0.06	0.02	0.03	0.03
Nb	5.42	1.92	2.31	0.36	1.29	1.80	2.19
Nd	9.90	3.40	5.10	6.50	5.10	4.70	6.00
Pr	2.37	0.82	1.12	1.18	1.04	1.00	1.30
Rb	3.80	1.80	1.80	0.40	1.00	2.40	1.70
Sm	2.25	0.72	1.19	2.25	1.32	1.04	1.48
Sn	0.70						
Sr	156.00	56.10	76.30	62.50	62.30	67.30	87.70
Та	0.30	0.20	0.10	0.10	0.10	0.10	0.20
Tb	0.24	0.06	0.14	0.29	0.18	0.13	0.17
Th	0.52	0.15	0.18	0.03	0.05	0.10	0.17
Tm	0.07	0.02	0.04	0.07	0.04	0.04	0.06
U	0.11						
V	120.00	68.00	94.00	235.00	132.00	98.00	121.00
W	1.20	0.50	0.60		0.90	12.00	
Υ	6.40	2.10	3.30	6.90	4.20	3.20	4.30
Yb	0.41	0.15	0.20	0.42	0.27	0.20	0.30
Zr	49.00	18.00	22.00	15.00	18.00	20.00	24.00
As		0.10	0.10				
Bi	0.14	0.05	0.02		0.01	0.01	0.01
Hg							
In	0.01	0.01	0.01		0.01	0.01	0.01
Re	0.00	0.00	0.00				
Sb							
Se	2.00	0.70	0.20				
Te	0.41	0.14	0.06	0.01	0.04	0.01	0.02
TI	0.02	0.02					
Ag	1.80						
Cd							
Co	126.00	211.00	181.00	92.00	146.00	177.00	161.00
Cu	2410.00	421.00	205.00	20.00	114.00	49.00	29.00
Li		10.00	10.00			10.00	10.00
Мо							
Ni	1090.00	1475.00	1195.00	405.00	884.00	1145.00	964.00
Pb	2.00						
Sc	29.00	9.00	16.00	55.00	28.00	17.00	23.00
Zn	66.00	115.00	105.00	54.00	93.00	102.00	93.00

Sample ID SL23KM60 SL23KM61 SL23KM62 SL23KM65 SL23KM68 SL23KM71

C (mmm)	0.05	0.04	0.04	0.03	0.02	0.04
C (ppm)	0.05	0.04	0.04	0.03	0.02	0.04
S	0.03	0.05	0.10	0.23	0.03	0.04
Ba	33.00	177.00	131.00	121.00	552.00	155.50
Ce	12.20	19.30	18.60	38.50	170.00	75.10
Cr	2200.00	207.00	12.00	11.00	8.00	6.00
Cs	0.09	0.58	0.86	0.20	0.26	0.16
Dy	2.00	2.23	2.23	3.64	10.10	5.39
Er	0.83	0.84	1.12	1.65	4.55	2.33
Eu	0.77	1.10	1.16	1.84	4.52	2.69
Ga	5.50	16.70	20.90	20.70	24.30	24.60
Gd	2.66	2.89	3.12	5.17	14.20	8.05
Ge	2.40	1.70	1.80	1.80	1.90	2.10
Hf	1.09	1.54	1.94	3.51	14.50	6.27
Но	0.33	0.36	0.38	0.60	1.74	0.92
La	4.90	8.50	7.80	17.60	81.90	35.80
Lu	0.09	0.08	0.12	0.17	0.45	0.25
Nb	2.67	5.21	5.29	15.85	54.60	25.30
Nd	10.40	13.80	13.80	24.30	92.80	45.30
Pr	1.93	2.76	2.76	5.43	21.60	9.98
Rb	2.70	15.70	15.70	9.50	61.60	17.20
Sm	2.47	3.05	3.38	5.56	17.05	8.65
Sn		0.50	0.70	1.10	4.50	2.10
Sr	134.00	908.00	786.00	423.00	249.00	198.00
Та	0.20	0.40	0.40	1.20	3.90	1.80
Tb	0.38	0.41	0.47	0.76	2.00	1.04
Th	0.36	0.60	0.61	1.32	7.72	2.90
Tm	0.11	0.12	0.13	0.19	0.63	0.30
U	0.15	0.20	0.22	0.41	2.15	0.84
V	213.00	172.00	991.00	712.00	12.00	453.00
W			1.30		0.50	0.60
Υ	8.10	8.80	9.70	14.40	44.90	22.80
Yb	0.58	0.63	0.72	1.31	3.74	1.70
Zr	35.00	55.00	59.00	130.00	595.00	243.00
As		0.10		0.10		
Bi	0.01	0.02	0.01	0.01	0.01	0.02
Hg						
In	0.01		0.01	0.02	0.04	0.03
Re				0.00		0.00
Sb						
Se		0.30	0.30			
Te	0.01	0.05	0.03	0.01	0.01	0.02

TI			0.03			
Ag		0.50				
Cd						
Со	100.00	42.00	84.00	58.00	10.00	50.00
Cu	29.00	345.00	978.00	221.00	8.00	231.00
Li		10.00	20.00	20.00	30.00	20.00
Mo					2.00	1.00
Ni	465.00	131.00	115.00	32.00	5.00	34.00
Pb			2.00	3.00	14.00	9.00
Sc	46.00	32.00	36.00	28.00	7.00	22.00
Zn	69.00	45.00	110.00	124.00	88.00	123.00

 $\label{eq:Appendix four-portable XRF} Appendix \ four-portable \ XRF$

Data taken from drill hole SL-17-18B

								420
TO	385.39	391.45	395.45	401.45	405.52	410.4	415.53	420.5
Mg								
(ppm)	0	39698	0		30661	24896	32427	
Mg								
	78631							
	6808		8240					
Ca error	103		101					
Al	34938	38684	21419	41386	38466	37335	40889	43485
Al error	1685	1532	1289	1280	1426	1323	1489	1453
Si	154183	145676	225924	166694	159375	154773	161353	175656
	1624	1909	1922	1324	1904	1777	2026	1568
Р	0	0	0	0	0	0	0	0
P error	1426	1082	1046	945	1024	1049	1060	1047
Cu	0	0	55	33	0	47	59	0
Cu error	107	96	8	6	86	7	8	82
S	3179	4296	1364	0	0	0	0	0
S error	125	114	107	651	748	698	735	781
K	13693	14880	1181	14343	15246	9365	10716	10601
K error	172	206	86	132	195	128	157	128
Ti	4086	5282	2804	11743	11109	12472	12633	12042
Ti error	215	215	182	257	286	285	313	293
V	79	70	0	102	100	107	122	81
V error	23	21	181	22	24	23	25	25
Cr	188	192	208	0	0	0	0	0
Cr error	35	32	33	270	295	282	312	321
Mn	425	635	711	635	581	1027	1237	909
Mn								
error	36	37	40	33	35	41	49	43
Fe	37597	47090	40181	49497	49227	61415	67957	66131
Fe error	373	586	354	367	565	664	807	543
Co	0	0	0	0	0	0	0	0
Co error	880	870	861	791	844	893	1008	1006
Ni	77	124	131	33	35	0	0	59
Ni error	12	12	12	8	9	106	119	11
Zn	54	52	48	74	43	79	94	84
Zn error	6	5	5	5	5	6	7	6

As	0	0	0	0	0	0	0	0
As error	60	52	54	44	47	45	51	49
Se	0	0	0	0	0	0	0	0
Se error	39	36	35	24	31	24	30	32
Rb	73	59	15	60	71	45	45	44
Rb error	3	2	1	2	2	2	2	2
Sr	132	150	46	111	152	213	230	332
Sr error	3	3	2	3	3	4	5	5
Υ	16	22	12	34	37	33	31	39
Y error	2	2	2	2	2	2	2	2
Zr	140	160	74	384	471	386	414	419
Zr error	4	4	3	5	7	6	7	6
Nb	19	11	14	36	47	34	44	38
Nb error	3	2	3	2	3	3	3	3
Mo	21	23	21	0	0	0	12	20
Mo								
error	4	3	3	249	276	248	4	4
Ag	0	0	0	0	0	0	0	0
Ag error	1897	1612	1771	1383	1502	1351	1480	1518
Cd	0	0	0	0	0	0	0	0
Cd error	2332	1982	2170	1679	1827	1650	1801	1852
Sn	0	0	0	0	0	0	0	0
Sn error	3816	3281	3580	2739	2994	2688	2926	3019
Sb	0	0	0	0	0	0	0	0
Sb error	5175	4425	4828	3725	4050	3643	3966	4056
Te	278	247	226	123	177	92	138	201
Te error	21	19	20	17	18	17	19	20
W	0	0	0	0	33	0	0	0
W error	646	537	576	453	10	479	520	529
Au	0	0	0	0	0	0	0	0
Au error	253	223	220	185	187	195	201	205
Hg	0	0	0	0	0	0	0	0
Hg error	327	291	321	253	292	259	281	275
Pb	0	0	0	0	0	0	0	0
Pb error	275	234	247	193	203	197	223	221
Bi	0	0	0	0	0	0	0	0
	820	720	739	605	664	598	655	690
Th	30	44	0	0	0	0	0	27
Th error	8	8	1007	817	895	809	887	8
U	0	0	0	0	0	0	0	0
U error	485	451	434	384	420	379	437	425

FROM	425	430	435	440	445	450	455	460
TO	425.5	430.45	435.39	440.58	445.51	450.48	455.59	460.48
Mg								_
(ppm)				24462				
Mg								
error	44561	50567	44309	7526	44790	46113		
Ca	20933	14473	8827	7007	8692	5855	8013	3714
Ca error	177	136	91	99	97	78	97	
Al	39277	37492	41652	41945	45990	44097	45923	46164
Al error	1352	1370	1288	1390	1406	1367	1462	1407
Si	159737	158699	172960	175694	186795	177087	186104	177923
Si error	1411	1437	1402	1957	1548	1453	1562	1467
Р	0	0	0	0	0	0	0	0
P error	1070	1199	1045	1007	1049	1018	1040	1014
Cu	0	0	17	0	0	21	0	0
Cu error	79	82	6	77	82	6	91	84
S	0	0	0	0	0	0	0	0
S error	781	889	767	722	753	740	734	725
K	10095	9579	10595	15081	12570	13544	18873	17640
K error	117	117	114	184	134	136	178	163
Ti	10455	9894	10760	10077	9160	8570	8298	8260
Ti error	261	257	249	260	247	234	245	232
V	101	124	79	84	0	79	68	0
V error	23	23	21	22	210	21	22	201
Cr	0	0	0	0	0	0	97	0
Cr error	287	303	269	288	295	277	28	284
Mn	1032	589	578	559	675	653	556	425
Mn								
error	43	35	32	33	36	34	35	30
Fe	64293	59984	58979	58303	59740	50874	51396	52765
Fe error	512	490	441	623	465	393	413	408
Со	0	0	0	0	0	0	0	0
Co error	957	952	872	877	926	835	891	866
Ni	30	38	36	43	48	36	40	32
Ni error	9	9	8	9	9	8	9	8
Zn	84	62	63	59	74	73	74	91
Zn error	6	5	5	5	6	5	6	6
As	0	0	0	0	0	0	0	0
As error	49	49	46	46	46	47	49	47

Se	0	0	0	0	0	0	0	0
Se error	32	31	29	27	30	28	32	23
Rb	43	44	46	56	51	55	61	60
Rb error	2	2	2	2	2	2	2	2
Sr	257	162	199	125	124	148	175	145
Sr error	4	3	3	3	3	3	3	3
Υ	40	44	42	40	39	40	42	39
Y error	2	2	2	2	2	2	2	2
Zr	459	474	516	479	511	513	458	527
Zr error	6	6	6	7	6	6	6	6
Nb	47	45	50	45	50	51	48	46
Nb error	3	3	3	3	3	3	3	3
Mo	0	12	12	14	14	0	12	0
Мо								
error	264	4	3	3	4	270	3	273
Ag	0	0	0	0	0	0	0	0
Ag error	1431	1485	1370	1420	1464	1453	1550	1455
Cd	0	0	0	0	0	0	0	0
Cd error	1741	1808	1650	1725	1784	1770	1889	1785
Sn	0	0	0	0	0	0	0	0
Sn error	2843	2967	2724	2821	2913	2903	3100	2887
Sb	0	0	0	0	0	0	0	0
Sb error	3862	3992	3684	3812	3913	3961	4170	3905
Te	168	147	136	127	174	174	163	127
Te error	19	19	17	18	18	18	18	18
W	0	0	0	0	0	0	0	0
W error	496	503	471	482	480	494	515	485
Au	0	0	0	0	0	0	0	0
Au error	207	214	184	190	182	198	208	193
Hg	0	0	0	0	0	0	0	0
Hg error	271	261	254	249	278	264	276	267
Pb	0	0	0	0	0	0	0	0
Pb error	212	221	203	212	214	204	227	209
Bi	0	0	0	0	0	0	0	0
Bi error	648	667	626	630	663	655	690	665
Th	0	0	30	0	32	24	0	26
Th error	877	901	7	851	8	7	934	7
U	0	0	0	0	0	0	0	0
U error	401	416	384	393	397	407	425	412

FROM	465	470	475	480	485	490	495	500
	465.52		475.28					
Mg	103.32	170.10	173.20	100.11	103.37	150.10	133.13	300.13
(ppm)	25454	31342	24437	24887				
Mg	25 .5 .	010.1	21.07	2.007				
error	7630	7829	7131	7253	45866	50382	41958	40922
Ca	3673	3485				5807		
Ca error	72	76	71	90	78	78	107	220
Al	42816	44957	44119	43364	37730	37927	47984	44264
Al error	1396	1478	1365	1353	1248	1334	1357	1362
Si	175987	186552	191376	178088	161953	160369	178499	155934
Si error	1980	2117	2021	1925	1319	1376	1424	1383
Р	0	0	0	0	0	0	0	1849
P error	1042	981	932	978	1003	1081	1003	133
Cu	0	0	0	0	0	0	0	31
Cu error	84	87	78	80	74	81	82	7
S	0	0	0	0	0	0	0	0
S error	768	723	670	722	735	824	654	658
K	11292	18313	14085	10232	12974	15206	14652	7397
K error	149	222	169	134	125	147	139	99
Ti	9429	8623	8035	8332	8647	5705	7173	15515
Ti error	252	252	230	232	222	197	215	312
V	92	0	0	0	0	0	0	169
V error	22	207	192	195	189	177	193	26
Cr	0	0	0	0	0	0	0	0
Cr error	286	280	266	279	266	272	281	308
Mn	571	452	609	818	671	607	750	1372
Mn								
error	33	32	33	37	33	33	36	49
	54539							74436
Fe error	590	552	606	599	395	400	402	587
Со	0	0	0	0	0	0	0	0
Co error	855	846	873	868	825	850	850	993
Ni	39	39	37	25	42	29	0	36
Ni error	9	9	9	8	8	8	108	10
Zn	70	47	74	104	85	54	73	112
Zn error	5	5	5	6	5	5	5	7
As	0	0	0	0	0	0	0	0
As error	46	47	44	42	45	49	47	53
Se	0	0	0	0	0	0	0	0
Se error	27	30	29	28	27	29	27	31

Rb	40	64	61	39	51	58	52	65
Rb error	2	2	2	2	2	2	2	2
Sr	126	94	108	134	116	169	293	550
Sr error	3	3	3	3	3	3	4	7
Υ	40	47	41	42	33	32	36	37
Y error	2	2	2	2	2	2	2	2
Zr	499	538	495	487	422	480	360	317
Zr error	7	7	7	7	5	6	5	5
Nb	51	55	34	60	43	35	36	33
Nb error	3	3	3	3	3	3	3	3
Mo	0	11	0	0	0	0	0	13
Mo								
error	266	3	255	254	250	269	256	4
Ag	0	0	0	0	0	0	0	0
Ag error	1422	1513	1384	1382	1368	1460	1431	1373
Cd	0	0	0	0	0	0	0	0
Cd error	1735	1837	1689	1690	1672	1784	1729	1675
Sn	0	0	0	0	0	0	0	0
Sn error	2826	3000	2737	2744	2732	2907	2838	2708
Sb	0	0	0	0	0	0	0	0
Sb error	3838	4073	3720	3714	3687	3962	3842	3647
Te	132	167	126	171	125	135	125	136
Te error	17	18	17	17	17	18	17	19
W	0	0	0	0	0	0	0	0
W error	487	506	458	485	472	485	455	502
Au	0	0	0	0	0	0	0	0
Au error	189	208	186	190	177	184	190	191
Hg	0	0	0	0	0	0	0	0
Hg error	254	262	248	251	252	275	247	264
Pb	9	0	0	0	0	8	0	16
Pb error	3	218	195	191	204	3	206	3
Bi	0	0	0	0	0	0	0	0
Bi error	647	669	610	625	603	643	644	637
Th	34	0	0	30	0	0	0	0
Th error	7	905	821	7	818	868	872	866
U	0	0	0	0	0	0	0	0
U error	391	416	391	362	366	402	398	417

FROM	505	510	515	520	525	530	536	540
TO		510.48						
Mg								
(ppm)			31652		26901		34245	
Mg								
error	41167	40099	7720	32510	7865	38536	7693	39255
Ca	35624	40264	43273					
Ca error	287		468	363	523		553	
Al	41502	47183	48334	49376	43565	46749	45617	46772
Al error	1352	1425	1446	1427	1396	1412	1402	1399
Si	145583	154087	161106	161657	139232	142721	149912	145673
Si error	1344	1410	1871	1406	1686	1347	1763	1358
Р	0	0	0	0	0	0	0	0
P error	986	977	868	831	938	947	874	970
Cu	55	58	65	173	214	213	345	356
Cu error	8	8	8	11	12	12	15	15
S	0	0	0	0	0	0	0	0
S error	693	685	586	561	635	649	599	643
K	4075	3900	3431	11813	2513	2626	1187	2359
K error	80	82	82	128	73	74	64	72
Ti	16230	15931	17177	19374	14193	13382	14436	13541
Ti error	325	333	363	365	325	308	328	304
V	100	139	92	167	145	145	196	142
V error	26	28	27	30	26	27	27	26
Cr	0	0	0	0	0	0	0	0
Cr error	298	305	294	323	300	329	333	309
Mn	1274	1145	1182	1217	1108	1139	1111	998
Mn								
error	48	48	48	50		48	47	45
	71197							
Fe error	578	571	784	617	882	664	905	666
Со	0	0	0	0	0	0	0	0
Co error	1002	1019	990	1041	1035			1082
Ni	0	38	0	42	57	61	67	96
Ni error	108	10	117	11	11	11	11	12
Zn	87	104	95	92	101	94	101	109
Zn error	6	7	7	7	7	7	7	7
As	0	0	0	10	0	0	0	0
As error	47	51	47	3	47	50	50	46
Se	0	0	0	0	0	0	0	0
Se error	28	29	33	31	31	29	28	30

Rb	20	19	17	26	13	13	45	16
Rb error	2	2	2	2	2	2	2	2
Sr	626	574	549	501	575	788	746	790
Sr error	8	7	8	7	9	9	10	9
Υ	30	29	23	25	22	19	22	15
Y error	2	2	2	2	2	2	2	2
Zr	229	212	194	187	170	149	153	121
Zr error	5	5	5	4	5	5	4	4
Nb	25	27	20	26	20	23	19	19
Nb error	3	3	3	3	3	3	3	3
Mo	0	17	0	17	14	13	12	19
Мо								
error	247	4	247	4	3	4	4	4
Ag	0	0	0	0	0	0	0	0
Ag error	1415	1475	1413	1434	1387	1439	1365	1408
Cd	0	0	0	0	0	0	0	0
Cd error	1720	1798	1718	1732	1689	1742	1666	1727
Sn	0	0	0	0	0	0	0	0
Sn error	2807	2917	2797	2815	2737	2831	2693	2780
Sb	0	0	0	0	0	0	0	0
Sb error	3785	3927	3796	3786	3681	3805	3668	3758
Te	108	149	101	120	85	121	81	97
Te error	19	20	19	20	19	20	19	20
W	0	0	0	0	0	0	0	0
W error	514	535	487	485	464	507	483	534
Au	0	0	0	0	0	0	0	0
Au error	201	197	189	177	183	202	186	209
Hg	0	0	0	0	0	0	0	0
Hg error	275	304	270	276	266	284	267	278
Pb	0	0	0	39	0	0	13	0
Pb error	212	230	210	4	213	224	3	211
Bi	0	0	0	0	0	0	0	0
Bi error	655	688	645	650	639	664	633	638
Th	0	31	0	0	27	0	0	0
Th error	891	9	883	883	8	903	864	871
U	0	0	0	0	0	0	0	0
U error	426	441	429	426	408	457	435	446

FROM	545	550	555	560	566	570	575	580
	545.54		555.46					
Mg								
(ppm)		25060	28391	34544	0	0	0	44443
Mg								
error	40254	7687	7891	7588	35784	35796	38809	7942
Ca	46396	52838	55495	54487	56339	50774	52624	69893
Ca error	371	565	604	574	417	368	400	762
Al	43897	48414	49398	52985	51825	48387	45471	31340
Al error	1350	1430	1463	1473	1402	1321	1374	1284
Si	130630	152089	149277	157409	156702	147454	150363	160905
Si error	1251	1773	1780	1804	1359	1262	1346	1904
Р	0	0	0	0	0	0	0	0
P error	969	914	917	896	901	923	946	870
Cu	335	202	189	176	170	188	86	97
Cu error	14	11	11	10	10	10	8	9
S	0	0	0	0	0	0	0	0
S error	663	614	626	586	609	599	632	540
K	1407	1671	1322	2256	3590	3693	3846	2420
K error	64	69	68	73	78	73	80	75
Ti	13811	8084	7816	7977	8093	7383	7279	8743
Ti error	299	251	252	251	247	225	237	271
V	183	0	96	0	73	114	123	89
V error	26	208	23	205	23	22	23	24
Cr	0	0	0	0	0	84	0	237
Cr error	319	302	307	287	314	28	325	35
Mn	968	984	933	999	995	866	1001	1271
Mn								
error	44	44	44	44	44	40	44	52
Fe								
Fe error	695	676	695	673	491	474	479	809
Со	0	0	0	0	0	0	0	0
Co error	1087	953	968	949	959	932	960	1044
Ni	110	98	94	94	106	82	84	179
Ni error	12	11	11	11	12	10	11	14
Zn –	99	84	105	93	101	105	81	97
Zn error	7	6	7	6	7	6	6	7
As	0	0	0	0	0	0	0	0
As error	48	49	48	47	53	48	51	48
Se	0	0	0	0	0	0	0	0
Se error	29	32	32	32	30	29	30	30

Rb	14	17	12	15	24	22	26	35
Rb error	2	2	1	2	2	2	2	2
Sr	560	821	673	793	869	814	664	358
Sr error	7	11	9	10	9	9	8	6
Υ	18	12	15	16	18	13	14	20
Y error	2	2	2	2	2	2	2	2
Zr	116	129	127	118	127	135	146	112
Zr error	4	4	4	4	4	4	4	4
Nb	19	22	23	20	20	14	24	15
Nb error	3	3	3	3	3	2	3	3
Mo	15	13	18	13	19	13	12	21
Mo								
error	4	3	3	3	3	3	3	4
Ag	0	0	0	0	0	0	0	0
Ag error	1343	1505	1509	1507	1525	1441	1554	1528
Cd	0	0	0	0	0	0	0	0
Cd error	1650	1822	1865	1823	1863	1754	1896	1865
Sn	0	0	0	0	0	0	0	0
Sn error	2675	2967	3021	2974	3040	2892	3096	3049
Sb	0	0	0	0	0	0	0	0
Sb error	3607	4068	4130	4073	4104	3901	4189	4134
Te	73	177	183	148	171	163	193	144
Te error	20	19	19	19	19	18	19	19
W	0	0	0	0	0	0	0	0
W error	482	519	491	498	543	511	542	510
Au	0	0	0	0	0	0	0	0
Au error	182	201	206	192	216	223	219	214
Hg	0	0	0	0	0	0	0	0
Hg error	276	278	276	271	293	268	298	276
Pb	0	0	0	0	0	10	0	0
Pb error	212	230	214	220	231	3	236	207
Bi	0	0	0	0	0	0	0	0
Bi error	618	700	701	687	717	656	703	661
Th	0	25	28	0	34	0	0	0
Th error	842	8	8	936	8	894	960	902
U	0	0	0	0	0	0	0	0
U error	398	475	439	452	464	437	477	401

FROM	585	590	595	600	605	610	615	620
TO	585.44	590.37	595.47	600.46	605.35	610.54	615.36	620.49
Mg								
(ppm)	32562	44777	45532	88559	74666	65570	79521	59615
Mg								
error	8125	7979	8095	7838	8268	7872	8303	7948
Ca	69837	66018	73882	68673	37451	39604	43391	56473
Ca error	781	728	824	747	438	445	508	629
Al	30813	28597	23969	21926	29208	24260	24360	22219
Al error	1282	1244	1193	1168	1298	1183	1234	1167
Si	145900	153722	149318	159779	150855	128875	139343	139315
Si error		1847	1823	1889	1898	1598	1779	1707
Р	0	0	0	0	0	0	0	0
P error	922	916	918	821	1027	1057	964	938
Cu	118	101	87	90	83	87	101	89
Cu error	10	9	9	10	10	10	11	10
S	0	0	0	0	0	0	0	0
S error	582	577	576	529	705	734	685	639
K	1132	393	0	0	1033	2156	1485	1633
K error	66	62	932	901	66	67	67	65
Ti	11867	10463	6933	5121	5527	5252	5815	6094
Ti error	313	291	245	213	212	198	216	220
V	86	0	0	66	80	66	62	95
V error	26	231	212	21	20	19	20	21
Cr	437	591	852	1241	1373	1189	1343	1116
Cr error	40	43	48	54	54	49	54	50
Mn	1238	1118	1259	1528	1475	1457	1616	1357
Mn								
error	52	50	53	57	56	53	58	53
Fe	73456	74675	80920	95122	104661	94203	105791	88171
Fe error	845	845	924	1050	1214	1056	1235	994
Со	0	0	0	0	0	0	0	0
Co error	1051	1044	1096	1130	1170	1089	1165	1093
Ni	208	239	356	574	687	658	741	522
Ni error	15	15	18	22	25	23	26	21
Zn	100	88	66	125	148	154	149	121
Zn error	7	7	6	8	9	8	9	8
As	0	0	0	0	0	0	0	0
As error	48	48	47	43	44	43	40	44
Se	0	0	0	0	0	0	0	0
Se error	33	32	31	24	26	27	28	25

Rb	13	13	8	11	8	14	20	15
Rb error	2	2	1	2	2	2	2	2
Sr	340	445	197	273	329	299	416	417
Sr error	6	7	4	5	6	5	7	7
Υ	21	19	14	11	14	12	8	10
Y error	2	2	2	2	2	2	2	2
Zr	158	165	90	72	96	69	71	84
Zr error	4	4	3	3	4	3	4	4
Nb	15	19	14	14	10	12	20	19
Nb error	3	3	3	3	3	3	3	3
Mo	11	20	12	14	12	0	16	11
Mo								
error	4	4	4	4	4	209	4	3
Ag	0	0	0	0	0	0	0	0
Ag error	1507	1501	1484	1376	1286	1281	1288	1374
Cd	0	0	0	0	0	0	0	0
Cd error	1847	1836	1808	1687	1571	1562	1578	1674
Sn	0	0	0	0	0	0	0	0
Sn error	3034	2979	2957	2730	2575	2557	2579	2747
Sb	0	0	0	0	0	0	0	0
Sb error	4106	4046	4035	3739	3509	3457	3491	3725
Te	167	203	188	120	150	156	163	151
Te error	20	20	20	20	21	20	21	20
W	0	0	0	0	0	0	0	0
W error	493	521	579	441	477	443	456	480
Au	0	0	0	0	0	0	0	0
Au error	198	198	223	161	171	163	169	169
Hg	0	0	0	0	0	0	0	0
Hg error	305	285	309	257	277	241	240	273
Pb	0	0	0	0	0	0	0	0
Pb error	217	212	220	204	201	186	187	200
Bi	0	0	0	0	0	0	0	0
Bi error	665	653	627	585	561	552	566	593
Th	0	0	0	0	0	0	0	0
Th error	906	891	857	794	764	752	774	809
U	0	0	0	0	0	0	0	0
U error	426	429	398	363	347	335	352	389

FROM	625	630	635	640	645	650	654	660
TO	625.5			640.5			654.46	
Mg	023.3	030.47	033.31	040.5	043.40	050.40	054.40	000.41
(ppm)	58796	51602	55692	38288	32684	39389	0	51298
Mg	30730	31002	33032	30200	32004	33363	O	31230
error	7992	8105	7877	8240	7679	7192	35483	7619
	69075	67435	74464	66326				65057
Ca error	765					715		689
Al	25379	23702	28838					32732
Al error	1217	1202	1252		1215			1261
Si	149369	140260	157794	139646				152273
	1812	1737	1871			1751		1766
P	0	0	0	0	0	0	0	0
	887	920	847	952	914	832	897	851
Cu	74	111	93	90	67	109	113	65
Cu error	9	10	10	9	8	9	10	8
S	0	0	0	0	0	0	0	0
S error	581	612	534	596	586	508	587	537
K	1126	1235	1452	980	2105	849	2627	1899
K error	65	65	68	63	68	59	72	68
Ti	7987	8505	9230	9151	11192	10547	10995	10479
Ti error	258	265	279	274	288	279	286	284
V	130	0	93	107	0	102	124	101
V error	24	219	25	24	229	24	26	24
Cr	1030	764	740	712	653	638	614	731
Cr error	52	46	47	45	42	42	43	44
Mn	1410	1168	1286	1150	1168	1166	1089	1146
Mn								
error	56	51	54	51	49	48	49	49
Fe	82583	74173	77545	75973	82219	71483	73062	75686
Fe error	935	855	868	886	902	742	593	823
Со	0	0	0	0	0	0	0	0
Co error	1091	1051	1081	1066	1056	986	1038	1028
Ni	371	311	319	244	254	225	223	241
Ni error	19	17	17	16	16	14	15	15
Zn	124	107	111	115	117	90	137	88
Zn error	8	7	7	7	7	6	8	6
As	0	0	0	0	0	0	0	0
As error	48	47	49	49	45	44	48	46
Se	0	0	0	0	0	0	0	0
Se error	29	30	28	30	29	32	30	29

Rb	14	15	15	13	20	10	21	14
Rb error	2	2	2	2	2	1	2	2
Sr	352	439	482	419	445	441	579	477
Sr error	6	7	8	7	7	7	7	7
Υ	18	16	18	15	16	16	19	22
Y error	2	2	2	2	2	2	2	2
Zr	93	75	110	101	138	106	119	124
Zr error	4	4	4	4	4	4	4	4
Nb	12	15	11	16	22	14	20	15
Nb error	3	3	3	3	3	3	3	3
Mo	14	13	19	0	18	0	14	13
Mo								
error	4	3	4	247	3	235	4	3
Ag	0	0	0	0	0	0	0	0
Ag error	1466	1488	1504	1486	1408	1426	1503	1438
Cd	0	0	0	0	0	0	0	0
Cd error	1785	1806	1832	1825	1710	1730	1833	1766
Sn	0	0	0	0	0	0	0	0
Sn error	2929	2934	3003	2958	2776	2833	2976	2877
Sb	0	0	0	0	0	0	0	0
Sb error	3928	4003	4090	4023	3766	3849	4081	3899
Te	190	202	220	161	156	130	193	163
Te error	20	20	20	20	19	18	20	19
W	0	0	0	0	0	0	0	0
W error	545	533	534	546	498	491	534	473
Au	0	0	0	0	0	0	0	0
Au error	213	203	204	221	197	199	208	199
Hg	0	0	0	0	0	0	0	0
Hg error	269	272	294	289	279	264	272	281
Pb	0	0	0	0	0	0	0	0
Pb error		214	224	215	210	199	222	213
Bi	0	0	0	0	0	0	0	0
Bi error	630	668	652	653	631	632	675	624
Th	0	29	0	0	32	0	0	0
Th error	859	8	886	891	8	864	920	844
U	0	0	0	0	0	0	0	0
U error	406	419	422	426	401	406	442	410

	665		674.13					
ТО	665.48	669.75	674.9	678.05	680.7	683.92	686.9	690.8
Mg								
	45295	99710	84042	98357	74177	60240	48128	76453
Mg								
error	8843	9149	9198	8947	8786	8235	8530	8557
Ca	77852	38094	39281	65916	69220	75276	81974	78793
Ca error	912	483				847	947	914
Al	31013	17953	12734	12327	11301	11164	17719	12307
Al error	1365	1222	1139	1144	1091	1029	1154	1096
Si	162593	133210	128272	144622	133679	141952	131079	148378
	2059	1837	1788	1927	1755	1756	1683	1881
Р	0	0	0	0	0	0	0	0
P error	854	972	1046	894	867	841	860	849
Cu	101	1679	1218	1368	2872	1013	3163	1596
Cu error	10	37	31	33	52	26	56	34
S	0	5004	1526	2695	13877	580	20036	762
S error	553	119	85	97	209	71	272	77
K	1700	0	0	0	0	0	0	0
K error	72	1175	1232	946	895	843	839	881
Ti	10838	4491	3733	3742	5414	5602	5997	5085
Ti error	313	198	185	199	222	219	234	220
V	0	0	0	0	84	88	0	65
V error	241	185	181	184	22	21	192	21
Cr	889	1403	1704	1293	1157	1054	1299	1037
Cr error	51	55	59	56	53	50	56	52
Mn	1262	1666	1549	1370	1078	1358	1389	1376
Mn								
error	55	60	58	57	51	54	58	56
Fe	75415	109093	101830	90960	89311	89330	102861	81095
Fe error	908	1371	1291	1125	1079	1024	1207	963
Co	0	0	0	0	0	0	0	0
Co error	1081	1193	1181	1172	1136	1109	1189	1111
Ni	254	874	984	895	1085	688	1287	577
Ni error	16	29	30	29	31	24	35	23
Zn	146	121	118	88	223	92	190	94
Zn error	8	9	8	8	11	7	11	8
As	0	0	0	0	0	0	0	0
As error	55	43	41	49	44	45	47	49

Se	0	0	0	0	0	0	0	0
Se error	31	31	29	31	35	32	34	34
Rb	19	5	6	0	0	9	11	7
Rb error	2	1	1	53	49	1	2	1
Sr	415	221	172	126	73	170	98	148
Sr error	7	5	4	4	3	4	3	4
Υ	19	8	9	7	9	9	13	14
Y error	2	2	2	2	2	2	2	2
Zr	125	50	45	35	44	53	78	53
Zr error	4	3	3	3	3	3	3	3
Nb	19	16	11	18	0	10	18	0
Nb error	3	3	3	3	161	3	3	173
Mo	21	13	15	0	14	14	21	15
Mo								
error	4	4	4	234	4	3	4	4
Ag	0	0	0	0	0	0	0	0
Ag error	1552	1257	1320	1440	1401	1383	1375	1483
Cd	0	0	0	0	0	0	0	0
Cd error	1916	1541	1596	1752	1708	1687	1677	1810
Sn	0	0	0	0	0	0	0	0
Sn error	3143	2509	2628	2880	2752	2750	2730	2945
Sb	0	0	0	0	0	0	0	0
Sb error	4246	3405	3515	3939	3734	3715	3689	4034
Te	216	94	146	159	113	150	165	145
Te error	21	21	21	21	20	20	21	20
W	0	0	0	0	0	0	0	0
W error	563	442	455	486	559	474	509	532
Au	0	0	0	0	0	0	0	0
Au error	210	178	174	212	211	178	195	200
Hg	0	0	0	0	0	0	0	0
Hg error	314	231	241	260	298	265	274	308
Pb	12	0	0	0	0	0	0	0
Pb error	3	199	192	219	195	201	210	211
Bi	0	0	0	0	0	0	0	0
Bi error	673	544	564	609	595	596	593	623
Th	0	0	0	0	0	0	0	0
Th error	917	744	769	825	805	811	803	842
U	0	0	0	0	0	0	0	0
U error	412	317	347	386	358	359	355	402

-								
FROM	692.85	695.8		700.15			707.2	
TO	693.45	696.65	698.65	701.05	702.1	705	707.75	713.68
Mg								
	79204	41490	30171	0	0	22428	21004	0
Mg								
error		8639						
	82982					1753		
Ca error		529				60		
Al		27648						
			1459					
	154490					226867		
	1968	2062	2191					
	0	0	0	0		0	0	0
P error			892	750		789		
	2749	4284	1081	706	966	0	22	100
Cu error	51	69	24	16	20	85	5	9
S		16980		0	0	0	0	0
S error		245	127	587	837		715	830
K	0	722	9462					
K error	872	69				121		65
Ti	5729	6791	2922		4404	4019		
	236	241	166		175	177	163	233
V	0	73	90	76	62	0	0	89
V error	207	22	19	18	18	167	152	21
Cr	1071	841	172	0	186	157	168	599
Cr error	54	47	29	255	27	27	26	38
Mn	1442	979	596	191	848	453	433	1201
Mn								
	59	48	34	23				46
Fe	95449			21738	51117	45302	44765	
Fe error	1137	1075	546	178	377	456	439	550
Со	0	0	0	0	0	0	0	0
Co error	1185	1154	853	538	829	772	747	987
Ni	951	1456	403	112	156	120	95	187
Ni error	30	37	17	9	11	10	9	13
Zn	120	116	69	190	91	43	34	103
Zn error	9	10	6	7	6	4	4	6
As	0	0	0	0	0	6	0	0
As error	49	51	53	58	56	2	44	46

Se	0	5	0	0	0	0	0	0
Se error	32	2	31	31	31	31	28	30
Rb	9	16	62	27	71	54	41	18
Rb error	2	2	2	1	2	2	2	2
Sr	117	228	311	361	282	145	195	222
Sr error	3	5	5	4	4	3	3	4
Υ	13	13	9	12	17	15	16	21
Y error	2	2	2	1	2	2	2	2
Zr	66	74	128	190	165	138	141	203
Zr error	3	3	3	3	3	3	3	4
Nb	13	15	12	13	17	14	10	28
Nb error	3	3	2	2	2	2	2	3
Mo	17	16	0	10	12	11	12	13
Мо								
error	4	4	253	3	3	3	3	3
Ag	0	0	0	0	0	0	0	0
Ag error	1450	1395	1510	1562	1422	1469	1401	1396
Cd	0	0	0	0	0	0	0	0
Cd error	1768	1686	1845	1907	1729	1787	1716	1707
Sn	0	0	0	0	0	0	0	0
Sn error	2888	2755	3021	3154	2845	2947	2814	2805
Sb	0	0	0	0	0	0	0	0
Sb error	3890	3713	4063	4266	3868	4018	3829	3805
Te	183	131	185	214	209	209	169	184
Te error	21	21	18	16	17	17	16	19
W	0	0	0	0	0	0	0	0
W error	536	503	492	533	461	464	412	487
Au	0	0	0	0	0	0	0	0
Au error	189	195	214	195	191	186	177	201
Hg	0	0	0	0	0	0	0	0
Hg error	271	274	268	280	254	260	237	245
Pb	0	0	13	21	19	0	0	0
Pb error	221	218	3	3	3	192	195	209
Bi	0	0	0	0	0	0	0	0
Bi error	604	600	648	697	625	632	606	608
Th	0	0	0	29	22	21	0	0
Th error	823	814	877	6	7	7	819	820
U	0	0	0	0	0	0	0	0
U error	369	389	428	423	396	395	377	373

FROM	718
TO	718.45
Mg	
(ppm)	24420
Mg	
error	7474
Ca	4816
Ca error	94
Al	69091
Al error	1733
Si	164844
Si error	1836
Р	0
P error	795
Cu	63
Cu error	7
S	0
S error	720
K	40050
K error	425
Ti	4389
Ti error	194
V	102
V error	21
Cr	282
Cr error	33
Mn	447
Mn	
error	32
Fe	43452
Fe error	470
Co	0
Co error	801
Ni	106
Ni error	10
Zn	40
Zn error	4
As	0

As error	50
Se	0
Se error	27
Rb	117
Rb error	3
Sr	261
Sr error	4
Υ	12
Y error	2
Zr	145
Zr error	4
Nb	13
Nb error	2
Мо	12
Мо	
error	3
Ag	0
Ag error	1568
Cd	0
Cd error	1904
Sn	0
Sn error	3149
Sb	0
Sb error	4267
Te	197
Te error	18
W	0
W error	511
Au	0
Au error	209
Hg	0
Hg error	291
Pb	0
Pb error	228
Bi	0
Bi error	686
Th	21
Th error	7
U	0
U error	457
0 01101	+31

Appendix five - Olivine compositions

Abbreviations. Chada- Chadacrystals. Pheno – Phenocrysts

**Fo= $(Mg/(Mg+Fe^{2+}))\times 100$ where Mg and Fe^{2+} are in atoms per formula unit (apfu).

Drill hole	SL-19-026	SL-19-026	SL-19-026	SL-19-026	SL-19-026
Sample	SL23KM44-A-1	SL23KM44-A-2	SL23KM44-A-3	SL23KM44-B-1	SL23KM44-B-2
Depth	1392	1392	1392	1392	1392
Grain area	Core	Core	Rim	Rim	Rim
Habit	Euhedral	Euhedral	Euhedral	Euhedral	Euhedral
Occurence	Chada	Chada	Chada	Pheno	Pheno
Zone	LUZ	LUZ	LUZ	LUZ	LUZ
MgO	41.649	41.296	41.059	40.007	39.774
SiO ₂	39.036	38.781	38.802	38.402	38.545
CaO	0.177	0.170	0.112	0.158	0.141
Cr_2O_3	0.000	0.031	0.000	0.003	0.014
MnO	0.273	0.268	0.279	0.294	0.359
FeO	19.141	18.659	19.464	20.334	20.319
AI_2O_3	0.014	0.012	0.012	0.012	0.015
TiO ₂	0.010	0.011	0.013	0.018	0.016
NiO	0.204	0.204	0.202	0.178	0.176
Total	100.502	99.432	99.943	99.405	99.360
Mg	25.115	24.903	24.760	24.125	23.985
Si	18.246	18.127	18.137	17.950	18.017
Ca	0.126	0.122	0.080	0.113	0.101
Cr	0.000	0.021	0.000	0.002	0.009
Mn	0.211	0.208	0.216	0.227	0.278
Fe	14.878	14.504	15.129	15.806	15.794
Al	0.008	0.006	0.006	0.007	0.008
Ti	0.006	0.007	0.008	0.011	0.009
Ni	0.161	0.160	0.159	0.140	0.138
0	41.751	41.375	41.448	41.025	41.019
Total	100.502	99.432	99.943	99.405	99.360
Fe³ (apfu)	0.010	0.002	0.006	0.006	0.000
Fe² (apfu)	0.398	0.399	0.412	0.435	0.441
Mg (apfu)	1.584	1.585	1.573	1.548	1.540
					184

^{*} Fe³ (apfu) and Fe² (apfu). Amount of ferros and ferric iron in atoms per formula unit, calculated from stoichiometry using charge-balance correction based on oxygen stoichiometry.

Drill hole	SL-19-026	SL-19-026	SL-19-026	SL-19-026	SL-19-026
Sample	SL23KM44-B-3	SL23KM44-C-1	SL23KM44-C-2	SL23KM44-D-1	SL23KM44-D-2
Depth	1392.000	1392.000	1392.000	1392.000	1392.000
Grain area	Rim	Rim	Rim	Rim	Core
Habit	Euhedral	Euhedral	Euhedral	Euhedral	Euhedral
Occurence	Pheno	Chada	Chada	Pheno	Pheno
Zone	LUZ	LUZ	LUZ	LUZ	LUZ
MgO	39.697	40.612	40.142	40.621	40.966
SiO ₂	38.624	38.667	38.833	38.496	39.085
CaO	0.192	0.169	0.233	0.253	0.217
Cr_2O_3	0.000	0.016	0.043	0.005	0.000
MnO	0.321	0.320	0.310	0.286	0.284
FeO	20.394	19.549	19.572	19.560	18.943
AI_2O_3	0.020	0.010	0.011	0.012	0.012
TiO ₂	0.027	0.011	0.011	0.013	0.017
NiO	0.176	0.191	0.191	0.195	0.208
Total	99.450	99.545	99.346	99.441	99.731
Mg	23.938	24.490	24.207	24.496	24.704
Si	18.054	18.074	18.152	17.994	18.269
Ca	0.138	0.121	0.167	0.181	0.155
Cr	0.000	0.011	0.030	0.004	0.000
Mn	0.249	0.248	0.240	0.222	0.220
Fe	15.852	15.196	15.214	15.204	14.724
Al	0.011	0.005	0.006	0.006	0.006
Ti	0.016	0.006	0.007	0.008	0.010
Ni	0.138	0.150	0.150	0.154	0.164
0	41.055	41.244	41.176	41.174	41.479
Total	99.450	99.545	99.346	99.441	99.731
Fe³ (apfu)	0.000	0.002	0.000	0.010	0.000
Fe² (apfu)	0.443	0.420	0.424	0.413	0.407
Mg (apfu)	1.535	1.564	1.548	1.567	1.568
Fo	0.771	0.783	0.780	0.782	0.789

Drill hole	SL-19-026	SL-19-026	SL-19-026	SL-19-026	SL-19-026
Sample	SL23KM44-D-3	SL23KM44-E-1	SL23KM44-E-2	SL23KM44-E-3	SL23KM44-F-1
Depth	1392.000	1392.000	1392.000	1392.000	1392.000
Grain area	Rim	Rim	Rim	Core	Rim
Habit	Euhedral	Subhedral	Subhedral	Subhedral	Subhedral

Occurence Zone	Chada LUZ									
MgO	LOZ	41.315	LOZ	40.317	LUZ	40.448	LUZ	40.394	LUZ	40.127
SiO ₂		38.477		38.446		38.403		38.526		38.362
CaO		0.173		0.125		0.101		0.131		0.187
Cr_2O_3		0.006		0.001		0.003		0.024		0.010
MnO		0.271		0.310		0.328		0.319		0.303
FeO		18.828		19.628		19.774		19.777		19.620
AI_2O_3		0.014		0.014		0.014		0.014		0.011
TiO ₂		0.017		0.016		0.011		0.017		0.012
NiO		0.192		0.184		0.181		0.184		0.190
Total		99.291		99.041		99.262		99.385		98.820
Mg		24.914		24.312		24.391		24.359		24.198
Si		17.985		17.971		17.950		18.008		17.931
Ca		0.124		0.089		0.072		0.094		0.134
Cr		0.004		0.001		0.002		0.016		0.007
Mn		0.210		0.240		0.254		0.247		0.234
Fe		14.635		15.257		15.370		15.373		15.250
Al		0.007		0.008		0.007		0.008		0.006
Ti		0.010		0.010		0.007		0.010		0.007
Ni		0.151		0.144		0.142		0.144		0.149
0		41.252		41.010		41.066		41.127		40.904
Total		99.291		99.041		99.262		99.385		98.820
Fe³ (apfu)		0.016		0.002		0.009		0.004		0.001
Fe² (apfu)		0.390		0.424		0.419		0.424		0.426
Mg (apfu)		1.590		1.561		1.564		1.560		1.558
Fo		0.792		0.781		0.781		0.780		0.780

Drill hole	SL-19-026	SL-19-026	SL-19-026	SL-19-026	SL-19-026
Sample	SL23KM44-F-2	SL23KM44-F-3	SL23KM44-G-1	SL23KM44-G-2	SL23KM44-G-3
Depth	1392.000	1392.000	1392.000	1392.000	1392.000
Grain area	Rim	Rim	Rim	Rim	Core
Habit	Subhedral	Subhedral	Subhedral	Subhedral	Subhedral
Occurence	Chada	Chada	Chada	Chada	Chada
Zone	LUZ	LUZ	LUZ	LUZ	LUZ
MgO	40.324	40.270	42.863	42.649	42.786
SiO ₂	38.593	38.141	39.613	39.646	39.240
CaO	0.135	0.126	0.120	0.137	0.092
Cr ₂ O ₃	0.006	0.000	0.035	0.009	0.008

MnO	0.313	0.312	0.258	0.283	0.253
FeO	19.618	19.439	18.078	17.731	17.825
AI_2O_3	0.015	0.012	0.015	0.020	0.012
TiO ₂	0.018	0.012	0.020	0.028	0.023
NiO	0.188	0.183	0.215	0.213	0.213
Total	99.210	98.494	101.215	100.714	100.451
Mg	24.316	24.284	25.847	25.719	25.801
Si	18.040	17.828	18.516	18.532	18.342
Ca	0.096	0.090	0.086	0.098	0.065
Cr	0.004	0.000	0.024	0.006	0.005
Mn	0.243	0.242	0.200	0.219	0.196
Fe	15.249	15.110	14.052	13.782	13.855
Al	0.008	0.006	0.008	0.010	0.007
Ti	0.011	0.007	0.012	0.017	0.014
Ni	0.147	0.144	0.169	0.167	0.167
0	41.096	40.783	42.302	42.165	41.999
Total	99.210	98.494	101.215	100.714	100.451
Fe³ (apfu)	0.000	0.009	0.004	0.000	0.011
Fe² (apfu)	0.425	0.415	0.376	0.375	0.367
Mg (apfu)	1.558	1.568	1.609	1.606	1.618
Fo	0.781	0.783	0.805	0.807	0.807

Drill hole	SL-19-026	SL-19-026	SL-19-026	SL-19-026	SL-19-026
Sample	SL23KM44-G-4	SL23KM44-H-1	SL23KM44-H-2	SL23KM44-H-3	SL23KM44-I-1
Depth	1392.000	1392.000	1392.000	1392.000	1392.000
Grain area	Core	Core	Rim	Rim	Core
Habit	Subhedral	Euhedral	Euhedral	Euhedral	Subhedral
Occurence	Chada	Chada	Chada	Chada	Chada
Zone	LUZ	LUZ	LUZ	LUZ	LUZ
MgO	42.126	40.623	41.005	41.362	39.989
SiO ₂	39.303	38.881	38.952	38.711	38.528
CaO	0.096	0.111	0.117	0.096	0.153
Cr ₂ O ₃	0.028	0.000	0.011	0.026	0.029
MnO	0.291	0.286	0.307	0.274	0.304
FeO	18.573	18.878	18.925	18.555	19.578
Al_2O_3	0.013	0.015	0.013	0.014	0.013
TiO ₂	0.012	0.017	0.009	0.020	0.019
NiO	0.203	0.194	0.191	0.187	0.192
Total	100.646	99.004	99.530	99.244	98.805

Mg	25.403	24.497	24.727	24.942	24.115
Si	18.371	18.174	18.207	18.095	18.009
Ca	0.068	0.079	0.084	0.069	0.109
Cr	0.019	0.000	0.008	0.018	0.020
Mn	0.225	0.221	0.237	0.212	0.236
Fe	14.437	14.674	14.711	14.423	15.218
Al	0.007	0.008	0.007	0.007	0.007
Ti	0.007	0.010	0.005	0.012	0.012
Ni	0.160	0.153	0.150	0.147	0.151
0	41.947	41.188	41.394	41.320	40.930
Total	100.646	99.004	99.530	99.244	98.805
Fe³ (apfu)	0.003	0.000	0.000	0.003	0.000
Fe ² (apfu)	0.391	0.409	0.408	0.397	0.427
Mg (apfu)	1.595	1.566	1.573	1.589	1.551
Fo	0.798	0.789	0.790	0.795	0.780

Drill hole	SL-19-026	SL-19-026	SL-19-026	SL-19-026	SL-19-026
Sample	SL23KM44-I-2	SL23KM44-J-1	SL23KM44-J-2	SL23KM44-J-3	SL23KM45-A-1
Depth	1392.000	1392.000	1392.000	1392.000	1384.000
Grain area	Rim	Rim	Core	Core	Rim
Habit	Subhedral	Euhedral	Euhedral	Euhedral	Euhedral
Occurence	Chada	Chada	Chada	Chada	Chada
Zone	LUZ	LUZ	LUZ	LUZ	LUZ
MgO	40.367	40.107	40.193	40.225	40.512
SiO ₂	38.898	38.310	38.721	38.492	38.92
CaO	0.081	0.078	0.122	0.154	0.13
Cr ₂ O ₃	0.028	0.018	0.011	0.013	0.038
MnO	0.297	0.347	0.328	0.311	0.31
FeO	19.024	19.909	19.285	19.523	18.902
Al_2O_3	0.015	0.011	0.012	0.010	0.009
TiO ₂	0.028	0.019	0.023	0.019	0.022
NiO	0.199	0.180	0.177	0.183	0.186
Total	98.937	98.978	98.871	98.929	99.037
Mg	24.343	24.186	24.238	24.257	24.430
Si	18.182	17.907	18.099	17.992	18.193
Ca	0.058	0.055	0.087	0.110	0.098
Cr	0.019	0.012	0.008	0.009	0.020
Mn	0.230	0.269	0.254	0.240	0.243
Fe	14.788	15.475	14.990	15.175	14.692
Al	0.008	0.006	0.006	0.005	0.00
					188

Ti	0.017	0.011	0.014	0.011	0.012
Ni	0.156	0.141	0.139	0.143	0.146
0	41.137	40.915	41.037	40.985	41.194
Total	98.937	98.978	98.871	98.929	99.037
Fe³ (apfu)	0.000	0.005	0.000	0.000	0.000
Fe ² (apfu)	0.413	0.428	0.419	0.424	0.410
Mg (apfu)	1.558	1.557	1.555	1.558	1.562
Fo	0.787	0.778	0.784	0.782	0.788

Drill hole	SL-19-026	SL-19-026	SL-19-026	SL-19-026	SL-19-026
Sample	SL23KM45-A-2	SL23KM45-A-3	SL23KM45-A-4	SL23KM45-A-5	SL23KM45-A-6
Depth	1384.000	1384.000	1384.000	1384.000	1384.000
Grain area	Rim	Core	Core	Core	Rim
Habit	Euhedral	Euhedral	Euhedral	Euhedral	Euhedral
Occurence	Chada	Chada	Chada	Chada	Chada
Zone	LUZ	LUZ	LUZ	LUZ	LUZ
MgO	40.661	40.788	40.650	41.143	41.005
SiO ₂	38.911	38.592	39.086	39.063	38.737
CaO	0.224	0.217	0.207	0.230	0.192
Cr_2O_3	0.039	0.009	0.023	0.016	0.037
MnO	0.273	0.256	0.284	0.281	0.281
FeO	18.387	18.222	18.110	18.429	18.195
Al_2O_3	0.013	0.013	0.017	0.021	0.011
TiO ₂	0.023	0.020	0.022	0.018	0.014
NiO	0.191	0.196	0.194	0.194	0.200
Total	98.721	98.314	98.594	99.395	98.671
Mg	24.520	24.596	24.513	24.810	24.727
Si	18.188	18.039	18.270	18.259	18.107
Ca	0.160	0.155	0.148	0.165	0.137
Cr	0.027	0.006	0.016	0.011	0.025
Mn	0.211	0.199	0.220	0.217	0.217
Fe	14.292	14.164	14.077	14.325	14.143
Al	0.007	0.007	0.009	0.011	0.006
Ti	0.014	0.012	0.013	0.011	0.008
Ni	0.150	0.154	0.152	0.153	0.157
0	41.153	40.982	41.175	41.434	41.143
Total	98.721	98.314	98.594	99.395	98.671
Fe³ (apfu)	0.000	0.000	0.000	0.000	0.000
Fe² (apfu)	0.399	0.397	0.393	0.397	0.394

Mg (apfu)	1.569	1.580	1.568	1.577	1.583
Fo	0.793	0.795	0.795	0.794	0.796

Drill hole	SL-19-026	SL-19-026	SL-19-026	SL-19-026	SL-19-026
Sample	SL23KM45-C-1	SL23KM45-C-2	SL23KM45-C-3	SL23KM45-D-1	SL23KM45-D-2
Depth	1384.000	1384.000	1384.000	1384.000	1384.000
Grain area	Rim	Core	Core	Core	Core
Habit	Euhedral	Euhedral	Euhedral	Subhedral	Subhedral
Occurence	Chada	Chada	Chada	Chada	Chada
Zone	LUZ	LUZ	LUZ	LUZ	LUZ
MgO	40.403	40.192	40.397	41.055	40.939
SiO ₂	38.737	38.796	39.084	39.111	38.732
CaO	0.115	0.205	0.129	0.129	0.169
Cr_2O_3	0.000	0.034	0.098	0.020	0.038
MnO	0.305	0.298	0.267	0.277	0.324
FeO	19.024	18.968	18.579	18.114	18.496
AI_2O_3	0.011	0.014	0.006	0.010	0.013
TiO ₂	0.015	0.019	0.017	0.016	0.024
NiO	0.177	0.175	0.185	0.175	0.186
Total	98.787	98.699	98.761	98.906	98.921
Mg	24.364	24.237	24.360	24.757	24.687
Si	18.107	18.134	18.269	18.282	18.104
Ca	0.082	0.146	0.092	0.092	0.121
Cr	0.000	0.023	0.067	0.013	0.026
Mn	0.237	0.231	0.207	0.215	0.251
Fe	14.788	14.744	14.442	14.080	14.377
Al	0.006	0.007	0.003	0.005	0.007
Ti	0.009	0.012	0.010	0.010	0.015
Ni	0.139	0.137	0.145	0.138	0.146
0	41.056	41.028	41.166	41.315	41.187
Total	98.787	98.699	98.761	98.906	98.921
Fe³ (apfu)	0.000	0.000	0.000	0.000	0.000
Fe² (apfu)	0.414	0.413	0.404	0.392	0.400
Mg (apfu)	1.563	1.555	1.558	1.578	1.578
Fo	0.787	0.786	0.791	0.798	0.793

Drill hole	SL-19-026	SL-19-026	SL-19-026	SL-19-026	SL-19-026
Sample	SL23KM45-C-1	SL23KM45-C-2	SL23KM45-C-3	SL23KM45-D-1	SL23KM45-D-2
Depth	1384.000	1384.000	1384.000	1384.000	1384.000
Grain area	Rim	Core	Core	Core	Core

Habit Occurence	Euhedral Chada	Euhedral Chada	Euhedral Chada	Subhedral Chada	Subhedral Chada
Zone MgO	LUZ 40.403	LUZ 40.192	LUZ 40.397	LUZ 41.055	LUZ 40.939
SiO ₂	38.737	38.796	39.084	39.111	38.732
CaO	0.115	0.205	0.129	0.129	0.169
Cr ₂ O ₃	0.000	0.034	0.098	0.020	0.038
MnO	0.305	0.298	0.267	0.277	0.324
FeO	19.024	18.968	18.579	18.114	18.496
AI_2O_3	0.011	0.014	0.006	0.010	0.013
TiO ₂	0.015	0.019	0.017	0.016	0.024
NiO	0.177	0.175	0.185	0.175	0.186
Total	98.787	98.699	98.761	98.906	98.921
Mg	24.364	24.237	24.360	24.757	24.687
Si	18.107	18.134	18.269	18.282	18.104
Ca	0.082	0.146	0.092	0.092	0.121
Cr	0.000	0.023	0.067	0.013	0.026
Mn	0.237	0.231	0.207	0.215	0.251
Fe	14.788	14.744	14.442	14.080	14.377
Al	0.006	0.007	0.003	0.005	0.007
Ti	0.009	0.012	0.010	0.010	0.015
Ni	0.139	0.137	0.145	0.138	0.146
0	41.056	41.028	41.166	41.315	41.187
Total	98.787	98.699	98.761	98.906	98.921
Fe³ (apfu)	0.000	0.000	0.000	0.000	0.000
Fe² (apfu)	0.414	0.413	0.404	0.392	0.400
Mg (apfu)	1.563	1.555	1.558	1.578	1.578
Fo	0.787	0.786	0.791	0.798	0.793

Drill hole	SL-19-026	SL-19-026	SL-19-026	SL-19-026	SL-19-026
Sample	SL23KM45-D-3	SL23KM45-E-1	SL23KM45-E-2	SL23KM45-E-3	SL23KM45-F-1
Depth	1384.000	1384.000	1384.000	1384.000	1384.000
Grain area	Rim	Rim	Rim	Core	Core
Habit	Subhedral	Euhedral	Euhedral	Euhedral	Subhedral
Occurence	Chada	Chada	Chada	Chada	Chada
Zone	LUZ	LUZ	LUZ	LUZ	LUZ
MgO	40.550	40.543	40.190	40.613	40.870
SiO ₂	38.524	38.919	38.802	38.466	38.953
CaO	0.096	0.063	0.173	0.179	0.157

Cr_2O_3	0.017	0.006	0.037	0.000	0.010
MnO	0.303	0.301	0.298	0.316	0.307
FeO	18.623	18.754	18.839	18.675	18.816
AI_2O_3	0.011	0.010	0.013	0.014	0.013
TiO ₂	0.023	0.020	0.017	0.018	0.020
NiO	0.185	0.176	0.180	0.182	0.174
Total	98.331	98.793	98.550	98.465	99.319
Mg	24.453	24.449	24.236	24.491	24.646
Si	18.007	18.192	18.137	17.980	18.208
Ca	0.069	0.045	0.123	0.128	0.112
Cr	0.011	0.004	0.026	0.000	0.007
Mn	0.234	0.233	0.231	0.245	0.238
Fe	14.476	14.577	14.644	14.516	14.626
Al	0.006	0.005	0.007	0.008	0.007
Ti	0.014	0.012	0.010	0.011	0.012
Ni	0.145	0.139	0.141	0.143	0.137
0	40.916	41.136	40.995	40.943	41.328
Total	98.331	98.793	98.550	98.465	99.319
Fe³ (apfu)	0.000	0.000	0.000	0.000	0.000
Fe² (apfu)	0.406	0.407	0.411	0.406	0.406
Mg (apfu)	1.574	1.565	1.557	1.575	1.570
Fo	0.791	0.791	0.787	0.790	0.790

Drill hole	SL-19-026	SL-19-026	SL-19-026	SL-19-026	SL-19-026
Sample	SL23KM45-F-2	SL23KM45-F-3	SL23KM45-G-1	SL23KM45-G-2	SL23KM45-G-3
Depth	1384.000	1384.000	1384.000	1384.000	1384.000
Grain area	Core	Rim	Rim	Core	Core
Habit	Subhedral	Subhedral	Subhedral	Subhedral	Subhedral
Occurence	Chada	Chada	Chada	Chada	Chada
Zone	LUZ	LUZ	LUZ	LUZ	LUZ
MgO	40.560	40.538	41.612	41.499	41.187
SiO ₂	38.751	38.945	38.595	38.737	39.015
CaO	0.214	0.158	0.107	0.180	0.090
Cr ₂ O ₃	0.027	0.008	0.015	0.016	0.014
MnO	0.274	0.322	0.297	0.307	0.269
FeO	18.697	19.428	17.748	18.081	17.961
Al_2O_3	0.011	0.016	0.012	0.013	0.015
TiO ₂	0.016	0.017	0.014	0.012	0.012
NiO	0.187	0.193	0.202	0.196	0.196

Total	98.738	99.624	98.601	99.042	98.758
Mg	24.459	24.446	25.093	25.025	24.837
Si	18.113	18.204	18.040	18.107	18.237
Ca	0.153	0.113	0.077	0.129	0.064
Cr	0.019	0.006	0.010	0.011	0.009
Mn	0.213	0.249	0.230	0.238	0.208
Fe	14.533	15.101	13.796	14.055	13.961
Al	0.006	0.008	0.006	0.007	0.008
Ti	0.010	0.010	0.008	0.007	0.007
Ni	0.147	0.152	0.159	0.154	0.154
0	41.086	41.336	41.182	41.310	41.273
Total	98.738	99.624	98.601	99.042	98.758
Fe³ (apfu)	0.000	0.000	0.003	0.002	0.000
Fe² (apfu)	0.406	0.419	0.381	0.388	0.389
Mg (apfu)	1.568	1.557	1.604	1.595	1.585
Fo	0.790	0.784	0.803	0.799	0.800

Drill hole	SL-19-026	SL-19-026	SL-19-026	SL-19-026	SL-19-026
Sample	SL23KM45-H-1	SL23KM45-H-2	SL23KM45-H-3	SL23KM45-H-4	SL23KM45-I-1
Depth	1384.000	1384.000	1384.000	1384.000	1384.000
Grain area	Rim	Rim	Rim	Core	Core
Habit	Subhedral	Subhedral	Subhedral	Subhedral	Euhedral
Occurence	Chada	Chada	Chada	Chada	Pheno
Zone	LUZ	LUZ	LUZ	LUZ	LUZ
MgO	41.784	41.139	41.141	41.363	40.553
SiO ₂	39.271	38.949	38.898	38.947	38.960
CaO	0.159	0.204	0.207	0.149	0.213
Cr ₂ O ₃	0.018	0.017	0.016	0.010	0.012
MnO	0.256	0.266	0.312	0.305	0.283
FeO	17.566	17.387	17.876	18.107	18.665
Al_2O_3	0.014	0.012	0.009	0.017	0.020
TiO ₂	0.024	0.007	0.019	0.002	0.017
NiO	0.202	0.200	0.203	0.199	0.200
Total	99.293	98.181	98.680	99.100	98.922
Mg	25.197	24.808	24.809	24.943	24.454
Si	18.356	18.206	18.182	18.205	18.211
Ca	0.114	0.146	0.148	0.107	0.152
Cr	0.013	0.012	0.011	0.007	0.008
Mn	0.198	0.206	0.241	0.236	0.219
Fe	13.654	13.515	13.895	14.075	14.508
					193

Al	0.007	0.007	0.005	0.009	0.010
Ti	0.014	0.004	0.011	0.001	0.010
Ni	0.159	0.157	0.160	0.156	0.157
0	41.581	41.121	41.218	41.361	41.191
Total	99.293	98.181	98.680	99.100	98.922
Fe³ (apfu)	0.000	0.000	0.000	0.000	0.000
Fe² (apfu)	0.377	0.378	0.387	0.390	0.405
Mg (apfu)	1.596	1.589	1.585	1.588	1.563
Fo	0.805	0.804	0.799	0.798	0.790

Drill hole	SL-19-026	SL-19-026	SL-19-026	SL-19-026	SL-19-026
Sample	SL23KM45-I-2	SL23KM45-I-3	SL23KM45-J-1	SL23KM45-J-2	SL23KM45-J-3
Depth	1384.000	1384.000	1384.000	1384.000	1384.000
Grain area	Core	Rim	Core	Core	Rim
Habit	Euhedral	Euhedral	Euhedral	Euhedral	Euhedral
Occurence	Pheno	Pheno	Chada	Chada	Chada
Zone	LUZ	LUZ	LUZ	LUZ	LUZ
MgO	40.934	40.547	40.521	40.378	40.331
SiO ₂	38.913	38.871	38.839	38.781	38.578
CaO	0.100	0.190	0.158	0.208	0.101
Cr_2O_3	0.011	0.027	0.000	0.032	0.023
MnO	0.308	0.277	0.308	0.315	0.278
FeO	18.328	18.893	18.461	18.319	18.626
Al_2O_3	0.010	0.005	0.016	0.014	0.010
TiO ₂	0.008	0.012	0.012	0.021	0.022
NiO	0.197	0.189	0.187	0.195	0.181
Total	98.809	99.010	98.502	98.264	98.150
Mg	24.684	24.451	24.435	24.349	24.321
Si	18.189	18.169	18.155	18.127	18.032
Ca	0.071	0.136	0.113	0.149	0.072
Cr	0.007	0.018	0.000	0.022	0.016
Mn	0.239	0.214	0.239	0.244	0.215
Fe	14.247	14.686	14.350	14.240	14.478
Al	0.006	0.003	0.008	0.007	0.005
Ti	0.005	0.007	0.007	0.012	0.013
Ni	0.155	0.148	0.147	0.154	0.142
О	41.207	41.178	41.048	40.960	40.855
Total	98.809	99.010	98.502	98.264	98.150
Fe ³ (apfu)	0.000	0.000	0.000	0.000	0.000

Fe² (apfu)	0.397	0.410	0.402	0.400	0.407
Mg (apfu)	1.577	1.564	1.567	1.565	1.568
Fo	0.795	0.788	0.792	0.792	0.791

Drill hole	SL-19-026	SL-19-026	SL-19-026	SL-19-026	SL-19-026	
Sample	SL23KM48-A-1	SL23KM48-A-2	SL23KM48-A-3	SL23KM48-B-1	SL23KM48-B-2	
Depth	1325.000	1325.000	1325.000	1325.000	1325.000	
Grain area	Core	Core	Rim	Rim	Core	
Habit	Euhedral	Euhedral	Euhedral	Subhedral	Subhedral	
Occurence	Chada	Chada	Chada	Chada	Chada	
Zone	LUZ	LUZ	LUZ	LUZ	LUZ	
MgO	42.275	42.135	42.255	42.596	42.490	
SiO ₂	39.358	39.598	39.079	39.348	39.232	
CaO	0.247	0.194	0.137	0.114	0.152	
Cr_2O_3	0.004	0.022	0.007	0.014	0.015	
MnO	0.289	0.296	0.271	0.246	0.204	
FeO	16.655	16.660	16.677	16.143	16.227	
AI_2O_3	0.016	0.014	0.011	0.015	0.021	
TiO ₂	0.021	0.012	0.027	0.028	0.016	
NiO	0.201	0.194	0.191	0.197	0.194	
Total	99.065	99.125	98.655	98.700	98.550	
Mg	25.493	25.409	25.481	25.687	25.622	
Si	18.397	18.509	18.267	18.392	18.338	
Ca	0.176	0.139	0.098	0.081	0.109	
Cr	0.003	0.015	0.005	0.010	0.010	
Mn	0.224	0.229	0.210	0.190	0.158	
Fe	12.946	12.950	12.963	12.548	12.613	
Al	0.008	0.007	0.006	0.008	0.011	
Ti	0.013	0.007	0.016	0.017	0.009	
Ni	0.158	0.152	0.150	0.155	0.153	
0	41.648	41.707	41.460	41.613	41.527	
Total	99.065	99.125	98.655	98.700	98.550	
Fe ³ (apfu)	0.000	0.000	0.000	0.000	0.000	
Fe² (apfu)	0.357	0.357	0.359	0.346	0.349	
Mg (apfu)	1.612	1.604	1.618	1.625	1.625	
Fo	0.814	0.814	0.815	0.821	0.820	

Drill hole	SL-19-026	SL-19-026	SL-19-026	SL-19-026	SL-19-026
Sample	SL23KM48-B-3	SL23KM48-C-1	SL23KM48-C-2	SL23KM48-C-3	SL23KM48-D-1

Grain area Habit Core Core Rim Core Habit Subhedral Subhedral Subhedral Subhedral Subhedral Occurence Chada Chada Chada Chada Chada Zone LUZ LUZ LUZ LUZ LUZ MgO 43.015 42.320 42.322 42.584 42.148 SiO2 39.230 39.473 39.611 39.359 39.178 CaO 0.165 0.231 0.173 0.054 0.168 Cr2O3 0.019 0.039 0.009 0.023 0.030 MnO 0.250 0.271 0.273 0.264 0.310 FeO 16.295 16.857 17.052 16.910 16.815 Al ₂ O3 0.017 0.014 0.020 0.015 0.014 TiO2 0.015 0.009 0.024 0.035 0.020 Nig 99.207 99.406 99.676 99.439 98.873 <th>Depth</th> <th>1325.000</th> <th>1325.000</th> <th>1325.000</th> <th>1325.000</th> <th>1325.000</th>	Depth	1325.000	1325.000	1325.000	1325.000	1325.000
Occurence Zone Chada LUZ AU2.148 AU2.148 AU2.148 AU2.148 AU2.148 AU2.148 AU2.148 AU2.148 AU2.149 AU2.149<	Grain area	Core	Core	Core	Rim	Core
Zone LUZ LUZ LUZ LUZ MgO 43.015 42.320 42.322 42.584 42.148 SiO2 39.230 39.473 39.611 39.359 39.178 CaO 0.165 0.231 0.173 0.054 0.168 Cr2O3 0.019 0.039 0.009 0.023 0.030 MnO 0.250 0.271 0.273 0.264 0.310 FeO 16.295 16.857 17.052 16.910 16.815 Al ₂ O3 0.017 0.014 0.020 0.015 0.014 TiO2 0.015 0.009 0.024 0.035 0.020 NiO 0.201 0.192 0.192 0.195 0.190 Total 99.207 99.406 99.676 99.439 98.873 Mg 25.939 25.520 25.522 25.679 25.416 Si 18.337 18.451 18.515 18.398 18.313	Habit	Subhedral	Subhedral	Subhedral	Subhedral	Subhedral
MgO 43.015 42.320 42.322 42.584 42.148 SiO2 39.230 39.473 39.611 39.359 39.178 CaO 0.165 0.231 0.173 0.054 0.168 Cr2O3 0.019 0.039 0.009 0.023 0.030 MnO 0.250 0.271 0.273 0.264 0.310 FeO 16.295 16.857 17.052 16.910 16.815 Al ₂ O3 0.017 0.014 0.020 0.015 0.014 TiO2 0.015 0.009 0.024 0.035 0.020 NiO 0.201 0.192 0.192 0.195 0.190 Total 99.207 99.406 99.676 99.439 98.873 Mg 25.939 25.520 25.522 25.679 25.416 Si 18.337 18.451 18.515 18.398 18.313 Ca 0.118 0.165 0.124 0.039 0.021	Occurence	Chada	Chada	Chada	Chada	Chada
SiO2 39.230 39.473 39.611 39.359 39.178 CaO 0.165 0.231 0.173 0.054 0.168 Cr2O3 0.019 0.039 0.009 0.023 0.030 MnO 0.250 0.271 0.273 0.264 0.310 FeO 16.295 16.857 17.052 16.910 16.815 Al ₂ O3 0.017 0.014 0.020 0.015 0.014 TiO2 0.015 0.009 0.024 0.035 0.020 NiO 0.201 0.192 0.192 0.195 0.190 Total 99.207 99.406 99.676 99.439 98.873 Mg 25.939 25.520 25.522 25.679 25.416 Si 18.337 18.451 18.515 18.398 18.313 Ca 0.118 0.165 0.124 0.039 0.120 Cr 0.013 0.027 0.006 0.015 0.021 <td>Zone</td> <td>LUZ</td> <td>LUZ</td> <td>LUZ</td> <td>LUZ</td> <td>LUZ</td>	Zone	LUZ	LUZ	LUZ	LUZ	LUZ
CaO 0.165 0.231 0.173 0.054 0.168 Cr₂O₃ 0.019 0.039 0.009 0.023 0.030 MnO 0.250 0.271 0.273 0.264 0.310 FeO 16.295 16.857 17.052 16.910 16.815 Al₂O₃ 0.017 0.014 0.020 0.015 0.014 TiO₂ 0.015 0.009 0.024 0.035 0.020 NiO 0.201 0.192 0.192 0.195 0.190 Total 99.207 99.406 99.676 99.439 98.873 Mg 25.939 25.520 25.522 25.679 25.416 Si 18.337 18.451 18.515 18.398 18.313 Ca 0.118 0.165 0.124 0.039 0.120 Cr 0.013 0.027 0.006 0.015 0.021 Mn 0.194 0.210 0.211 0.204 0.240 <t< td=""><td>MgO</td><td>43.015</td><td>42.320</td><td>42.322</td><td>42.584</td><td>42.148</td></t<>	MgO	43.015	42.320	42.322	42.584	42.148
Cr ₂ O ₃ 0.019 0.039 0.009 0.023 0.030 MnO 0.250 0.271 0.273 0.264 0.310 FeO 16.295 16.857 17.052 16.910 16.815 Al ₂ O ₃ 0.017 0.014 0.020 0.015 0.014 TiO ₂ 0.015 0.009 0.024 0.035 0.020 NiO 0.201 0.192 0.192 0.195 0.190 Total 99.207 99.406 99.676 99.439 98.873 Mg 25.939 25.520 25.522 25.679 25.416 Si 18.337 18.451 18.515 18.398 18.313 Ca 0.118 0.165 0.124 0.039 0.120 Cr 0.013 0.027 0.006 0.015 0.021 Mn 0.194 0.210 0.211 0.204 0.240 Fe 12.666 13.103 13.255 13.144 13.070	SiO ₂	39.230	39.473	39.611	39.359	39.178
MnO 0.250 0.271 0.273 0.264 0.310 FeO 16.295 16.857 17.052 16.910 16.815 Al₂O₃ 0.017 0.014 0.020 0.015 0.014 TiO₂ 0.015 0.009 0.024 0.035 0.020 NiO 0.201 0.192 0.192 0.195 0.190 Total 99.207 99.406 99.676 99.439 98.873 Mg 25.939 25.520 25.522 25.679 25.416 Si 18.337 18.451 18.515 18.398 18.313 Ca 0.118 0.165 0.124 0.039 0.120 Cr 0.013 0.027 0.006 0.015 0.021 Mn 0.194 0.210 0.211 0.204 0.240 Fe 12.666 13.103 13.255 13.144 13.070 Al 0.009 0.008 0.014 0.021 0.012 <	CaO	0.165	0.231	0.173	0.054	0.168
$ \begin{array}{c ccccccccccccccccccccccccccccccccccc$	Cr_2O_3	0.019	0.039	0.009	0.023	0.030
$\begin{array}{c ccccccccccccccccccccccccccccccccccc$	MnO	0.250	0.271	0.273	0.264	0.310
TiO2 0.015 0.009 0.024 0.035 0.020 NiO 0.201 0.192 0.192 0.195 0.190 Total 99.207 99.406 99.676 99.439 98.873 Mg 25.939 25.520 25.522 25.679 25.416 Si 18.337 18.451 18.515 18.398 18.313 Ca 0.118 0.165 0.124 0.039 0.120 Cr 0.013 0.027 0.006 0.015 0.021 Mn 0.194 0.210 0.211 0.204 0.240 Fe 12.666 13.103 13.255 13.144 13.070 Al 0.009 0.008 0.011 0.008 0.007 Ti 0.009 0.005 0.014 0.021 0.012 Ni 0.158 0.151 0.151 0.154 0.149 O 41.764 41.767 41.868 41.777 41.524	FeO	16.295	16.857	17.052	16.910	16.815
NiO 0.201 0.192 0.192 0.195 0.190 Total 99.207 99.406 99.676 99.439 98.873 Mg 25.939 25.520 25.522 25.679 25.416 Si 18.337 18.451 18.515 18.398 18.313 Ca 0.118 0.165 0.124 0.039 0.120 Cr 0.013 0.027 0.006 0.015 0.021 Mn 0.194 0.210 0.211 0.204 0.240 Fe 12.666 13.103 13.255 13.144 13.070 Al 0.009 0.008 0.011 0.008 0.007 Ti 0.009 0.005 0.014 0.021 0.012 Ni 0.158 0.151 0.151 0.154 0.149 O 41.764 41.767 41.868 41.777 41.524 Total 99.207 99.406 99.676 99.439 98.873 <t< td=""><td>Al_2O_3</td><td>0.017</td><td>0.014</td><td>0.020</td><td>0.015</td><td>0.014</td></t<>	Al_2O_3	0.017	0.014	0.020	0.015	0.014
Total 99.207 99.406 99.676 99.439 98.873 Mg 25.939 25.520 25.522 25.679 25.416 Si 18.337 18.451 18.515 18.398 18.313 Ca 0.118 0.165 0.124 0.039 0.120 Cr 0.013 0.027 0.006 0.015 0.021 Mn 0.194 0.210 0.211 0.204 0.240 Fe 12.666 13.103 13.255 13.144 13.070 Al 0.009 0.008 0.011 0.008 0.007 Ti 0.009 0.005 0.014 0.021 0.012 Ni 0.158 0.151 0.151 0.154 0.149 O 41.764 41.767 41.868 41.777 41.524 Total 99.207 99.406 99.676 99.439 98.873 Fe³ (apfu) 0.348 0.360 0.364 0.361 0.361	TiO ₂	0.015	0.009	0.024	0.035	0.020
Mg 25.939 25.520 25.522 25.679 25.416 Si 18.337 18.451 18.515 18.398 18.313 Ca 0.118 0.165 0.124 0.039 0.120 Cr 0.013 0.027 0.006 0.015 0.021 Mn 0.194 0.210 0.211 0.204 0.240 Fe 12.666 13.103 13.255 13.144 13.070 Al 0.009 0.008 0.011 0.008 0.007 Ti 0.009 0.005 0.014 0.021 0.012 Ni 0.158 0.151 0.151 0.154 0.149 O 41.764 41.767 41.868 41.777 41.524 Total 99.207 99.406 99.676 99.439 98.873 Fe³ (apfu) 0.348 0.360 0.364 0.361 0.361 Mg (apfu) 1.635 1.609 1.605 1.619 1.612	NiO	0.201	0.192	0.192	0.195	0.190
Si 18.337 18.451 18.515 18.398 18.313 Ca 0.118 0.165 0.124 0.039 0.120 Cr 0.013 0.027 0.006 0.015 0.021 Mn 0.194 0.210 0.211 0.204 0.240 Fe 12.666 13.103 13.255 13.144 13.070 Al 0.009 0.008 0.011 0.008 0.007 Ti 0.009 0.005 0.014 0.021 0.012 Ni 0.158 0.151 0.151 0.154 0.149 O 41.764 41.767 41.868 41.777 41.524 Total 99.207 99.406 99.676 99.439 98.873 Fe³ (apfu) 0.000 0.000 0.000 0.000 0.000 Fe² (apfu) 0.348 0.360 0.364 0.361 0.361 Mg (apfu) 1.635 1.609 1.605 1.619 1.612	Total	99.207	99.406	99.676	99.439	98.873
Ca 0.118 0.165 0.124 0.039 0.120 Cr 0.013 0.027 0.006 0.015 0.021 Mn 0.194 0.210 0.211 0.204 0.240 Fe 12.666 13.103 13.255 13.144 13.070 Al 0.009 0.008 0.011 0.008 0.007 Ti 0.009 0.005 0.014 0.021 0.012 Ni 0.158 0.151 0.151 0.154 0.149 O 41.764 41.767 41.868 41.777 41.524 Total 99.207 99.406 99.676 99.439 98.873 Fe³ (apfu) 0.000 0.000 0.000 0.000 0.000 Fe² (apfu) 0.348 0.360 0.364 0.361 0.361 Mg (apfu) 1.635 1.609 1.605 1.619 1.612	Mg	25.939	25.520	25.522	25.679	25.416
Cr 0.013 0.027 0.006 0.015 0.021 Mn 0.194 0.210 0.211 0.204 0.240 Fe 12.666 13.103 13.255 13.144 13.070 Al 0.009 0.008 0.011 0.008 0.007 Ti 0.009 0.005 0.014 0.021 0.012 Ni 0.158 0.151 0.151 0.154 0.149 O 41.764 41.767 41.868 41.777 41.524 Total 99.207 99.406 99.676 99.439 98.873 Fe³ (apfu) 0.000 0.000 0.000 0.000 0.000 Fe² (apfu) 0.348 0.360 0.364 0.361 0.361 Mg (apfu) 1.635 1.609 1.605 1.619 1.612	Si	18.337	18.451	18.515	18.398	18.313
Mn 0.194 0.210 0.211 0.204 0.240 Fe 12.666 13.103 13.255 13.144 13.070 Al 0.009 0.008 0.011 0.008 0.007 Ti 0.009 0.005 0.014 0.021 0.012 Ni 0.158 0.151 0.151 0.154 0.149 O 41.764 41.767 41.868 41.777 41.524 Total 99.207 99.406 99.676 99.439 98.873 Fe³ (apfu) 0.000 0.000 0.000 0.000 0.000 Fe² (apfu) 0.348 0.360 0.364 0.361 0.361 Mg (apfu) 1.635 1.609 1.605 1.619 1.612	Ca	0.118	0.165	0.124	0.039	0.120
Fe 12.666 13.103 13.255 13.144 13.070 Al 0.009 0.008 0.011 0.008 0.007 Ti 0.009 0.005 0.014 0.021 0.012 Ni 0.158 0.151 0.151 0.154 0.149 O 41.764 41.767 41.868 41.777 41.524 Total 99.207 99.406 99.676 99.439 98.873 Fe³ (apfu) 0.000 0.000 0.000 0.000 0.000 Fe² (apfu) 0.348 0.360 0.364 0.361 0.361 Mg (apfu) 1.635 1.609 1.605 1.619 1.612	Cr	0.013	0.027	0.006	0.015	0.021
Al 0.009 0.008 0.011 0.008 0.007 Ti 0.009 0.005 0.014 0.021 0.012 Ni 0.158 0.151 0.151 0.154 0.149 O 41.764 41.767 41.868 41.777 41.524 Total 99.207 99.406 99.676 99.439 98.873 Fe³ (apfu) 0.000 0.000 0.000 0.000 0.000 Fe² (apfu) 0.348 0.360 0.364 0.361 0.361 Mg (apfu) 1.635 1.609 1.605 1.619 1.612	Mn	0.194	0.210	0.211	0.204	0.240
Ti 0.009 0.005 0.014 0.021 0.012 Ni 0.158 0.151 0.151 0.154 0.149 O 41.764 41.767 41.868 41.777 41.524 Total 99.207 99.406 99.676 99.439 98.873 Fe³ (apfu) 0.000 0.000 0.000 0.000 0.000 Fe² (apfu) 0.348 0.360 0.364 0.361 0.361 Mg (apfu) 1.635 1.609 1.605 1.619 1.612	Fe	12.666	13.103	13.255	13.144	13.070
Ni 0.158 0.151 0.151 0.154 0.149 O 41.764 41.767 41.868 41.777 41.524 Total 99.207 99.406 99.676 99.439 98.873 Fe³ (apfu) 0.000 0.000 0.000 0.000 0.000 Fe² (apfu) 0.348 0.360 0.364 0.361 0.361 Mg (apfu) 1.635 1.609 1.605 1.619 1.612	Al	0.009	0.008	0.011	0.008	0.007
O 41.764 41.767 41.868 41.777 41.524 Total 99.207 99.406 99.676 99.439 98.873 Fe³ (apfu) 0.000 0.000 0.000 0.000 0.000 Fe² (apfu) 0.348 0.360 0.364 0.361 0.361 Mg (apfu) 1.635 1.609 1.605 1.619 1.612	Ti	0.009	0.005	0.014	0.021	0.012
Total 99.207 99.406 99.676 99.439 98.873 Fe³ (apfu) 0.000 0.000 0.000 0.000 0.000 Fe² (apfu) 0.348 0.360 0.364 0.361 0.361 Mg (apfu) 1.635 1.609 1.605 1.619 1.612	Ni	0.158	0.151	0.151	0.154	0.149
Fe³ (apfu) 0.000 0.000 0.000 0.000 Fe² (apfu) 0.348 0.360 0.364 0.361 0.361 Mg (apfu) 1.635 1.609 1.605 1.619 1.612	0	41.764	41.767	41.868	41.777	41.524
Fe² (apfu) 0.348 0.360 0.364 0.361 0.361 Mg (apfu) 1.635 1.609 1.605 1.619 1.612	Total	99.207	99.406	99.676	99.439	98.873
Mg (apfu) 1.635 1.609 1.605 1.619 1.612	Fe³ (apfu)	0.000	0.000	0.000	0.000	0.000
	Fe² (apfu)	0.348	0.360	0.364	0.361	0.361
0.024 0.042 0.044 0.045 0.043	Mg (apfu)	1.635	1.609	1.605	1.619	1.612
<u>ro 0.821 0.812 0.811 0.815 0.812</u>	Fo	0.821	0.812	0.811	0.815	0.812

Drill hole	SL-19-026	SL-19-026	SL-19-026	SL-19-026	SL-19-026
Sample	SL23KM48-D-2	SL23KM48-E-1	SL23KM48-E-2	SL23KM48-E-3	SL23KM48-E-4
Depth	1325.000	1325.000	1325.000	1325.000	1325.000
Grain area	Rim	Rim	Rim	Core	Core
Habit	Subhedral	Euhedral	Euhedral	Euhedral	Euhedral
Occurence	Chada	Chada	Chada	Chada	Chada
Zone	LUZ	LUZ	LUZ	LUZ	LUZ
MgO	42.332	42.221	42.251	42.188	42.184
SiO ₂	39.161	39.107	39.168	39.331	39.362 196

CaO	0.120	0.155	0.208	0.214	0.202
Cr ₂ O ₃	0.011	0.016	0.018	0.026	0.000
MnO	0.269	0.263	0.245	0.274	0.260
FeO	16.846	16.751	16.477	16.630	16.624
Al_2O_3	0.009	0.012	0.017	0.011	0.014
TiO ₂	0.025	0.015	0.018	0.018	0.018
NiO	0.192	0.186	0.194	0.192	0.196
Total	98.964	98.726	98.595	98.883	98.860
Mg	25.527	25.461	25.479	25.440	25.438
Si	18.305	18.280	18.308	18.385	18.399
Ca	0.085	0.111	0.149	0.153	0.144
Cr	0.008	0.011	0.012	0.017	0.000
Mn	0.209	0.203	0.189	0.212	0.201
Fe	13.094	13.021	12.808	12.927	12.922
Al	0.005	0.006	0.009	0.006	0.007
Ti	0.015	0.009	0.011	0.011	0.011
Ni	0.151	0.146	0.153	0.151	0.154
0	41.566	41.478	41.479	41.582	41.583
Total	98.964	98.726	98.595	98.883	98.860
Fe ³ (apfu)	0.000	0.000	0.000	0.000	0.000
Fe ² (apfu)	0.362	0.360	0.355	0.357	0.357
Mg (apfu)	1.617	1.616	1.617	1.611	1.611
Fo	0.814	0.814	0.816	0.814	0.814

Drill hole	SL-19-026	SL-19-026	SL-19-026	SL-19-026	SL-19-026
Sample	SL23KM48-E-5	SL23KM48-E-6	SL23KM48-F-1	SL23KM48-F-2	SL23KM48-F-3
Depth	1325.000	1325.000	1325.000	1325.000	1325.000
Grain area	Rim	Rim	Rim	Core	Core
Habit	Euhedral	Euhedral	Subhedral	Subhedral	Subhedral
Occurence	Chada	Chada	Chada	Chada	Chada
Zone	LUZ	LUZ	LUZ	LUZ	LUZ
MgO	41.983	42.062	42.053	42.120	42.294
SiO ₂	39.454	39.515	39.159	38.979	39.148
CaO	0.170	0.215	0.112	0.200	0.201
Cr_2O_3	0.018	0.013	0.021	0.020	0.034
MnO	0.268	0.267	0.278	0.302	0.267
FeO	16.847	16.685	16.894	16.744	16.718
Al_2O_3	0.011	0.020	0.014	0.011	0.016
TiO ₂	0.023	0.012	0.020	0.013	0.017

NiO	0.190	0.197	0.197	0.190	0.193
Total	98.964	98.984	98.748	98.578	98.886
Mg	25.317	25.365	25.359	25.400	25.504
Si	18.442	18.470	18.304	18.220	18.299
Ca	0.122	0.153	0.080	0.143	0.144
Cr	0.012	0.009	0.015	0.013	0.023
Mn	0.207	0.207	0.215	0.234	0.207
Fe	13.095	12.969	13.132	13.015	12.995
Al	0.006	0.011	0.007	0.006	0.008
Ti	0.014	0.007	0.012	0.008	0.010
Ni	0.149	0.155	0.155	0.149	0.152
0	41.600	41.639	41.469	41.391	41.545
Total	98.964	98.984	98.748	98.578	98.886
Fe³ (apfu)	0.000	0.000	0.000	0.000	0.000
Fe² (apfu)	0.362	0.358	0.364	0.361	0.359
Mg (apfu)	1.602	1.604	1.610	1.616	1.616
Fo	0.812	0.813	0.812	0.813	0.814

Drill hole	SL-19-026	SL-19-026	SL-19-026	SL-19-026	SL-19-026
Sample	SL23KM48-G-1	SL23KM48-G-2	SL23KM48-G-3	SL23KM48-H-1	SL23KM48-H-2
Depth	1325.000	1325.000	1325.000	1325.000	1325.000
Grain area	Rim	Rim	Core	Core	Core
Habit	Euhedral	Euhedral	Euhedral	Subhedral	Subhedral
Occurence	Chada	Chada	Chada	Chada	Chada
Zone	LUZ	LUZ	LUZ	LUZ	LUZ
MgO	42.258	42.175	42.322	41.925	42.53
SiO ₂	39.035	39.327	39.487	39.357	39.25
CaO	0.108	0.207	0.217	0.268	0.17
Cr ₂ O ₃	0.000	0.022	0.028	0.020	0.00
MnO	0.282	0.288	0.265	0.271	0.25
FeO	16.615	16.805	16.812	16.596	16.56
AI_2O_3	0.019	0.014	0.018	0.015	0.01
TiO ₂	0.025	0.019	0.013	0.013	0.02
NiO	0.190	0.196	0.200	0.187	0.19
Total	98.530	99.053	99.360	98.653	99.01
Mg	25.483	25.433	25.521	25.282	25.65
Si	18.246	18.382	18.457	18.397	18.34
Ca	0.077	0.148	0.155	0.192	0.12
Cr	0.000	0.015	0.019	0.014	0.00
Mn	0.218	0.223	0.205	0.210	0.19
					198

Fe	12.915	13.063	13.068	12.900	12.876
Al	0.010	0.008	0.009	0.008	0.008
Ti	0.015	0.011	0.008	0.008	0.014
Ni	0.149	0.154	0.157	0.147	0.154
0	41.418	41.616	41.761	41.496	41.645
Total	98.530	99.053	99.360	98.653	99.017
Fe³ (apfu)	0.000	0.000	0.000	0.000	0.000
Fe ² (apfu)	0.358	0.361	0.360	0.358	0.355
Mg (apfu)	1.620	1.609	1.609	1.604	1.622
Fo	0.816	0.812	0.813	0.813	0.816

Drill hole	SL-19-026	SL-19-026	SL-19-026	SL-19-026	SL-19-026
Sample	SL23KM48-H-3	SL23KM48-I-1	SL23KM48-I-2	SL23KM48-I-3	SL23KM48-I-4
Depth	1325.000	1325.000	1325.000	1325.000	1325.000
Grain area	Rim	Rim	Core	Core	Rim
Habit	Subhedral	Euhedral	Euhedral	Euhedral	Euhedral
Occurence	Chada	Chada	Chada	Chada	Chada
Zone	LUZ	LUZ	LUZ	LUZ	LUZ
MgO	42.181	42.014	42.177	42.034	42.135
SiO ₂	39.693	39.513	39.621	39.353	39.459
CaO	0.140	0.108	0.151	0.166	0.116
Cr_2O_3	0.000	0.000	0.035	0.025	0.000
MnO	0.267	0.253	0.276	0.261	0.280
FeO	16.913	16.970	16.824	16.575	16.726
AI_2O_3	0.013	0.013	0.023	0.015	0.015
TiO ₂	0.019	0.036	0.014	0.012	0.021
NiO	0.190	0.195	0.193	0.193	0.187
Total	99.415	99.102	99.313	98.634	98.939
Mg	25.436	25.336	25.434	25.347	25.409
Si	18.554	18.469	18.520	18.395	18.444
Ca	0.100	0.077	0.108	0.119	0.083
Cr	0.000	0.000	0.024	0.017	0.000
Mn	0.207	0.196	0.213	0.202	0.216
Fe	13.147	13.191	13.077	12.884	13.001
Al	0.007	0.007	0.012	0.008	0.008
Ti	0.011	0.022	0.009	0.007	0.013
Ni	0.149	0.153	0.152	0.152	0.147
0	41.805	41.651	41.765	41.503	41.618
Total	99.415	99.102	99.313	98.634	98.939
Fe ³ (apfu)	0.000	0.000	0.000	0.000	0.000 199

Fe² (apfu)	0.362	0.364	0.360	0.357	0.359
Mg (apfu)	1.602	1.602	1.604	1.608	1.608
Fo	0.812	0.812	0.813	0.815	0.814

Drill hole	SL-19-026	SL-19-026	SL-19-026	SL-19-026	SL-19-026
Sample	SL23KM48-I-5	SL23KM48-J-1	SL23KM48-J-2	SL23KM48-J-3	SL23KM50-A-1
Depth	1325.000	1325.000	1325.000	1325.000	1236.000
Grain area	Rim	Rim	Rim	Core	Rim
Habit	Euhedral	Euhedral	Euhedral	Euhedral	Euhedral
Occurence	Chada	Chada	Chada	Chada	Pheno
Zone	LUZ	LUZ	LUZ	LUZ	LUZ
MgO	41.920	42.175	42.146	42.079	42.335
SiO ₂	39.758	39.554	39.465	39.296	39.788
CaO	0.123	0.116	0.186	0.203	0.154
Cr_2O_3	0.008	0.004	0.008	0.028	0.022
MnO	0.275	0.245	0.249	0.283	0.264
FeO	16.752	17.258	16.869	16.852	16.745
Al_2O_3	0.015	0.011	0.022	0.012	0.012
TiO ₂	0.023	0.019	0.020	0.007	0.018
NiO	0.191	0.195	0.197	0.183	0.180
Total	99.066	99.577	99.162	98.944	99.518
Mg	25.279	25.433	25.415	25.375	25.529
Si	18.584	18.488	18.447	18.368	18.598
Ca	0.088	0.083	0.133	0.145	0.110
Cr	0.006	0.003	0.006	0.020	0.015
Mn	0.213	0.190	0.193	0.220	0.204
Fe	13.022	13.415	13.112	13.099	13.016
Al	0.008	0.006	0.012	0.006	0.006
Ti	0.014	0.012	0.012	0.004	0.011
Ni	0.150	0.153	0.155	0.144	0.141
0	41.703	41.795	41.678	41.564	41.887
Total	99.066	99.577	99.162	98.945	99.518
Fe ³ (apfu)	0.000	0.000	0.000	0.000	0.000
Fe ² (apfu)	0.360	0.369	0.362	0.362	0.358
Mg (apfu)	1.596	1.602	1.606	1.608	1.605
Fo	0.813	0.810	0.812	0.812	0.814

Drill hole	SL-19-026	SL-19-026	SL-19-026	SL-19-026	SL-19-026
Sample	SL23KM50-A-2	SL23KM50-A-3	SL23KM50-B-1	SL23KM50-B-2	SL23KM50-B-3

Depth	1236.000	1236.000	1236.000	1236.000	1236.000
Grain area	Core	Core	Core	Core	Rim
Habit	Euhedral	Euhedral	Euhedral	Euhedral	Euhedral
Occurence	Pheno	Pheno	Pheno	Pheno	Pheno
Zone	LUZ	LUZ	LUZ	LUZ	LUZ
MgO	42.160	42.435	42.695	42.291	42.267
SiO ₂	39.359	39.547	39.606	39.469	39.374
CaO	0.224	0.179	0.219	0.224	0.143
Cr_2O_3	0.021	0.029	0.006	0.038	0.013
MnO	0.260	0.267	0.273	0.268	0.230
FeO	16.817	16.272	16.406	16.704	16.679
Al_2O_3	0.022	0.022	0.015	0.012	0.016
TiO ₂	0.014	0.022	0.019	0.015	0.020
NiO	0.185	0.183	0.183	0.183	0.188
Total	99.062	98.955	99.422	99.205	98.931
Mg	25.424	25.589	25.746	25.503	25.488
Si	18.397	18.485	18.513	18.449	18.405
Ca	0.160	0.128	0.156	0.160	0.102
Cr	0.014	0.020	0.004	0.026	0.009
Mn	0.201	0.207	0.211	0.208	0.178
Fe	13.072	12.648	12.753	12.984	12.965
Al	0.012	0.011	0.008	0.007	0.009
Ti	0.009	0.013	0.011	0.009	0.012
Ni	0.145	0.144	0.144	0.144	0.148
0	41.628	41.709	41.875	41.716	41.616
Total	99.062	98.955	99.422	99.205	98.931
Fe³ (apfu)	0.000	0.000	0.000	0.000	0.000
Fe ² (apfu)	0.361	0.349	0.350	0.358	0.358
Mg (apfu)	1.608	1.615	1.619	1.610	1.613
Fo	0.812	0.819	0.818	0.814	0.815

Drill hole	SL-19-026	SL-19-026	SL-19-026	SL-19-026	SL-19-026
Sample	SL23KM50-C-1	SL23KM50-C-2	SL23KM50-C-3	SL23KM50-D-1	SL23KM50-D-2
Depth	1236.000	1236.000	1236.000	1236.000	1236.000
Grain area	Rim	Core	Core	Core	Core
Habit	Euhedral	Euhedral	Euhedral	Subhedral	Subhedral
Occurence	Pheno	Pheno	Pheno	Pheno	Pheno
Zone	LUZ	LUZ	LUZ	LUZ	LUZ
MgO	42.566	42.286	42.384	42.656	42.603
SiO ₂	39.441	39.787	39.578	39.689	39.822 201

CaO	0.148	0.208	0.223	0.209	0.211
Cr ₂ O ₃	0.023	0.020	0.015	0.015	0.025
MnO	0.252	0.232	0.246	0.250	0.258
FeO	16.795	16.636	16.921	16.466	16.641
Al_2O_3	0.008	0.011	0.014	0.020	0.021
TiO ₂	0.020	0.010	0.018	0.022	0.017
NiO	0.186	0.185	0.187	0.192	0.191
Total	99.439	99.373	99.587	99.519	99.789
Mg	25.669	25.500	25.559	25.723	25.691
Si	18.436	18.598	18.500	18.552	18.614
Ca	0.105	0.148	0.159	0.149	0.151
Cr	0.016	0.014	0.010	0.010	0.017
Mn	0.195	0.179	0.190	0.194	0.200
Fe	13.055	12.931	13.153	12.799	12.935
Al	0.004	0.006	0.008	0.011	0.011
Ti	0.012	0.006	0.011	0.013	0.010
Ni	0.146	0.145	0.147	0.151	0.150
0	41.801	41.847	41.850	41.918	42.010
Total	99.439	99.373	99.587	99.519	99.789
Fe ³ (apfu)	0.000	0.000	0.000	0.000	0.000
Fe² (apfu)	0.359	0.356	0.361	0.351	0.354
Mg (apfu)	1.617	1.605	1.608	1.616	1.610
Fo	0.815	0.815	0.812	0.817	0.816

Drill hole	SL-19-026	SL-19-026	SL-19-026	SL-19-026	SL-19-026
Sample	SL23KM50-D-3	SL23KM50-E-1	SL23KM50-E-2	SL23KM50-E-3	SL23KM50-F-1
Depth	1236.000	1236.000	1236.000	1236.000	1236.000
Grain area	Rim	Rim	Core	Core	Rim
Habit	Subhedral	Subhedral	Subhedral	Subhedral	Subhedral
Occurence	Pheno	Pheno	Pheno	Pheno	Pheno
Zone	LUZ	LUZ	LUZ	LUZ	LUZ
MgO	42.773	42.523	42.450	42.746	42.600
SiO ₂	39.684	39.723	39.543	39.587	39.810
CaO	0.156	0.151	0.178	0.199	0.091
Cr_2O_3	0.034	0.029	0.039	0.030	0.004
MnO	0.274	0.294	0.264	0.262	0.296
FeO	16.615	17.047	16.493	16.364	16.495
Al_2O_3	0.011	0.012	0.013	0.008	0.009
TiO ₂	0.017	0.018	0.019	0.024	0.025

NiO	0.186	0.189	0.185	0.186	0.184
Total	99.752	99.987	99.185	99.406	99.514
Mg	25.794	25.643	25.598	25.777	25.689
Si	18.549	18.568	18.484	18.504	18.608
Ca	0.112	0.108	0.127	0.142	0.065
Cr	0.024	0.020	0.027	0.021	0.003
Mn	0.212	0.228	0.204	0.203	0.229
Fe	12.915	13.251	12.820	12.720	12.822
Al	0.006	0.007	0.007	0.004	0.005
Ti	0.010	0.011	0.012	0.014	0.015
Ni	0.147	0.148	0.146	0.146	0.145
0	41.984	42.004	41.760	41.875	41.934
Total	99.752	99.987	99.185	99.406	99.514
Fe³ (apfu)	0.000	0.000	0.000	0.000	0.000
Fe² (apfu)	0.353	0.362	0.353	0.349	0.352
Mg (apfu)	1.618	1.607	1.614	1.621	1.613
Fo	0.817	0.812	0.817	0.819	0.818

Drill hole	SL-19-026	SL-19-026	SL-19-026	SL-19-026	SL-19-026
Sample	SL23KM50-F-2	SL23KM50-F-3	SL23KM50-G-1	SL23KM50-G-2	SL23KM50-G-3
Depth	1236.000	1236.000	1236.000	1236.000	1236.000
Grain area	Core	Core	Rim	Core	Core
Habit	Subhedral	Subhedral	Euhedral	Euhedral	Euhedral
Occurence	Pheno	Pheno	Pheno	Pheno	Pheno
Zone	LUZ	LUZ	LUZ	LUZ	LUZ
MgO	42.455	42.185	42.232	42.113	42.40
SiO ₂	39.239	39.557	39.588	39.520	39.34
CaO	0.206	0.198	0.106	0.252	0.22
Cr ₂ O ₃	0.000	0.042	0.033	0.000	0.04
MnO	0.243	0.287	0.294	0.228	0.25
FeO	16.794	16.491	16.654	16.540	16.49
AI_2O_3	0.018	0.014	0.013	0.011	0.02
TiO ₂	0.026	0.023	0.031	0.014	0.01
NiO	0.187	0.188	0.191	0.182	0.18
Total	99.167	98.983	99.142	98.860	98.98
Mg	25.601	25.439	25.467	25.395	25.57
Si	18.341	18.490	18.505	18.473	18.39
Ca	0.147	0.141	0.076	0.180	0.16
Cr	0.000	0.028	0.022	0.000	0.03
Mn	0.189	0.223	0.228	0.177	0.19
					203

Fe	13.054	12.818	12.946	12.857	12.819
Al	0.010	0.008	0.007	0.006	0.011
Ti	0.016	0.014	0.018	0.008	0.010
Ni	0.147	0.148	0.150	0.143	0.146
0	41.663	41.676	41.723	41.621	41.652
Total	99.167	98.983	99.142	98.860	98.987
Fe³ (apfu)	0.000	0.000	0.000	0.000	0.000
Fe² (apfu)	0.360	0.354	0.357	0.355	0.354
Mg (apfu)	1.618	1.607	1.607	1.607	1.616
Fo	0.814	0.815	0.815	0.815	0.816

Drill hole	SL-19-026	SL-19-026	SL-19-026	SL-19-026	SL-19-026
Sample	SL23KM50-H-1	SL23KM50-H-2	SL23KM50-H-3	SL23KM50-I-1	SL23KM50-I-2
Depth	1236.000	1236.000	1236.000	1236.000	1236.000
Grain area	Core	Core	Rim	Core	Core
Habit	Subhedral	Subhedral	Subhedral	Subhedral	Subhedral
Occurence	Pheno	Pheno	Pheno	Pheno	Pheno
Zone	LUZ	LUZ	LUZ	LUZ	LUZ
MgO	42.802	42.493	42.482	42.758	42.639
SiO ₂	39.745	39.349	39.512	39.650	39.552
CaO	0.209	0.234	0.117	0.188	0.224
Cr ₂ O ₃	0.032	0.047	0.003	0.017	0.027
MnO	0.259	0.268	0.266	0.260	0.249
FeO	16.447	16.487	16.607	16.142	16.311
AI_2O_3	0.017	0.015	0.012	0.015	0.022
TiO ₂	0.017	0.013	0.015	0.028	0.021
NiO	0.193	0.187	0.181	0.186	0.182
Total	99.722	99.092	99.194	99.244	99.228
Mg	25.811	25.624	25.618	25.785	25.713
Si	18.578	18.393	18.469	18.534	18.488
Ca	0.149	0.168	0.083	0.134	0.160
Cr	0.022	0.032	0.002	0.011	0.019
Mn	0.201	0.207	0.206	0.202	0.193
Fe	12.784	12.815	12.909	12.548	12.679
Al	0.009	0.008	0.006	0.008	0.011
Ti	0.010	0.008	0.009	0.017	0.013
Ni	0.152	0.147	0.142	0.146	0.143
0	42.006	41.690	41.750	41.861	41.810
Total	99.722	99.092	99.194	99.244	99.228
Fe ³ (apfu)	0.000	0.000	0.000	0.000	0.000 204

Fe² (apfu)	0.350	0.353	0.355	0.345	0.349
Mg (apfu)	1.618	1.618	1.616	1.622	1.619
Fo	0.818	0.816	0.816	0.821	0.819

Drill hole	SL-19-026	SL-19-026	SL-19-026	SL-19-026	SL-19-026
Sample	SL23KM50-I-3	SL23KM50-J-1	SL23KM50-J-2	SL23KM50-J-3	SL23KM56-B-1
Depth	1236.000	1236.000	1236.000	1236.000	1040.000
Grain area	Rim	Rim	Core	Rim	Rim
Habit	Subhedral	Subhedral	Subhedral	Subhedral	Subhedral
Occurence	Pheno	Pheno	Pheno	Pheno	Pheno
Zone	LUZ	LUZ	LUZ	LUZ	UUZ
MgO	42.604	42.691	42.559	42.511	38.274
SiO ₂	39.317	39.485	39.450	39.370	38.484
CaO	0.111	0.204	0.187	0.160	0.133
Cr_2O_3	0.028	0.015	0.032	0.019	0.006
MnO	0.285	0.301	0.263	0.240	0.343
FeO	16.631	16.475	16.502	16.644	21.495
AI_2O_3	0.014	0.017	0.008	0.018	0.011
TiO ₂	0.025	0.014	0.031	0.022	0.024
NiO	0.185	0.184	0.194	0.188	0.152
Total	99.200	99.385	99.224	99.172	98.922
Mg	25.691	25.744	25.664	25.635	23.081
Si	18.378	18.456	18.440	18.403	17.988
Ca	0.079	0.146	0.133	0.114	0.095
Cr	0.019	0.010	0.022	0.013	0.004
Mn	0.220	0.233	0.204	0.186	0.266
Fe	12.927	12.806	12.827	12.938	16.708
Al	0.008	0.009	0.004	0.010	0.006
Ti	0.015	0.008	0.019	0.013	0.014
Ni	0.146	0.145	0.152	0.148	0.119
0	41.716	41.828	41.760	41.713	40.641
Total	99.200	99.385	99.224	99.172	98.922
Fe³ (apfu)	0.000	0.000	0.000	0.000	0.000
Fe² (apfu)	0.356	0.352	0.353	0.356	0.473
Mg (apfu)	1.622	1.621	1.618	1.618	1.495
Fo	0.817	0.817	0.817	0.816	0.756

Drill hole	SL-19-026	SL-19-026	SL-19-026	SL-19-026	SL-19-026
Sample	SL23KM56-B-2	SL23KM56-C-1	SL23KM56-C-2	SL23KM56-D-1	SL23KM56-D-2

Grain area Rim Rim Rim Rim Rim Subhedral Pheno	Depth	1040.000	1040.000	1040.000	1040.000	1040.000
Occurence Zone Pheno UUZ Pheno UUZ	Grain area	Rim	Rim	Rim	Rim	Rim
Zone UUZ UUZ UUZ UUZ MgO 38.480 38.209 38.521 38.437 38.412 SiO₂ 38.821 38.667 38.675 38.632 38.853 CaO 0.165 0.143 0.184 0.156 0.132 Cr₂O₃ 0.000 0.004 0.007 0.006 0.000 MnO 0.313 0.319 0.303 0.329 0.284 FeO 21.046 21.079 21.064 20.583 20.877 Al₂O₃ 0.006 0.016 0.020 0.011 0.016 TiO₂ 0.022 0.034 0.018 0.013 0.017 NiO 0.165 0.151 0.157 0.160 0.159 Total 99.018 98.623 98.950 98.327 98.751 Mg 23.205 23.041 23.229 23.178 23.164 Si 18.146 18.074 18.078 18.058 18.161 C	Habit	Subhedral	Subhedral	Subhedral	Subhedral	Subhedral
MgO 38.480 38.209 38.521 38.437 38.412 SiO₂ 38.821 38.667 38.675 38.632 38.853 CaO 0.165 0.143 0.184 0.156 0.132 Cr₂O₃ 0.000 0.004 0.007 0.006 0.000 MnO 0.313 0.319 0.303 0.329 0.284 FeO 21.046 21.079 21.064 20.583 20.877 Al₂O₃ 0.006 0.016 0.020 0.011 0.016 TiO₂ 0.022 0.034 0.018 0.013 0.017 NiO 0.165 0.151 0.157 0.160 0.159 Total 99.018 98.623 98.950 98.327 98.751 Mg 23.205 23.041 23.229 23.178 23.164 Si 18.146 18.074 18.078 18.058 18.161 Ca 0.118 0.102 0.132 0.111 0.095	Occurence	Pheno	Pheno	Pheno	Pheno	Pheno
SiO2 38.821 38.667 38.675 38.632 38.853 CaO 0.165 0.143 0.184 0.156 0.132 Cr2O3 0.000 0.004 0.007 0.006 0.000 MnO 0.313 0.319 0.303 0.329 0.284 FeO 21.046 21.079 21.064 20.583 20.877 Al ₂ O3 0.006 0.016 0.020 0.011 0.016 TiO2 0.022 0.034 0.018 0.013 0.017 NiO 0.165 0.151 0.157 0.160 0.159 Total 99.018 98.623 98.950 98.327 98.751 Mg 23.205 23.041 23.229 23.178 23.164 Si 18.146 18.074 18.078 18.058 18.161 Ca 0.118 0.102 0.132 0.111 0.095 Cr 0.000 0.003 0.005 0.004 0.000 <td>Zone</td> <td>UUZ</td> <td>UUZ</td> <td>UUZ</td> <td>UUZ</td> <td>UUZ</td>	Zone	UUZ	UUZ	UUZ	UUZ	UUZ
CaO 0.165 0.143 0.184 0.156 0.132 Cr₂O₃ 0.000 0.004 0.007 0.006 0.000 MnO 0.313 0.319 0.303 0.329 0.284 FeO 21.046 21.079 21.064 20.583 20.877 Al₂O₃ 0.006 0.016 0.020 0.011 0.016 TiO₂ 0.022 0.034 0.018 0.013 0.017 NiO 0.165 0.151 0.157 0.160 0.159 Total 99.018 98.623 98.950 98.327 98.751 Mg 23.205 23.041 23.229 23.178 23.164 Si 18.146 18.074 18.078 18.058 18.161 Ca 0.118 0.102 0.132 0.111 0.095 Cr 0.000 0.003 0.005 0.004 0.000 Mn 0.243 0.247 0.234 0.255 0.220 <t< td=""><td>MgO</td><td>38.480</td><td>38.209</td><td>38.521</td><td>38.437</td><td>38.412</td></t<>	MgO	38.480	38.209	38.521	38.437	38.412
Cr₂O₃ 0.000 0.004 0.007 0.006 0.000 MnO 0.313 0.319 0.303 0.329 0.284 FeO 21.046 21.079 21.064 20.583 20.877 Al₂O₃ 0.006 0.016 0.020 0.011 0.016 TiO₂ 0.022 0.034 0.018 0.013 0.017 NiO 0.165 0.151 0.157 0.160 0.159 Total 99.018 98.623 98.950 98.327 98.751 Mg 23.205 23.041 23.229 23.178 23.164 Si 18.146 18.074 18.078 18.058 18.161 Ca 0.118 0.102 0.132 0.111 0.095 Cr 0.000 0.003 0.005 0.004 0.000 Mn 0.243 0.247 0.234 0.255 0.220 Fe 16.359 16.385 16.373 16.000 16.228	SiO ₂	38.821	38.667	38.675	38.632	38.853
MnO 0.313 0.319 0.303 0.329 0.284 FeO 21.046 21.079 21.064 20.583 20.877 Al ₂ O ₃ 0.006 0.016 0.020 0.011 0.016 TiO ₂ 0.022 0.034 0.018 0.013 0.017 NiO 0.165 0.151 0.157 0.160 0.159 Total 99.018 98.623 98.950 98.327 98.751 Mg 23.205 23.041 23.229 23.178 23.164 Si 18.146 18.074 18.078 18.058 18.161 Ca 0.118 0.102 0.132 0.111 0.095 Cr 0.000 0.003 0.005 0.004 0.000 Mn 0.243 0.247 0.234 0.255 0.220 Fe 16.359 16.385 16.373 16.000 16.228 Al 0.003 0.009 0.010 0.006 0.008	CaO	0.165	0.143	0.184	0.156	0.132
FeO 21.046 21.079 21.064 20.583 20.877 Al ₂ O ₃ 0.006 0.016 0.020 0.011 0.016 TiO ₂ 0.022 0.034 0.018 0.013 0.017 NiO 0.165 0.151 0.157 0.160 0.159 Total 99.018 98.623 98.950 98.327 98.751 Mg 23.205 23.041 23.229 23.178 23.164 Si 18.146 18.074 18.078 18.058 18.161 Ca 0.118 0.102 0.132 0.111 0.095 Cr 0.000 0.003 0.005 0.004 0.000 Mn 0.243 0.247 0.234 0.255 0.220 Fe 16.359 16.385 16.373 16.000 16.228 Al 0.003 0.009 0.010 0.006 0.008 Ti 0.013 0.021 0.011 0.008 0.010	Cr_2O_3	0.000	0.004	0.007	0.006	0.000
$\begin{array}{c ccccccccccccccccccccccccccccccccccc$	MnO	0.313	0.319	0.303	0.329	0.284
TiO2 0.022 0.034 0.018 0.013 0.017 NiO 0.165 0.151 0.157 0.160 0.159 Total 99.018 98.623 98.950 98.327 98.751 Mg 23.205 23.041 23.229 23.178 23.164 Si 18.146 18.074 18.078 18.058 18.161 Ca 0.118 0.102 0.132 0.111 0.095 Cr 0.000 0.003 0.005 0.004 0.000 Mn 0.243 0.247 0.234 0.255 0.220 Fe 16.359 16.385 16.373 16.000 16.228 Al 0.003 0.009 0.010 0.006 0.008 Ti 0.013 0.021 0.011 0.008 0.010 Ni 0.130 0.118 0.124 0.126 0.125 O 40.802 40.623 40.753 40.582 40.740	FeO	21.046	21.079	21.064	20.583	20.877
NiO 0.165 0.151 0.157 0.160 0.159 Total 99.018 98.623 98.950 98.327 98.751 Mg 23.205 23.041 23.229 23.178 23.164 Si 18.146 18.074 18.078 18.058 18.161 Ca 0.118 0.102 0.132 0.111 0.095 Cr 0.000 0.003 0.005 0.004 0.000 Mn 0.243 0.247 0.234 0.255 0.220 Fe 16.359 16.385 16.373 16.000 16.228 Al 0.003 0.009 0.010 0.006 0.008 Ti 0.013 0.021 0.011 0.008 0.010 Ni 0.130 0.118 0.124 0.126 0.125 O 40.802 40.623 40.753 40.582 40.740 Total 99.018 98.623 98.950 98.327 98.751 <t< td=""><td>Al_2O_3</td><td>0.006</td><td>0.016</td><td>0.020</td><td>0.011</td><td>0.016</td></t<>	Al_2O_3	0.006	0.016	0.020	0.011	0.016
Total 99.018 98.623 98.950 98.327 98.751 Mg 23.205 23.041 23.229 23.178 23.164 Si 18.146 18.074 18.078 18.058 18.161 Ca 0.118 0.102 0.132 0.111 0.095 Cr 0.000 0.003 0.005 0.004 0.000 Mn 0.243 0.247 0.234 0.255 0.220 Fe 16.359 16.385 16.373 16.000 16.228 Al 0.003 0.009 0.010 0.006 0.008 Ti 0.013 0.021 0.011 0.008 0.010 Ni 0.130 0.118 0.124 0.126 0.125 O 40.802 40.623 40.753 40.582 40.740 Total 99.018 98.623 98.950 98.327 98.751 Fe³ (apfu) 0.000 0.000 0.000 0.000 0.000 <	TiO ₂	0.022	0.034	0.018	0.013	0.017
Mg 23.205 23.041 23.229 23.178 23.164 Si 18.146 18.074 18.078 18.058 18.161 Ca 0.118 0.102 0.132 0.111 0.095 Cr 0.000 0.003 0.005 0.004 0.000 Mn 0.243 0.247 0.234 0.255 0.220 Fe 16.359 16.385 16.373 16.000 16.228 Al 0.003 0.009 0.010 0.006 0.008 Ti 0.013 0.021 0.011 0.008 0.010 Ni 0.130 0.118 0.124 0.126 0.125 O 40.802 40.623 40.753 40.582 40.740 Total 99.018 98.623 98.950 98.327 98.751 Fe³ (apfu) 0.000 0.000 0.000 0.000 0.000 0.000	NiO	0.165	0.151	0.157	0.160	0.159
Si 18.146 18.074 18.078 18.058 18.161 Ca 0.118 0.102 0.132 0.111 0.095 Cr 0.000 0.003 0.005 0.004 0.000 Mn 0.243 0.247 0.234 0.255 0.220 Fe 16.359 16.385 16.373 16.000 16.228 Al 0.003 0.009 0.010 0.006 0.008 Ti 0.013 0.021 0.011 0.008 0.010 Ni 0.130 0.118 0.124 0.126 0.125 O 40.802 40.623 40.753 40.582 40.740 Total 99.018 98.623 98.950 98.327 98.751 Fe³ (apfu) 0.000 0.000 0.000 0.000 0.000 0.000	Total	99.018	98.623	98.950	98.327	98.751
Ca 0.118 0.102 0.132 0.111 0.095 Cr 0.000 0.003 0.005 0.004 0.000 Mn 0.243 0.247 0.234 0.255 0.220 Fe 16.359 16.385 16.373 16.000 16.228 Al 0.003 0.009 0.010 0.006 0.008 Ti 0.013 0.021 0.011 0.008 0.010 Ni 0.130 0.118 0.124 0.126 0.125 O 40.802 40.623 40.753 40.582 40.740 Total 99.018 98.623 98.950 98.327 98.751 Fe³ (apfu) 0.000 0.000 0.000 0.000 0.000 0.000	Mg	23.205	23.041	23.229	23.178	23.164
Cr 0.000 0.003 0.005 0.004 0.000 Mn 0.243 0.247 0.234 0.255 0.220 Fe 16.359 16.385 16.373 16.000 16.228 Al 0.003 0.009 0.010 0.006 0.008 Ti 0.013 0.021 0.011 0.008 0.010 Ni 0.130 0.118 0.124 0.126 0.125 O 40.802 40.623 40.753 40.582 40.740 Total 99.018 98.623 98.950 98.327 98.751 Fe³ (apfu) 0.000 0.000 0.000 0.000 0.000 0.000	Si	18.146	18.074	18.078	18.058	18.161
Mn 0.243 0.247 0.234 0.255 0.220 Fe 16.359 16.385 16.373 16.000 16.228 Al 0.003 0.009 0.010 0.006 0.008 Ti 0.013 0.021 0.011 0.008 0.010 Ni 0.130 0.118 0.124 0.126 0.125 O 40.802 40.623 40.753 40.582 40.740 Total 99.018 98.623 98.950 98.327 98.751 Fe³ (apfu) 0.000 0.000 0.000 0.000 0.000	Ca	0.118	0.102	0.132	0.111	0.095
Fe 16.359 16.385 16.373 16.000 16.228 Al 0.003 0.009 0.010 0.006 0.008 Ti 0.013 0.021 0.011 0.008 0.010 Ni 0.130 0.118 0.124 0.126 0.125 O 40.802 40.623 40.753 40.582 40.740 Total 99.018 98.623 98.950 98.327 98.751 Fe³ (apfu) 0.000 0.000 0.000 0.000 0.000	Cr	0.000	0.003	0.005	0.004	0.000
Al 0.003 0.009 0.010 0.006 0.008 Ti 0.013 0.021 0.011 0.008 0.010 Ni 0.130 0.118 0.124 0.126 0.125 O 40.802 40.623 40.753 40.582 40.740 Total 99.018 98.623 98.950 98.327 98.751 Fe³ (apfu) 0.000 0.000 0.000 0.000 0.000	Mn	0.243	0.247	0.234	0.255	0.220
Ti 0.013 0.021 0.011 0.008 0.010 Ni 0.130 0.118 0.124 0.126 0.125 O 40.802 40.623 40.753 40.582 40.740 Total 99.018 98.623 98.950 98.327 98.751 Fe³ (apfu) 0.000 0.000 0.000 0.000 0.000	Fe	16.359	16.385	16.373	16.000	16.228
Ni 0.130 0.118 0.124 0.126 0.125 O 40.802 40.623 40.753 40.582 40.740 Total 99.018 98.623 98.950 98.327 98.751 Fe³ (apfu) 0.000 0.000 0.000 0.000 0.000	Al	0.003	0.009	0.010	0.006	0.008
O 40.802 40.623 40.753 40.582 40.740 Total 99.018 98.623 98.950 98.327 98.751 Fe³ (apfu) 0.000 0.000 0.000 0.000 0.000	Ti	0.013	0.021	0.011	0.008	0.010
Total 99.018 98.623 98.950 98.327 98.751 Fe³ (apfu) 0.000 0.000 0.000 0.000 0.000	Ni	0.130	0.118	0.124	0.126	0.125
Fe ³ (apfu) 0.000 0.000 0.000 0.000	0	40.802	40.623	40.753	40.582	40.740
	Total	99.018	98.623	98.950	98.327	98.751
Fe ² (apfu) 0.462 0.465 0.462 0.454 0.459	Fe³ (apfu)	0.000	0.000	0.000	0.000	0.000
	Fe² (apfu)	0.462	0.465	0.462	0.454	0.459
Mg (apfu) 1.498 1.494 1.501 1.504 1.497	Mg (apfu)	1.498	1.494	1.501	1.504	1.497
Fo 0.761 0.759 0.761 0.764 0.762	Fo	0.761	0.759	0.761	0.764	0.762

Drill hole	SL-19-026	SL-19-026	SL-19-026	SL-19-026	SL-19-026
Sample	SL23KM56-E-1	SL23KM56-E-2	SL23KM56-F-1	SL23KM56-F-2	SL23KM56-G-1
Depth	1040.000	1040.000	1040.000	1040.000	1040.000
Grain area	Rim	Rim	Rim	Rim	Core
Habit	Subhedral	Subhedral	Subhedral	Subhedral	Subhedral
Occurence	Pheno	Pheno	Pheno	Pheno	Pheno
Zone	UUZ	UUZ	UUZ	UUZ	UUZ
MgO	38.702	38.628	38.501	38.710	38.423
SiO ₂	38.401	38.597	38.618	38.576	38.467
					206

CaO	0.148	0.153	0.131	0.139	0.163
Cr_2O_3	0.012	0.000	0.000	0.009	0.000
MnO	0.310	0.332	0.318	0.305	0.330
FeO	21.054	21.344	21.126	21.307	20.972
Al_2O_3	0.020	0.014	0.020	0.020	0.016
TiO ₂	0.018	0.021	0.022	0.026	0.014
NiO	0.155	0.159	0.157	0.162	0.156
Total	98.820	99.247	98.894	99.253	98.541
Mg	23.338	23.294	23.217	23.343	23.170
Si	17.950	18.041	18.051	18.031	17.980
Ca	0.106	0.109	0.093	0.099	0.117
Cr	0.008	0.000	0.000	0.006	0.000
Mn	0.240	0.257	0.246	0.236	0.256
Fe	16.365	16.591	16.422	16.562	16.302
Al	0.011	0.007	0.011	0.011	0.009
Ti	0.011	0.012	0.013	0.015	0.008
Ni	0.122	0.125	0.124	0.128	0.123
0	40.669	40.810	40.717	40.822	40.577
Total	98.820	99.247	98.894	99.253	98.541
Fe ³ (apfu)	0.000	0.000	0.000	0.000	0.000
Fe ² (apfu)	0.462	0.467	0.464	0.466	0.462
Mg (apfu)	1.511	1.503	1.501	1.506	1.504
Fo	0.762	0.759	0.760	0.760	0.761

Drill hole	SL-19-026	SL-19-026	SL-19-026	SL-19-026	SL-19-026
Sample	SL23KM56-G-2	SL23KM56-H-2	SL23KM56-I-1	SL23KM56-I-2	SL23KM56-J-1
Depth	1040.000	1040.000	1040.000	1040.000	1040.000
Grain area	Rim	Core	Core	Rim	Rim
Habit	Subhedral	Subhedral	Subhedral	Subhedral	Subhedral
Occurence	Pheno	Pheno	Pheno	Pheno	Pheno
Zone	UUZ	UUZ	UUZ	UUZ	UUZ
MgO	38.475	38.737	38.370	38.174	38.336
SiO ₂	38.676	38.584	38.945	38.501	38.706
CaO	0.148	0.118	0.165	0.160	0.166
Cr_2O_3	0.016	0.020	0.000	0.002	0.000
MnO	0.307	0.271	0.327	0.329	0.298
FeO	20.759	21.214	21.169	20.967	21.278
Al_2O_3	0.009	0.016	0.016	0.019	0.016
TiO ₂	0.021	0.022	0.021	0.024	0.018

NiO	0.157	0.151	0.154	0.151	0.151
Total	98.568	99.133	99.168	98.328	98.968
Mg	23.201	23.360	23.138	23.020	23.118
Si	18.078	18.035	18.204	17.996	18.092
Ca	0.106	0.085	0.118	0.115	0.119
Cr	0.011	0.014	0.000	0.001	0.000
Mn	0.238	0.210	0.253	0.255	0.231
Fe	16.136	16.489	16.455	16.298	16.539
Al	0.005	0.009	0.008	0.010	0.009
Ti	0.013	0.013	0.013	0.014	0.011
Ni	0.124	0.118	0.121	0.119	0.118
0	40.657	40.800	40.857	40.500	40.732
Total	98.568	99.133	99.168	98.328	98.968
Fe³ (apfu)	0.000	0.000	0.000	0.000	0.000
Fe² (apfu)	0.457	0.464	0.464	0.463	0.467
Mg (apfu)	1.503	1.508	1.491	1.497	1.494
Fo	0.763	0.761	0.759	0.760	0.758

Drill hole	SL-19-026	SL-19-026	SL-19-026	SL-19-026	SL-19-026
Sample	SL23KM56-J-2	SL23KM60-A-1	SL23KM60-A-2	SL23KM60-A-3	SL23KM60-B-1
Depth	1040.000	895.250	895.250	895.250	895.250
Grain area	Core	Rim	Core	Rim	Rim
Habit	Subhedral	Subhedral	Subhedral	Subhedral	Subhedral
Occurence	Pheno	Pheno	Pheno	Pheno	Pheno
Zone	UUZ	UUZ	UUZ	UUZ	UUZ
MgO	38.388	37.932	37.854	38.128	37.977
SiO ₂	38.724	38.249	38.145	38.163	38.173
CaO	0.199	0.127	0.143	0.107	0.109
Cr ₂ O ₃	0.000	0.000	0.016	0.000	0.000
MnO	0.328	0.335	0.327	0.320	0.302
FeO	21.036	21.693	21.743	21.678	21.609
AI_2O_3	0.022	0.012	0.011	0.012	0.01
TiO ₂	0.025	0.032	0.022	0.031	0.028
NiO	0.152	0.157	0.154	0.156	0.15
Total	98.874	98.536	98.415	98.596	98.369
Mg	23.149	22.874	22.827	22.992	22.903
Si	18.101	17.879	17.830	17.839	17.843
Ca	0.142	0.091	0.102	0.077	0.078
Cr	0.000	0.000	0.011	0.000	0.000
Mn	0.254	0.260	0.254	0.248	0.234
					208

Fe	16.352	16.862	16.901	16.850	16.797
Al	0.012	0.006	0.006	0.006	0.008
Ti	0.015	0.019	0.013	0.019	0.017
Ni	0.119	0.123	0.121	0.123	0.124
0	40.731	40.423	40.351	40.442	40.369
Total	98.874	98.536	98.415	98.596	98.369
Fe³ (apfu)	0.000	0.000	0.000	0.000	0.000
Fe² (apfu)	0.462	0.479	0.481	0.478	0.478
Mg (apfu)	1.497	1.490	1.490	1.497	1.494
Fo	0.760	0.753	0.752	0.754	0.754

Drill hole	SL-19-026	SL-19-026	SL-19-026	SL-19-026	SL-19-026
Sample	SL23KM60-B-2	SL23KM60-B-3	SL23KM60-B-4	SL23KM60-C-1	SL23KM60-C-2
Depth	895.250	895.250	895.250	895.250	895.250
Grain area	Core	Core	Rim	Rim	Core
Habit	Subhedral	Subhedral	Subhedral	Subhedral	Subhedral
Occurence	Pheno	Pheno	Pheno	Pheno	Pheno
Zone	UUZ	UUZ	UUZ	UUZ	UUZ
MgO	38.037	37.956	37.798	38.244	37.854
SiO ₂	38.157	38.593	38.449	38.364	38.367
CaO	0.150	0.131	0.126	0.137	0.146
Cr ₂ O ₃	0.037	0.000	0.024	0.003	0.003
MnO	0.346	0.317	0.337	0.296	0.312
FeO	21.695	21.660	21.473	21.415	21.407
AI_2O_3	0.014	0.015	0.010	0.013	0.014
TiO ₂	0.030	0.023	0.026	0.026	0.023
NiO	0.153	0.147	0.150	0.151	0.149
Total	98.619	98.840	98.394	98.647	98.275
Mg	22.938	22.888	22.793	23.062	22.827
Si	17.835	18.039	17.972	17.932	17.934
Ca	0.108	0.093	0.090	0.098	0.104
Cr	0.025	0.000	0.017	0.002	0.002
Mn	0.268	0.245	0.261	0.229	0.242
Fe	16.864	16.836	16.691	16.646	16.640
Al	0.008	0.008	0.005	0.007	0.008
Ti	0.018	0.014	0.016	0.016	0.014
Ni	0.120	0.116	0.118	0.118	0.117
0	40.436	40.601	40.430	40.538	40.388
Total	98.619	98.840	98.394	98.647	98.275
Fe ³ (apfu)	0.000	0.000	0.000	0.000	0.000 209

Fe² (apfu)	0.479	0.477	0.475	0.472	0.474
Mg (apfu)	1.494	1.484	1.484	1.498	1.488
Fo	0.753	0.753	0.754	0.757	0.755

Drill hole	SL-19-026	SL-19-026	SL-19-026	SL-19-026	SL-19-026
Sample	SL23KM60-C-3	SL23KM60-D-1	SL23KM60-D-2	L23KM60-D-2 SL23KM60-E-1 SL23KM60-	
Depth	895.250	895.250	895.250	895.250	895.250
Grain area	Core	Core	Rim	Rim	Rim
Habit	Subhedral	Subhedral	Subhedral	Subhedral	Subhedral
Occurence	Pheno	Pheno	Pheno	Pheno	Pheno
Zone	UUZ	UUZ	UUZ	UUZ	UUZ
MgO	37.990	37.953	37.853	37.952	37.941
SiO ₂	38.316	38.359	38.396	38.574	38.604
CaO	0.157	0.155	0.145	0.099	0.116
Cr_2O_3	0.030	0.000	0.000	0.000	0.001
MnO	0.328	0.329	0.332	0.309	0.353
FeO	21.771	21.899	21.468	21.699	21.971
Al_2O_3	0.014	0.012	0.012	0.018	0.018
TiO ₂	0.016	0.021	0.024	0.032	0.027
NiO	0.149	0.157	0.157	0.155	0.155
Total	98.770	98.884	98.388	98.839	99.186
Mg	22.909	22.887	22.827	22.886	22.879
Si	17.910	17.930	17.948	18.031	18.045
Ca	0.112	0.111	0.104	0.071	0.083
Cr	0.020	0.000	0.000	0.000	0.001
Mn	0.254	0.254	0.257	0.240	0.273
Fe	16.923	17.022	16.687	16.867	17.078
Al	0.007	0.006	0.006	0.010	0.009
Ti	0.010	0.013	0.014	0.019	0.016
Ni	0.117	0.124	0.123	0.122	0.122
0	40.508	40.538	40.422	40.595	40.679
Total	98.770	98.884	98.388	98.839	99.186
Fe³ (apfu)	0.000	0.000	0.000	0.000	0.000
Fe² (apfu)	0.480	0.483	0.475	0.478	0.483
Mg (apfu)	1.489	1.487	1.487	1.485	1.481
Fo	0.752	0.751	0.754	0.753	0.751

Drill hole	SL-19-026	SL-19-026	SL-19-026	SL-19-026	SL-19-026
Sample	SL23KM60-F-1	SL23KM60-F-2	SL23KM60-G-1	SL23KM60-G-2	SL23KM60-H-1

Depth	895.250	895.250	895.250	895.250	895.250
Grain area	Rim	Core	Rim	Core	Rim
Habit	Subhedral	Subhedral	Subhedral	Subhedral	Subhedral
Occurence	Pheno	Pheno	Pheno	Pheno	Pheno
Zone	UUZ	UUZ	UUZ	UUZ	UUZ
MgO	38.001	38.187	37.709	37.985	38.005
SiO ₂	38.099	38.416	37.976	37.676	38.337
CaO	0.156	0.152	0.128	0.113	0.121
Cr_2O_3	0.009	0.000	0.008	0.010	0.008
MnO	0.318	0.311	0.323	0.293	0.324
FeO	21.475	21.815	21.539	21.686	21.443
Al_2O_3	0.015	0.016	0.012	0.010	0.014
TiO ₂	0.019	0.033	0.025	0.028	0.025
NiO	0.146	0.154	0.151	0.153	0.144
Total	98.236	99.082	97.870	97.952	98.422
Mg	22.915	23.028	22.740	22.906	22.918
Si	17.808	17.957	17.751	17.611	17.920
Ca	0.112	0.109	0.092	0.081	0.087
Cr	0.006	0.000	0.006	0.007	0.006
Mn	0.246	0.241	0.250	0.227	0.251
Fe	16.693	16.957	16.742	16.857	16.668
Al	0.008	0.009	0.006	0.005	0.008
Ti	0.011	0.020	0.015	0.017	0.015
Ni	0.115	0.121	0.119	0.120	0.113
0	40.323	40.643	40.151	40.123	40.437
Total	98.236	99.082	97.870	97.952	98.422
Fe³ (apfu)	0.000	0.000	0.000	0.000	0.000
Fe² (apfu)	0.476	0.479	0.479	0.482	0.474
Mg (apfu)	1.496	1.492	1.491	1.503	1.492
Fo	0.755	0.753	0.753	0.754	0.755

Drill hole	SL-19-026	SL-19-026	SL-19-026	SL-19-026	SL-19-026
Sample	SL23KM60-H-2	SL23KM60-I-1	SL23KM60-I-2	SL23KM60-I-3	SL23KM60-J-1
Depth	895.250	895.250	895.250	895.250	895.250
Grain area	Core	Rim	Core	Core	Rim
Habit	Euhedral	Euhedral	Euhedral	Euhedral	Subhedral
Occurence	Pheno	Pheno	Pheno	Pheno	Pheno
Zone	UUZ	UUZ	UUZ	UUZ	UUZ
MgO	37.971	37.620	37.685	37.772	37.716
SiO ₂	38.519	38.587	38.367	38.509	38.624
					211

CaO	0.170	0.122	0.136	0.141	0.133
Cr ₂ O ₃	0.026	0.000	0.000	0.003	0.027
MnO	0.290	0.319	0.313	0.316	0.294
FeO	21.532	21.346	21.542	21.739	21.466
AI_2O_3	0.013	0.011	0.014	0.014	0.009
TiO ₂	0.019	0.028	0.025	0.024	0.023
NiO	0.150	0.156	0.150	0.152	0.151
Total	98.689	98.191	98.230	98.670	98.442
Mg	22.898	22.686	22.725	22.777	22.744
Si	18.005	18.037	17.934	18.000	18.054
Ca	0.122	0.088	0.097	0.101	0.095
Cr	0.018	0.000	0.000	0.002	0.018
Mn	0.224	0.247	0.242	0.245	0.227
Fe	16.737	16.592	16.745	16.898	16.686
Al	0.007	0.006	0.007	0.007	0.005
Ti	0.012	0.017	0.015	0.014	0.014
Ni	0.117	0.123	0.118	0.119	0.118
0	40.551	40.395	40.348	40.506	40.481
Total	98.689	98.191	98.230	98.670	98.442
Fe³ (apfu)	0.000	0.000	0.000	0.000	0.000
Fe² (apfu)	0.475	0.474	0.478	0.480	0.475
Mg (apfu)	1.487	1.479	1.483	1.481	1.479
Fo	0.754	0.754	0.753	0.752	0.754

Drill hole	SL-19-026	SL-17-18B	SL-17-18B	SL-17-18B	SL-17-18B
Sample	SL23KM60-J-2	SL23KM16-A-1	SL23KM16-A-2	SL23KM16-A-3	SL23KM16-A-4
Depth	895.250	620.000	620.000	620.000	620.000
Grain area	Rim	Rim	Core	Core	Rim
Habit	Subhedral	Euhedral	Euhedral	Euhedral	Euhedral
Occurence	Pheno	Chada	Chada	Chada	Chada
Zone	UUZ	UUZ	UUZ	UUZ	UUZ
MgO	37.955	37.757	37.802	37.562	37.375
SiO ₂	38.092	38.473	38.272	38.528	38.397
CaO	0.136	0.113	0.164	0.139	0.098
Cr_2O_3	0.000	0.018	0.000	0.000	0.031
MnO	0.308	0.322	0.368	0.359	0.373
FeO	21.506	24.160	23.805	23.884	23.511
Al_2O_3	0.009	0.014	0.015	0.023	0.026
TiO ₂	0.023	0.019	0.018	0.024	0.032

NiO	0.156	0.151	0.141	0.140	0.142
Total	98.186	101.026	100.585	100.659	99.984
Mg	22.888	22.768	22.796	22.651	22.538
Si	17.805	17.983	17.889	18.009	17.948
Ca	0.097	0.081	0.117	0.099	0.070
Cr	0.000	0.013	0.000	0.000	0.021
Mn	0.239	0.249	0.285	0.278	0.289
Fe	16.717	18.780	18.504	18.566	18.275
Al	0.005	0.007	0.008	0.012	0.014
Ti	0.014	0.011	0.011	0.014	0.019
Ni	0.123	0.119	0.111	0.110	0.112
0	40.299	41.015	40.865	40.920	40.699
Total	98.186	101.026	100.585	100.659	99.984
Fe³ (apfu)	0.000	0.000	0.005	0.000	0.000
Fe² (apfu)	0.477	0.524	0.514	0.521	0.516
Mg (apfu)	1.496	1.462	1.469	1.458	1.458
Fo	0.755	0.732	0.734	0.733	0.735

-					
Drill hole	SL-17-18B	SL-17-18B	SL-17-18B	SL-17-18B	SL-17-18B
Sample	SL23KM16-B-1	SL23KM16-B-2	SL23KM16-B-3	SL23KM16-C-1	SL23KM16-C-2
Depth	620.000	620.000	620.000	620.000	620.000
Grain area	Rim	Core	Rim	Core	Rim
Habit	Euhedral	Euhedral	Euhedral	Subhedral	Subhedral
Occurence	Chada	Chada	Chada	Pheno	Pheno
Zone	UUZ	UUZ	UUZ	UUZ	UUZ
MgO	37.392	37.205	37.048	37.112	37.043
SiO ₂	38.248	38.258	38.256	38.147	38.026
CaO	0.084	0.160	0.135	0.124	0.135
Cr_2O_3	0.018	0.012	0.004	0.012	0.002
MnO	0.338	0.380	0.380	0.382	0.393
FeO	24.180	24.467	24.338	24.345	24.588
AI_2O_3	0.010	0.009	0.017	0.010	0.009
TiO ₂	0.025	0.025	0.023	0.030	0.017
NiO	0.147	0.154	0.154	0.147	0.149
Total	100.441	100.670	100.353	100.310	100.361
Mg	22.548	22.436	22.341	22.380	22.338
Si	17.878	17.883	17.882	17.831	17.774
Ca	0.060	0.114	0.096	0.089	0.097
Cr	0.012	0.008	0.002	0.008	0.002
Mn	0.262	0.295	0.294	0.296	0.304
					213

Fe	18.795	19.018	18.918	18.924	19.112
Al	0.005	0.005	0.009	0.005	0.005
Ti	0.015	0.015	0.014	0.018	0.010
Ni	0.115	0.121	0.121	0.116	0.117
0	40.750	40.776	40.676	40.644	40.603
Total	100.441	100.670	100.353	100.310	100.361
Fe³ (apfu)	0.000	0.000	0.000	0.000	0.005
Fe ² (apfu)	0.529	0.535	0.533	0.534	0.534
Mg (apfu)	1.457	1.449	1.446	1.450	1.449
Fo	0.730	0.726	0.726	0.727	0.724

Drill hole	SL-17-18B	SL-17-18B	SL-17-18B	SL-17-18B	SL-17-18B
Sample	SL23KM16-C-3	SL23KM16-D-1	SL23KM16-D-2	SL23KM16-E-1	SL23KM16-E-2
Depth	620.000	620.000	620.000	620.000	620.000
Grain area	Rim	Rim	Core	Rim	Rim
Habit	Subhedral	Subhedral	Subhedral	Subhedral	Subhedral
Occurence	Pheno	Pheno	Pheno	Pheno	Pheno
Zone	UUZ	UUZ	UUZ	UUZ	UUZ
MgO	37.301	37.497	37.270	36.864	37.294
SiO ₂	38.637	38.352	38.248	38.130	38.365
CaO	0.141	0.106	0.145	0.108	0.144
Cr ₂ O ₃	0.000	0.000	0.000	0.000	0.029
MnO	0.394	0.367	0.366	0.372	0.360
FeO	24.445	24.185	24.487	24.953	24.366
Al_2O_3	0.010	0.012	0.009	0.009	0.013
TiO ₂	0.024	0.040	0.026	0.018	0.023
NiO	0.142	0.140	0.154	0.155	0.150
Total	101.095	100.700	100.704	100.608	100.743
Mg	22.493	22.612	22.475	22.230	22.490
Si	18.060	17.927	17.878	17.823	17.933
Ca	0.101	0.076	0.104	0.077	0.103
Cr	0.000	0.000	0.000	0.000	0.020
Mn	0.305	0.284	0.284	0.288	0.279
Fe	19.001	18.799	19.034	19.396	18.940
Al	0.005	0.007	0.005	0.005	0.007
Ti	0.015	0.024	0.016	0.011	0.014
Ni	0.111	0.110	0.121	0.122	0.118
0	41.002	40.862	40.789	40.657	40.842
Total	101.095	100.700	100.704	100.608	100.743
Fe ³ (apfu)	0.000	0.000	0.002	0.001	0.000 214

Fe² (apfu)	0.532	0.527	0.533	0.545	0.532
Mg (apfu)	1.445	1.457	1.451	1.440	1.450
Fo	0.727	0.730	0.726	0.721	0.727

Drill hole	SL-17-18B	SL-17-18B	SL-17-18B	SL-17-18B	SL-17-18B
Sample	SL23KM16-E-3	SL23KM16-E-4	SL23KM16-E-5	SL23KM16-F-1	SL23KM16-F-2
Depth	620.000	620.000	620.000	620.000	620.000
Grain area	Core	Core	Rim	Rim	Core
Habit	Subhedral	Subhedral	Subhedral	Subhedral	Subhedral
Occurence	Pheno	Pheno	Pheno	Pheno	Pheno
Zone	UUZ	UUZ	UUZ	UUZ	UUZ
MgO	37.605	36.966	36.996	37.367	36.712
SiO ₂	38.482	38.148	38.049	38.162	37.976
CaO	0.187	0.155	0.084	0.102	0.187
Cr_2O_3	0.000	0.025	0.005	0.003	0.009
MnO	0.356	0.356	0.335	0.331	0.346
FeO	24.284	24.379	24.711	24.435	23.743
AI_2O_3	0.014	0.015	0.013	0.011	0.012
TiO ₂	0.027	0.018	0.028	0.022	0.022
NiO	0.149	0.150	0.151	0.140	0.137
Total	101.103	100.212	100.371	100.573	99.145
Mg	22.677	22.291	22.309	22.534	22.139
Si	17.988	17.831	17.785	17.838	17.751
Ca	0.134	0.111	0.060	0.073	0.133
Cr	0.000	0.017	0.004	0.002	0.006
Mn	0.275	0.276	0.259	0.257	0.268
Fe	18.876	18.950	19.208	18.993	18.455
Al	0.007	0.008	0.007	0.006	0.007
Ti	0.016	0.011	0.017	0.013	0.013
Ni	0.117	0.118	0.118	0.110	0.108
0	41.013	40.599	40.604	40.748	40.265
Total	101.103	100.212	100.371	100.573	99.145
Fe ³ (apfu)	0.000	0.000	0.003	0.005	0.000
Fe ² (apfu)	0.527	0.535	0.539	0.529	0.526
Mg (apfu)	1.456	1.446	1.447	1.456	1.448
Fo	0.729	0.725	0.724	0.728	0.729

Drill hole	SL-17-18B	SL-17-18B	SL-17-18B	SL-17-18B	SL-17-18B
Sample	SL23KM16-F-3	SL23KM16-G-1	SL23KM16-G-2	SL23KM16-G-3	SL23KM16-H-1

Depth	620.000	620.000	620.000	620.000	620.000
Grain area	Core	Rim	Core	Core	Rim
Habit	Subhedral	Subhedral	Subhedral	Subhedral	Euhedral
Occurence	Pheno	Pheno	Pheno	Pheno	Chada
Zone	UUZ	UUZ	UUZ	UUZ	UUZ
MgO	37.248	36.917	37.360	37.497	37.563
SiO ₂	38.540	37.965	38.189	38.003	38.382
CaO	0.139	0.136	0.130	0.137	0.148
Cr ₂ O ₃	0.010	0.005	0.002	0.013	0.021
MnO	0.366	0.365	0.362	0.337	0.372
FeO	23.933	24.416	23.978	24.294	24.148
Al_2O_3	0.015	0.010	0.008	0.008	0.012
TiO ₂	0.020	0.027	0.019	0.022	0.015
NiO	0.147	0.145	0.143	0.144	0.154
Total	100.417	99.986	100.189	100.456	100.815
Mg	22.462	22.262	22.529	22.612	22.651
Si	18.015	17.746	17.851	17.764	17.941
Ca	0.100	0.097	0.093	0.098	0.106
Cr	0.007	0.003	0.001	0.009	0.015
Mn	0.283	0.283	0.280	0.261	0.288
Fe	18.603	18.979	18.638	18.884	18.771
Al	0.008	0.005	0.004	0.004	0.007
Ti	0.012	0.016	0.011	0.013	0.009
Ni	0.116	0.114	0.112	0.114	0.121
0	40.813	40.481	40.670	40.698	40.908
Total	100.417	99.986	100.189	100.456	100.815
Fe³ (apfu)	0.000	0.001	0.000	0.012	0.000
Fe ² (apfu)	0.523	0.536	0.525	0.518	0.526
Mg (apfu)	1.449	1.448	1.459	1.463	1.458
Fo	0.731	0.725	0.731	0.729	0.730

Drill hole	SL-17-18B	SL-17-18B	SL-17-18B	SL-17-18B	SL-17-18B
Sample	SL23KM16-H-2	SL23KM16-H-3	SL23KM16-I-1	SL23KM16-I-2	SL23KM16-J-1
Depth	620.000	620.000	620.000	620.000	620.000
Grain area	Core	Rim	Rim	Core	Core
Habit	Euhedral	Euhedral	Subhedral	Subhedral	Euhedral
Occurence	Chada	Chada	Chada	Chada	Chada
Zone	UUZ	UUZ	UUZ	UUZ	UUZ
MgO	37.960	37.516	37.623	37.709	37.175
SiO ₂	38.681	38.267	38.202	38.100	38.685 216

CaO	0.194	0.106	0.137	0.119	0.157
Cr_2O_3	0.016	0.003	0.000	0.006	0.035
MnO	0.341	0.347	0.366	0.357	0.351
FeO	23.790	24.379	24.373	23.842	24.179
AI_2O_3	0.009	0.012	0.008	0.015	0.006
TiO ₂	0.014	0.024	0.028	0.016	0.017
NiO	0.152	0.144	0.155	0.147	0.146
Total	101.156	100.796	100.891	100.311	100.750
Mg	22.891	22.623	22.688	22.740	22.417
Si	18.080	17.887	17.857	17.809	18.082
Ca	0.139	0.076	0.098	0.085	0.112
Cr	0.011	0.002	0.000	0.004	0.024
Mn	0.264	0.268	0.283	0.276	0.272
Fe	18.492	18.950	18.945	18.532	18.794
Al	0.005	0.007	0.004	0.008	0.003
Ti	0.008	0.014	0.017	0.010	0.010
Ni	0.119	0.113	0.121	0.116	0.114
0	41.147	40.857	40.878	40.731	40.920
Total	101.156	100.796	100.891	100.311	100.750
Fe³ (apfu)	0.000	0.005	0.010	0.008	0.000
Fe² (apfu)	0.515	0.527	0.520	0.513	0.528
Mg (apfu)	1.465	1.458	1.461	1.470	1.443
Fo	0.735	0.729	0.729	0.734	0.728

Drill hole	SL-17-18B
Sample	SL23KM16-J-2
Depth	620.000
Grain area	Rim
Habit	Euhedral
Occurence	Chada
Zone	UUZ
MgO	37.229
SiO ₂	38.426
CaO	0.146
Cr_2O_3	0.000
MnO	0.345
FeO	24.408
AI_2O_3	0.012
TiO ₂	0.019

NiO	0.147
Total	100.731
Mg	22.450
Si	17.962
Ca	0.104
Cr	0.000
Mn	0.267
Fe	18.973
Al	0.006
Ti	0.011
Ni	0.115
0	40.843
Total	100.731
Fe³ (apfu)	0.000
Fe² (apfu)	0.533
Mg (apfu)	1.447
Fo	0.727

Appendix six – Sulfur isotopes

Data obtain by the microdrilling method:

Sample ID	δ^{34} S ‰	Mineral
SL23KM04	-1.3200948	Po (+Ccp)
SL23KM05	-1.4056794	Ро
SL23KM06	-1.6381314	Po (+Ccp)
SL23KM07	-0.6871914	Po (+Ccp)
SL23KM07_duplicate	-0.9122472	
SL23KM08	-1.2281706	Ро
SL23KM09	-0.8657568	Po (+Ccp)
SL23KM10	-1.0432656	Ро
SL23KM41	-1.3496796	Ро
SL23KM42	-0.6100596	Ро
SL23KM43	0.2563524	Ро

Data obtained by the in-situ laser ablation:

Sample ID	Mineral	δ^{34} S ‰
SL23KM05 Ccp-01	Chalcopyrite	-0.65447
SL23KM05 Ccp-02	Chalcopyrite	-0.33035
SL23KM05 Ccp-03	Chalcopyrite	-0.40011
SL23KM05 Ccp-04	Chalcopyrite	-0.62526
SL23KM05 Ccp-05	Chalcopyrite	-0.47853
SL23KM05 Ccp-06	Chalcopyrite	-0.77223
SL23KM05 Ccp-07	Chalcopyrite	-0.36704
SL23KM42 Ccp-01	Chalcopyrite	-0.8263
SL23KM42 Ccp-02	Chalcopyrite	-0.937
SL23KM42 Ccp-03	Chalcopyrite	-0.6391
SL23KM42 Ccp-04	Chalcopyrite	-1.18401
SL23KM42 Ccp-05	Chalcopyrite	-0.90269
SL23KM42 Ccp-06	Chalcopyrite	-0.68941
SL23KM42 Ccp-07	Chalcopyrite	-0.95404
SL23KM42 Ccp-08	Chalcopyrite	-1.42533
SL23KM05 Po-01	Pyrrhotite	-2.29102
SL23KM05 Po-02	Pyrrhotite	-2.09543
SL23KM05 Po-03	Pyrrhotite	-1.73904
SL23KM05 Po-04	Pyrrhotite	-2.56684
SL23KM05 Po-05	Pyrrhotite	-2.19291
SL23KM05 Po-06	Pyrrhotite	-1.18325
SL23KM05 Po-07	Pyrrhotite	-0.63057

SL23KM42 Po-01	Pyrrhotite	-1.15766
SL23KM42 Po-02	Pyrrhotite	-0.75147
SL23KM42 Po-03	Pyrrhotite	-2.06773
SL23KM42 Po-04	Pyrrhotite	-1.5426
SL23KM42 Po-05	Pyrrhotite	-2.43731
SL23KM42 Po-06	Pyrrhotite	-1.4368
SL23KM42 Po-07	Pyrrhotite	-1.9155
SL23KM42 Po-08	Pyrrhotite	-2.68492

Appendix seven – Radiogenic isotopes

 $^{\star}\epsilon Nd$ expresses the deviation of a sample's $^{143}Nd/^{144}Nd$ ratio from the chondritic uniform reservoir

Sample ID	SL23KM01	SL23KM04	SL23KM09	SL23KM22
Depth	718.20	695.20	677.50	560.00
Zone	Quetico	MZ	MZ	UUZ
87Sr/86Sr (init)	0.7168	0.7051	0.7027	0.7039
87Sr/86Sr (current)	0.7342	0.7102	0.7041	0.7046
¹⁴³ Nd/ ¹⁴⁴ Nd (init)	0.5102	0.5106	0.5112	0.5111
¹⁴³ Nd/ ¹⁴⁴ Nd				
(current)	0.5109	0.5116	0.5123	0.5121
¹⁴⁷ Sm/ ¹⁴⁴ Nd	0.0995	0.1399	0.1491	0.1259
*εNd	-18.90	-11.45	0.18	-0.18
Sample ID	SL23KM31	SL23KM40	SL23KM43	SL23KM35
Depth	440.00	1444.18	1406.75	397.50
Zone	GZ	Quetico	MZ	GZ
⁸⁷ Sr/ ⁸⁶ Sr (init)	0.7036	0.7101	0.7048	0.7061
87Sr/86Sr (current)	0.7243	0.7156	0.7072	0.7286
¹⁴³ Nd/ ¹⁴⁴ Nd (init)	0.5112	0.5102	0.5111	0.5110
¹⁴³ Nd/ ¹⁴⁴ Nd				
(current)	0.5120	0.5110	0.5121	0.5118
¹⁴⁷ Sm/ ¹⁴⁴ Nd	0.1127	0.1056	0.1321	0.1127
εNd	0.02	-18.63	-0.21	-2.91
	0.00.00.00	0.00.00.454	010010150	010014150
Sample ID	SL23KM48	SL23KM51	SL23KM56	SL23KM59
Depth	1325.00	1200.05	1040.00	951.60
Zone	LUZ	LUZ	UUZ	UUZ
⁸⁷ Sr/ ⁸⁶ Sr (init)	0.7028	0.7042	0.7028	0.7025
87Sr/86Sr (current)	0.7038	0.7055	0.7036	0.7034
¹⁴³ Nd/ ¹⁴⁴ Nd (init)	0.5111	0.5112	0.5112	0.5112
¹⁴³ Nd/ ¹⁴⁴ Nd	0.5420	0.5422	0.5424	0.5422
(current)	0.5120	0.5123	0.5121	0.5122
¹⁴⁷ Sm/ ¹⁴⁴ Nd	0.1218	0.1574	0.1244	0.1426
εNd	-0.33	0.42	0.05	0.15
Sample ID	SL23KM60	SL23KM65	SL23KM68	SL23KM71
Depth	895.25	630.35	560.70	450.00
Deptil	893.23	030.33	500.70	450.00

Zone	UUZ	GZ	GZ	GZ
87Sr/86Sr (init)	0.7026	0.7038	0.7042	0.7062
87Sr/86Sr (current)	0.7035	0.7049	0.7156	0.7102
¹⁴³ Nd/ ¹⁴⁴ Nd (init)	0.5112	0.5112	0.5112	0.5112
¹⁴³ Nd/ ¹⁴⁴ Nd				
(current)	0.5123	0.5121	0.5120	0.5120
¹⁴⁷ Sm/ ¹⁴⁴ Nd	0.1542	0.1302	0.1125	0.1193
εNd	0.42	0.14	0.33	0.28